X-ray imaging by partially coherent synchrotron light: Application to metallic alloys, tooth dentin and natural rock

vorgelegt von
Diplom-Physiker
Simon Andreas Zabler
aus Karlsruhe

Von der Fakultät III - Prozesswissenschaften
der Technischen Universität Berlin
zur Erlangung des akademischen Grades
Doktor der Naturwissenschaften
Dr. rer. nat.

genehmigte Dissertation

Promotionsausschuss:

Vorsitzender:	Prof. Dr. Helmut Schubert
Berichter:	Prof. Dr. John Banhart
Berichter:	Dr. habil. Oskar Paris

Tag der wissenschaftlichen Aussprache: 9.10.2007

Berlin 2007

D 83

Contents

Introduction

X-rays have strongly influenced a large variety of scientific domains ever since their discovery 120 years ago. First experiments with primitive X-ray tubes began in 1887 with the serbian engineer Nikola Tesla observing visible and *invisible waves*, the latter were later identified as *Bremsstrahlung*. In the year 1897, when Joseph Thomson discovered the electron, Tesla, in his X-ray lecture before the New York Academy of Sciences, could already resume the pioneering work of many scientists that followed his initial observations. First images of of a coin on photographic plates after exposure to X-rays were published in 1894 by Fernando Sanford [San94]. Yet the interpretation of this new photographic effect was discussed controversely [San03]. Heinrich Hertz and Philipp Lenard were making similar experiments and Hermann von Helmholtz formulated mathematical equations based on the electromagnetic theory of light, ignoring the existance of X-rays [Hel92]. In his preliminary communication "Über eine neue Art von Strahlen", submitted to the Würzburg physical-medical society on December 28, 1895, Wilhelm Conrad Röntgen first classified this new radiation as X-rays [Rön95]. His wife's hand's photograph was the first radiography ever showing a human body part. The success was immense and in the following months, Thomas Edison developed a first *real-time* medical radiography device based on a X-ray fluorenscence screen of calcium thungstate. Due to the complete transparency of soft matter, and the translucency of hard mineralized parts in the human body, radiography immediantely became a standard tool in clinical medicine where it is used ever since to study bone fracture and healing.

Meanwhile in 1898 two new highly radioactive substances were discovered by Marie Curie and her husband Pierre: Polonium and Radium [Cur98]. Thanks to their discovery, X-ray imaging made another breakthrough during World War I, with the use of mobile radiography units for the treatment of wounded soldiers, which became popular as "petites Curies", named after their inventor. Unlike the electron-stimulated X-ray emission of a cathode target, these units were carrying tubes of radon gas.

In 1905 Albert Einstein postulated the *photoelectric effect* [Ein05], and almost at the same time Charles Barkla (1906) started to develop a theory of X-ray scattering and discovered the characteristic X-ray emission lines of elements [Bar06]. Experimental physicists discovered the use of X-ray diffraction for the study of solid state and crystallography was born from the important work of Max von Laue, Paul Knipping and Walter Friedrich, published in 1912 [Lau12]. The same year, William Lawrence Bragg formulated an equivalent *law of X-ray diffraction* and developed a X-ray spectrometer, with the help of his father William Henry Bragg [Bra13, Bra14b]. 60 years after Angstrom's first report on the Hα-line, Niels Bohr postulated his model of discrete atomic shells [Boh13], and in 1914 the German physicist Walther Kossel was the first to explain the theory of absorption limits in X-ray spectra

[Kos14]. His studies led Kossel to another discovery in 1920: the X-ray absorption near edge structure [Kos20]. In 1923, Lise Meitner explained the Auger-effect, as a competing process to X-ray fluorescence [Mei23]. The ground was laid for modern quantum mechanics, initiated by Arthur Compton's 1923 paper "A Quantum Theory of the Scattering of X-rays by Light Elements" [Com23]. Ever since, X-ray interactions with matter have played a key role in physics, medicine, astronomy and engineering sciences, fostering our understanding of the physical universe, whereas X-ray imaging had somehow remained at the level of 1895.

Although the mathematical concepts of tomography were published in 1917 - during the blossom of X-ray physics - by the Czech mathematician Johann Radon [Rad17], it took almost 50 years until Allan Cormack found the "missing link" between X-ray radioscopy and the numerical reconstruction of a function from its line integrals [Cor63]. He was not the first to reinvent the early work of Radon. Ronald N. Bracewell developed the well known *projection slice theorem* for celestial strip integration in 1956 [Bra56], and Shinji Takahashi was the first to conceive the idea of X-ray tomography in 1957 [Tak57]. Ten years later Allan Hounsfield decided to build a medical CT scanner (1967). Yet, 30 years after Conrad Zuse's 'Z1', 20 years after the invention of the transistor at Bell Labs and three years after the launch of IBM's most successful mainframe computer system (S/360), computed tomography was still a costly venture. This may be one reason why - unlike Marie Curie's mobile radiography stations - Hounsfield patented his scanner for commercial purposes before announcing it publicly in 1972 [Hou73].

Again medicine had been given an incredible tool for clinical diagnosis exploring the human body in three-dimensions. During the following years most attention was paid to improve temporal resolution and detector efficiency in order to limit the radiation dose received by the patient (already in 1897 Nikola Tesla alerted his audience - in vain - to the biological hazards associated with X-ray exposure). Ten years passed until spatial resolution reached a sufficient detail, allowing materials scientists to discover the non-destructive virtue of X-ray microtomography [Ell82]. μCT became the state-of-the-art tool for studying defects and structure in metals, concrete and other construction materials [Rei83].

Going back in time, X-rays are found to play another important role, namely in the history of high-energy physics. By the early 1920s the structure of matter was mostly revealed thanks to the major discoveries in X-ray physics that were described above. Now, experimental physicists were eager to test these protons, neutrons and electrons which constitute atoms and molecules. First, linear particle accellerators were used until Ernest Lawrence invented the *cyclotron* in 1929. In a cyclotron, high-frequency voltage is applied across two electrode plates in order to accelerate charged particles forcing them on a spiral trajectory, which converges to a circular path when the revolution frequency of the particles synchronizes with the alternating field. These devices reach $\sim 10\,\mathrm{MeV}$ until relativistic effects corrupt the synchronization. To solve this problem, a first synchrotron - named *betatron* due to the fact that electrons were accelerated - was built by Donald Kerst in 1940 at the university of Illinois for the production of $2.3\,\mathrm{MeV}$ electrons [Ker40]. During operation of the following devices ($20\,\mathrm{MeV}$ and

$100\,\mathrm{MeV}$), a continuous energy loss was observed as predicted by calculations of Ivanenko and Pomeranchuk who postulated an upper limit for the betatron energy, due to the radiation of electrons in the magnetic field [Iva44]. Unfortunately, Lawrence meanwhile pursued the development of *his* cyclotron, leading him to build similar *calutron* mass spectrometers for the refinement of the uranium isotope U-235 that lead to the killing of 237.000 civilians on August 6, 1945. After World War II, Julian Schwinger started working on the energy loss in betatrons at Harvard and published his paper "On the Classical Radiation of Accelerated Electrons" in 1949, including a very accurate estimate of the radiation energy: $\delta E_{keV} = 88.5(E_{GeV})^4/R_m$, where E_{GeV} is the electron energy in units of GeV and R_m the radius of the electron orbit in meters [Sch49]. The emission of this *Schwinger radiation* was first observed in the visible spectral range (white light) in 1947 at a $70\,\mathrm{MeV}$ betatron which was built for this unique purpose at General Electric's research laboratory in New York [Eld47]. Detailed characterization of the spectral and angular distributions of this radiation, which was soon renamed "synchrotron light", started in the 1950s at the $250\,\mathrm{MeV}$ synchrotron at Lebedev Institute in Moscow, and at the $320\,\mathrm{MeV}$ synchrotron at Cornell [Tom56]. Continuous work on these "first generation sources" was not possible until the early 1960s when access was granted to the $180\,\mathrm{MeV}$ Synchrotron Ultraviolet Radiation Facility (SURF) in the US, soon followed by the $1.15\,\mathrm{GeV}$ synchrotron of the Frascati laboratory in Italy and the $750\,\mathrm{MeV}$ synchrotron in Tokyo, Japan. The German $6\,\mathrm{GeV}$ synchrotron DESY began operating for both high-energy physics and synchrotron radiation in 1964 with available wavelengths down to 0.1 Å, allowing for the first time to measure the X-ray absorption in metals.

Following the example of DESY, other high-energy synchrotrons were build and powerful magnets were used to maintain the ultra-relativistic particles on quasi-circular trajectories outlined by large storage rings. In each of these *bending magnets*, the particles interact with strong magnetic fields, causing emission of a highly brilliant X-ray beam tangentially to their curved trajectory. Although this effect is still considered an unwanted energy loss, the growing demands of scientists to study and use synchrotron light, forced the designers of new facilities to include experimental access to their radiation sources.

In 1974, a first $300\,\mathrm{MeV}$ storage ring was build specifically for the production of synchrotron light in Tokyo, Japan [Miy76]. The same year the $2.5\,\mathrm{GeV}$ SPEAR ring opened a synchrotron X-ray beamline with five experimental end-stations to a large user community in the US. Unlike operating particle colliders, storage rings that were build expressly to generate X-rays and UV light could incorporate a higher particle current thus producing a much higher photon flux. Many of these second generation devices were built in the early 80s: SRS in 1981 at Daresbury (UK), NSLS in 1981 at Brookhaven (US), Photon Factory in 1982 at Tsukuba (Japan), BESSY in 1982 at Berlin (Germany) and LURE in 1984 at Orsay (France). First generation facilities in Standford (US) and Hamburg (Germany) were upgraded to be able to compete with the second generation. It was about the same time when X-ray tomography and radiography started to quit the exclusive area of medical imaging to make their start as important tools in materials science and engineering. Just-in-time, the same materials scientists started to discover

the high-resolution imaging potential of synchrotron radiation to explore new ways of imaging structural details [Spi80]. Many physical and /or biological questions were thus reviewed and solved with exemplary multi-disciplinary approaches, theories could be better tested - and were often extended - on the basis of high-resolution 2D and /or 3D measurements.
Major experimental developments over the following years included angle-resolved photoemission, extended X-ray absorption fine structure spectroscopy (EXAFS), high-resolution protein cystallography, X-ray microscopy (using zone plates or grazing incidence multilayer mirrors) and X-ray holography. Most of these achievements came along with an improved brilliance (flux per unit area of the source, per unit solid angle of the radiation cone and per spectral bandwidth) of the X-ray beam. Since most experiments required a highly collimated quasi-monochromatic beam, brilliance was much more important than flux alone. New insertion devices (IDs) - undulators and wigglers - were developed to satisfy this growing demand. The IDs owe their name to their placement in the straight sections that connect the curved arcs of the storage rings. An undulator is an array of closely spaced vertically oriented dipole magnets of alternating polarity. Electrons passing through this array oscillate in the horizontal plane. Relatively weak magnetic fields are applied to allow the radiation cones emitted at each bend in the undulated trajectory to overlap, giving rise to constructive interference that results in spectrally narrow equidistant emission peaks. The characteristic wavelenth of these peaks can be tuned by asjusting the vertical gap between the pole caps. Wigglers are similar to undulators but higher magnetic fields are applied to fewer dipoles in order to avoid interfercences and obtain a continuous spectrum. Modern wigglers are based on high-field superconductors to shift the spectrum to higher energies (e.g. BESSY/BAM*line*).
Third generation synchrotrons are being built until today. They incorporate long straight sections for undulators and wigglers and their design is optimized for highest brilliance in order to achieve a considerable degree of spatial coherence. The European Synchrotron Facility (ESRF) in Grenoble, France, was the first third generation hard X-ray source to start operating a $6\,\mathrm{GeV}$ ring and first beamlines in 1994, followed by the Advanced Photon Source (APS, $7\,\mathrm{GeV}$) in 1996 and SPring-8 ($8\,\mathrm{GeV}$) in Japan 1997. These storage rings are $850 - 1\,440\,\mathrm{m}$ in circumference and each facility hosts more than 30 IDs plus a comparable number of bending-magnet beamlines. Ever since, many smaller sources were build all around the world, many of which replaced the first and/or second generation *on-site*: ALS in Berkely (US), ELLETRA in Trieste (Italy), SRRC in Hsinchu (Taiwan), PLS in Pohang (Korea), BESSY II in Berlin (Germany), SLS in Villingen (Switzerland), SOLEIL in Orsay (France), ANKA in Karlsruhe (Germany) and many more in Russia, Japan, Thailand, India, Brasil, China, Sweden, Canada, England, Spain and Australia. These facilities contain fewer straight sections but their spectrum and performance is comparable to the three large facilities. Most synchrotrons host one or more imaging beamlines some of which extend more than $145\,\mathrm{m}$ away from the source in order to obtain the highest spatial coherence. The scientists and students working on these beamlines have developed a whole array of new X-ray imaging techniques most of which combine with tomography, thus mapping a large number of physical observables in two and/or

three dimensions. Among the most important achievements are: Fresnel-propagated imaging [Sni95], holotomography [Clo99b], diffraction enhanced imaging [Cha97], fluorescence imaging [Gol04], near edge absorption imaging [Sch03] and refraction imaging [Mü04]. Whilst the resolution limit of planar X-ray imaging methods is restricted to $0.5-0.6\,\mu\mathrm{m}$, nano-focusing techniques have evolved to overcome this limitation. Asymetric Bragg-magnification yields a lensless magnification with resolutions in the sub-micrometer range [Mod06], high aspect ratio zone-lenses are fabricated with electron beam lithography yielding spot sizes of $<100\,\mathrm{nm}$ at $1\,$Å wavelength [Tod06] and Kirkpatrick-Beatz mirrors have been used to obtain Fresnel-propagated images of biological tissue with $50-60\,\mathrm{nm}$ spatial resolution under similar conditions [Mok07]. Beamtime is allocated to scientific users via a peer-reviewed proposal system, whereby an overload factor of 4-5 is commonly observed for the imaging beamlines, despite the growing number of available end-stations all over the world. In the near future, these techniques and the coming *fourth generation* of free electron lasers will keep the synchrotron beamlines far ahead of the latest commercial products in terms of high-resolution X-ray imaging. It is further worth noting that most X-ray scanners that are used in modern materials science laboratories and in industry are self-assembled [Goe99, GM04, Ber05, Mas07]. Scientific efforts in this field are encouraged by observing how pioneering research institutes are developing their own new imaging techniques [Pfe06] and laboratory X-ray sources [Hem03], outclassing the poor performance of commercial scanners. This trend is observed even stronger in the domains of reconstruction software and image analysis [Vla07].

Along with the development of new characterization methods, many groups from different research fields have joined to specialize in X-ray imaging by synchrotron light: metallic and non-metallic materials, biomaterials and medicine, paleontology, geology and many more. In this work, the latest varieties of high-resolution X-ray tomography (absorption tomography, Fresnel-propagated imaging and holotomography) are applied to three specific problems/ materials from different research fields: metallic alloys, tooth dentin and natural rock.

The microstructure of metallic alloys exhibits a large variety of geometrical forms (globular, lamellar, dendritic, etc.). The interface between the different phases which characterizes this geometry, changes its shape under certain experimental conditions, in particular when the material is processed in the semisolid state. In this state the alloy is characterized by a solid-liquid mixture which is obtained by partial melting. An isotropic dispersion of globular particles is desired in order to realize good casting and uniform mechanical properties of the components. Yet, both static particle coarsening and external shearing forces are known to alter the microstructure of the alloy. Precise knowledge about the coarsening kinetics of metallic alloys is thus necessary in order to control the microstructure and the overall performance of the cast components. In this work, static and dynamic 2D and 3D images were recorded from a variety of aluminum-based alloys (Al-Ge, Al-Si, Al-Cu, Al-Mg). Unlike surface imaging methods, X-ray radiography and particularily tomography provide direct access to the 3D particle chararacteristics, e.g. size, shape, orientation, connectivity and contiguity. Coarsening of particle agglomerates (at high solid volume fraction) in liquid solution, as well as rheological

properties of semi-solid alloys are investigated [Rue06, Zab07b].
Biomaterials represent the natural adaptation to a mechanical-biological problem and the most important work of a scientist is to determine the problem /constraint and /or function to which the material adapted. Human teeth are known to be the answer to the quest for tough, long-living chewing tools. The bulk material of teeth is dentin, covered with a cap of dense enamel. Dentin is characterized by a quasi-parallel arrangement of micrometer-sized tubules which are commonly believed to incarnate a natural mechanical design. Despite numerous measurements on 2D sections and structural models, the structure function relationship between dentinal tubuli and tooth performance is still far from beeing fully understood which is why three-dimensional maps of dentin microstructure are needed. Fresnel-propagated imaging is shown to be the ideal technique to measure the 3D arrangement of the tubuli [Zab07a]. This work shows how high-resolution 3D images of water-immersed tooth dentin are recorded, and detailed simulations of the optical wave propagation reveal that Fresnel-images contain additional 3D information about the dense cuff of peritubular dentin surrounding the tubules. The thickness of the latter can be extrapolated from the interference fringes that form the propagated images of tubules. Thus, 3D images are shown to contain far more information than the mere position ond orientation of the individual tubules [Zab06].
Understanding rock fracture is one of the fundamental problems in earth science. Although rocks are an extremely inhomogeneous material, cracks do not occur randomly but they follow a well known en-echelon (staggered) propagation that results from mechanical interaction between tensile and shear cracks. Absorption and Fresnel-propagated X-ray microtomography is applied to measure samples of different rocks before and after mechanical compression non-destructively [Zab07c]. In a first approach, limestone and greywacke are investigated, representing two sedimentary rocks of different grain-size. Basalt and granite are tested in a second approach to compare different rock types. Development of cracks is observed in all materials, leading to fracture when increasing mechanical load is applied. It is known that the fracture behaviour of rocks is reproduced on a large variety of length scales. In this work, relatively small mm-sized samples are used in order to test a classical fracture model wherein microflaws initiate the formation of larger cracks. For the first time, Fresnel-propagated imaging is applied to rock samples, highlighting micrometer-sized intergranular porosity and different material phases. The latter can thus be compared to the topology of the propagating cracks in each material.
In the framework of this thesis, a high-resolution imaging system was constructed, assembled and comissioned at BESSY/BAM*line* . The capabilities of this system to perform Fresnel-propagated imaging, holotomography and conventional high-resolution absorption tomography are demonstrated and applied to the problems mentioned above. In addition to the hardware, many image processing tools were created to provide the best possible insight into the specific microstructure wich is different for each field of application. The instrumentation as well as the 2D and 3D image processing and analysis are detailed in the appendices.

Chapter 1

Image formation

1.1 Interaction of X-rays with matter

On the spectral band of light, X-rays are situated between the UV spectrum and high-energy gamma radiation, filling a broad band of wavelengths from 0.1 Å to 10 Å. Particularly *hard* X-rays (λ<1 Å) are appreciated in materials science due to their short wavelength and generally weak interaction with matter. The latter is commonly described by a complex refractive index that is very close to unity.

$$n = 1 - \delta + i\beta \tag{1.1}$$

where the imaginary component β is mainly due to the photoelectric effect and inelastic Compton scattering, and the real decrement δ is commonly attributed to Thomson scattering. In this work combinations of elements with atomic numbers ranging from $Z = 12$ (magnesium) to 32 (germanium) are used for imaging experiments. At typical energies E $\sim$25 keV (λ $\sim$0.5 Å), the magnitude of β is of the order 10^{-9} to 10^{-8}, whereas values ranging from 10^{-7} to 10^{-6} are known for δ. Note that the ratio δ/β increases for lighter elements, i.e. smaller Z.
For conventional tomography β is readily obtained from simple absorption images where it is usually evaluated in terms of the linear attenuation coefficient $\mu = (4\pi/\lambda)\beta$. The latter decreases with higher energy, i.e. materials are generally more transparent for shorter wavelengths. Yet, the contrary is observed in terms of abruptly increasing absorption, occuring at discrete wavelengths that are characteristic to each element. These absorption edges coincide with the ionization energy of the "deepest" electron states in the atoms. The complete absorption of a photon accompanied by the ejection of a photoelectron is called the photoelectric effect [Ein05]. Unlike X-ray fluorescence, where a large variety of spectral lines is observed, X-ray absorption features only few spectral lines: one K-line (ionization of the 1s electrons), three L-line (2s, $2p_{1/2}$ and $2p_{3/2}$), five L-lines, etc. . Closer angular resolution reveals oscillations in $\mu(E)$ at these edges which result from resonant back-scattering of the photoelectrons at neighboring atoms. In very close vincinity, $\pm$50 eV around the absorption edge, such oscillations are used for X-ray absorption near edge spectroscopy (XANES), whereas the damped oscillations at slightly higher energies (up to $\sim$1000 eV) are called "extended X-ray absorption fine structure" (EXAFS).

1.2 Absorption image formation

Absorption of photons yields an overall attenuation of the beam intensity. For a heterogeneous sample, the number of registered photons $N(x, y)$ per pixel at the image coordinates (x, y) is approximately described by the number of incident photons per pixel $N_0(x, y)$ and the line integral over the absorption coefficient $\mu(x, y, z)$ of the sample along the ray path.

$$N(x, y) = N_0(x, y) \exp\left[-\int dz\ \mu(x, y, z)\right] \tag{1.2}$$

The stochastic features of N_0 and N are described by Poisson statistics and the quantum noise on N_0 and N is uncorrelated. Consequently N has a mean squared deviation

$$\sigma_N^2 = N \tag{1.3}$$

and $\sigma_{N_0}^2 = N_0$ respectively. In conventional absorption imaging the logarithmic attenuation $\alpha = -\ln(N/N_0)$ is measured with the mean squared deviation

$$\sigma_\alpha^2 = \left|\frac{d\alpha}{dN}\right|^2 \sigma_N^2 + \left|\frac{d\alpha}{dN_0}\right|^2 \sigma_{N_0}^2 = \frac{1}{N} + \frac{1}{N_0}. \tag{1.4}$$

For a sample of thickness t, α can be expressed in terms of the average attenuation coefficient $\langle\mu\rangle(x, y)$. The standard deviation of $\langle\mu\rangle$ is proportional to σ_α and consequently

$$\sigma_{\langle\mu\rangle} \propto \sqrt{\frac{1}{N} + \frac{1}{N_0}} = \sqrt{\frac{1 + \exp(\langle\mu\rangle t)}{N_0}}. \tag{1.5}$$

For clinical applications, Brooks and DiChiro explicitly calculated $\sigma_{\langle\mu\rangle}$ which is a function of the X-ray energy, the maximum skin dose, the Nyquist frequency of the detector and the beam spreading [Bro76]. Supposing all these experimatal parameters constant, the minimum of the relative error (in other words the maximum of the signal to noise ratio) $\sigma_{\langle\mu\rangle}/\langle\mu\rangle$ with respect to $\langle\mu\rangle t$ for any given t is found at $\langle\mu\rangle t = 2.22$ (cf. Fig. 1.1). Therefore a minimal transmission of $\approx 11\%$ is desirable in standard radiographic and tomographic imaging [Gra91]. An optimum $\langle\mu\rangle t = 2$ is often mentioned, resulting from neglecting the noise on N_0 in eq. 1.4.
Eq. 1.2 is strictly only valid for the statistical process of complete photon absorption and ideal monochromatic plane-waves. For polychromatic irradiation *beam-hardening* occurs, i.e. the spectrum of the outgoing X-rays is shifted towards shorter wavelengths with respect to the incoming beam: Soft X-rays are mostly absorbed whereas hard X-rays are transmitted. Consequently mere intensity measurements that are not sensitive to the X-rays wavelength would lead to false interpretation of the images. Eq. 1.2 is also invalid for phase-contrast imaging whereby elastic scattering causes intensity shifts due to angular deviation of the X-rays. De facto the linear attenuation coefficient μ is proportional to the number of atoms per unit volume and the atomic cross section σ_{at} of the material. The latter comprises three physical processes: 1. Ejection of bound electrons by the photoelectric effect, 2. Coherent Rayleigh scattering with bound electrons (Thomson scattering for free electrons) and 3. Incoherent scattering with free

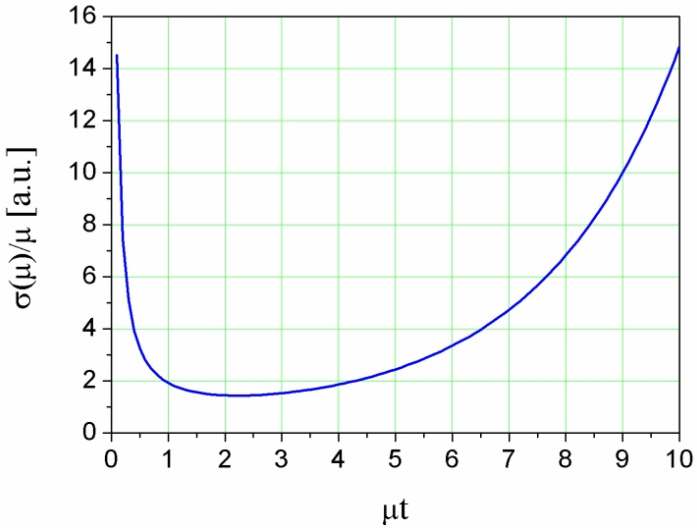

Figure 1.1: Plot of the relative error $\sigma_{\langle\mu\rangle}/\langle\mu\rangle$ versus the logarithmic attenuation $\langle\mu\rangle t$. The lowest error, i.e. the best signal to noise ratio, is found at $\langle\mu\rangle t = 2.22$. For small $\langle\mu\rangle t < 1$ obviously too few photons are absorbed, whereas for large $\langle\mu\rangle t \gg 2.22$ too few photons are transmitted.

electrons, known as the *Compton effect*. Above the K-edge and for non-relativistic s-electrons, the plane-wave Born approximation shows the first contribution (photoelectric effect) to be proportional to $Z^5E^{-3.5}$, at higher energies relativistic theory yields Z^5E^{-1} [Jac81]. Yet, for all more accurate theories σ_{at} does not factorize into a function of E and a function of Z (this had been first suggested by Bragg and Peirce who postulated $Z^5E^{-2.5}$ [Bra14a]). The result-

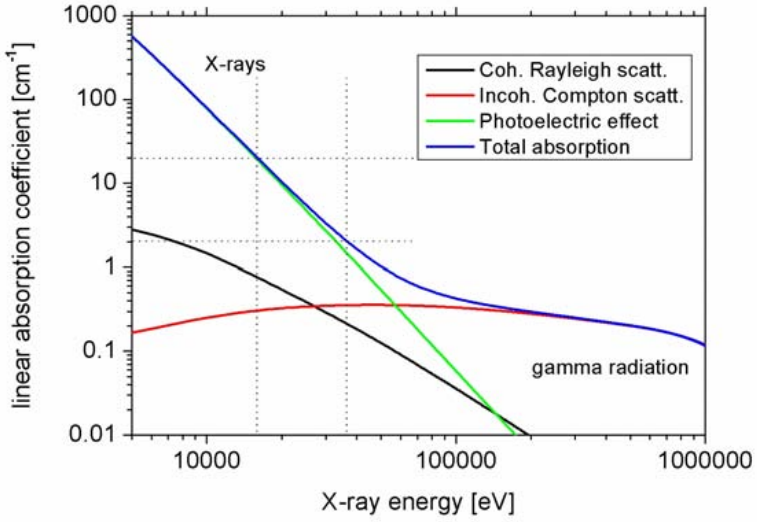

Figure 1.2: The linear X-ray absorption coefficient of silicon, decomposed into the photoelectric effect, coherent (Rayleigh) and incoherent (Compton) scattering [Dej96]. The dashed lines indicate the typical window of X-ray micro-tomography.

ing ionized atoms can either relax by X-ray fluorescence, which is the preferred process for high-Z materials, or by emission of Auger-electrons (low-Z). Coherent scattering preserves the energy of the photons. Incoherent photon scattering from a single free electron is descibed by the relativistic Klein-Nishina formula, which converges to (coherent) Thomson-scattering at lower photon energies. Note that during (incoherent) Compton scattering, energy is transferred from the photon to the ejected electron. The scattered photons are not absorbed but with increasing scattering angle the spectrum is shifted towards longer wavelengths. Fig. 1.2 shows $\mu(E)$ of silicon, for all three contributions. Typical μCT samples are of mm to cm size and require X-ray energies in the range of 15 to $35\,\mathrm{keV}$ for optimal imaging. The corresponding 'window' is indicated by the dashed lines in Fig. 1.2 showing that the photoelectric effect is indeed the dominant process observed by standard X-ray absorption imaging. For high-energy gamma radiation (E>$100\,\mathrm{keV}$), absorption is mostly described by Compton scattering. Note that the destructive effects on the monochromaticity and the angular divergence of the beam due to Compton scattering inside the sample are not included in eq. 1.2 and have to be reconsidered for high-energy imaging experiments.

1.3 Fresnel-propagation

For imaging of structural details in materials and tissues of similar composition, retrieving δ (cf. eq. 1.1) rather than μ is considerably more informative. In other words, the phase shift effect on the propagating wave is far greater than the absorption effect and this can be exploited if the phase shift can be determined (see section B.3). For the retrieval of δ it is necessary to determine phase shift differences across the propagating X-ray field. Using interferometric methods, such differences can be determined if at least partially coherent illumination is used, as is available in third generation synchrotron facilities [Rav96] and certain conventional sources [Wil96, Dav95]. Three approaches have been reported: X-ray interferometry, diffraction enhanced imaging and Fresnel-propagation based phase imaging (e.g. holotomography). For overviews, see [Mom03, May03, Clo99b]. It is possible to determine δ with all these approaches, each having significant benefits, but Fresnel-propagation imaging clearly has the advantage of employing the simplest component setup: phase modulation is achieved by changing the sample-detector distance. To apply classical optics, a sample is required to obey the *thin lens approximation*, in other words a X-ray entering at coordinates (x, y) on one face of the sample exits at approximately the same coordinates on the opposite face, i.e. angular deviation of the ray within the sample is negligible [Goo96]. The Maxwell equations describe most generally the propagation of electromagnetic waves in inhomogeneous media:

$$\vec{\nabla} \cdot \vec{D}(\vec{r},t) = \rho_c(\vec{r},t) \tag{1.6}$$

$$\vec{\nabla} \cdot \vec{B}(\vec{r},t) = 0 \tag{1.7}$$

$$\vec{\nabla} \times \vec{E}(\vec{r},t) + \partial\vec{B}(\vec{r},t)/\partial t = 0 \tag{1.8}$$

$$\vec{\nabla} \times \vec{H}(\vec{r},t) - \partial\vec{D}(\vec{r},t)/\partial t = \vec{J}(\vec{r},t) \tag{1.9}$$

where $\vec{D}$ is the electric displacement, ρ_c the charge density, $\vec{B}$ the magnetic induction , $\vec{E}$ the electric and $\vec{H}$ the magnetic fields. $\vec{J}$ is the electric current density and $\vec{r} = (x, y, z)^T$ the coordinate vector. For linear isotropic media, eq. 1.6-1.9 can be simplified by $\vec{D} = \epsilon\vec{E}$ and $\vec{B} = \mu_m\vec{H}$, introducing the electric permettivity ϵ and the magnetic permeability μ_m (the subscript 'm' is used to distinguish μ_m from the linear attenuation coefficient μ). The latter turns into the vacuum permeability μ_0 when a non-magnetic material is assumed. In the absence of charges and/or electrical currents, the electric field decouples from the magnetic field and the four Maxwell equations reduce to two.

$$\left(\epsilon(\vec{r})\mu_0\frac{\partial^2}{\partial t^2} - \nabla^2\right)\vec{E}(\vec{r},t) = -\vec{\nabla}\left(\vec{\nabla}\cdot\vec{E}(\vec{r},t)\right) \tag{1.10}$$

$$\left(\epsilon(\vec{r})\mu_0\frac{\partial^2}{\partial t^2} - \nabla^2\right)\vec{H}(\vec{r},t) = \frac{1}{\epsilon(\vec{r})}\vec{\nabla}\epsilon(\vec{r})\times\left(\vec{\nabla}\times\vec{H}(\vec{r},t)\right) \tag{1.11}$$

The right hand side of these two equations can be neglected assuming a sufficiently homogeneous material (with respect typical X-ray wavelengths). The decoupling of $\vec{E}$ and $\vec{H}$ gives rise to a simple scalar wave equation.

$$\left(\epsilon(\vec{r})\mu_0\frac{\partial^2}{\partial t^2} - \nabla^2\right)\Psi(\vec{r},t) = 0 \tag{1.12}$$

Decomposing the propagating wave $\Psi(\vec{r},t) = \int d\omega\ \psi_\omega(\vec{r})\exp(-i\omega t)$ into its frequency spectrum allows to solve eq. 1.12 for each component ψ_ω

$$\left(\nabla^2 + \epsilon_\omega(\vec{r})\mu_0\omega^2\right)\psi_\omega(\vec{r}) = 0 \tag{1.13}$$

Using $\omega = 2\pi c/\lambda$, with $c = 1/\sqrt{\epsilon_0\mu_0}$ the speed of light and inserting the complex refractive index - which depends on the X-ray energy and is defined as $n_\omega(\vec{r}) = \sqrt{\epsilon_\omega(\vec{r})/\epsilon_0}$ - into eq. 1.13, yields the *inhomogeneous Helmholtz equation*.

$$\left(\nabla^2 + \left[\frac{2\pi}{\lambda}\right]^2 n_\omega(\vec{r})\right)\psi_\omega(\vec{r}) = 0 \tag{1.14}$$

Considering plane wave propagation $\psi_\omega(\vec{r}) = u(\vec{r})\exp(i2\pi z/\lambda)$ along the z-axis yields the *inhomogeneous paraxial equation*:

$$\left(\frac{4\pi i}{\lambda}\frac{\partial}{\partial z} + \nabla_\perp^2 + \left[\frac{2\pi}{\lambda}\right]^2 [n_\omega^2(\vec{r}) - 1]\right)u(\vec{r}) = 0 \tag{1.15}$$

with the *transverse* Laplacian $\nabla_\perp^2 = \partial_x^2 + \partial_y^2$. Neglecting $\nabla_\perp^2 u(\vec{r})$ is called the *projection approximation*, and is equivalent to the thin lens approximation mentioned above. Thus, a linear relation is obtained between the incoming and the exit wave u_{inc} and u_0, respectively.

$$u_0(x,y) \approx T(x,y)\cdot u_{inc}(x,y) \tag{1.16}$$

The subscript '0' was introduces to mark the position directly behind the sample ($z = 0$). Thus the effect of the sample on the wave is given by the complex transmission function $T(x, y)$, which varies with the angle of projection when tomographic datasets are recorded.

$$T(x,y) = \exp\left(\frac{\pi}{\lambda i}\int_s dz[1 - n_\omega^2(\vec{r})]\right) \approx \exp(i\phi_\omega(x,y) - B_\omega(x,y)) \tag{1.17}$$

with $1 - n_\omega^2(\vec{r}) \approx 2(\delta(\vec{r}) - i\beta(\vec{r}))$, assuming a refractive index n_ω close to unity (eq. 1.1). Note that ϕ and B represent the outcomes of propagation through the sample ('s' under the integral). They are related to the real decrements and the imaginary part of n_ω by line integrals of δ and β along the propagation direction z.

$$B_\omega(x,y) = \frac{2\pi}{\lambda}\int_s dz\ \beta(x,y,z) \tag{1.18}$$

$$\phi_\omega(x,y) = \frac{2\pi}{\lambda}\int_s dz\ \delta(x,y,z) \tag{1.19}$$

Downstream of the sample n_ω is 1 and eq. 1.15 turns into the paraxial equation for which an exact solution is given by the Fresnel diffraction theory. The latter requires a *paraxial* scalar wave-field, i.e. all non-negligible components of $u(\vec{r})$ make a small angle with respect to the axis of propagation. This is certainly true for a plane wave, whereas spherical waves have to be considered under realistic conditions. The long source-to-sample distance L at synchrotron beamlines allows to approximate an incoming spherical by a parabolic wave.

$$u_{inc}(r) = \frac{\exp(i2\pi r/\lambda)}{r} \overset{z=L>>\sqrt{x^2+y^2}}{\Longrightarrow} \frac{\exp(i2\pi L/\lambda)}{L}\exp\left(\frac{i\pi}{\lambda L}[x^2+y^2]\right) \tag{1.20}$$

According to the Huygens-Fresnel principle, the wave amplitude $u_d(x, y)$ in the (x, y) plane at a distance d behind the sample - which lies in the (η, ξ) plane parallel to (x, y) - is found by integration over virtual spherical waves of amplitude $u_0(\eta, \xi)$ and emitted from each point of the sample exit surface s

$$u_d(x,y) = \frac{1}{i\lambda}\int\int_s d\eta d\xi\ u_0(\eta,\xi)\frac{\exp(i2\pi p/\lambda)}{p}cos(\theta) \tag{1.21}$$

wherein $p = \sqrt{d^2 + (x-\eta)^2 + (y-\xi)^2}$, with θ the angle between the z-axis and the vector $\vec{p} = (x - \eta, y - \xi, d)^T$ and $cos(\theta) = d/p$. The *stationary phase approximation* is based on the binomial expansion $\sqrt{1-x} = 1 + x/2 - x^2/8 + \cdots$ and replaces the phase term in eq. 1.21 with $\exp\{i2\pi[d + [(x-\eta)^2 + (y-\xi)^2]/(2d)]/\lambda\}$, whereas $p \approx d$ is used for the denominator. Eq. 1.21 then takes the well known form of the Fresnel integral

$$u_d(x,y) = \frac{e^{\frac{i2\pi}{\lambda}d}}{i\lambda d}\int\int_{-\infty}^{\infty} d\eta d\xi\ u_0(\eta,\xi)\exp\left(\frac{i\pi}{\lambda d}\left[(x-\eta)^2 + (y-\xi)^2\right]\right) \tag{1.22}$$

which is readily seen to be a convolution. Before writing out the latter, it is convenient to replace $u_0(\eta, \xi)$ with $T(\eta, \xi)u_{inc}(\eta, \xi)$, whereby u_{inc} is given by eq. 1.20.

$$u_d(x,y) = \frac{e^{\frac{i2\pi}{\lambda}(d+L)}}{i\lambda dL}\int\int_{-\infty}^{\infty} d\eta d\xi\ T(\eta,\xi)\cdot e^{\frac{i\pi}{\lambda L}\left(\eta^2+\xi^2\right)}e^{\frac{i\pi}{\lambda d}\left[(x-\eta)^2+(y-\xi)^2\right]} \tag{1.23}$$

$$\approx \frac{e^{\frac{i2\pi}{\lambda}(d+L)}}{i\lambda dL}\int\int_{-\infty}^{\infty} d\eta d\xi\ T(\eta,\xi)\cdot e^{\frac{i\pi}{\lambda D}\left[(X-\eta)^2+(Y-\xi)^2\right]} \tag{1.24}$$

whereby the magnification $M = (d + L)/L$ was introduced to change variables: $d \mapsto D = d/M$, $x \mapsto X = x/M$ and $y \mapsto Y = y/M$ and a phase term of the order $(X/L)^2$ was dropped. M accounts for the finite image magnification, and allows to write a demagnified wave $u_D(X, Y)$ in a virtual plane at the propagation distance D as the convolution of $T(x, y)$ with the *Fresnel propagator* $P_D(X, Y)$.

$$u_D(X,Y) = (P_D * T)(X,Y) \quad \leftrightarrow \quad P_D(X,Y) = \frac{e^{\frac{i2\pi}{\lambda}(d+L)}}{i\lambda dL} e^{\frac{i\pi}{\lambda D}\left(X^2+Y^2\right)} \tag{1.25}$$

In reciprocal space eq. 1.25 assumes the familiar form of a multiplication (note that the Fourier transform of a function a is denoted $\hat{a}$)

$$\hat{u}_D(f_X, f_Y) = \hat{P}_D(f_X, f_Y) \cdot \hat{T}(f_X, f_Y) \quad \leftrightarrow \quad \hat{P}_D(f_X, f_Y) \propto e^{-i\pi\lambda D(f_X^2+f_Y^2)} \tag{1.26}$$

with f_X and f_Y the spatial frequencies, conjugates to X and Y in real space. Eq. 1.26 is sometimes referred to as the *operator formulation*. Fig. 1.3 shows a series of radiographic images of two hairs recorded at increasing sample-detector distance d. Radiographs were recorded

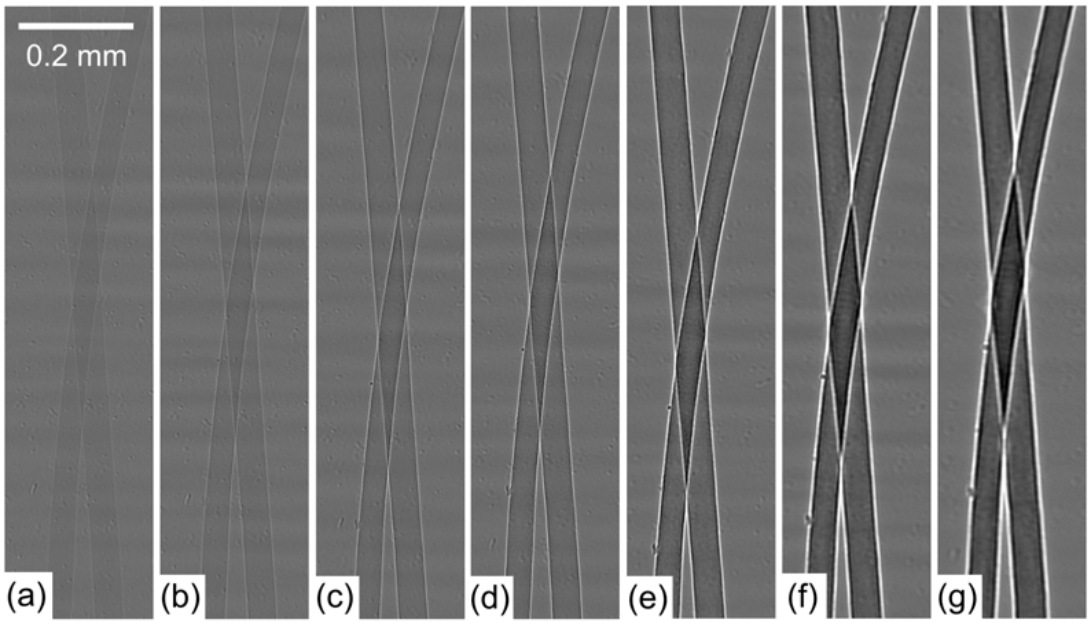

Figure 1.3: Fresnel-propagated X-ray imaging illustrated for radiographs of human hairs recorded at increasing sample-detector distance d. (a) d =5 mm, (b) d =25 mm, (c) d =75 mm, (d) d =125 mm, (e) d =325 mm, (f) d =725 mm, (f) d =1125 mm.

with E =17 keV photon energy at BESSY/BAMline. The image pixel size was $\Delta x \approx$0.6 µm at $R \sim 1{-}2$ µm resolution. This example illustrates the effect of Fresnel propagation on the intensity contrast forming in the images. Hardly any contrast is visible for the absorption radiograph (d =5 mm, Fig. 1.3a), whereas edge-enhancement of the hair's contour characterizes the *near* Fresnel-regime ($d = 25{-}125$ mm, Fig. 1.3b-d). In the *far* Fresnel-regime (Fig. 1.3e-g), radiographs feature extended interference lobes and the hairs appear darker towards the center due to strong diffraction.

Chapter 2

Image analysis

Standard radiography and tomography produce image data where different grey values, assigned to each pixel (voxel in 3D), represent the extent of X-ray absorption at each point, i.e. the linear attenuation coefficient $\mu(x, y, z)$ which is proportional to the imaginary part β of the refrective index n (eq. 1.1). If necessary, Fresnel-propagated imaging and/or holotomography can be employed to obtain improved datasets of the real decrement δ which is a good approximation of the electron density in the material (note that far from absorption edges $\delta \propto \lambda^2 \rho_{el}$). Ideally both imaging modes allow for direct binarization and analysis of the material phase that is of interest. If not, binarization may be preceded by image alignment, filtering and/or interpolation which are applied according to standard methods from digital signal processing. These methods are descibed in the first, whereas statistical image anaysis is presented in the second part of this chapter. The techniques which are presented here are very general and apply to 2D and 3D images.

2.1 Filtering and correlation

The fundamental principle for 2D/3D image filtering and correlation is the equivalence between the measured data in real space and its Fourier transform in reciprocal space. For the sake of simplicity the following calculations will be restricted to one dimension x in real space, and f - the conjugate variable to x - in reciprocal space. The transform $\hat{s}$ of the function $s(x)$, which might be an image or an any kind of signal, is defined by a Fourier-integral

$$\hat{s}(f) = \int_{-\infty}^{\infty} dt\ s(x) e^{2\pi i f x} \tag{2.1}$$

and $s(x)$ can be recovered via the the inverse transform changing the sign of the exponent

$$s(x) = \int_{-\infty}^{\infty} d\eta\ \hat{s}(f) e^{-2\pi i f x} \tag{2.2}$$

These relations are used in sections 1.3 and B.3 to derive the formalism of Fresnel-propagation and to retrieve approximate phase maps $\phi(x)$ from a series of propagated X-ray images. With digital images, intensity is measured in terms of pixels on a CCD array, in other words discretization (subscript '*samp*') is introduced with a spatial sampling rate of Δx: the pixel size. The discrete values of the pixels are obtained by multiplying $s(x)$ with a *Dirac-comb*

$$s_{samp}(x) \approx s(x) \sum_{n=-N/2}^{N/2-1} \delta_D\left(x - n\Delta x\right) \tag{2.3}$$

with N the total number of pixels and δ_D the Dirac delta function: $\delta_D(x) = \infty$ for $x = 0$ with $\int \delta_D(x) = 1$, and $\delta_D(x) = 0$ for $x \neq 0$. For convenience the sampling interval $[-N/2, N/2-1]$ is defined symetrically. An equivalent discretization of $\hat{s}$ may be found in reciprocal space by inserting eq. 2.3 into eq. 2.1 and solving the Fourier integral.

$$\hat{s}_{samp}(f) = \sum_{n=-N/2}^{N/2-1} s(n\Delta x) e^{2\pi i f n \Delta x} = \frac{\hat{s}(f)}{N\Delta x} \sum_{m=-N/2}^{N/2-1} \delta_D \left(f - \frac{m}{N\Delta x} \right) \tag{2.4}$$

For $N \mapsto \infty$ this series turns into the discrete Fourier transform $\hat{s}(f)$ with the Fourier coefficients $s(n\Delta x)$. In reality signals and/or images are of limited size and N is finite. Consequently, the Fourier transform of the truncated signal is obtained by periodic continuation of eq. 2.4 and the spatial frequencies f are non-zero for discrete values only. In other words, the Fourier transform of a Dirac-comb is another Dirac-comb with the sampling frequency $\Delta f = 1/(N\Delta x)$. The inverse discrete Fourier transform of $\hat{s}_{samp}$ takes the approximate form

$$s_{samp}(x) = \frac{1}{N\Delta x} \sum_{m=-N/2}^{N/2-1} \hat{s}(\frac{m}{N\Delta x}) \exp \left(-2\pi i \frac{xm}{N\Delta x} \right) \tag{2.5}$$

Note that the right hand side of eq. 2.4 implies the existance of a maximal sampling frequency $f_{max} = 1/(2\Delta x)$ known as the *Nyquist frequency* [Nyq28]. Consequently the sampling frequency has to be at least twice as high as the highest frequency contained in the signal, in order to fully sample the latter. This is known as the *Shannon theorem* [Sha49]. Violation of this theorem occurs when signals containing high frequency components are under-sampled, causing artificial intensities at lower frequencies (*aliasing effects*).

The *fast Fourier tranformation* (FFT, [Fri05]) algorithm makes use of eq. 2.4 to calculate $\hat{s}(f)$ from a discrete set of measurements $s_{samp}(x)$ in one, two or three dimensions. It is frequently used in the present work for filtering, correlating and translating images. In real space, a filter $r(x)$ (e.g. a Gauss function $r(x) = \exp[-x^2/(2\sigma^2)]/(\sigma\sqrt{2\pi})$) is applied to the signal $s(x)$ in terms of a convolution sum (convolution integral for continuous signals). The outcome $s'(x)$ of filtering the discrete truncated signal $s_{samp}(x)$ with the filter $r(x)$ is

$$s'(x) = \sum_{n=-N/2}^{N/2-1} s(n\Delta x) r(x - n\Delta x) = (s * r)(x). \tag{2.6}$$

The operator '$*$' is commonly used to abbreviate the convolution sum/integral. The *cross-correlation* function of s and r is obtained similarly: $C(x) = s^{cc}(-x) * r(x)$, where the superscript "cc" denotes the complex conjugate. For $s = r$, $C(x)$ turns into $A(x)$, the *auto-correlation* function. Calculating $C(x)$ for large images is very time consuming, compared to the calculation time of $\hat{s}$ via the FFT. *Parsival's* theorem (also known as the convolution theorem) states that a convolution integral in real space is equivalent to a multiplication in reciprocal space [Bra65].

$$\hat{s}'(f) = \int_{-\infty}^{\infty} dx \left(\int dt\ s(t) r(x-t) \right) e^{2\pi i f x} = \hat{r}(f) \int dt\ s(t) e^{2\pi i f t} = \hat{r}(f) \cdot \hat{s}(f) \tag{2.7}$$

Consequently convolution is a commutative operation and the filtered image $s'(x)$ is directly obtained by inverse Fourier transforming $\hat{s}'(f)$. This theorem also applies to discrete truncated signals and is commonly used to calculate the image cross-correlation, e.g. for finding the displacement vector of two quasi-identical, shifted images, which is indicated by the maximum of $C(x)$. Note that $C(x)$ is not commutative and $\hat{C}(f) = \hat{s}^{cc}(f) \cdot \hat{r}(f)$. The Fourier transform of the autocorrelation function is the power spectral density $\gamma(f) = \hat{A}(f) = |\hat{s}(f)|^2$ (Wiener-Khinchin theorem) [Wie30, Khi34]. Applying a window in real space leads to frequency filtering in reciprocal space. Analytical expressions of $\hat{r}(f)$ are known for some filters/windows, e.g. the transform of a Gauss function is another Gauss function, a rectangle transforms into a *sinc* function ($sinc(x) = \sin(x)/x$), and the transform of a triangle is a $sinc^2$ function (this can be easily verified by considering the triangle as the autocorrelation function of a rectangle). Sub-pixel image translation is another complicated procedure in real space involving pixel-interpolation. Fortunately, this procedure becomes very elegant when applied in reciprocal space. The Fourier transform of a shifted signal $s(x - \tau)$ is

$$\hat{s}_\tau(f) = \int_{-\infty}^{\infty} dt\ s(t-\tau)e^{2\pi i f t} = e^{2\pi i f \tau} \int_{-\infty}^{\infty} dt'\ s(t')e^{2\pi i f t'} \tag{2.8}$$

The last term is found by replacing t with $t' = t - \tau$. Hence, a real-space translation is expressed by a simple multiplication with a phase term $\exp(2\pi i f \tau)$ in reciprocal space. The first derivative $\partial s(x)/\partial x$ can be approximated in real space by convolution with a *structuring element*. The derivative at the sampling point j is calculated from j and the nearest neighbors $j - 1$ and $j + 1$ with the coefficient vector $\{-1/2, 0, 1/2\}$. The coefficients $\{1, 2, -1\}$ are commonly used to calculate the second derivative $\partial^2 s(x)/\partial x^2$. Additionally, Fourier transformation offers a more elegant way:

$$\frac{\partial s(x)}{\partial x} = \frac{\partial}{\partial x} \int_{-\infty}^{\infty} d\eta\ \hat{s}(\eta)e^{-2\pi i \eta x} = \int_{-\infty}^{\infty} d\eta\ (-2\pi i \eta)\hat{s}(\eta)e^{-2\pi i \eta x} \tag{2.9}$$

Consequently, the first derivative is obtained by Fourier transforming $s(x)$, followed by multiplication of $\hat{s}(f)$ with a linear ramp $-2\pi i f$ and inverse Fourier transformation. This relation is for example used during filtered back-projection of tomographic datasets in order to avoid time consuming application of the corresponding *Ram-Lak* filter in real-space.

2.2 Statistical image analysis

Statistical image analysis of particles and/or pores requires a binary (two-phase) image as input. This binary format is commonly obtained by threshold binarization of 8-bit, 16-bit or 32-bit data. Fig. 2.1 illustrates particle analysis for a binary Al-Ge32 alloy. The two phases (α-particles and surrounding eutectic matrix) are represented by dark and bright gray values, respectively. A threshold value h is chosen according to the histogram of gray values in the complete image (Fig. 2.1a) in order to separate particles and matrix. Every value above h is set to '1' (*foreground*, values to the right of the dashed line in Fig. 2.1a correspond to the

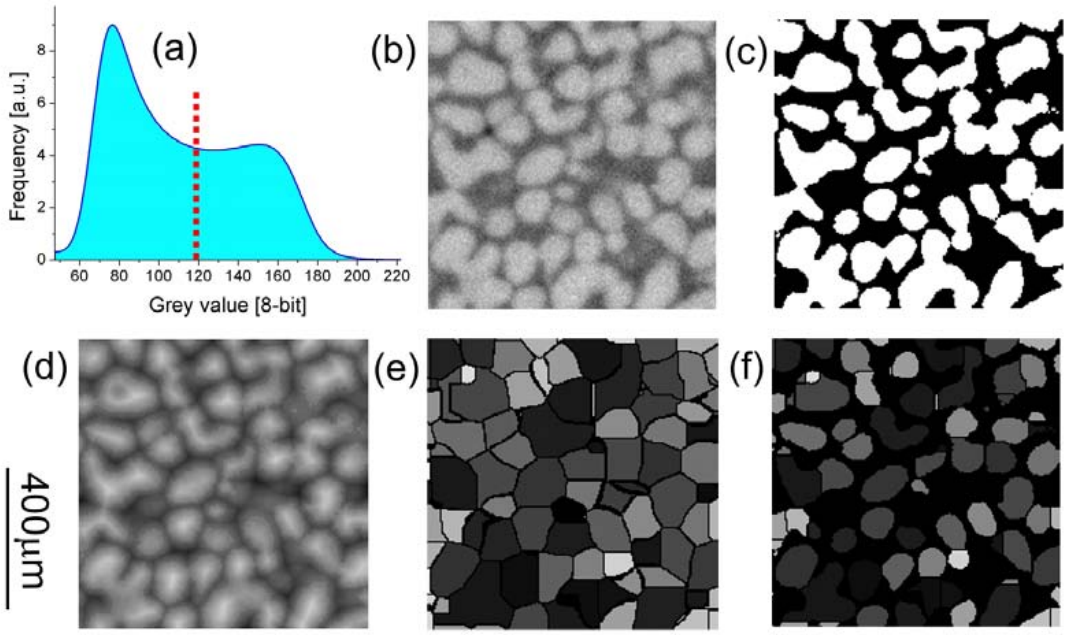

Figure 2.1: (a) Histogram of 8-bit grey values in a typical dataset (dashed line symbolizes the application of a threshold). (b) Typical image showing α-particles in Al-Ge matrix. (c) Binary image after application of median filter and threshold binarization. (d) Euclidean distance transform (EDT) calculated from the binary image. (e) Labeled image with watersheds calculated from the EDT. (f) Multiplication of the labeled watershed image with the binary map (b) yields a labeled image of the segmented particles.

α-particles), and all other values to '0' (*background*). Noisy images often require *smoothing* prior to threshold binarization in order to avoid artificially ragged interfaces between particles and matrix. More sophisticated binarization methods have to be used if the data contains more than two phases (e.g. pores in metallic alloys). Instead of a single threshold, two values can be defined to select an interval $[l, u]$ of gray values by applying a lower (l) and upper (u) threshold to the histogram. If blurring occurs due to limited resolution of the imaging system the gray values which represent the different material phases will overlap (as seen in the histogram Fig. 2.1a) making their separation difficult. In such cases it proves to be very convenient to make a *two-step* binarization [Kir04]. First a *reduced* interval of gray values $[l_1, u_1]$ is binarized followed by the conditioned binarization of a larger interval $[l_2, u_2]$ with $l_2 < l_1$ and $u_2 > u_1$. "Conditioned" means that during the second binarization only those pixels/voxels that are connected to the foreground of the first binarization are taken into account. Consequently the particles grow during the second step, which is why this method is often referred to as "region-growth binarization".

If the concentration of particles/pores in the image is very low they might be treated as separate (not connected) objects allowing to quantify their distribution and characteristics directly. However, for higher concentrations involving clusters of interconnected particles/pores seg-

mentation methods have to be used to separate and identify individual objects. For this purpose a large number of boolean operations and morphological transformations exist applying to binary images. The core of all these operations is a structuring element which is often called the *convolution kernel*. Unlike Fourier-filters (see previous subsection), the structuring element applies to each pixel/voxel and its nearest neighbors in real-space. Fig. 2.2 shows the $3 \times 3 \times 3$ neighborhood of each voxel in a 3D image along with three common structuring elements (6-, 14- and 26-neighbors). Typical boolean operations are *dilation* and *erosion*

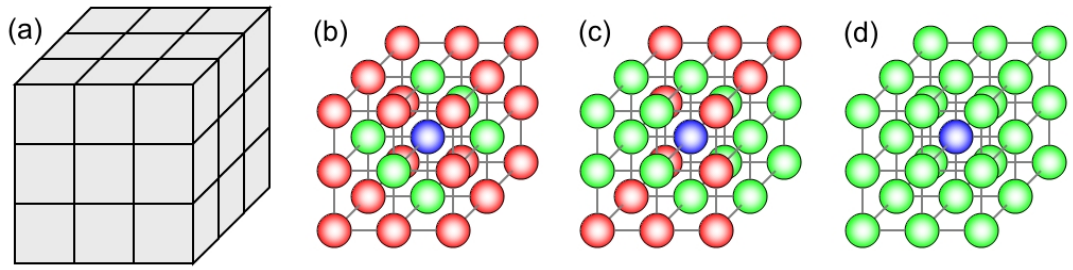

Figure 2.2: Typical structuring elements applying to the (a) $3 \times 3 \times 3$ environment of each voxel in a 3D image. (b) 6-neighbor element (the green points are considered as neighbors of the central blue point whereas the red voxels are not). (c) 14-neighbor element, (d) 26-neighbor element. Note that unlike (b), (d) and other possible symmetrical elemets (e.g. 18-neighbors), the element (c) is asymmetric and has 4 possible configurations. The pros and cons of each structuring element are detailed by Ohser and Mücklich [Ohs00].

of the foreground objects. Dilation applies to each background voxel looking for foreground voxels among its nearest neighbors (which are defined by the structuring element). If there is a foreground voxel in the neighborhood of the background voxel, the latter transforms into a foreground voxel which is stored in a twin image that will become the dilated image when the procedure is complete. Erosion is the opposite of dilation: If a background voxel is found among the neighbors of a foreground voxel, the latter is erased. The sequential application of a dilation followed by an erosion is called *closure* due to the fact that small voids in the foreground are closed by this procedure. Closure is applied to smooth ragged surfaces or to fill pores that are not entirely binarized and contain random background voxels that result from image noise. The inverse combination (erosion followed by dilation) is named *opening* for similar reasons. The radius of opening and closure operations can be extended in two ways: (a) By using a larger structuring element or (b) by applying repeated dilations and erosions. However, with a larger radius the shape of the particles is bound to change. Similar to faceted crytal growth the structuring element favours dilation/erosion along certain directions. In the worst case a very strong opening might transform spherical particles into octahedra (using a 6-neighbor element) or cubes (using a 26-neighbor element). In addition to the boolean operations, structuring elements are commonly applied filter 8-bit gray images, e.g. to calculate mean values (coefficients {1,1,1}) or gradient images (coefficients {1,0,-1}).
The morphological transformations used during this work require calculation of the Euclidean

distance transform map from the binary image [Cui99] (EDT, see Fig. 2.1d). In such EDT maps, every point corresponding to foreground voxels contains a value representing the distance (in voxels) to the nearest background point, and similar - but negative - values are calculated for points corresponding to background pixels. The maxima in these maps represent the centers of the particles, and the minima represent points at equal distance between neighboring particles. EDT maps are used to identify the boundaries of each particle using *region growing* also known as "watershed transformation" (Fig. 2.1e) [Soi90, Vin91]. This title is understood when considering the inverted EDT map where the particles are represented by valleys with the lowest point at the center. A stepwise binarization with increasing threshold values results in flooding of the valleys. During flooding, watersheds are created wherever two *lakes* join. Further multiplication (masking) with the binary image (Fig. 2.1c) allows for automatic identification of each particle, its position and size (Fig. 2.1f). While calculations in 3D were done with MAVI (ITWM Fraunhofer Kaiserslautern, Germany), ImageJ [Abr04] was used for binarization and watershedding of 2D images. Note that in order to prevent oversegmentation in 3D with this procedure, whereby non-spherical particles become artificially fragmented, a pre-flooding algorithm was used to exclude very small particles and speckles from the analysis (e.g. for the analysis of Al-Ge32 alloy, particles smaller than $12\,\mu\mathrm{m}$ were merged with their larger neighbors, see section 3.1.1). The labeled and segmented 3D data allows to calculate volume V, surface A, sphericity $F = 6V\sqrt{\pi/A^3}$, connectivity n (average number of contacts per particle) and contiguity G of each particle. Assuming spherical particles, it is convenient to calculate an equivalent spherical particle diameter $a = \sqrt[3]{6V/\pi}$, e.g. to describe particle coarsening. For 2D images a is calculated similarly from the planar surface A_{2D}: $a_{2D} = \sqrt[3]{4A_{2D}/\pi}$. The contiguity G represents the fraction of a particle's surface that is connected to neighboring particles, commonly defined by average values [Ugg04]:

$$G = \frac{2S_{SS}}{2S_{SS} + S_{SL}} \tag{2.10}$$

with S_{SS} the average solid-solid interface, equivalent to the fraction of surface area of a particle that is connected to neighboring particles (accounted for twice in eq. 2.10 due to the existence of a single connection between two adjacent particles) and S_{SL} the average remaining particle-matrix interface. $G = 0$ for isolated particles and $G = 1$ for bulk material.
Additionally, the orientation of each particle can be computed from its inertia tensor J_{ij}

$$J_{ij} = \sum_{\vec{x} \in particle} m(\vec{x}) \cdot x_i x_j \tag{2.11}$$

with $\vec{x} = (x_1, x_2, x_3)^T$ the coordinate vector of each voxel relative to the centre of mass of the particle, and $m(\vec{x})$ the *mass* of the voxel $\vec{x}$. For a binary image, $m = 1$ for all voxels belonging to a particle and J_{ij} becomes the orientation tensor T_{ij} from which the eigenvalues λ_i and eigenvectors $\vec{t_i}$ are obtained by calculating the roots of the characteristic polynomial $P(\lambda) = Det(T - \lambda I)$ (with I the unitary 3×3 matrix). T is symmetric ($T_{ab} = T_{ba}$) and therefore its eigenvalues are real. The eigenvectors span an orthogonal basis in Euclidian

space, thus defining the orientation ellipsoid of the particle. It is further useful to calculate a transformation matrix $A^{-1} = \{\vec{t}_1, \vec{t}_2, \vec{t}_3\}$ which is orthogonal ($A^{-1} = A^T$) and is constructed directly from the eigenvectors. A can be used to transform a voxel $\vec{x}$ into the coordinate system of the particle whereby the new coordinates $\vec{\epsilon} = (\epsilon_1, \epsilon_2, \epsilon_3)^T = A^T\vec{x}$ are calculated. This method was applied for example to study the orientation and topography of cracks in fractured rocks (see section 3.3).

Chapter 3

Applications and results

3.1 Metallic alloys

The microstructure of binary metallic alloys such as Al-Si and Al-Ge is characterized by a primary solid phase and an eutectic phase: during solidification the primary solid phase nucleates at the liquidus temperature and continues to grow until the solidus temperature is reached and when remaining melt freezes, forming the fine structured eutectic phase. The resulting primary solid phase microstructure depends to a large extent on the cooling rate and the distribution of nucleation sites, and it is desirable that a globular microstructure forms. Whenever alloys are partially remelted and are then annealed at a temperature above the solidus, as often occurs in industrial casting processes, coarsening of the primary solid is observed [Rat01, Ann95]. Coarsening occurs due to dissolution of the eutectic phase, which results in additional 'ripening' of the solid phase [Ost00, Voo85]. In particular, during rheo- and thixocasting, the alloy is heated to the semi-solid state before it is cast [Ugg04, Fan02] (for reliable and successful casting processes and obtaining the designed final components, stringent control over the microstructure is crucial). The morphology of the primary phase can coarsen in various ways when an alloy is held in the semi-solid state during processing [Fle74]. Many parameters contribute to this variation, including flow of the slurry, temperature and possibly sample dimensions [Thi87, Die99]. Under the assumption that the primary phase forms an agglomeration of many particles, coarsening is considered to be the result of two processes: isolated particles grow at the expense of smaller particles [Voo92, Eno87] (cf. Fig. 3.1a) or connected "touching" particles merge into larger particles by coalescence [War96, Tak84] (Fig. 3.1b). Naturally, these descriptions are just models, because in reality many engineering alloys form a primary phase with a more complex morphology that coarsens in a different way (see Fig. 3.1c).

3.1.1 Coarsening of grain-refined Al-Ge32 alloy

The partition of solid (S) and liquid (L) phases in binary alloys can be expressed in terms of volume fractions g_S and g_L (note that $g_S + g_L = 1$). During annealing, the solid particles change their volume and grow. The average volume, which for sufficiently round particles can be approximated to be proportional to the cube of the average diameter, increases linearly with the annealing time, according to

$$a(t) = K(t - t_0)^{1/3} \tag{3.1}$$

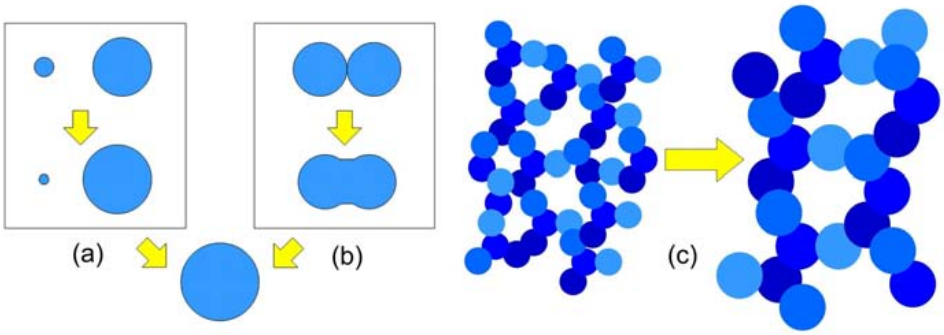

Figure 3.1: (a) Coarsening of dispersed particles. Larger spheres grow at the expense of smaller ones. (b) Coarsening of connected particles of similar size via coalescence. (c) Coarsening of a network of agglomerated particles preserving its self-similar morphology.

Here, $a(t)$ is the average diameter at time t, t_0 the time when $a = 0$ and K is the growth rate and the coarsening exponent is 1/3 according to Lifshitz, Slyozov and Wagner (LSW-theory) [Lif61, Wag61]. Equation 3.1 is considered a valid description for coarsening of spherical particles in a supersaturated solution. However eq. 3.1 has to be considered the idealized description of a very complex physical process. For the limit $t \rightarrow 0$, the coarsening speed $\dot{a}$ becomes ∞, therefore a statistical distribution of particle nuclei of zero size have to be considered. The LSW theory also claims that at any time during coarsening, the average particle diameter maintains a constant ratio to the width of the particle diameter distribution at any given time. Consequently, self-similarity is an expected characteristic of the structural morphology as it coarsens.

One of the assumptions of the LSW theory is that g_S has to be small, so that individual particles may be considered 'non interacting'. A small g_S is fundamental to the interpretation of many of the dynamic processes that are related to coarsening. This is because moderate g_s values result in interactions between neighboring grains, that bring about higher concentration gradients in the liquid while increasing K [Eno86, Wol97, Tzi00]. For semi-solids note that with g_S exceeding a percolation threshold (all particles become interconnected) the particles start to form a three-dimensional skeleton which is characterized by agglomerates that make identification of single particles difficult [Wol97, Nir00].

The liquid film migration model [MW02] extends LSW further to include significantly higher solid fractions than originally proposed, accounting for connected particles whereby mass transfer occurs along the connection necks. Most experimental models explicitly predict broader size distributions of particles, compared to the ideal dispersion that was considered in the LSW theory. Theoretical predictions of the dynamics of the process have provided possible explanatory mechanisms for deviations from classical LSW theory [Hoy91]. Despite these differences, coarsening theories confirm eq. 3.1 and most assumptions result in similar linear relationships between average particle volume and annealing time. By using scaling functions and assuming self-similar statistical ensembles, the universality of the $t^{1/3}$ growth has

been demonstrated in three-dimensions for a variety of phase-separating processes [Fra91]. Recently it has been shown that even for anisotropic metallic microstructures consisting of dendrites, the $t^{1/3}$ relation holds, if $a(t)$ in eq. 3.1 is replaced by a length scale characteristic of the solid-liquid interface [Men04]. Exponents of $1/4$ and $1/5$ are thought to be related to the coarsening of precipitates located at grain boundaries and dislocations respectively. However, even these cases are only different from LSW if volume diffusion is truly negligible [Hoy91]. The coarsening of such nanometer-sized precipitates in metallic alloys has been well explored in situ by means of small angle X-ray scattering (SAXS [Par97, Tsa03]) and/or in a similar way by neutron scattering (SANS [Hen81]). However for a semi-solid network of binary metallic alloys, only few in situ imaging experiments have provided direct evidence for any of the theoretical predictions of coarsening kinetics on the micrometer-scale [Lud04, Lim07]. What is known about the evolution of the particle size distribution is mainly based on measurements obtained from 2D images [Ann95, Lou95, Kai99] and much remains unknown about the 3D coarsening. Current state-of-the-art technology allows to visualize the 3D characteristics of the particles of the primary solid, allowing to provide direct answers to many questions. In this work, the coarsening of a non-agitated semi-solid network of particles (cf. Fig. 3.1c) is monitored in grain refined AlGe32(wt.%) alloy. When this alloy is heated to a temperature above the solidus and below the liquidus, a dispersion of solid Al-rich particles in a liquid Al-Ge solution takes place. In contrast to the destructive and time-consuming serial sectioning methods [Wol97, Nir00, Men04, Alk02] non-destructive X-ray imaging is employed to produce dynamic radiographs and static tomograms of the microstructure in a binary aluminum-germanium alloy of AlGe32. These data are then used to quantify various coarsening parameters such as the particle size, nearest-neighbor characteristics and connectivity.

Materials: The binary alloy AlGe32 was selected for this investigation because its structural properties are most similar to the important class of casting alloys based on AlSi7 (e.g. A356). To create a microstructure comparable to AlSi7 a composition of 68 wt.% Al and 32 wt.% Ge was chosen to yield a 0.5 volume fraction of the α-particles at the eutectic temperature $T_e = 420\,°\text{C}$. Aluminum and silicon have very similar X-ray absorption coefficients, which is why the AlSi7 alloy microstructure cannot be visualized by conventional absorption CT (a solution to this problem is provided by holotomography, see section 3.1.5). The higher atomic mass of germanium generates strong absorption contrast relative to aluminum when X-ray images are observed, making it much more amenable to this type of investigation. The simple-eutectic equilibrium binary phase-diagram [Mas90] of Al-Ge is depicted in Fig. 3.2. A homogeneous equiaxed distribution of fine aluminum α-grains embedded in a matrix of the eutectic composition was produced by melting and quenching AlGe32 ingots. The ingots were formed by combining the pure elements (>99.99%) with 4 wt.% commercial AlTi5B grain refiner (KBM AFFILIPS, Netherlands) followed by levitation melting and casting in a cold crucible. The grain refiner contains sub-micrometer sized titanium boride particles which act as nucleation sites for α-Al. Note that, although the grain refined alloy is stricly not a binary system any-

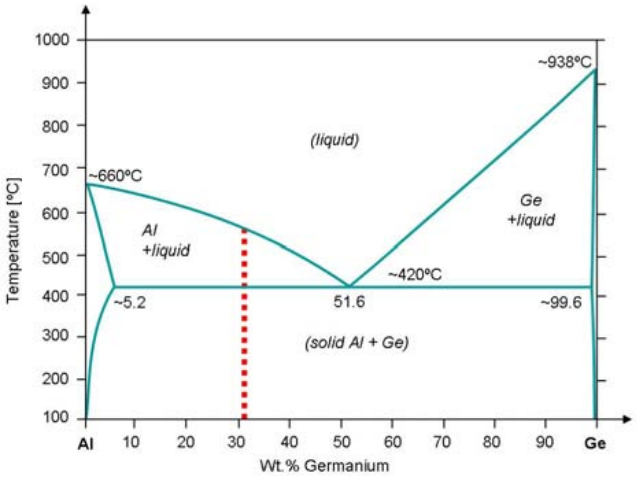

Figure 3.2: Binary phase diagram of Al-Ge alloy (dashed line indicates the composition of 32 wt.% germanium). The liquidus temperature of AlGe32 is approx. 560 °C.

more, the mixing of the Al and Ge crystals with the TiB_2 particles (e.g. the occurence of a $AlTi_3$ phase) is neglected. The grain refiner was used only to reduce the grain size and to minimize directional growth of dendrites during solidification [Naf04, Kas01]. Fig. 3.3 illustrates the difference between grain refined produced microstructure (a) and dendritic non grain refined microstructure (b) of AlGe32 alloy.

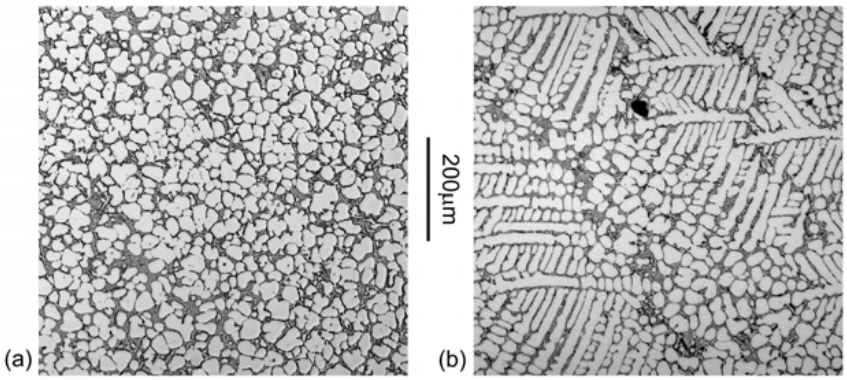

Figure 3.3: Two polished micrographs showing as-cast AlGe32 alloy: (a) alloy with addition of 4wt.% of AlTi5B grain refiner and (b) without additional grain refiner.

Samples for radiography and tomography were cut from the cast AlGe32 ingot. For the radiography experiments thin foils of AlGe32 were used for the purpose of observing the ripening of solid Al-particles in the melt in situ. Foils of thicknesses: $0.1\,\mathrm{mm}$, $0.2\,\mathrm{mm}$, $0.4\,\mathrm{mm}$ and $0.5\,\mathrm{mm}$ each $3\,\mathrm{mm} \times 3\,\mathrm{mm}$ in width and height were used. During radiography the samples were annealed at a constant temperature of $450\,°\mathrm{C}$ ($470\,°\mathrm{C}$ for the $0.5\,\mathrm{mm}$ foil to improve the visibility of the solid particles by reducing the solid volume fraction).
Heat absorption was measured during remelting of the Al-Ge32 alloy using a differential scan-

ning calorimeter and the weight fractions $f_S = 0.41$ at $450\,°\mathrm{C}$ and $f_S = 0.37$ at $470\,°\mathrm{C}$ were found by integration of the heat flow graph [Rue06]. Taking the concentrations $C^{(S)}$ and $C^{(L)}$ of solid and liquid from the phase diagram in Fig. 3.2 and the densities $\rho_{Al}^{(L)} = 2.4\,\mathrm{g/cm^3}$, $\rho_{Ge}^{(L)} = 5.5\,\mathrm{g/cm^3}$, $\rho_{Al}^{(S)} = 2.6\,\mathrm{g/cm^3}$ and $\rho_{Ge}^{(S)} = 5.3\,\mathrm{g/cm^3}$ of solid (S) and liquid (L) aluminum and germanium [Kam95, Dis64], the volume fractions $g_S = 0.49$ at $450\,°\mathrm{C}$ and $g_S = 0.45$ at $470\,°\mathrm{C}$ were calculated using the method of partial areas [Che98]:

$$g_S = \frac{f_S}{f_S + (1 - f_S)\rho^{(S)}/\rho^{(L)}} \tag{3.2}$$

For the tomography experiment, a cylindrical sample $6\ mm$ in diameter and approx. $15\,\mathrm{mm}$ high was cut out of the ingot that provided the samples for radiography. The sample was repeatedly heat-treated by annealing at $T = 450\,°\mathrm{C}$ for 8 minutes followed by air cooling. Prior to and following each treatment, complete tomograms were recorded. Altogether six 3D images of the cylindrical sample were obtained, with the last tomogram corresponding to a total accumulated annealing time of 40 minutes. A second cylinder of a non grain refined alloy of the same dimensions was heat-treated and imaged similarly. This sample, which contained an initial dendritic microstructure (cf. Fig. 3.3b), was used for comparison.

Image acquisition: Radiography and tomography were carried out at BESSY/BAMline. Fig. 3.4 illustrates the experimental setup for radiography as well as a typical image obtained during such experiments. Thin AlGe32 foils of different thicknesses $b = 0.1 - 0.5\,\mathrm{mm}$

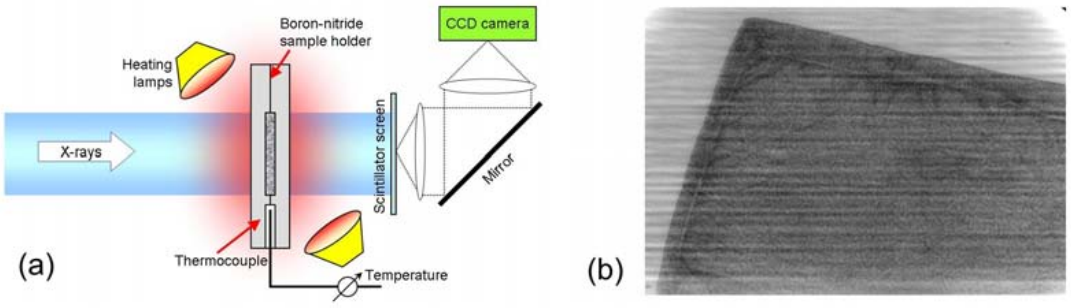

Figure 3.4: (a) Schematic illustration of the real-time radiographic experiment at BESSY/BAMline. (b) Image of a semi-solid AlGe32 foil in the BN sample holder (note the horizontal stripes overlaying the image are due to inhomogeneous beam intensity; the upper edges appear brighter due to the edge of the optical lenses).

were inserted between two $1\,\mathrm{mm}$ thick boron nitride (BN) plates which absorb X-rays only weakly, allowing placement in the beam. Temperature was monitored by a thermocouple element placed close to the alloy. The photon energy for the radiography experiments was set to $E = 25\,\mathrm{keV}$. Temperature T, number of images N (at $0.23\,\mathrm{fps}$) and effective annealing time t (during which the material was in the semi-solid state) are listed in table 3.1.
Images were acquired using a $12\,\mu\mathrm{m}$ YAG:Ce scintillator with an effective pixel size of $\Delta x = 1.6\,\mu\mathrm{m}$ and a resolution $R \approx 6 - 7\,\mu\mathrm{m}$. As can be seen from Fig. 3.4a, the sample was arrested

sample	b [mm]	$T\,[^{\circ}C]$	g_S	N	t [min]	growth rate K	growth exponent
1	0.1	450	0.49	540	29	20.64 ± 0.25	0.1708 ± 0.0037
2	0.2	450	0.49	540	33	13.71 ± 0.18	0.2498 ± 0.0035
3	0.4	450	0.49	660	45	16.33 ± 0.11	0.2143 ± 0.0019
4	0.5	470	0.45	660	38	17.70 ± 0.14	0.2071 ± 0.0023

Table 3.1: Results from in situ radiography of coarsening semi-solid Al-Ge32 alloy.

in the focus of two heating lamps and could therefore not be moved off the beam in order to record brightfield images (best suited for normalization). To correct for beam inhomogeneities (seen as blurred horizontal lines overlying the silhouette of the sample, shown in Fig 3.4b) a virtual brightfield image was created by applying a stripe-shaped median-filter and assuming slow horizontal modulations in the intensity. The experimental radiographs were then normal-

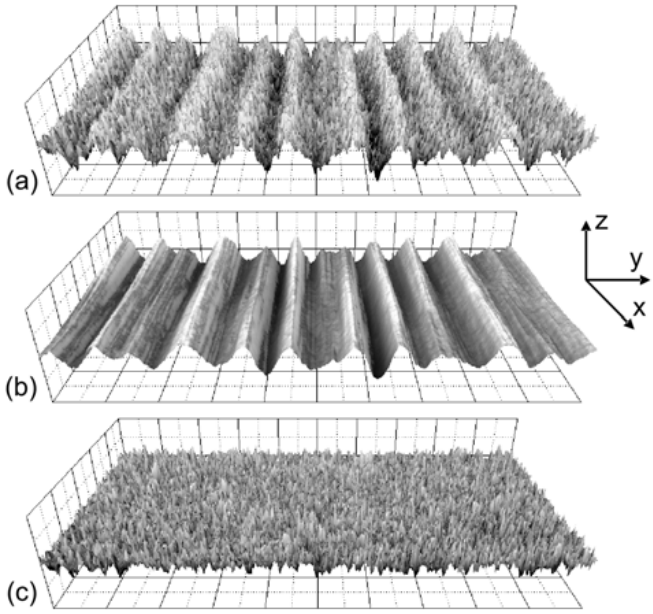

Figure 3.5: Virtual ßtripe-filterfor beam normalization: Grey values representing the image intensity are represented as a z-value in a pseudo 3D topography in the (x, y)-plane. (a) Every radiographic image is a superposition of underlying background and structural information. (b) The background (virtual brightfield) image is characterized by horizontal stripes originating from the beam reflections by a double multilayer monochromator. (c) After application of a stripe-filter we obtain an image of the structural information only.

ized by this corrective background (schematically illustrated in Fig. 3.5) by simple division, as is usually done in tomographic imaging. An example of the resulting images at annealing times of $3\,\mathrm{min}$ and $33\,\mathrm{min}$ is shown in Fig. 3.6, along with a metallurgical micrograph of a polished section of the same sample, shown for comparison. A $10\,\mu\mathrm{m}$ thick GADOX scintillator screen was used for the tomographic data acquisition, with a resulting pixel size

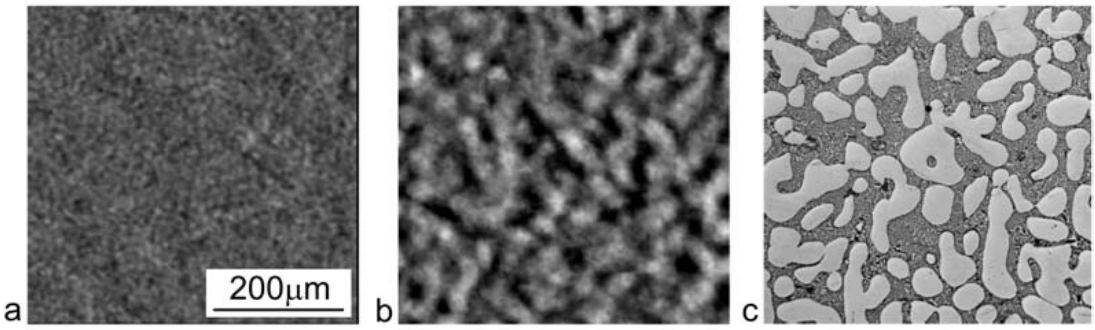

Figure 3.6: Coarsening of $0.2\,\mathrm{mm}$ thick Al-Ge32 foil in a boron nitride sample holder: (a) Radiograph taken after the alloy was annealed at $T = 450\,°\mathrm{C}$ for $3\,\mathrm{min}$, (b) image of the same foil after $33\,\mathrm{min}$ annealing time in the semi-solid state, (c) Metallurgical micrograph of a polished section of the same sample after annealing (a,b and c share the same scale).

$\Delta x = 3.5\,\mu\mathrm{m}$ and an optical resolution of approx. $12\,\mu\mathrm{m}$. For each tomogram 900 angular projections were recorded using X-rays of $E = 50\,\mathrm{keV}$ photon energy. The six measurements were aligned so as to allow matching the particles allowing comparison of the differences in microstructure. Numerical image analysis was used to identify and quantify particles of the primary solid phase (for details on the algorithm see section 2.2). The average particle diameter and standard deviations were calculated from the 2D/3D images and the data was fit to a power law similar to eq. 3.1 (Origin7.0, Northhampton, MA, USA).

In situ radiography: Obviously the choice of the binarization threshold has an effect on the resulting growth rate and exponent. There exist two ways to determine this threshold value: a) Select a value so that the fraction of foreground pixels in the images correponds exactly to the measured solid fraction, or b) test a wide range of threshold values for each sample and look for a parameter range for which the image analysis results are fairly unchanged. Admitting that the exact measurement of g_S only leads to a correct binarization when there is no overlay between particles in the beam direction, testing the effect of different threshold values is necessary either-way. Fig. 3.7 shows a plot of the coarsening exponent calculated for several binarization thresholds which correspond to solid area fractions between 20% and 80%. Fortunately, the calculated exponents show minimal scatter and their value is almost constant for solid fractions between 40% and 60%. Similar test results were obtained for the coarsening rate K. A binarization threshold of approx. 50% (notably close to the measured value of g_S) was therefore chosen for the analysis of all the datasets. Results for the mean 2D equivalent sphere diameter $\langle a_{2D} \rangle$ and the standard deviation $(SD)_{2D}$ of $\langle a_{2D} \rangle$ as a function of annealing time are given in Fig. 3.8 for the four different sample thicknesses (solid lines represent the fit). As can be seen, following an initial plateau prior to reaching the annealing temperature, a significant rise in average particle diameter is observed. With increasing annealing time the coarsening slows down. The standard deviation of average particle diameter is shown as an

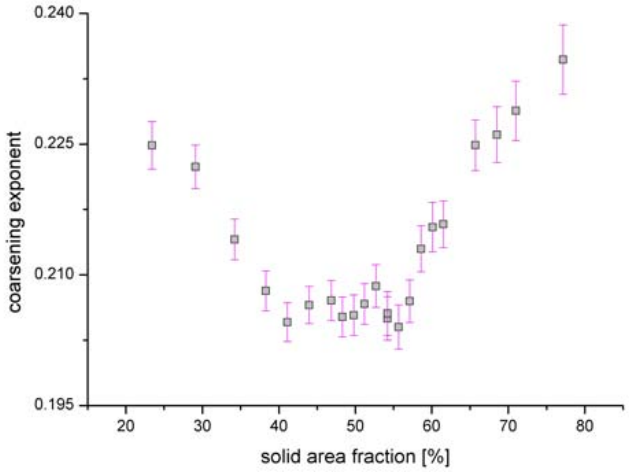

Figure 3.7: The coarsening exponent from the fit of the data of the $0.5\,\mathrm{mm}$ foil as a function of different solid area fractions (confidence intervals are shown with data points). The different solid fractions were obtained by changing the binarization threshold whereby higher threshold values correspond to larger solid area fractions.

inset in each graph, reflecting the fact that the width of the diameter distribution increases concomitant with the average values. The calculated growth rates and exponents are shown along with their corresponding error values in table 3.1. Note that a median filter of size 7×7 (instead of 3×3) was applied to the images recorded from the thinnest sample. This was done because the $0.1\,\mathrm{mm}$ of AlGe32 created only weak contrast, resulting in poor signal to noise ratios due to the additional signal from the BN sample holder and the inhomogeneous beam profile.

Microtomography of cyclically annealed samples: In addition to the equivalent sphere diameter a, the labeled and segmented 3D data allowed to calculate the particle connectivity n (average number of contacts per particle) and the contiguity G of the particles (cf. section 2.2). Distributions of a, G and n of the six 3D datasets of the grain refined alloy and four datasets of the non grain refined alloy recorded at different annealing times are shown in Fig. 3.9. A constant threshold value was chosen for each alloy by assuming $g_S = 0.5$ in the initial state ($t = 0$). Due to the fact that the same region in each alloy was measured at different annealing stages, calculating g_S from the binarized datasets recorded at $t > 0$ resulted in values very close to 0.5 ($\approx \pm 0.01$ error). Particle diameters (panels a and b) and particle contiguity (panels c and d) were fitted with Gaussian distributions while connectivity was fitted to a log-normal distribution function (panels e and f). As can be seen, the average particle diameter as well as the width of each distribution increase during annealing, shifting from ~ 70 to $100\,\mu\mathrm{m}$ in the grain refined and from 75 to $110\,\mu\mathrm{m}$ in the non grain refined sample. Contiguity of the grain refined alloy shows only minor changes in the average values (≈ 0.21) while for the non grain refined alloy contiguity only starts around 0.1 and increases with the annealing time. No

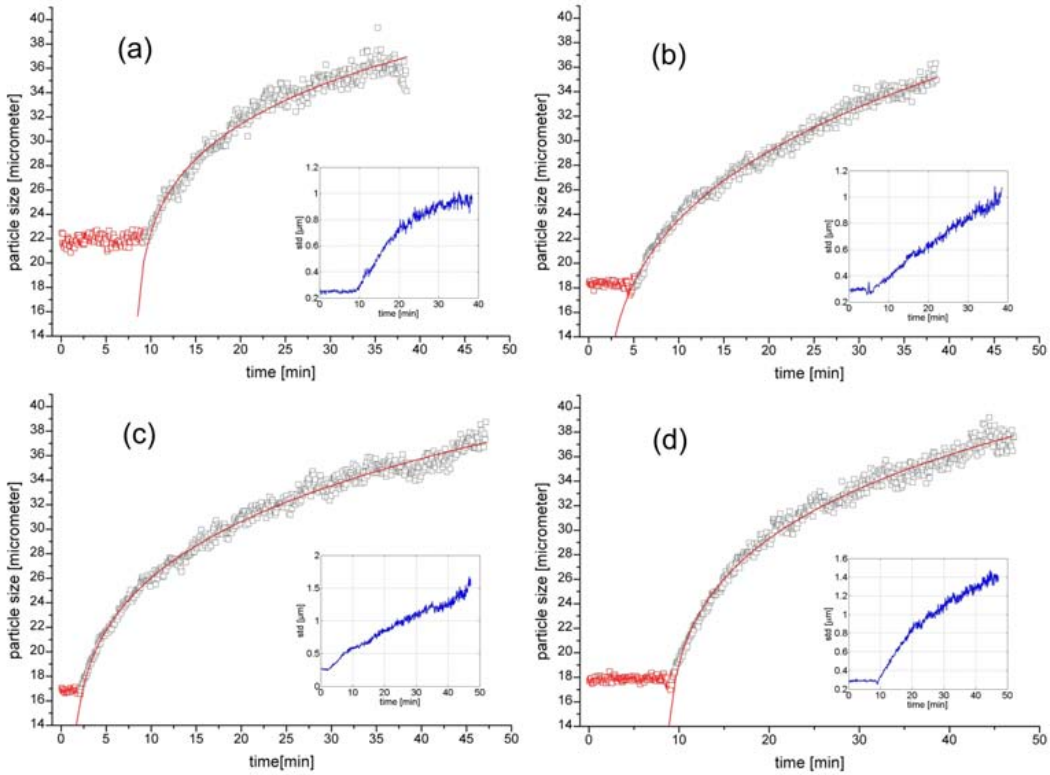

Figure 3.8: Comparison of the evolution of the mean particle diameter derived from radiographic films of four AlGe32 foils of increasing thicknesses: (a) $0.1\,\mathrm{mm}$, (b) $0.2\,\mathrm{mm}$, (c) $0.4\,\mathrm{mm}$ and (d) $0.5\,\mathrm{mm}$. The red measurement point have been masked as they correspond to times before the coarsening started. The insets show the standard deviation of the average particle diameter as a function of annealing time.

significant shift of the maximum connectivity in the grain refined sample (≈ 4) is observed. For the non grain refined alloy connectivity drops from about 5 to 4. All distributions show the total number of particles to decrease with increasing annealing time. For the 3D data, the cummulated annealing time t, the number of analyzed particles N, the mean equivalent sphere diameter $\langle a \rangle$, the standard deviation (SD) and the ratio $\langle a \rangle / (SD)$ of the diameter distributions as well maximum values of connectivity n and contiguity G are shown in table 3.2.
Fig. 3.10 shows the correlation plots for the mean particle diameter $\langle a \rangle_n$ (restricted to particles of connectivity n) and n for the grain refined (a) and the non grain refined alloy (b). The coarsening of a small particle cluster is depicted in Fig. 3.11. In this figure, grain refined and non grain refined alloy microstructures are shown together with the results obtained from fitting $\langle a \rangle$ to a power law similar to eq. 3.1 (dashed lines show the confidence intervals of the fit). For the grain refined alloy we obtain a groeth rate $K = 41.5 \pm 2.5$ with a growth exponent 0.21 ± 0.02, and for the non grain refined alloy $K = 32 \pm 12$ and the exponent 0.30 ± 0.08.

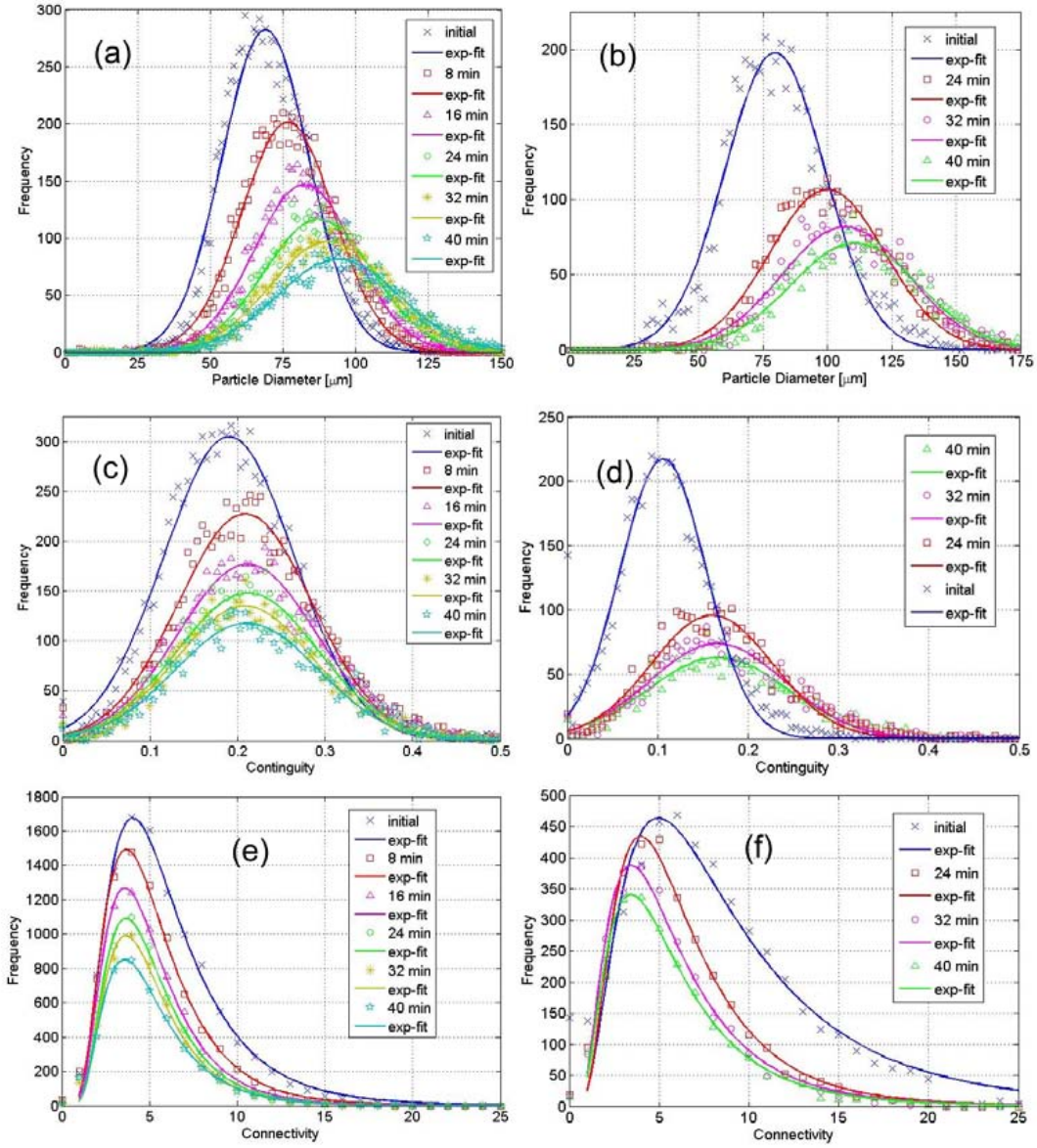

Figure 3.9: (a,b) Histograms of particle diameter and Gaussian fitting curves for (a) equiaxed AlGe32 structure and (b) non equiaxed structure from the initial state up to $40\,\mathrm{min}$ of annealing time at $450\,°\mathrm{C}$. (c,d) Contiguity distributions and Gaussian fits for (c) equiaxed and (d) non equiaxed structure. (e,f) Connectivity and log-normal fitting curves for (e) the equiaxed and (f) the non equiaxed structure.

Discussion: By comparison of the bulk AlGe32 microstructure with observations from thin foils, deviations in the coarsening kinetics are found when the sample thickness decreases, approaching the average particle size. Both from observations of thin foils and bulk samples, the microstructure of semi-solid AlGe32 alloy appears to evolve in reasonably good agreement with the $t^{1/3}$ power law which is predicted by classical LSW theory [Lif61, Wag61]. Thus coarsening of a solid network of agglomerated particles in a liquid solution is well de-

sample	t [min]	N	$\langle a \rangle$ [µm]	(SD) [µm]	$\langle a \rangle / (SD)$	G	n
Al-Ge32 + AlTiB	0	10485	70.72	14.87	4.762	0.190	4.0
Al-Ge32 + AlTiB	8	8011	77.82	16.03	4.854	0.209	3.6
Al-Ge32 + AlTiB	16	6393	83.62	17.65	4.738	0.210	3.6
Al-Ge32 + AlTiB	24	5438	88.20	18.70	4.717	0.212	3.6
Al-Ge32 + AlTiB	32	4832	91.35	20.09	4.547	0.209	3.6
Al-Ge32 + AlTiB	40	4278	94.68	20.95	4.574	0.210	3.6
Al-Ge32	0	4906	81.65	20.95	3.897	0.107	5.0
Al-Ge32	24	2977	102.15	22.53	4.534	0.160	4.0
Al-Ge32	32	2497	108.17	24.05	4.500	0.165	3.4
Al-Ge32	40	2209	112.01	25.04	4.473	0.167	3.4

Table 3.2: Resulting values of the particle number N, mean particle diameter $\langle a \rangle$, standard deviation (SD), $\langle a \rangle / (SD)$ of the distribution function as well as maximum contiguity G and connectivity n (determined from the fitting curves) in samples of grain refined AlGe32 (+ AlTi5B) and non grain refined AlGe32 measured for different annealing times between 0 and $40\,\mathrm{min}$.

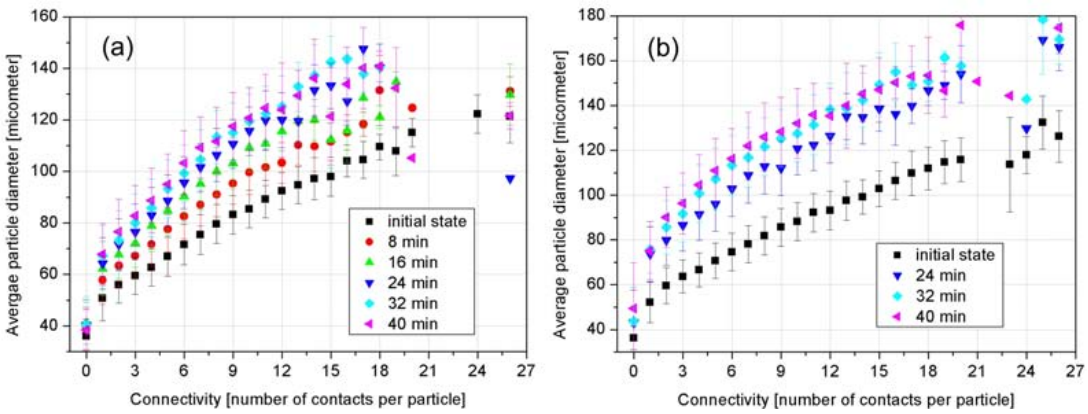

Figure 3.10: Correlation plots of mean particle diameter $\langle a \rangle_n$ vs. connectivity n for the (a) grain refined and (b) the non grain refined alloy. Error bars show the scattering of $\langle a \rangle_n$.

scribed by considering the particles as separate entities. By measuring their size distribution as a function of annealing time, the evolution of a network consisting of round but non-spherical particles is found to behave very similar to coarsening of dispersed spherical particles which are described by LSW theory. The transition from bulk samples to thin foils of thicknesses which approach the average particle diameter does not significantly alter the coarsening law. The coarsening exponent derived from the measurements of non equiaxed AlGe32 reasonably agrees with theory, yet a smaller exponent is found for the coarsening grain-refined sample. Theory predicts a $t^{1/3}$ growth of the particles, yet both 2D and 3D observations of the grain refined microstructure are closer to $t^{1/4} - t^{1/5}$. This was not reported by Rowenhorst et al., who extrapolated a $t^{1/3}$ coarsening behaviour from 2D plane section measurements [Row06]

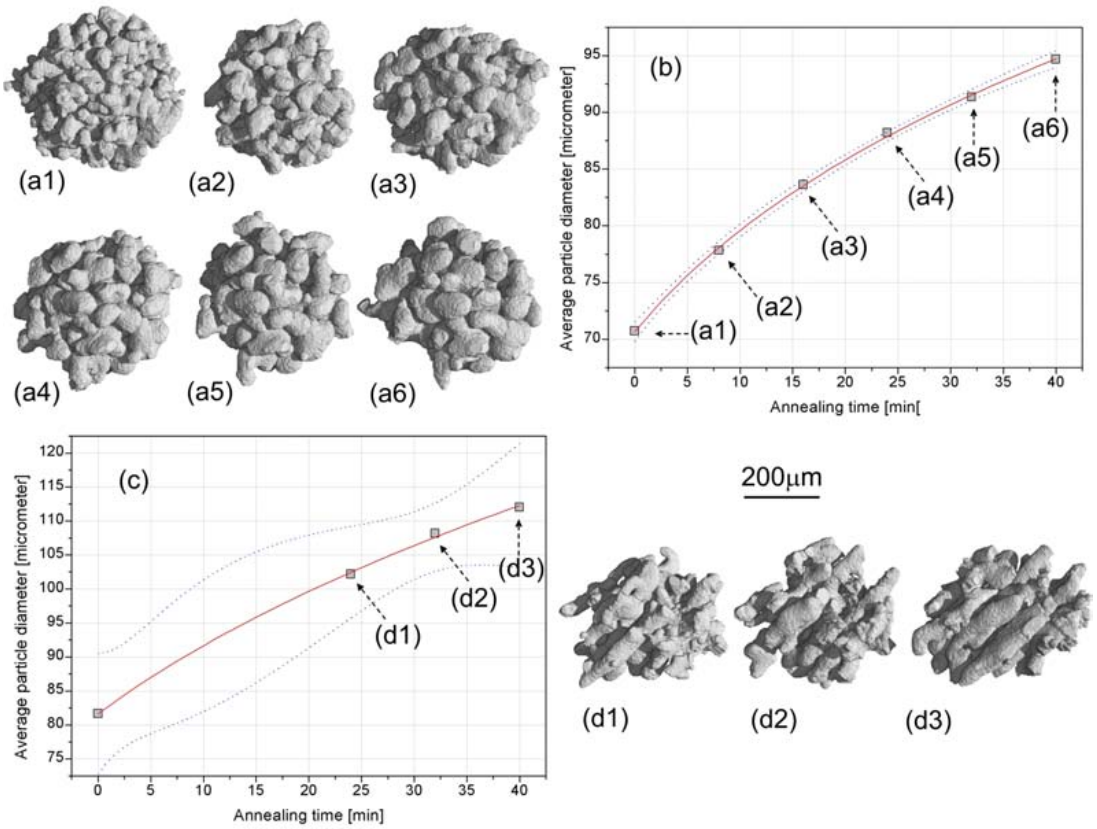

Figure 3.11: Coarsening of equiaxed microstructure of grain refined AlGe32: (a1-6) Small cluster of particles inside a virtual confinement of $250\,\mu\mathrm{m}$ in diameter, cut at the same position in the 6 datasets, each representing an annealing at $450\,°\mathrm{C}$ with a holding time of (a1) $0\,\mathrm{min}$ (initial structure), (a2) $8\,\mathrm{min}$, (a3) $16\,\mathrm{min}$, (a4) $24\,\mathrm{min}$, (a5) $32\,\mathrm{min}$ and a(6) $40\,\mathrm{min}$. (b) Non-linear fit (dashed lines show the confidence intervals) of the average particle diameter. (c) Fit for the non grain-refined alloy (note the confidence intervals are broader than in (b) due to the fact that only four measurement point are available; (d1-3) Small cluster for $24\,\mathrm{min}$, $32\,\mathrm{min}$ and $40\,\mathrm{min}$ annealing time.

perhaps due to particulars of their system or the unavailability of true 3D data. The high solid volume fraction of the present AlGe32 mixture is most likely the cause for a smaller exponent compared to that predicted by the LSW theory. Indeed, Rowenhorst et al hypothesize that thin liquid films might separate adjacent particles which, if relevant to AlGe32, could lead to an increased interfacial curvature stabilizing the larger particles and reducing the growth rate [Row06]. Alternatively, $t^{1/4}$ and $t^{1/5}$ growth exponents have been suggested for precipitates assuming 2D and 1D diffusion mechanisms respectively [Hoy91]. And yet, it is difficult to compare such mechanisms to semi-solid binary alloys, since the inter-particle mass transport occurs mainly by diffusion through the liquid matrix, and not via a solid phase. The measured contiguity of 0.21 shows that a significant fraction of the particles surface appears to be

connected or in close proximity to neighboring particles thereby reducing the free solid-liquid interface. Thus, it is possible that diffusion occurs through inter-particle wetting layers, which similarly to grain boundaries in solids [Hoy91], results in a reduced coarsening exponent.
The self-similar character of coarsening of a network is an important statement of LSW theory: For dispersed spherical particles the ratio of the average diameter versus the width of the diameter distribution is time-independent. This is also true for a network of agglomerated Al-particles in the present AlGe32 system. Two additional parameters were found to characterize self-similar growth of such a particle network, namely the distributions of particle connectivity and contiguity which maintain constant maximum values independently of the annealing time. Hence at any given time at which a particle is observed in a coarsening semi-solid network, the number of connections to other particles, the relative size of the connecting necks and the normalized size distribution of the surrounding particles is constant. The maximum connectivity of the equiaxed Al-particles was found to be ~ 3.6 which is in excellent agreement with recent studies reported on Sn-Pb alloy where a value of 3.66 was found for $g_S = 0.52$ [Row06]. Rowenhorst et al. showed for this system that the average connectivity is mainly a function of g_S, reaching values of $8 - 9$ for $g_S > 0.7$. Similar to their work on Sn-Pb, the present AlGe32 alloy reveals a correlation between particle diameter and connectivity where larger particles exhibit a higher number of contacts.
Significant differences are observed between grain-refined and non grain-refined alloys: while the grain-refined alloy fulfills the criteria for self-similar coarsening predicted by the LSW theory, the same alloy but without additional grain-refiner does not. In contrast to the segmentation of equiaxed grain-refined AlGe32 microstructure, numerically segmenting elongated Al-dendrites which characterize the non-equiaxed structure results in strongly asymmetric objects. Using a different approach based on parameterization and curvature analysis of the solid-liquid interface, Mendoza et al. 2004 have recently shown violation of the self similarity in the coarsening of non-equiaxed Al-Cu alloy [Men04]. A similar violation is found for the non grain refined AlGe32 system. In particular, connectivity decreases and contiguity increases during the annealing of the non equiaxed structure which is in contradiction to self-similar growth. Compared to grain-refined AlGe32 structure at similar annealing times, average particle size and contiguity are larger while contiguity is smaller: This can be interpreted as a direct result of the elongated asymmetric shape of the dendrites which is maintained during coarsening. Extending their approach, Mendoza et al. have also shown that the non-equiaxed Al-Cu microstructure evolves towards an anisotropic morphology aligned with the orientation of solidification [Men06]. A slightly different coarsening rate and exponent are found for the dendritic AlGe32 alloy compared to the grain refined network which could be a result of such an anisotropic coarsening process.
Compared to the bulk samples, a slightly lower coarsening exponent is observed for thinner foils, an effect probably related to the reduced availability of the liquid phase at the container walls. The thinner foils are characterized by a thickness that is close to the average particle size. Coarsening is likely to be hindered when samples of dimensions close to the particle size

distribution are annealed because the particles cannot grow into one direction. Changing the solid fraction by increasing the annealing temperature for the thickest radiography sample did not have a significant effect on the coarsening rate or the exponent. The standard deviation of gray values in the radiographs taken at different annealing times is an additional measure of the statistical significance of the 2D results. The gray levels in these images represent the attenuation of X-rays, which for a constant sample thickness, is approximately proportional to the partition of the solid phase. Consequently, the gray value distribution broadens due to the growing average particle diameter. The broadness (SD) of the gray level distribution was plotted as a function of annealing time (data not shown) and fitted similarly to Fig 3.7. Exponents of 0.175, 0.224, 0.233 and 0.313 are thus obtained for the $0.1\,\mathrm{mm}$, $0.2\,\mathrm{mm}$, $0.4\,\mathrm{mm}$ and $0.5\,\mathrm{mm}$ thick samples, which is remarkably close to the results of the statistical image analysis. This provides corroborating evidence to the robustness of the segmentation, labeling and image processing procedure.
Note that the particle analysis of the radiographs accurately reproduces the coarsening trend but underestimates the particle size (as can be seen by comparing the particle dimensions in 2D with the 3D results: e.g. $38\,\mu\mathrm{m}$ vs. $95\,\mu\mathrm{m}$ after $40\,\mathrm{min}$ annealing time). Note that similarly, the diameter of spherical particles is underestimated when measured from metallographic micrographs, and has to be corrected for the case that the particles are not ideally cut at their equator. Radiographic images can only be used to determine the absolute particle sizes, when the particles lie separated from one another in a plane perpendicular to the beam direction. The tomography datasets on the other hand, allow calculation of the true particle sizes in a network as well as the coarsening kinetics (eq. 3.1) including both exponent and rate. However tomography is performed on cold samples, possibly introducing additional coarsening effects due to the repeated cooling and reheating of the microstructure between two tomographic scans. These effects might result in different particle growth kinetics compared to continuous coarsening. Nevertheless the good correspondence between 2D in situ and 3D cyclic annealing indicates that these differences are minor.

3.1.2 Continuous annealing and powder compaction

In order to quantify the effects of repeated cooling and remelting on the coarsening of AlGe32 alloy (reported in the previous subsection), two grain refined samples (AlGe32 + 4 wt.% AlTi5B) were continuously annealed for $20\,\mathrm{min}$ and $60\,\mathrm{min}$ at $T = 450\,°\mathrm{C}$. Static tomograms of the microstructure in these two stages were acquired under experimental conditions similar to those reported on the cyclic annealing: $\Delta x = 3.6\,\mu\mathrm{m}$ pixel size at $R \approx 12\,\mu\mathrm{m}$ resolution (GADOX) and $E = 50\,\mathrm{keV}$ X-ray energy. Fig. 3.12 shows the distributions of the effective particle diameter a (a), the particle contiguity G (b) and connectivity n (c) along with a correlation plot similar to Fig. 3.10 ($\langle a \rangle_n$ vs. n). The distribution of these values looks similar to what was found for the cyclic experiments and the number of particle-particle contacts increases with the size of the particles. The number of analyzed particles N, the mean

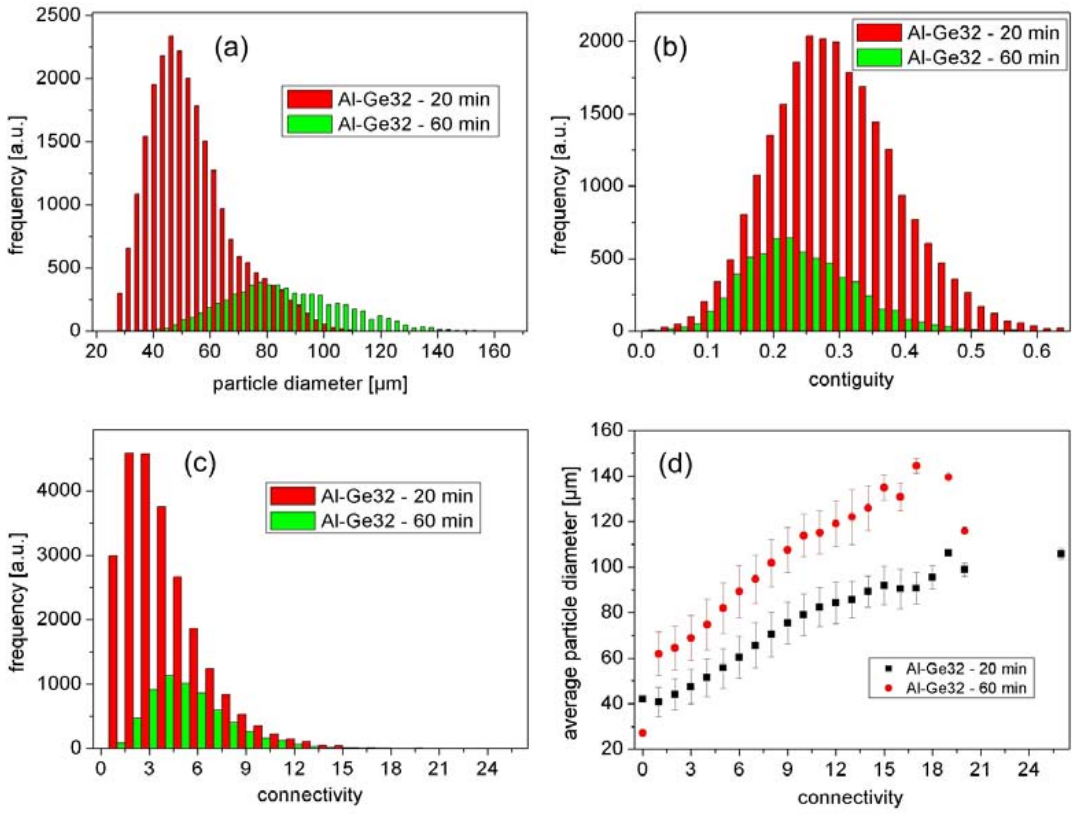

Figure 3.12: Analysis of AlGe32 microstructure produced by continuous annealing (20 min and 60 min). (a) Histogram of particle diameter, (b) particle contiguity and (c) connectivity. (d) Correlation plot (mean particle diameter vs. connectivity).

particle diameter $\langle a \rangle$ and standard deviation (SD) as well as the mean contiguity $\langle G \rangle$ and the maximum connectivity n are listed in table 3.3. Unlike the cyclic experiments, where the same

sample	g_S	t [min]	N	$\langle a \rangle$ [µm]	(SD) [µm]	$\langle a \rangle / (SD)$	$\langle G \rangle$	n
1	0.45	20	25447	52.27	11.51	4.541	0.287	2.5
2	0.50	60	4772	84.18	16.27	5.174	0.226	4.1

Table 3.3: Results from continuous annealing of grain refined semi-solid AlGe32 alloy. Obviously, the solid volume fraction in the two samples was different, leading to different values g_S calculated after binarizing the two datasets with the same threshold.

sample was repeatedly annealed and scanned, the two datasets correspond to different samples that were annealed for 20 min and 60 min. The initial state of these samples was not measured, therefore the results in table 3.3 must be compared to the first row in table 3.2. The mean particle diameter $\langle a \rangle$ increases with time but is found much smaller than what would be expected from the previous results (cf. table 3.2). Due to local variations of the solid volume fraction in the cast material, g_S is different for the two samples (20 min and 60 min) although the same

binarization threshold was applied to both datasets. Consequently, the ratio $\langle a \rangle / (SD)$, the mean contiguity and particularly the connectivity are not constant.
Furthermore, dendritic AlGe32 microstructure resulting from continuous annealing was measured for comparison with the non grain refined sample described in the previous subsection, which was repeatedly heat treated. Fig. 3.13 shows the distributions of particle diameter a, particle contiguity G and connectivity n as well as the correlation plot $\langle a \rangle_n$ vs. n for a sample of non equiaxed AlGe32 ($g_S = 0.49$) after $60\,\mathrm{min}$ continuous annealing at $T = 450\,°\mathrm{C}$. Similar

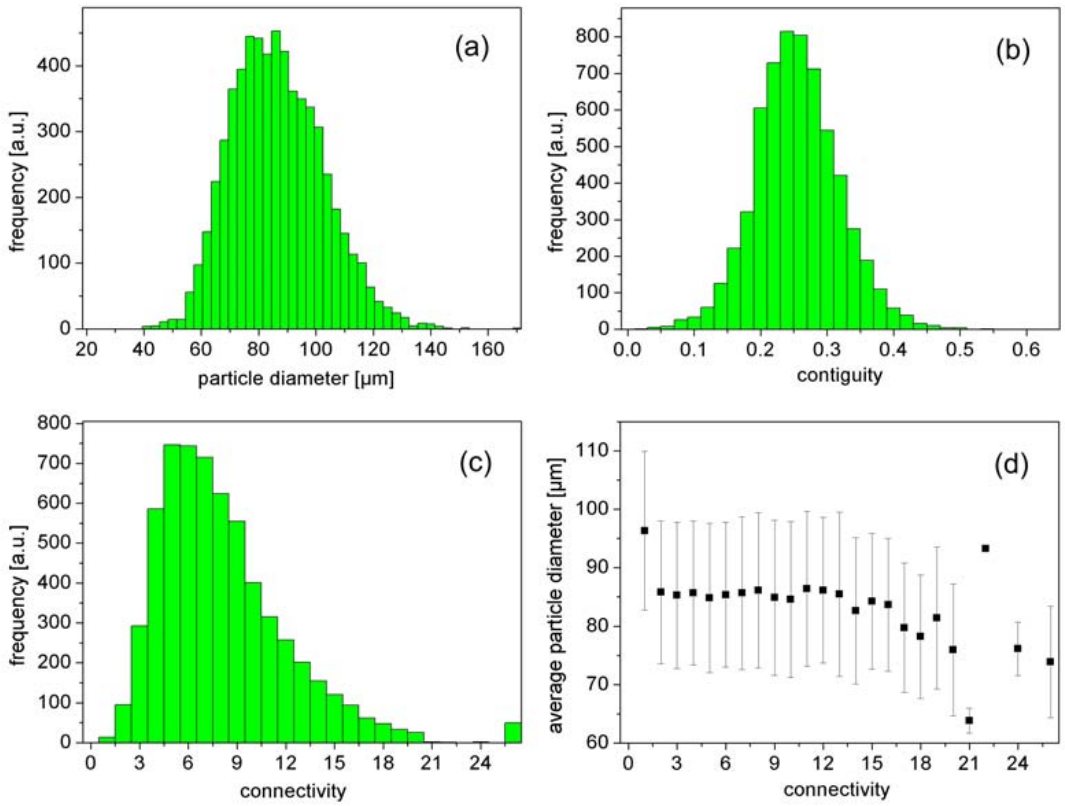

Figure 3.13: Dendritic AlGe32 microstructure after $60\,\mathrm{min}$ of continuous annealing: Histograms of (a) effective particle diameter, (b) particle contiguity and (c) connectivity. (d) Correlation plot: mean diameter vs. connectivity.

to the comparison of the grain refined samples, a smaller average diameter $\langle a \rangle = 85.08 \pm 12.85\,\mu\mathrm{m}$ is found than what would be expected from the cyclic experiments. On the other hand comparably high values are found for the ratio $\langle a \rangle / (SD) = 6.621$, the maximum connectivity $n = 6.8$ and the mean contiguity $\langle G \rangle = 0.245$. Surprisingly the correlation between mean particle diameter and connectivity (Fig. 3.13d) is not observed for this particular sample. Fig. 3.14 shows an axial slice of the grain-refined (a) and the non grain refined sample (b) after $60\,\mathrm{min}$ continuous annealing.
In order to compare the coarsening of AlGe32 to that of a different alloy, a globular microstructure of AlCu21 alloy was produced via a different production route (The composition Al + 21

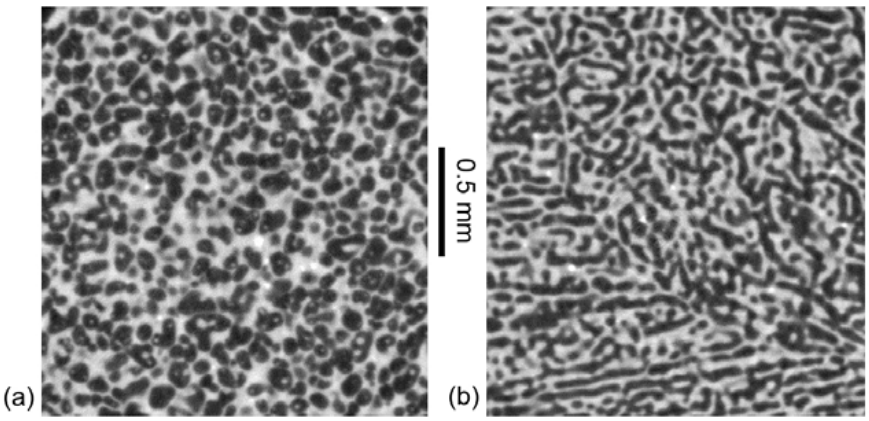

Figure 3.14: Axial tomographic slices of AlGe32 alloy after $60\,\mathrm{min}$ of continuous annealing: (a) grain refined and (b) non grain refined sample.

wt.% Cu was chosen to yield a solid volume fraction ($g_S = 0.52$) similar to AlGe32). Fine powders of the pure elements Al and Cu were sieved (particle size < $40\,\mu\mathrm{m}$) and mixed, followed by uniaxial double-sided compaction for $5\,\mathrm{min}$ with $298\,\mathrm{MPa}$ at $T = 400\,°\mathrm{C}$. The precursor (flat cylinder of $36\,\mathrm{mm}$ diameter and $7\,\mathrm{mm}$ height) was then annealed for $60\,\mathrm{min}$ at $T = 570\,°\mathrm{C}$ in the semi-solid temperature range. In this range the copper is mostly molten in the liquid Al-Cu mixture, the little remanent Cu is diluted in the solid Al crystals. When the sample is cooled, the copper recristallizes into an eutectic Al-Al_2Cu matrix which surrounds the clustered α-Al particles. The desired homogeneous, equiaxed distribution of globular particles is obtained thanks to the fine grained initial microstructure predetermined by the Al powder grains. However, formation of a significant porosity is observed during annealing. This 'foaming effect' is commonly observed when compacted precursors containing consolidated aluminum powder grains are annealed at high temperature. Compared to bulk material, the powder particles have a huge free surface which contains layers of aluminum-hydroxides. Additionally, air bubbles are trapped during the compaction/ consolidation. When the alloy is partially molten, oxygen and hydrogen outgas, forming pores in the material. Hot compaction under vacuum might be one way to avoid this porosity. For the annealed sample, distributions of particle diameter a, particle contiguity G and connectivity n as well as the correlation plot $\langle a \rangle_n$ vs. n are shown in Fig. 3.15 together with an inset illustrating the three-dimensional arrangement of the Al-particles with the eutectic matrix set transparent.

The particle diameters a of the powder compacted annealed AlCu21 sample are somewhat smaller than the particles in grain refined AlGe32 alloy (for comparison see Fig. 3.12a), with a mean value $\langle a \rangle = 62.26 \pm 15.58\,\mu\mathrm{m}$ and a ratio $\langle a \rangle / (SD) = 3.996$. The mean contiguity is $\langle G \rangle = 0.192$ but unlike for the samples of AlGe32, a significant number of particles in the AlCu21 sample has no contacts with their neighbors (220 out of 11135, i.e. ca. 2%). Nevertheless the connectivity is maximum at $n = 3.9$ which is in good agreement with the grain refined annealed AlGe32 alloy ($n = 4.1$).

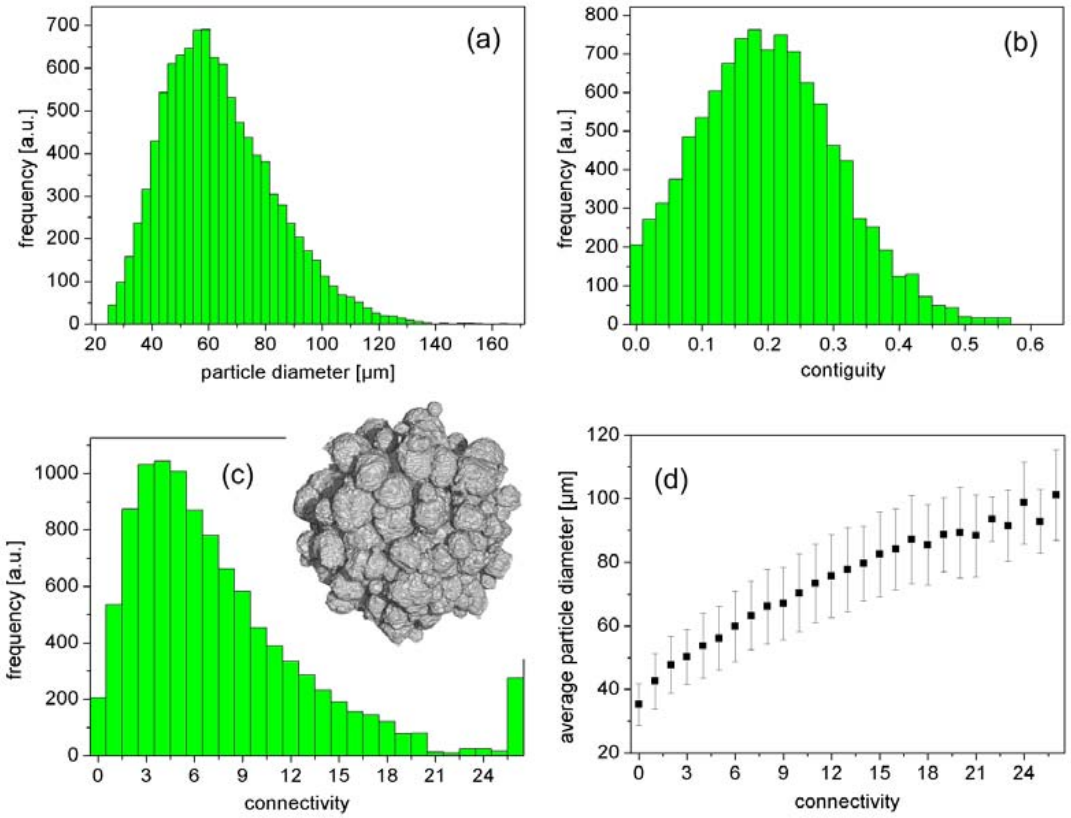

Figure 3.15: Particle analysis of powder compacted AlCu21 alloy after $60\,\mathrm{min}$ continuous annealing. (a) Particle diameter a distribution, (b) particle contiguity G and (c) connectivity n. (d) Correlation plot: $\langle a \rangle_n$ vs. n.

Discussion: Two routes for producing equiaxed globular microstructure were successfully tested and statistical image analysis was applied to heat treated samples after continuous and/or cyclic annealing. Grain refinement was used for Al-Ge alloy whereas an equiaxed particle distribution in Al-Cu was achieved by hot powder compaction. Statistical image analysis revealed subtile differences between the two processing routes/ alloys, visible in the particle size distribution and the inter-particle connectivity. More experiments must be carried out in order to quantify these differences accurately: e.g. annealing of powder compacted AlGe32 samples for comparison with the AlCu21 measurement. In general, the annealed particles tend to have a smaller diameter when they are continuously heat treated (i.e. $\approx 84\,\mu\mathrm{m}$ after $60\,\mathrm{min}$), whereas cyclic treatment produces larger particles probably as a result of repeated quenching and remelting ($\approx 95\,\mu\mathrm{m}$ after $40\,\mathrm{min}$). The same trend was even more pronounced for the non equiaxed microstructures: the average eqivalent sphere diameter was $\approx 85\,\mu\mathrm{m}$ after $60\,\mathrm{min}$ of continuous heat treatment, whereas on the average $112\,\mu\mathrm{m}$ particles were found after $40\,\mathrm{min}$ of cyclic remelting and annealing. For the growth kinetics of the Al-particles reported in the previous subsection this difference between cyclic and continuous annealing has mainly an effect on the growth rate K but not on the coarsening exponent as was confirmed by the 2D in

situ measurements. Yet this conclusion is not firm because of a strongly varying ab initio size distribution of the Al-particles in the different samples that were continuously heat treated. Comparing table 3.3 with table 3.2 leads to the assumtion that the differences between cyclic and continuous annealing are at least partly due to the different initial microstructures in the samples. The microstructure depends on the location where the test cylinders are cut from the AlGe32 ingot. Ingots are produced by levitation melting and casting in a cold crucible and are known to exhibit a gradient of particle sizes whereby the smallest particles form on the lower side of the ingot which comes first in contact with the crucible walls during quenching and larger particles are found on the upper surface of the ingot. The initial microstructure of the as-cast samples is probably the reason for these discrepancies. Consequently statistical image analysis does not allow to distinguish between *ab initio* effects and those related to the cyclic and continuous annealing procedures. This problem further highlights the importance of developing *in situ* experiments where 2D and/or 3D images are recorded at high speed (compared to the morphological changes), and the sample is continuously maintained in the semi-solid state [Lim07] in order to exclude colling and reheating effects.

3.1.3 Rheology of AZ91 (Mg-Al9-Zn1) alloy

Introduction: The engineering alloy AZ91 (composition 90 wt.% magnesium, 9 wt.% aluminum and 1 wt.% Zn) is very similar to the binary magnesium-aluminum system, with its equilibrium thermal properties approximately described by the binary phase-diagram shown in Fig. 3.16. AZ91 is very common in the automotive industry as well as in the consumer

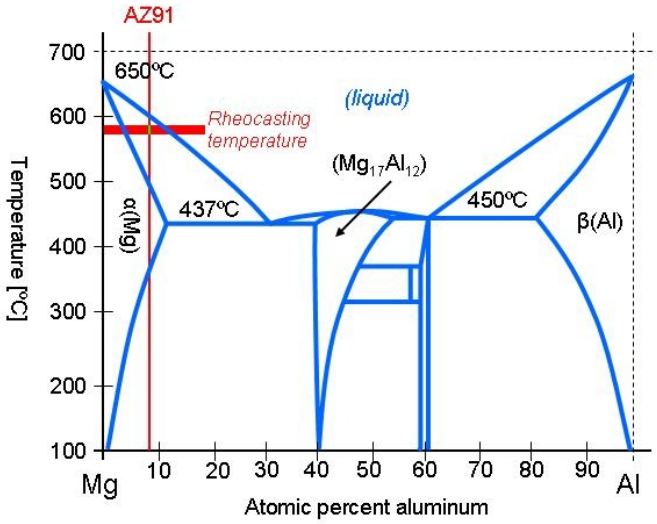

Figure 3.16: Equilibrium phase diagram of the binary magnesium-aluminum system. The vertical red line indicates the composition of AZ91 alloy (neglecting the 1at.% of zinc) and the red horizontal bar shows the typical temperature range semi-solid casting.

electronics market. Due to the low density of magnesium, cast AZ91 components are both

very light and strong. Rheocasting and/or thixomolding are two new processing routes for casting AZ91 in the semi-solid state, i.e. at a much lower temperature compared to conventional squeeze casting. Porosity is the main problem when thick walled AZ91 components are squeeze cast. Such defects deteriorate the mechanical properties and are mainly caused by turbulent die filling and solidification shrinkage. Semi-solid casting of AZ91 reduces porosity and yields components of very good ductility, due to the globular Mg particles who characterize the alloy microstructure. Note that both squeeze cast and semi-solid cast AZ91 contain brittle Mg_17Al_12 β-phase which is created during rapid quenching. Particularly in semi-solid cast AZ91 this β-phase forms a continuous network between the α-magnesium particles, resulting in a rather poor strength and fracture toughness. During heat treatment the β-phase can be completely dissolved in order to improve ductility [Kle02]. The semi-solid casting temperature determines the solid volume fraction of the Mg-globules and ranges from $490\,°C$ ($g_S = 1.0$) to $610\,°C$ ($g_S = 0$). For casting thin-walled ($1-2\,\mathrm{mm}$) components, a solid volume fraction of ca. 0.25 is preferred, thus fixing the casting temperature to $580-590\,°C$. Prior to the casting, a mixture of liquid melt and solid Mg particles ($0.1-0.5\,\mathrm{mm}$ in size) is created by continuously shearing the semi-solid slurry at constant temperature. Under the shearing forces, small Mg-dentrites which are the first crystallization product are deformed and broken into small fragments which coarsen and agglomerate (like snowballs) forming the large globular particles. This microstructural transformation is depicted in Fig. 3.17. Models

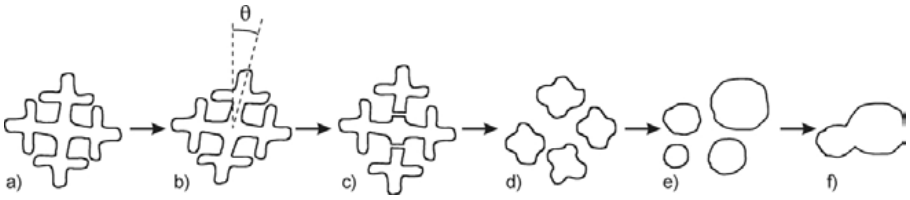

Figure 3.17: Morphological transformation of semi-solid AZ91. Shearing forces cause deformation and fracture of the magnesium dendrite arms (a-c). Via coarsening the fragments obtain a round shape and larger particles form by coalescence (d-f).

predict this microstructural transformation to yield a *thixotropic* behaviour of the semi-solid slurry which is favourable for a complete and homogeneous filling of the casting mold. A lot of experimental work on Sn-Pb alloy has shown that when increasing shear forces are applied the viscosity of the semi-solid melt decreases by several orders of magnitude. This behaviour is similar to a suspension of adhesive polymer particles in a liquid suspension, hence the term *thixotropy*. Quantitative evaluation of the structural changes in the sheared AZ91 alloy are conventionally limited to microscopic images of plane sections of quenched microstructures. Such a 2D metallographic section of sheared AZ91 is shown in Fig. 3.18 Note that a lot of information is not visible in such plane sections, e.g. particle size, shape, connectivity, etc. In order to quantify the distribution of Mg particles in the alloy, a series of 3D images of AZ91 samples was recorded at BESSY/BAM*line* in the framework of this thesis. Samples were pro-

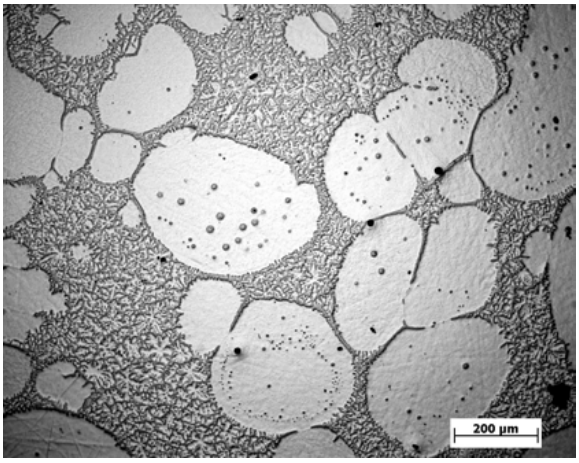

Figure 3.18: metallographic section of AZ91 microstructure. Large Mg particles form when the alloy is sheared in the semi-solid state ($T = 590\,°\mathrm{C}$). The matrix surrounding these particles shows a very fine structure resulting from rapid quenching.

vided by R. Jenning and Dr. A. Lohmueller, Neue Materialien Fürth GmbH (NMF), affiliated to the materials department of the University of Erlangen (Prof. R. F. Singer). NMF operates a $22\,\mathrm{t}$ thixomolding machine from Japanese Steel Works (JSW) dedicated to the productions of light weight parts in future car generations, e.g. at BMW AG. For the optimization of the machine parameters, accompanied by FEM simulations of the die filling during thixomolding, additional shearing experiments are carried out with a self-assembled rheometer at NMF. The rheometer consists of a cylindrical cup (inner radius R_1) which houses a slighly smaller motor-driven bob (outer radius R_2. The rheometer is designed to provide absolutely stable conditions concerning temperature and laminar flow of the semi-solid slurry, therefore the gap between cup and rotating bob has to be bigger than the largest magnesium particles but not too thick in order to prevent turbulant flow: $R_2 \approx 20\,\mathrm{mm}$ and $R_1 - R_2 \approx 3\,\mathrm{mm}$. For newtonian fluids, the effective shear rate is given by $\dot{\gamma} = 2\Omega\epsilon^2/(\epsilon^2 - 1)$ with $\epsilon = R_1/R_2$ and Ω the angular velocity of the bob [Sch81]. The customary unit for the shear rate is reciprocal seconds (s^{-1}). In this small space the rheometer is supposedly able to imitate the evolution of AZ91 alloy in the large JSW machine. The process parameters of the latter are difficult to alter, whereas changing temperature, shearing time and/or rate in the rheometer is rather simple.

Materials and method: The samples that are discussed in the following were produced by filling granular pre-alloyed AZ91 into the rheometer and replacing the atmosphere by argon before heating the material to $590\,°\mathrm{C}$. After the shearing time t the apparatus is opened, the rotating bob is removed and the slurry is quenched in cold water. From the solidified remains, small columns are cut respecting the limited field-of-view of the X-ray macroscope (ca. $3.2{\times}3.2\,\mathrm{mm}^2$). In contrast to the previously discussed Al-Cu and Al-Ge alloys the chemical phases present in samples of AZ91 do not produce a sufficient absorption contrast for conven-

	Production parameters			Imaging parameters		
no	t [s]	$\dot{\gamma}$ [s^{-1}]	T [°C]	E [keV]	d [mm]	V [mm^3]
1	1200	240	587	23	350	1.7
2	1200	0	587	23	350	2.0
3	10	80	590	25	370	3.0
4	200	80	590	25	370	4.1
5	250	80	590	25	370	4.2
6	350	80	590	25	370	4.1
7	400	80	590	25	370	4.1
8	3600	20	590	25	370	4.5
9	3600	720	590	25	370	4.5

Table 3.4: Production parameters (shear rate $\dot{\gamma}$, time t and temperature T) of the AZ91 samples and imaging parameters BESSY/BAM*line* measurements.

tional μCT. Therefore Fresnel-propagation is indispensable for imaging AZ91 microstructure. Table 3.4 shows a list of the nine samples that were measured and analyzed during this work along with the shearing time t, shear rate $\dot{\gamma}$, temperature T, X-ray energy E, sample-detector distance d and the effective sample volume V which was used for numerical particle analysis. The samples 1 and 2 were chosen to represent the common structures of AZ91 alloy with and without shearing. Tomograms were recorded with the X-ray macroscope at BESSY/BAM*line* using a $55\,\mu m$ thick CWO scintillator (effective pixel size $\Delta x = 1.6\,\mu m$ and $R \sim 3-4\,\mu m$). The photon energy was set to $E = 23\,keV$ and 1200 projections were recorded for each dataset at $d = 350\,mm$ sample-detector distance. Fig. 3.19 shows two axial slices reconstructed from

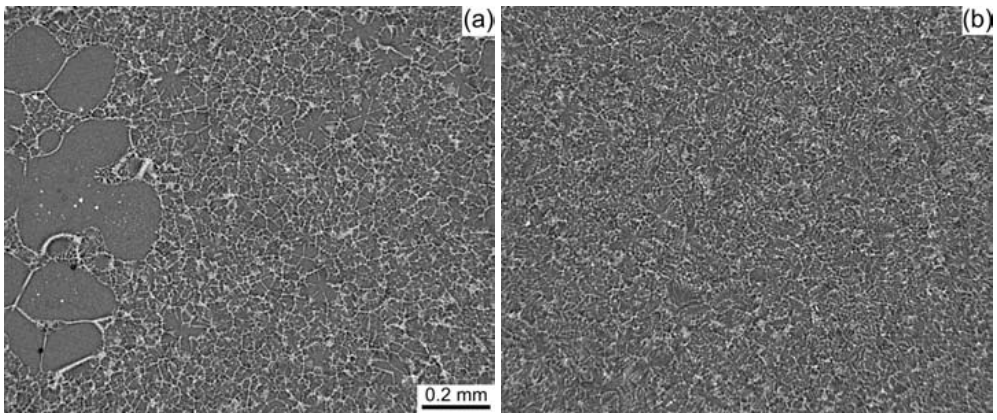

Figure 3.19: (a) Axial slice of AZ91 sample no. 1 ($20\,min$ shearing at $240\,s^{-1}$) recorded at $350\,mm$ propagation distance. (b) Slice of AZ91 sample no. 2 (no shearing).

Fresnel-propagated images of (a) AZ91 sheared for $t = 20\,min$ at a rate of $\dot{\gamma} = 240\,s^{-1}$ and

at $T = 587\,°\mathrm{C}$, and (b) common AZ91 alloy annealed for $t = 20\,\mathrm{min}$ without shearing. The difference in the two microstructures is obvious: Formation of large Mg particles is observed for the sheared sample (Fig. 3.19a) whereas the same alloy but without shearing is characterized by a homogeneous fine structured matrix. Statistical image analysis was applied to the Mg particles in sample no. 1, following a routine that is depicted in Fig. 3.20.

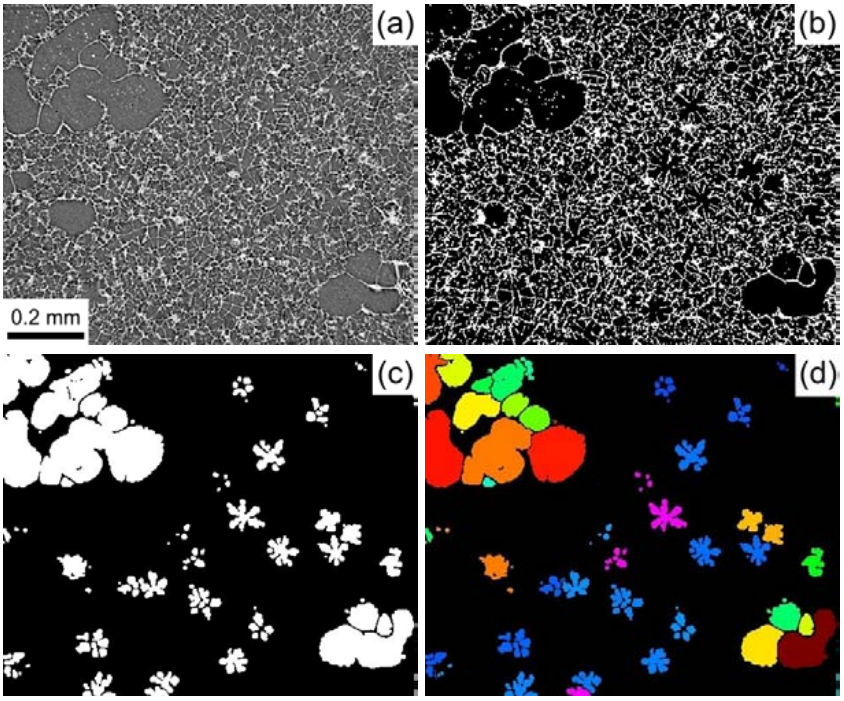

Figure 3.20: (a) Axial slice of sample 1 ($20\,\mathrm{min}$ shearing at $\gamma = 240\,\mathrm{s}^{-1}$) recorded at $d = 350\,\mathrm{mm}$ sample-detector distance. (b) Binarization of (a) yields an image of the particle edges. (c) Structural opening based on the Euclidian distance transform (EDT) of (b) followed by size filtering the small background objects reveals only the larger Mg particles. (d) Preflooded watershedding is used for particle segmentation and labeling. The labeled particles are colored with a rainbow color table. Due to the properties of the watershed algorithm, the biggest particles are segmented first and are colored red whereas the smallest particles appear in blue.

Since the Mg particles are large compared to the smallest details in the images, the amount of data can be reduced by a factor 8 by application of $2 \times 2 \times 2$ binning. This reduction is very helpful as the following 3D algorithm for particle analysis is limited to a 8-bit volume of [512 pixel]^3 size. As can be seen from Fig. 3.20b a simple threshold binarization does not allow to separate Mg particles from the fine structured matrix. The latter has to be erased by a morphological *dilation* whereby the 3D Euclidian distance transform (EDT) of the background (black) of Fig. 3.20b is calculated and binarized (the binarization was set to yield a dilation radius of 3 pixels). Most of the smaller particles in the matrix are thus *closed* and a new EDT is calculated on the foreground of the dilated image. Binarization of this new EDT yields an

erosion (again of 3 pixels radius) and the overall effect on the image corresponds to a *closure* (or *opening* with respect to the inverse image). Additional application of a size filter removes the remaining objects of volume $V \leq 10.000$ voxels (i.e. $\leq 3.3 \times 10^{-4}\,\mathrm{mm}^3$). The resulting slice is shown in Fig. 3.20c and statistical image analysis is performed in the conventional manner (see section 2.2) to segment and label the particles (Fig. 3.20d). A perspective 3D

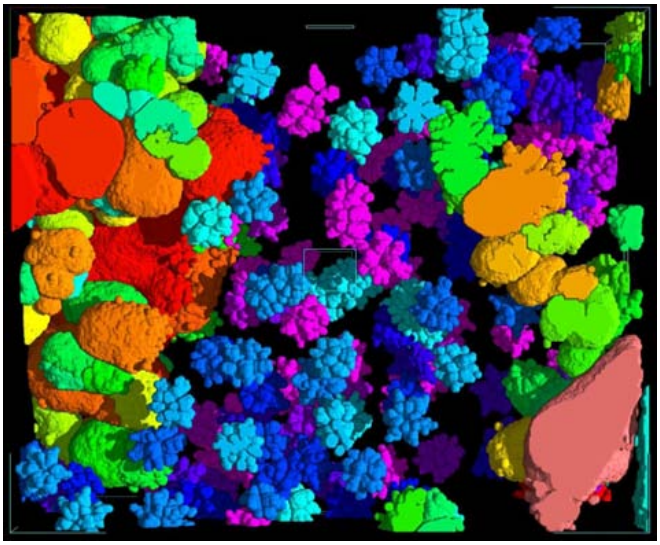

Figure 3.21: Perspective 3D view onto the segmented and labeled sample no. 1. Big globular particles are seen in the upper left and lower right corners whereas small dendrites (star shaped particles) occupy the space between these larger particles. Due to the properties of the watershed algorithm, the colors represent the particle size (large:red, small:blue).

view onto these particles is depicted in Fig. 3.21.

Results: The size and shape distributions of the magnesium particles appear strongly inhomogeneous featuring clusters of large round and/or oval particles on the sides and smaller star-shaped dendrites in between. Applying the same segmentation and labeling to sample no. 2 (no shearing), no particles bigger than $V = 3.3 \times 10^{-4}\,\mathrm{mm}^3$ are found. Tomograms of sample no. $3-7$ were recorded with the same detector setup, at $E = 25\,\mathrm{keV}$ energy and $d = 370\,\mathrm{mm}$ sample-detector distance. These five samples represent a constant shear rate $\dot{\gamma} = 80\,\mathrm{s}^{-1}$ that was applied to shear semi-solid AZ91 at a constant temperature $T = 583\,^{\circ}\mathrm{C}$ for different shearing times: $t = 10$, 200, 250, 350 and $400\,\mathrm{s}$. The motivation for choosing these particular time intervals were microscopy images of metallographic sections which indicated changes in the particles size and shape between $200\,\mathrm{s}$ and $400\,\mathrm{s}$ shearing time. Sample no. 3 was ment to be a reference for the higher shear rates. Fig. 3.22 shows the calculated size distributions obtained from 3D particle analysis of sample no. $3-7$. The changes in the particle size are visualized by showing the particle volume partition (the corresponding volume that is filled with particles of a certain size, in other words *frequency times volume*) at one

shearing time (light green) along with the volume partition observed at the next longer time (dark blue). From 10 s to 200 s shearing time (Fig. 3.22a) the volume partition increased con-

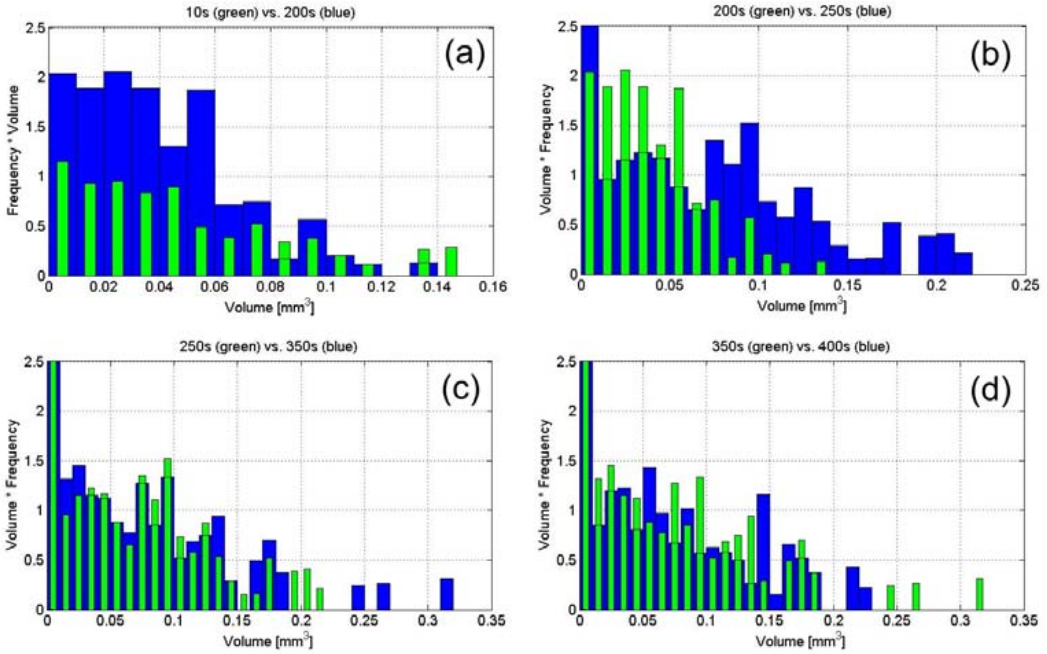

Figure 3.22: Comparison of histograms showing the particle volume partition in sample no. $3-7$: (a) 10 s (light green) vs. 200 s (dark blue) shearing time. (b) 200 s (green) vs. 250 s (blue). (c) 250 s (green) vs. 350 s (blue). (d) 350 s (green) vs. 400 s (blue).

stantly for particle of all sizes, in other words more particles are found after 200 s. At 250 s (Fig. 3.22b) larger particles ($V > 0.15\,\mathrm{mm}^3$) appear while the volume occupied by the small particles has shrinked compared to the 200 s sample, probably due to coalescence. Hardly any changes appear in the volume partition at 350 s shearing time (Fig. 3.22c) and/or at 400 s (Fig. 3.22d), except for some very large particles ($V \leq 0.25\,\mathrm{mm}^3$). Note that although the volume frequency of the smallest particles ($V < 0.01\,\mathrm{mm}^3$) is cut off in Fig. 3.22 their number is particularly high for the sample no. 6 which corresponds to 350 s shearing time.
Fig. 3.23 compares an axial slice of the binary image of sample no. 6 (350 s) to sample no. 7 (400 s). The same dendrites that occupied a large region in sample no. 1 are found clustered around the large Mg particles in Fig. 3.23a, whereas no dendrites are seen in sample no. 7 (Fig. 3.23b). Note that this phenomenon is also absent in sample no. 3, 4 and 5 and must therefore be attributed to anomalies that have occurred during sample preparation (e.g. a few seconds pause between unclosing the rheometer and quenching the alloy would be sufficiently long for the nucleation and growth of such small dendrites). The corresponding histograms of the particles shape factor $F = 6V\sqrt{\pi/A^3}$ are shown in Fig. 3.24 (note that $F = 1$ for a sphere and $F < 1$ for any other object). No change in the particles shape distribution but a net increase in the number of particles is observed from 10 s to 200 s (Fig. 3.24a). After 250 s

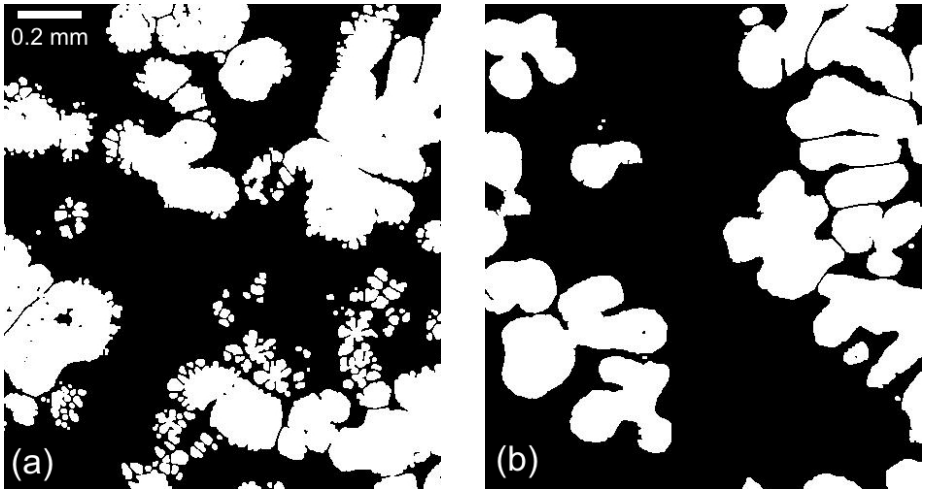

Figure 3.23: (a) A binary slice of the 350 s sample after applying structural opening on the Mg particles. (b) Similar slice of the 400 s sample: no star-shaped dendrites are visible.

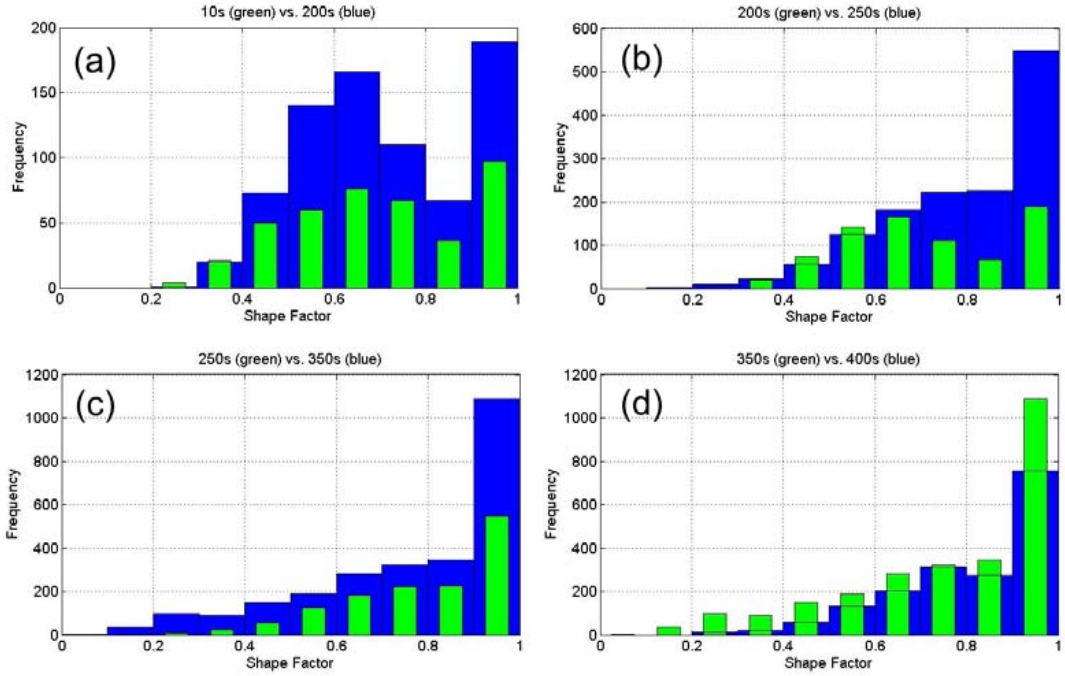

Figure 3.24: Histograms of the particles shape factors: (a) 10 s (light green) vs. 200 s (dark blue) shearing time. (b) 200 s (light green) vs. 250 s (dark blue). (c) 250 s (light green) vs. 350 s (dark blue). (d) 350 s (light green) vs. 400 s (dark blue).

shearing time the corresponding sample features more round particles as seen in the shape distribution for $F > 0.6$. No changes in the distribution but an overall increase in the number of particles is found when the 250 s is compared to the 350 s sample. A little peak appears for

the latter at $F \approx 0.3$ which corresponds to little dendrites that have an extremely aspherical shape. The shape distribution after $400\,\mathrm{s}$ appears very similar to the distribution after $250\,\mathrm{s}$ shearing time.

In the limit of very long shearing times (one hour) two samples were analyzed, one corresponding to a low shear rate of $\dot{\gamma} = 20\,\mathrm{s}^{-1}$, the other to a high shear rate of $\dot{\gamma} = 720\,\mathrm{s}^{-1}$ (mechanical limit of the experimental rheometer). Shape distribution and volume partition for these two samples (no. 8 and 9 in table 3.4) are shown in Fig. 3.25. Obviously the slowly

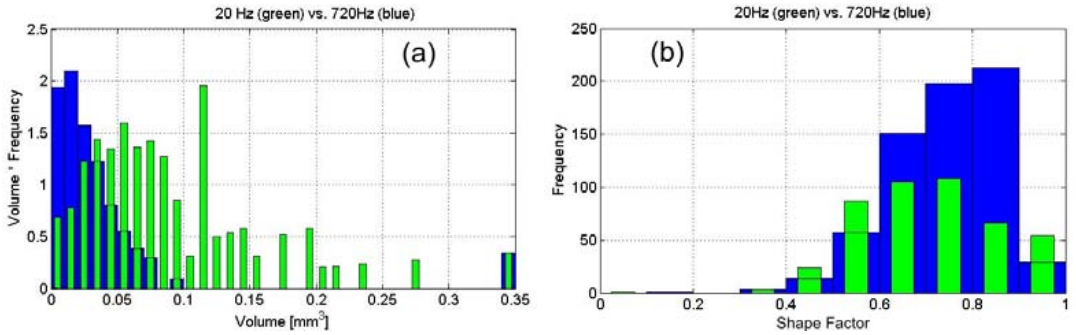

Figure 3.25: Low shear rate ($\dot{\gamma} = 20\,\mathrm{s}^{-1}$ in light green) vs. fast shear rate ($\gamma = 720\,\mathrm{s}^{-1}$ in dark blue): (a) Particle volume partitions (volume times frequency), (b) Histograms of the shape factor F.

sheared sample is characterized by larger oval particles ($V_{max} \sim 0.05\,\mathrm{mm}^3$ and $F_{max} \sim 0.7$) while a high shear rate produces smaller quasi-spherical particles ($V_{max} \sim 0.02\,\mathrm{mm}^3$ and $F_{max} \sim 0.85$). Note that two classes of particles that were found for shorter shearing times appear to have vanished in the limit of long shearing: (a) The smallest particles in sample no. $1-7$ which have a volume $V < 0.01\,\mathrm{mm}^3$ and almost spherical shape ($F > 0.9$), and (b) the aspherical star-shaped dendrites that were found in sample no. 1 and 6. After one hour of shearing and independently of the shear rate both types of particles appear to have merged with the large Mg particles.

Yet, there is another indicator for clustering of small dendrites and/or dendrite fragments. In microscopic images of metallographic sections and in the tomography data *entrapped liquid phase* is found within the large globular particles. A common explanation is that liquid metal in the inter-dendritic spaces is trapped whenever small dendrites merge with larger particles due to shearing. However, the entrapped liquid often appears as a *belt* at a discrete distance underneath the surface of the large globules (see for example the metallographic section in Fig. 3.18). This phenomenon can be inerpreted by assuming that the dendrites that merge with the particles are more or less of the same size.

The dendrites in Fig. 3.21 seem to fullfill this assumption and correlation plots are used to find out if these are indeed of similar shape and size. Fig. 3.26 shows shape factor vs. particle volume for the samples representing (a) $200\,\mathrm{s}$, (b) $250\,\mathrm{s}$, (c) $350\,\mathrm{s}$ and (d) $400\,\mathrm{s}$ of shearing time. The particle volume is drawn on logarithmic scale to account for the fact that most par-

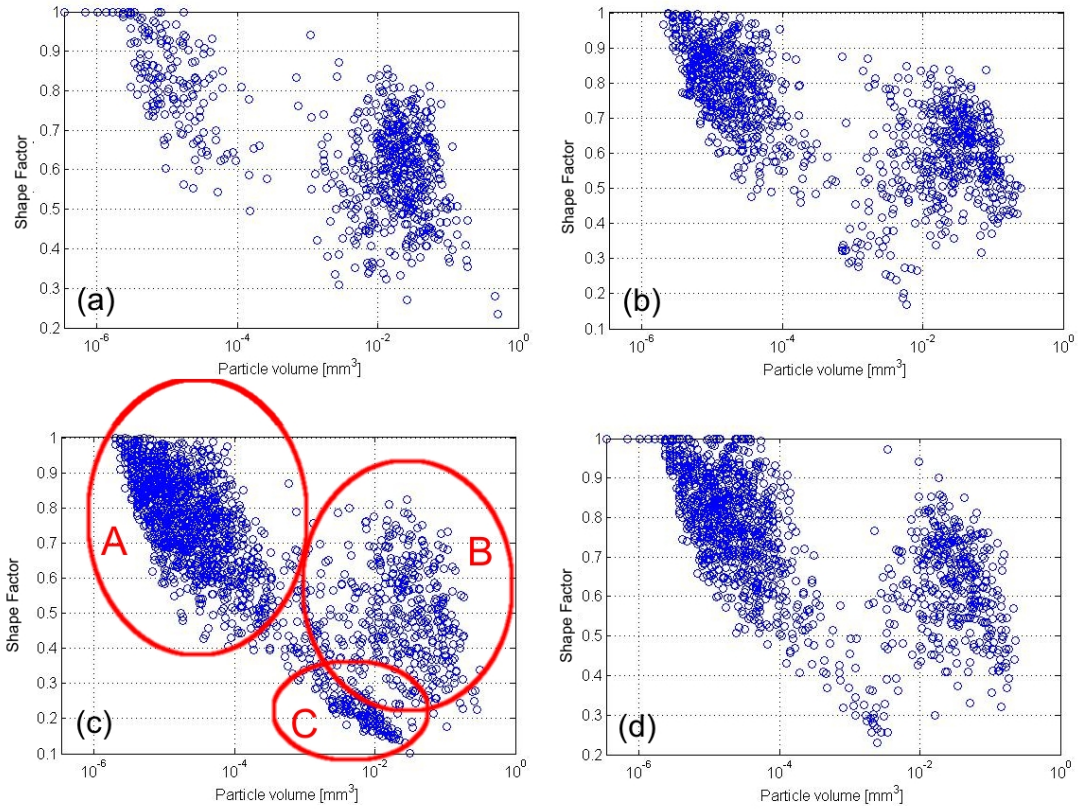

Figure 3.26: Correlation plots of particle shape factor (sphericity) vs. particle volume (on log scale) for (a) 200 s, (b) 250 s, (c) 350 s and (d) 400 s shearing time at constant shear rate $\dot{\gamma} = 80\,\mathrm{s}^{-1}$.

ticles are very small. Fig. 3.26c shows three distinct classes of particles (labeled A, B and C) in the 350 s sample: small round particles (A), large slightly oval particles (B) and aspherical particles of an intermediate size (C). The latter correspond to the star-shaped dendrites and a small trace of this particle class is found in the sample no. 7 (400 s, Fig. 3.26d) whereas samples no. 4 and 5 only contain particles of class A and B. Fig. 3.27 shows similar correlation plots for the samples no. 1 and 3, i.e. 20 min and 10 s shearing time at $240\,\mathrm{s}^{-1}$ and $80\,\mathrm{s}^{-1}$ rate respectively. In sample no. 1 the star-shaped dendrites (class C) from Fig. 3.21 localize at the same position in the correlation plot (Fig. 3.27a) as observed for sample no. 6 (Fig. 3.26c while they are completely absent in sample no. 3.

Fig. 3.28 shows particle shape-volume correlation plots for samples no. 8 (1 h shearing at $\dot{\gamma} = 20\,\mathrm{s}^{-1}$) and no. 9 (1 h at $\dot{\gamma} = 720\,\mathrm{s}^{-1}$). In addition to the fact that smaller and rounder particles are observed for longer shearing times (see also Fig. 3.25) it is worth noting that no particles of class C and only few of class A are observed in sample no. 8, whereas sample no. 9 is etirely composed of the globular, class B particles.

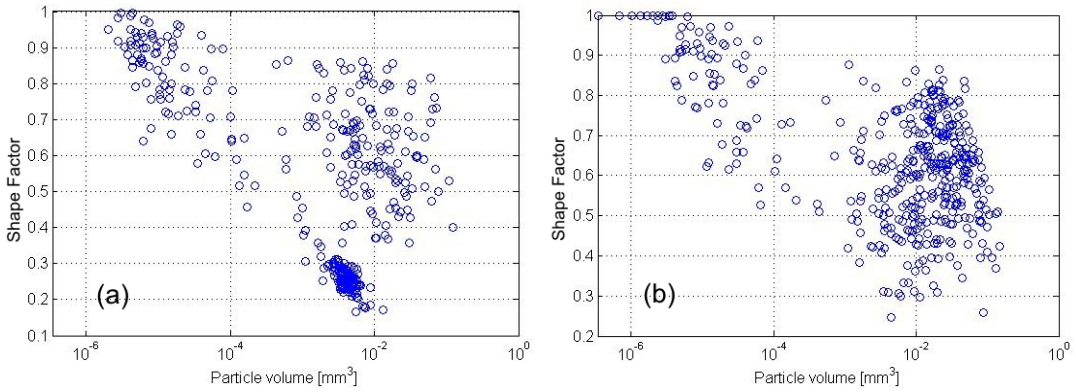

Figure 3.27: Correlation plots of (a) sample no.1 ($20\,\mathrm{min}$ at $240\,\mathrm{s}^{-1}$) and (b) sample no.3 ($10\,\mathrm{s}$ at $80\,\mathrm{s}^{-1}$) showing shape factor vs. particle volume.

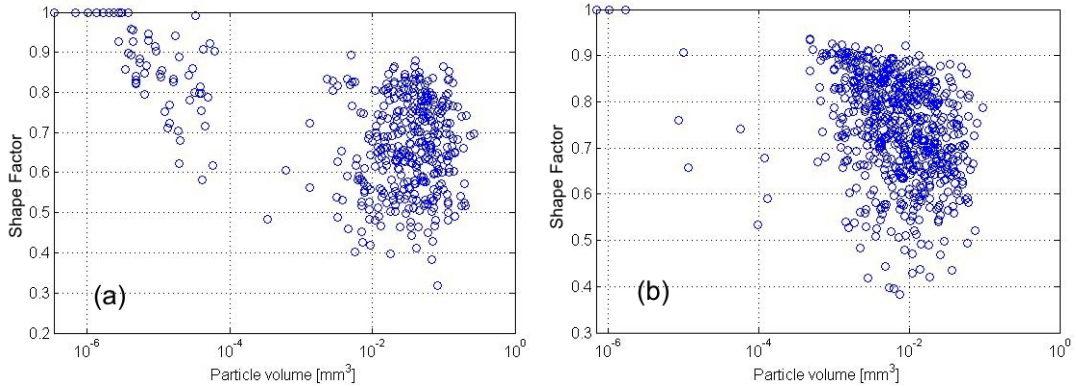

Figure 3.28: Correlation plots of (a) sample no.8 ($1\,\mathrm{h}$ at $20\,\mathrm{s}^{-1}$) and (b) sample no.9 ($1\,\mathrm{h}$ at $720\,\mathrm{s}^{-1}$) showing shape factor vs. particle volume.

Discussion: Both the star-shaped dendrites and the small spherical particles seem to vanish in the limit of long shearing times. For short times both small round particles and larger oval particles were found in all the samples. The star-shaped dendrites that were all characterized by very similar shape and size are probably the unwanted result of a short delay after opening the rheometer and before quenching the samples. While in sample no. 1 these dendrites *float* in the space between the large globules which was occupied by the liquid before quenching the sample, they are found clustered around the globules in sample no. 6. The very inhomogeneous distribution of the magnesium prticles in sample no. 1 is probably the result of inhomogeneous flow and temperature in the rheometer chamber. This work has shown that statistical variations in shape and size of the orimary magnesium phase can be measured and quantified as a function of shear rate, temperature and/or shear time. Such valuable information is not accessible in metallographic 2D sections, only in Fresnel-propagated X-ray μCT. Towards tayloring the AZ91 microstructure, further measurements and better sample prepara-

tion techniques are needed. Viscosity measurements of semi-solid aluminum-base alloys were carried out with a commercial rheometer (Anton Paar GmbH, Stuttgart, Germany), revealing serious difficulties in measuring $\eta(t, T, \dot{\gamma})$ of semi-solid melt over many orders of magnitude [Rue06]. The relatively small community of rheocasting companies and research institutes working on the rheological properties of semi-solid slurry has favored self-assembled rheometers rather than commercial devices. At the time this text is written NMF is completing the developpement of a second generation rheometer surpassing the precision of the first generation device which produced the samples for this work.

3.1.4 Holotomography on AZ91 alloy

Acquiring full tomographic datasets (900 projection angles each) at four increasing sample-detector distances (20 mm, 144 mm, 370 mm and 720 mm) a holotomographic 3D image of the real decrement $\delta(x, y, z)$ of the material refractive index $n(x, y, z)$ was reconstructed for sample no. 7 (cf. table 3.4). The BESSY/BAM*line* macroscope was used for recording the images at $E = 23\,\mathrm{keV}$ X-ray energy with $\Delta x = 1.6\,\mu\mathrm{m}$ effective pixel size. The image resolution was limited by the blurring of the $22\,\mu\mathrm{m}$ thin CWO scintillator to approx. $R \sim 3-4\,\mu\mathrm{m}$. Fig. 3.29 shows a reconstructed axial slice of this sample obtained from (a) the absorption data ($d = 20\,\mathrm{mm}$), (b) the Fresnel-propagated data ($d = 370\,\mathrm{mm}$) and (c) the retrieved phase-maps (holotomography). As can be seen from the corresponding line profiles (Fig. 3.29) the chemical contrast in the absorption data (d) between Mg-particles and the matrix is lost in the image noise. Fresnel-propgation yields an improved signal to noise ratio (Fig. 3.29e) but complicates the image analysis due to the dark-bright contrast appears at the particle-matrix interfaces due to edge-enhancement (a method for extracting the large globular Mg-particles from edge-enhanced 3D images was described in the previous subsection). Finally, a convenient two-phase picture of large globular Mg particles, small Mg dendrites and matrix is obtained with holotomography (Fig. 3.29f). Therefore, tomographic *phase-only* datasets were calculated by dividing the three Fresnel-propagated radiographs at each projection angle by the corresponding absorption image (recorded at $d = 20\,\mathrm{mm}$, cf. Fig. 3.29a) thus eliminating the part of the signal which is related to absorption. Following the CTF method depicted in Fig. B.24 approximate maps of $\phi(x, y, \theta)$ are obtained, leading to the 3D representation of $\delta(x, y, z)$ as shown in Fig. 3.29c (holotomography).
This result is the first holotomographic record at BESSY/BAMline and a significant improvement in terms of resolution and detail visibility is expected for the new microscope (commissioning was completed end of 2006). During beamtime at the ESRF/ID19 (experiment MA-104, April/May 2006) holotomograms of AZ91 samples were acquired with a high-resolution setup similar to the X-ray microscope at BESSY/BAM*line* . 1500 projection images with an effective pixel size of $\Delta x = 0.7\,\mu\mathrm{m}$ were recorded from a $12\,\mu\mathrm{m}$ thin LAG:Eu scintillator at $E = 19\,\mathrm{keV}$ X-ray energy yielding an image resolution of ca. $1\ \mu m$. Phase-maps were retrieved from four Fresnel-propagated images recorded at $d = 8\,\mathrm{mm}$, $34\,\mathrm{mm}$, $70\,\mathrm{mm}$

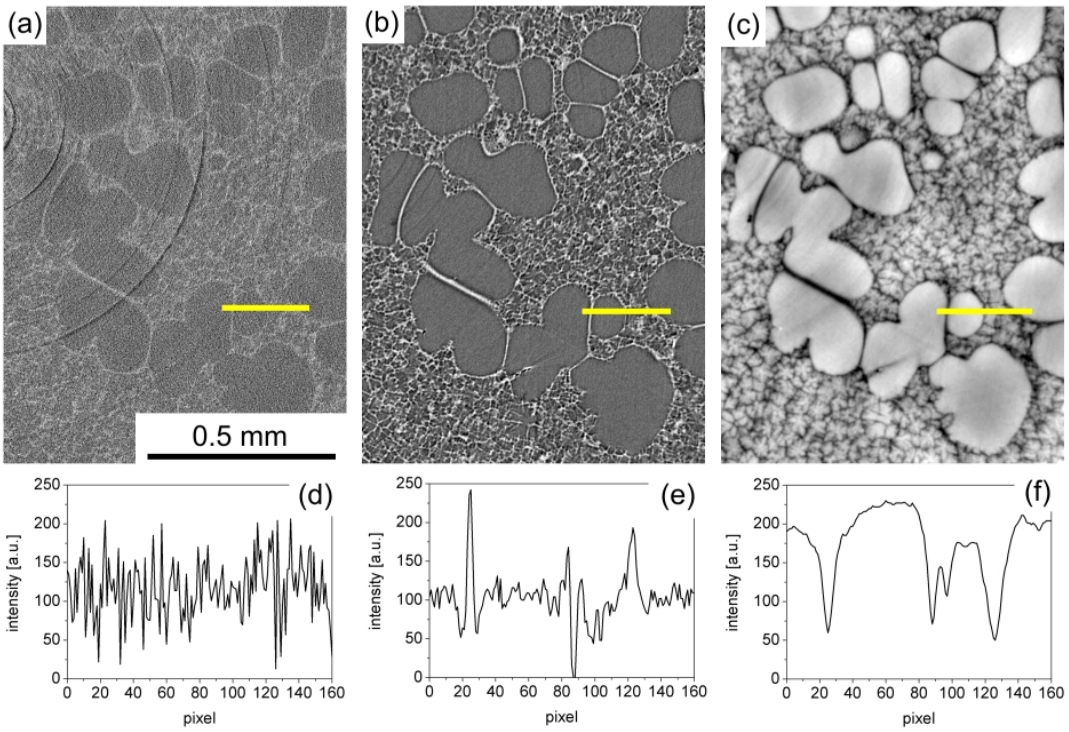

Figure 3.29: Axial slice of AZ91 alloy (sample no. 7). (a) Absorption tomogram ($d = 20\,\mathrm{mm}$), (b) Fresnel-propagated tomogram ($d = 370\,\mathrm{mm}$), (c) Holotomography using one absorption and three Fresnel-propagated datasets ($d = 144\,\mathrm{mm}$, $370\,\mathrm{mm}$ and $720\,\mathrm{mm}$). (d-f) Intensity profiles along the horizontal yellow lines in the (d) absorption, (e) Fresnel-propagated and (f) Holotomography image.

and $100\,\mathrm{mm}$ and using an iterative phase-retrieval method which combines TIE and CTF approaches (see section B.3.3). An axial slice of AZ91 alloy reconstructed from the approximate maps $\phi(x, y, \theta)$ is shown in Fig. 3.30. The picture reveals sub-micrometer details of the Mg dendrites (secondary crystallization product), whereby inidividual dendrite arms can be identified as well as density fluctuations (bright spots) and entrapped liquid (dark spots) that are found inside the large Mg globules (not observed in Fig. 3.29). Note that due to the high photon flux at the ESRF/ID19 (approx. $10 - 20$ times more than at BESSY/BAM*line*) full acquisition of such a holotomogram takes ~ 1 hour of time, whereas a similar record would at least require 10 hours of beamtime at BESSY.

3.1.5 Holotomography on aluminum-silicon alloys

During beamtime at the ESRF/ID19 further holotomograms were recorded from samples of aluminum-silicon engineering alloys, namely A356, 357 and A390 (compositions are listed in teble 3.5. Test samples were provided by the Salzburger Aluminium AG, Austria. The sample of A390 was labeled "AlSi17" but the high concentration of copper indicated that this *hyper-eutectic* alloy was most likely A390. The term hyper-eutectic refers to alloys of higher

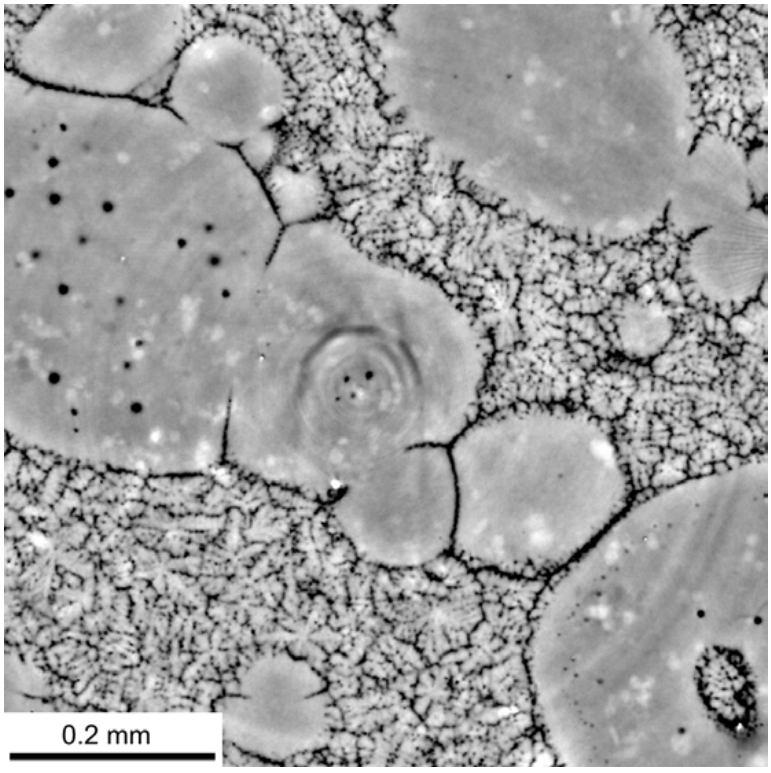

Figure 3.30: Holotomography of AZ91 alloy obtained from high resolution images ($\Delta = 0.7\,\mu\mathrm{m}$ pixel size at $R \sim 1.5\,\mu\mathrm{m}$ resolution) recorded at the ESRF/ID19 at $E = 19\,\mathrm{keV}$ photon energy. Four datasets ($d = 8\,\mathrm{mm}$, $34\,\mathrm{mm}$, $70\,\mathrm{mm}$ and $100\,\mathrm{mm}$) were used for the iterative phase retrieval procedure [Yam04].

alloy	Al	Si	Fe	Cu	Mn	Mg	Zn	Ti	others
A356	91.7	7.0	0.2	0.2	0.1	0.35	0.1	0.2	0.15
357	91.85	7.0	0.15	0.05	0.03	0.52	0.05	0.2	0.15
A390	77.3	17.0	0.1	4.5	0.1	0.55	0.1	0.2	0.15

Table 3.5: Compositions of the Al-Si alloys in terms of wt.% of the most abundant elements.

Si-concentration than the Al-Si eutectic composition, i.e. ≥ 12.5 wt.% Si, in contrast to *hypo-eutectic* alloys with a Si-concentration < 12.5 wt.%.

Small cylinders of $1.2\,\mathrm{mm}$ diameter were prepared and complete tomograms (1500 projections) were recorded at four sample-detector distances ($d = 8\,\mathrm{mm}$, $34\,\mathrm{mm}$, $70\,\mathrm{mm}$ and $100\,\mathrm{mm}$) for each alloy. A high-resolution detector system ($\Delta x = 0.7\,\mu\mathrm{m}$ at $R \approx 1\,\mu\mathrm{m}$) and X-rays of $E = 19\,\mathrm{keV}$ energy were used for acquiring the Fresnel-propagated radiographs. Fig. 3.31 shows images of A356 microstructure that were obtained by (a) absorption, (b) Fresnel-propagated ($d = 100\,\mathrm{mm}$ sample-detector distance) and (c) holotomographic imaging. The compositions of A356 and 357 are very similar to the binary system AlSi7 which has a solid

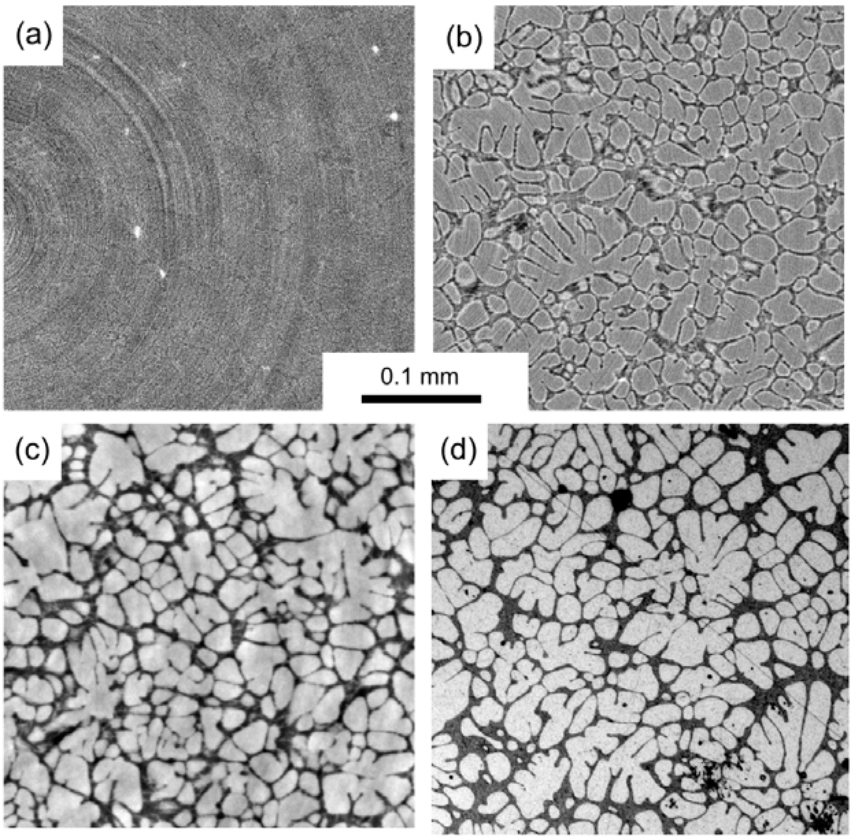

Figure 3.31: A356 microstructure seen in different imaging modes: (a) absorption tomography ($d = 8\,\mathrm{mm}$), (b) Fresnel-propagated imaging ($d = 100\,\mathrm{mm}$), (c) holotomography (combining images at $d = 8\,\mathrm{mm}$, $34\,\mathrm{mm}$, $70\,\mathrm{mm}$ and $100\,\mathrm{mm}$), (d) light microscopy.

volume fraction of primary Al particles of $g_S = 0.52$ at room temperature. A light microscopy image of a polished section of the same material is shown in Fig. 3.31 for comparison. Unlike the absorption image (Fig. 3.31a) which shows no structural information at all, the resemblance of holotomography (c) and light microscopy (d) is striking. Fresnel-propagated imaging (Fig. 3.31b) reveals the structure but the interference fringes that enhance the material interfaces cannot be used for direct threshold binarization and hence such data is inconvenient for 3D image analysis. The latter was used to segment and label the Al particles (watershed algorithm, for details see section 2.2) in order to quantify the equivalent sphere diameter a, the contiguity G and the connectivity n of the agglomerated Al particles in A356 and 357. The resulting distributions are shown for both alloys in Fig. 3.32. Although they appear similar in 2D sections the Al particles in the two alloys show significantly different characteristics. A volume fraction of $g_S = 0.66$ and 0.67 is found for the particles in A356 and 357 respectively, which is in fact much closer to the binary system AlSi5 than AlSi7 ($g_S = 0.52$). More particles are found in A356 with a mean particle diameter of $\langle a \rangle = 23.6 \pm 5.7\,\mu\mathrm{m}$ whereas 357 is characterized by bigger particles and $\langle a \rangle = 32.0 \pm 7.7\,\mu\mathrm{m}$. The mean contiguity (Fig. 3.32c)

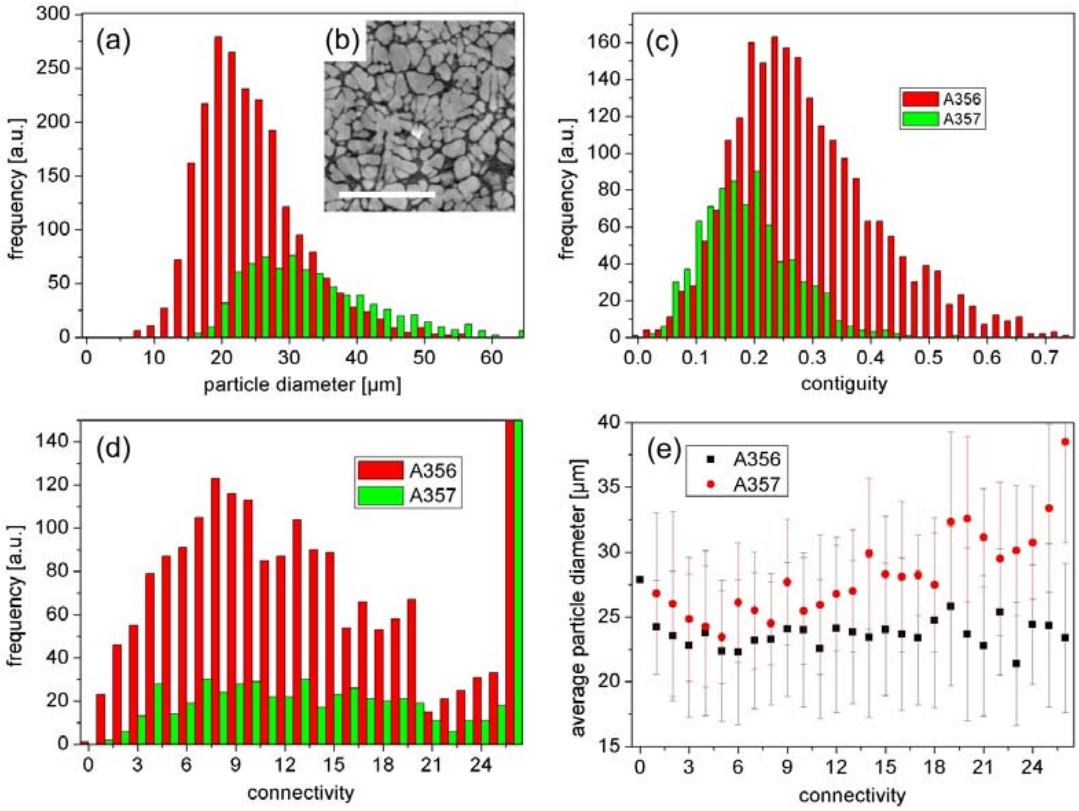

Figure 3.32: 3D analysis of Al particles in A356 (dark red) and 357 alloy (light green). (a) Histograms of the effective particle diameters, (the inset (b) shows a typical axial slice of the 357 alloy with a white bar of $0.2\,\mathrm{mm}$ length), (c) particle contiguity and (d) connectivity. (e) Correlation plot mean particle diameter vs. connectivity.

is rather high for the particles in A356 ($\langle G \rangle = 0.285$) and very low for 357: $\langle G \rangle = 0.174$ compared to the results obtained from Al-Ge and Al-Cu systems (see subsections 3.1.1 and 3.1.2). The connectivity is very high for both systems with the mean values $n_{mean} = 11.47$ and 12.77 for A356 and 357 respectively. A large number of particles could not be used for calculating these mean values because their connectivity was higher than 26 - the maximum value detected by the analysis method. The correlation plot (mean particle diameter vs. connectivity, see Fig. 3.32e) does not reveal the expected correlation where larger particles exhibit a higher number of contacts. The data further shows the particles to have a strongly aspherical *rosette-like* shape which makes the interpretation of the statistical results difficult. The samples were cut from slugs that are produced by electro-mechanical stirring and are sold as feedstock material for thixocasting applications where a globular microstructure is needed. Following this 3D analysis and comparing the results with AlGe32 and AlCu21 alloys that were produced and invesitgated in this work, the suitability of commercial A356 and 357 for thixocasting can be questioned.

Results from the analysis on hyper-eutectic A390 alloy are shown in Fig. 3.33. A total volume

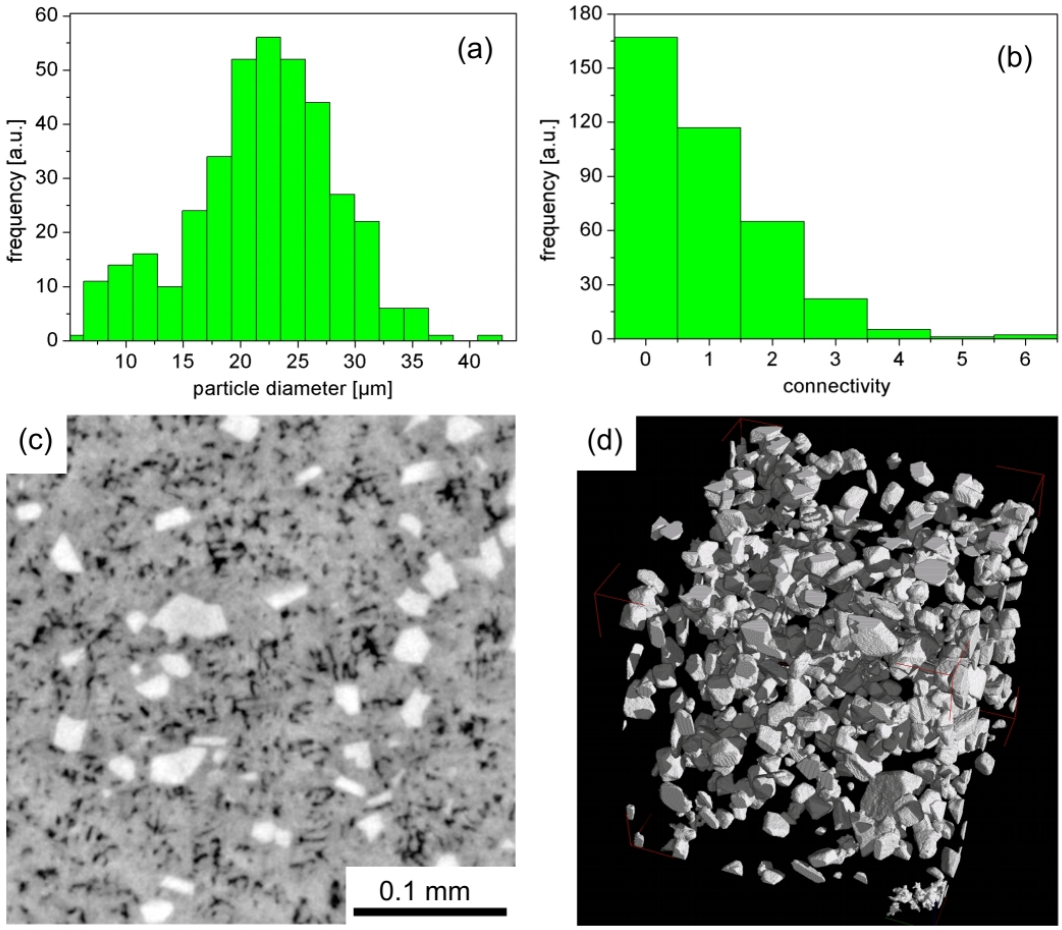

Figure 3.33: 3D image analysis on hyper-eutectic A390 alloy. (a) Distribution of the effective diameter of the angular Si-particles. (b) Connectivity of the Si-particles. (c) Typical axial slice of the holotomogram of A390 (Si particles appear bright whereas Cu precipitates are dark due to their high density). (d) 3D perspective view on the total 605 Si-particles in the subvolume that was used for analysis ($0.35\,\mathrm{mm}$ cube).

fraction of $g_S = 0.075$ was found for the 605 angular Si-particles (shown in a 3d perspective view in Fig. 3.33d) that were contained in the $0.35\,\mathrm{mm}$ cube that was used for the 3D image analysis. This value is slightly higher than the $g_S = 0.065$ that would be expected for a binary Al-Si mixture, probably due to the addition of copper. The latter forms an intermetalic phase only with aluminum (Al_2Cu) and $g_S = 0.052$ is found which is slightly less than what would be expected for 4.5 wt% pure copper [Pla98]. The effective diameter of the Si-particles features a normal distribution with a mean value $\langle a \rangle = 21.0 \pm 5.1\,\mu\mathrm{m}$ (see Fig. 3.33a). Due to the low volume fraction most particles have no or only one contact to their neighbors (Fig. 3.33b). In contrast to the less dense Si particles, the Cu precipitates appear dark in the holotomographic data due to their high density, as seen in Fig. 3.33c.

Short summary

The need for microtructural analysis of metallic alloys is as old as materials science itself: Towards tayloring engineering aluminum alloys and establishing new semi-solid processing routes, the microstructure has to be monitored non destructively, desirably in situ. Conventional 2D analysis of metallographic sections is unable to describe the 3D microstructural characteristics. With this work, three-dimensional non destructive imaging techniques were developed and applied to Al-Ge, Al-Cu, Al-Mg and Al-Si alloys to study non-agitated coarsening as well as microstructural transformation under shear stress. High-resolution absorption tomography revealed new insights about 3D particle coarsening in the semi-solid state and the influence of cyclic remelting and cooling on AlGe32 alloy. Fresnel-propagated imaging was used to characterize magnesium particles in AZ91 alloy after shearing in the rheometer. Finally holotomography served to characterize the distribution of aluminum particles in hypo-eutectic A356 and 357 alloy as well as silicon particles in hyper-eutectic A390 alloy. X-ray μCT of these microstructures was shown to yield three-dimensional images of a quality which is comparable to light microscopy. The scientific potential of such imaging methods, particularly for the techniques involving Fresnel-propagation and phase retrieval, is extremely wide and only limited by the time resolution of the experiment. By the end of this thesis, new devices are being built to study solidification, coarsening and shear deformation in situ, whereby the alloy is imaged in the semi-solid state.

3.2 Human tooth dentin

Teeth are known to have complex and graded structures [Tes01]. These cutting tools have undergone 500.000.000 years of evolutionary “testing”, and as a result appear to perform far better and longer than artificial replacements such as restorations, crowns or implants. Dentin is considered to be a highly organized variant of the bone family of materials [Wei98] forming the major bulk of all mammals teeth. This material is characterized by having tubules extending more than $1\,\mathrm{mm}$ in length, running more or less parallel to each other across the entire dentin thickness. The tubules are known to have profound impact on mechanical as well as other properties of dentin. Yet surprisingly, their 3D arrangement and contribution to the mechanical function is still poorly understood. The most common assumption was that the materials strength would increase along the tubules direction. This ’anisotropic stiffening effect’ was promoted by the discovery of sheaths of peritubular dentin (PTD), a very dense and highly mineralized material surounding most of the tubules in human teeth. The PTD forms cylinders spanning $2-5\,\mu\mathrm{m}$ and housing empty voids of $1-2\,\mu\mathrm{m}$ in diameter (in the living body these cores are filled with living soft tissue). They are embedded in a less mineralised intertubular dentin. However, experimentalists proved recently that no mechanical anisotropy was induced by the dentinal tubules [Kin99]. Some experimental results even suggest that ’softening’ occurs along the tubules in a thin layer right below the enamel cap where the PTD

is particularly thin [Zas06]. Furthermore, the simple model of tubules that are reinforced by highly mineralized cuffs and are suspended in a softer dentin matrix, cannot account for the unique and durable performance of natural teeth [Luc04]. To this end, little evidence has been presented so far, highlighting the relations between the structural details, contributing to the mechanical compressive functions of functioning teeth. Consequently, understanding the improved fracture resistance and durability of teeth requires mapping the subtle structural variations that appear in the microstructure.

3.2.1 Fresnel-propagated imaging of dentinal tubuli

In partnership with the Max-Planck Institute for Colloids and Interfaces (Dr. P. Zaslansky, Dept. of Biomaterials) along with test measurements at BESSY/BAMline, a detailed analysis of X-ray propagation through tooth dentin was carried out. To interpret the interference patterns produced by a partially coherent wave propagating through the quasi-ordered tubular structures of dentin, a simple analytical solution was derived, further interpreted by simulations and analysis of experimentally recorded tomograms. The results show how structural insights can be obtained by interpreting the outcomes of propagation for the purpose of performing 3D virtual microscopy in teeth.

The formalism of Fresnel-diffraction derived in section 1.3 (eq. 1.25 and 1.26) can be used to analytically interpret X-ray propagation through samples with tubular inclusions. Propagation is considered parallel to a cross-section, which is perpendicular to the tubule long axis. For simplicity this axis shall align with the y-axis of the imaging system. Furthermore, translational invariance along the entire y-axis is assumed, consequently it is sufficient to consider a (x, z) slice across the tubule, i.e. $y = 0$. An estimate of the magnitude of $\phi(x)$ for a single void surrounded by dentin reveals that the maximal effect of phase shift is $\phi_{max} = 2\pi/\lambda \cdot (\delta_{void} - \delta_{dentin}) \cdot 2r_{void} \approx 0.12\,\mathrm{rad}$. This estimate is based on the experimental results of this work ($\lambda = 0.5\,\text{Å}$, $r_{tubule} \sim 1\,\mu\mathrm{m}$ and $(\delta_{void} - \delta_{dentin}) \sim 5 \times 10^{-7}$) and forms the justification for linearization of the transmission function, i.e. $T(x, y = 0) \approx 1 + i\phi(x)$. With $\beta << \delta$ the tubules are thus assumed to be pure phase objects. Now, instead of developing the one-dimensional Fourier transform of $\phi(x)$ the transform of the map of its components $\delta(x, z)$ is calculated across the tubule, parallel to the (x, z) plane. The analytical transform of such a 2D circularly symmetric tubule cross-section is easier to calculate than the transform of its projection. An intuitive justification for taking this approach arises when considering the construction of a tomogram to be a process of image formation. Such a tomographic image, although virtual, may be imaged onto a detector array at d. Points on any plane in this 3D image can therefore be Fresnel-propagated along z.

A formal argument arises in the Fourier projection-slice theorem [Bra56, Mal93]. Simply stated, a one-dimensional Fourier transform of a parallel projection of a two-dimensional object is equal to a slice through the two-dimensional Fourier transform of the same object, orthogonal to the direction of projection. The tubular geometry facilitates treating all radial

projections as identical both in real space and in the Fourier domain. This can now be further analyzed by treating tomography and propagation as two invariant linear transformations, the order of which can merely be exchanged [Goo96]. For the simple case of projecting a cylindri-

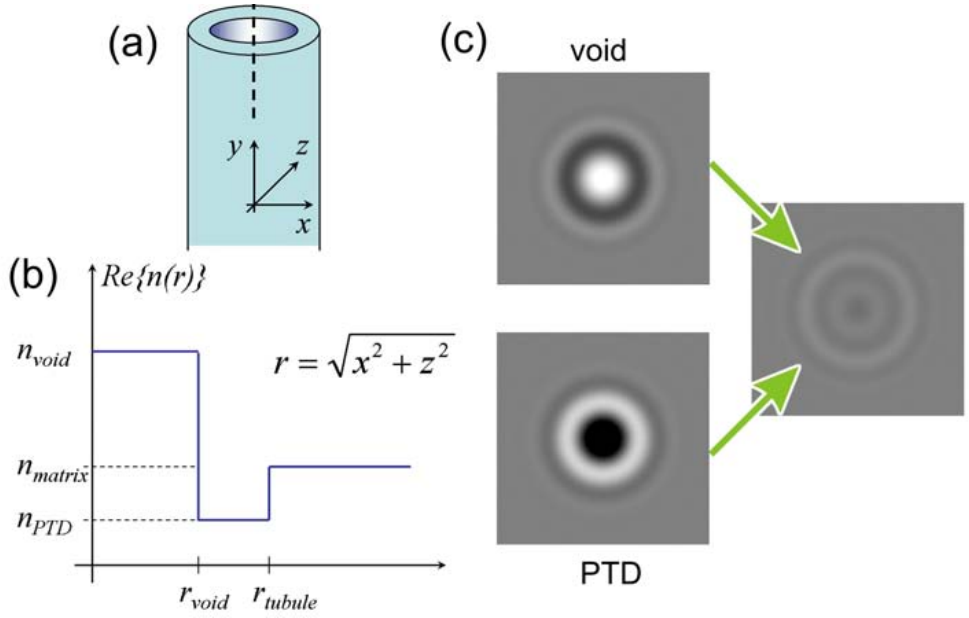

Figure 3.34: Model of the distribution of the refractive index $n(x, y, z)$ in a single tubule and resulting fresnel propagated images. (a) Schematic of tubule (b) Schematic illustration of the real component of the refractive indices of void, PTD and matrix (c) The outcomes of propagation of a tubule with only a void (constructive interference), only PTD without void (destructive interference) and the sum of both. When the interference patterns overlap, image contrast vanishes. The analytical model (eq. 3.5) was used to construct both contributions in Fourier space using Bessel functions. Propagation over $d = 433\,\mathrm{mm}$ was assumed, and the tubule was set to have a radius of $r_{tubule} = 1.67 \times r_{void}$ with $r_{void} = 0.8\,\mu\mathrm{m}$. Pictures show the squared modulus of the inverse Fourier transforms.

cal tube filled with water, consider the true 3D form of the material refractive index $n(x, y, z)$ which (far from any absorption edges) can be seen as a 3D representation of the microstructural electron density (cf. Fig. 3.34a). The tubule is approximated to be a water-filled circular void with a dense collar of PTD which is embedded in intertubular dentin matrix. Constructing the distribution of the object refractive index (Fig. 3.34b) in the (x, z) plane by superposing two circular step functions $\Theta(r)$ with $r = \sqrt{x^2 + z^2}$, where $\Theta(r) = 1$ for all $r \leq 1$ and 0 for $r > 1$, the refractive index becomes $n(r)$ and is written

$$n(r) = n_{mat} + (n_{ptd} - n_{mat}) \cdot \Theta\left(\frac{r}{r_{tub}}\right) + (n_{void} - n_{ptd}) \cdot \Theta\left(\frac{r}{r_{void}}\right) \tag{3.3}$$

where $r_{void} \leq r_{tub}$ are the void and tubule radii respectively, and $n_\alpha = 1 - \delta_\alpha + i\beta_\alpha$ with $\alpha = \{void,\ ptd,\ mat\}$ - water, peritubular dentin and matrix, respectively. The Fourier

transform of $n(r)$ is obtained by applying the Hankel transform of zero order, yielding $\hat{n}(\rho)$:

$$\hat{n}(\rho) = 2\pi \int_0^\infty dr\ rn(r)J_0(2\pi\rho) \tag{3.4}$$

where ρ is the conjugate variable to r in reciprocal space and J_0 a Bessel function of first kind and order zero. Inserting $n(r)$ from eq. 3.3 into eq. 3.4 yields

$$\hat{n}(\rho) = n_{mat}\delta_D + (n_{ptd} - n_{mat})\frac{r_{tub}J_1(2\pi\rho r_{tub})}{\rho} + (n_{void} - n_{ptd})\frac{r_{void}J_1(2\pi\rho r_{void})}{\rho} \tag{3.5}$$

with $\rho = \sqrt{f_x^2 + f_z^2}$, f_x and f_z the spatial frequencies conjugates to x and z. J_1 represents a Bessel function of first kind and order one and δ_D is the Dirac delta distribution at $\rho = 0$. The projection-slice theorem now states that $\hat{n}(\rho) = \hat{N}(f_x)$ with $\hat{N}(f_x)$ the one-dimensional Fourier transform of the refractive index $N(x) = \int dz\ n(x, y = 0, z)$ projected along the z-direction (note that due to the circular symmetry the projection angle $0°$ is equivalent to all other angles). Fresnel-propagation is applied to eq. 3.5 by multiplication with the propagator $\hat{P}_D(f_x, f_z) = \hat{P}_D(f_x^2 + f_z^2) = \hat{P}_D(\rho)$ and inverse transforming. While in Fourier space the result is a sum of two concentric oscillating damped Bessel functions of differing complex amplitudes, in real space, intensity - the squared modulus of the inverse transform - in the tubules center can be > 1, < 1 or ≈ 0, as explained by Fig. 3.34c. Shown are plots of a tubule with no PTD, tubule built only of PTD and the damped amplitude resulting from the cancellation of both contributions (assuming a sample-detector distance $d = 433\,\mathrm{mm}$).
To substantiate these results, both numerical simulations and measurements of propagation were carried out. As shown in the following, the results closely match the analytical solution and can therefore be used to interpret experimental results of human tooth dentin measurements. A comparison between the outcome of simulation and experimental results is essential if Fresnel-propagated microtomograms are to be used for dentin microstructural investigations.

Experimental: Dentin samples were prepared from human teeth that were extracted and discarded during routine dental treatment. Samples were prepared by cutting small cuboids that included both enamel and dentin ($2 \times 2 \times 3\,\mathrm{mm}^3$) spanning the so-called dentin-enamel junction (DEJ) as shown in Fig. 3.35a [Zas06]. About $0.5\,\mathrm{mm}$ enamel and the adjacent $1.5\,\mathrm{mm}$ dentin beneath it were imaged (Fig. 3.35b). All samples were kept wet during preparation and during all stages of data collection, having been placed in small thin-walled cylindrical plexiglass vials filled with water.
An additional sample was used to prepare several 2D slices across the dentin microstructure for scanning electron microscopy (SEM). The sample was dehydrated in a series of ethanol solutions, embedded in polymethylmethacrylate, then sliced and polished orthogonal to the tubular orientation. This revealed the cross-section at a depth of approximately $500\,\mu\mathrm{m}$ below the enamel and DEJ (shown in Fig. 3.36a). The uncoated backscattered SEM image reveals a distribution of tubule sizes, with corresponding voids and mineral content. For imaging dentin, the tomographic setup on BESSY/BAM*line* was used. Employing the X-ray macroscope with

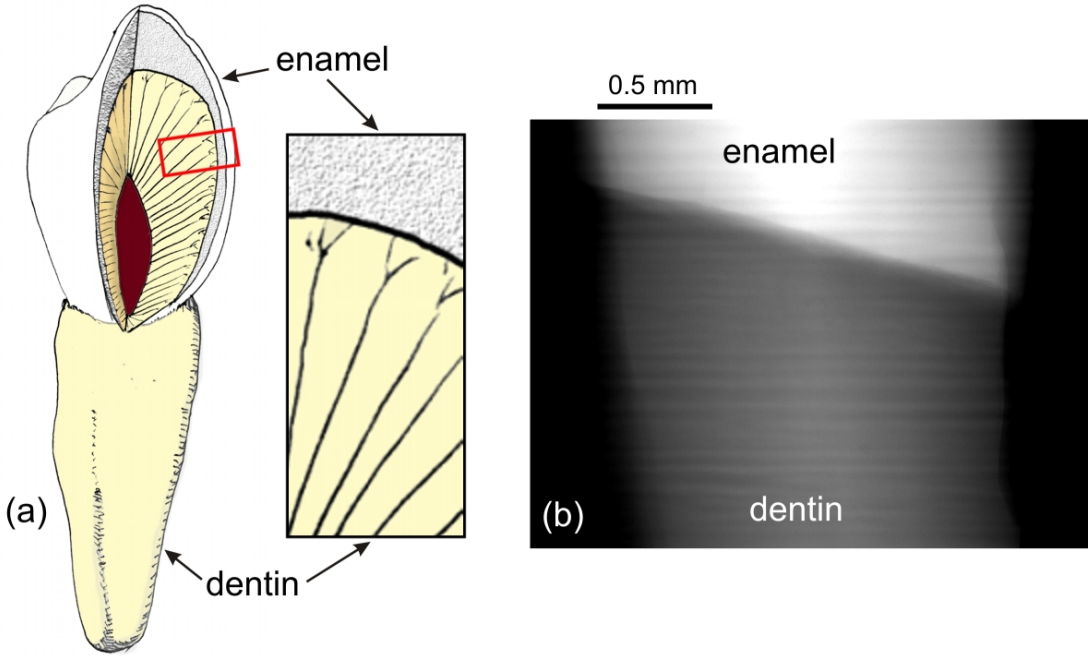

Figure 3.35: Sample of human crown dentin with attached enamel: (a) Schematic illustration of the position and form of typical samples cut out of the intact tooth. (b) An experimental contact (absorption) radiogram of a sample prepared as shown in (a). The denser enamel appears brighter due to the convention of representing absorption images using a (-log) scale.

a magnified pixel size of $1.6\,\mu\mathrm{m}$ and a $22\,\mu\mathrm{m}$ thin CWO scintillator screen yielded images of $\approx 3\,\mu\mathrm{m}$ lateral optical resolution. Radiographs were acquired using a $25\,\mathrm{keV}$ photon energy at $d_0 = 5\,\mathrm{mm}$ (absorption regime), $d_1 = 144\,\mathrm{mm}$ ("near" Fresnel regime) $d_2 = 433\,\mathrm{mm}$ and $d_3 = 720\,\mathrm{mm}$ ("far" Fresnel regime) sample-detector distance. These distances were chosen to allow for imaging of the full range of spatial frequencies in the structure [Zab05]. 900 angular projections were used to reconstruct Fresnel-propagated tomograms by means of filtered back-projection and without using the conventional negative logarithm scale normally employed for absorption tomogram representation. As a result, constructive interferences appear as bright, destructive interferences as dark patterns. A quantitative structural interpretation of the tomographic cross-sections thus requires a detailed analysis of the interactions of the beam with the underlying dentinal microstructures. This analysis was performed by simulating the propagation of a wave transmitted by a single tubule.

Results: The inherent blurring of CCD camera, optics and scintillator screen have to be considered for this simulation. They are described by an overall point spread function assumed to have Gaussian shape with a FWHM of $3.0\,\mu\mathrm{m}$. The partial coherence of the X-ray beam is described by the lateral extension of the source s and results in an additional blurring of the Fresnel-propagated images with an additional Gaussian kernel (sized $2\,\mu\mathrm{m}$ at most for $d =$

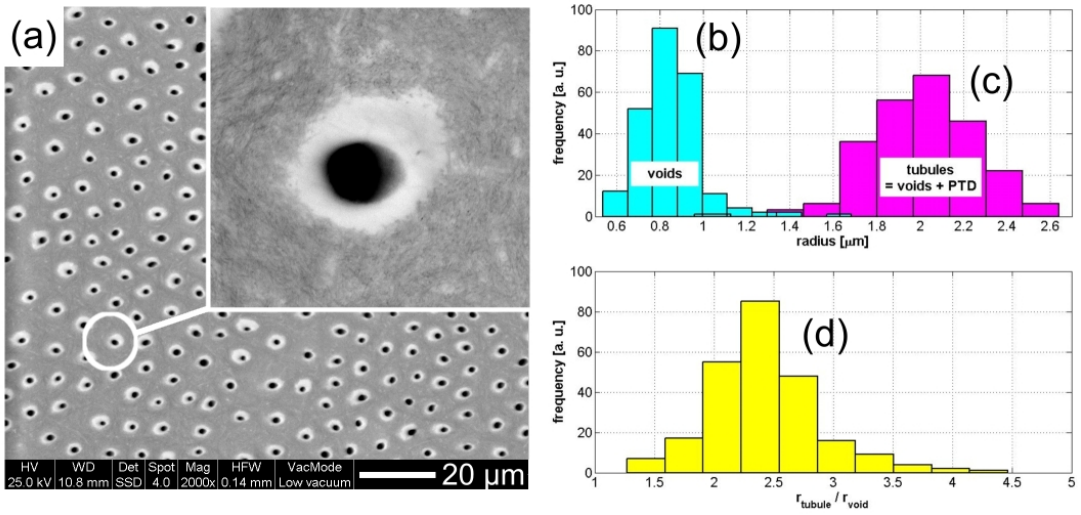

Figure 3.36: Tubules in dentin as seen in scanning electron microscopy. (a) An image of 244 tubules seen in one of the backscattered SEM images of a polished slice of dentin. The inset shows a magnified tubule which includes a void and a dense peritubular sheath. (b) Distribution of sizes of void radii and (c) tubule radii as derived from the SEM images. (d) Histogram of ratios of tubule and void radii. $\langle r_{void} \rangle = 0.8\,\mu\mathrm{m}$, $\langle r_{tub} \rangle = 1.9\,\mu\mathrm{m}$. The highest frequency of r_{tub}/r_{void} is a ratio of 2.4.

$433\,\mathrm{mm}$). SEM images (Fig. 3.36a) were used to estimate the average radius of the voids $\langle r_{void} \rangle$ and the average radius of the entire tubule $\langle r_{tub} \rangle$ (= PTD + void). The distribution of radii of voids and tubuli as well as their mutual ratios r_{tub}/r_{void} are shown in Fig. 3.36b, c and d. Some 244 tubules were measured by binarization from which $\langle r_{void} \rangle = 0.8\,\mu\mathrm{m}$ and $\langle r_{tub} \rangle = 1.9\,\mu\mathrm{m}$ were determined. These numbers are well within the range reported in the literature [Pas89, Got06]. The average distance between tubule centers was found to be $9\,\mu\mathrm{m}$ but this is known to vary [Pas89]. From the distribution of ratios r_{tub}/r_{void}, the ratio of 2.4 was found with the highest frequency, however a wide range of ratios is seen.

The values of δ and β that were used in the simulations were calculated for carbonated hydroxyapatite ($Ca_{10}[PO_4]_{5.5}[CO_3]_{0.5}[OH]_{1.9}[F,Cl]_{0.1}$) [Ell97] using the public-domain ESRF XOP tool (XOP v 1.8, Shanze, ESRF, Grenoble, France). The density of the constituents severely affects the calculated δ and β. For simplicity, all non mineralized points were assumed to be composed of water. For the PTD apatite a density estimate of $2.6\,\mathrm{g/cm^3}$ was used, whereas for the interdental matrix $2.0\,\mathrm{g/cm^3}$ were used [Gil69]. Note that a wide range of values has been reported in the literature [Ell97, Gil69, Wei99]. The PTD appeared remarkably similar to enamel when observed in backscattered SEM images at depths of $300-\ 500\,\mu\mathrm{m}$ beneath the DEJ (Backscattering SEM image gray values are well known to correlate with mineral density in apatite tissues [Ros98]). Therefore the above mentioned estimate is moderate, well below the $\sim 3.0\,\mathrm{g/cm^3}$ known for enamel. All these parameters are listed in Table 3.6. Propagation of X-rays of $0.5\,\text{Å}$ wavelength ($25\,\mathrm{keV}$) was simulated according to the operator formalism developed in section 1.3 and the resulting image intensities were calculated. Line profiles

material	density [g/cm^3]	$\delta(25\,\mathrm{keV})$	$\beta(25\,\mathrm{keV})$
enamel	3.0	1.0×10^{-6}	3.8×10^{-9}
void (water)	1.0	3.7×10^{-7}	1.0×10^{-9}
PTD	2.6	8.6×10^{-7}	3.3×10^{-9}
matrix	2.0	6.6×10^{-7}	2.5×10^{-9}

Table 3.6: Values for the density and refractive index used for the numerical simulations.

across the virtual wave propagating through and beyond a tubule was plotted for a range of tubule to void radii ratios and also at various propagation distances. Fig. 3.37 shows such line

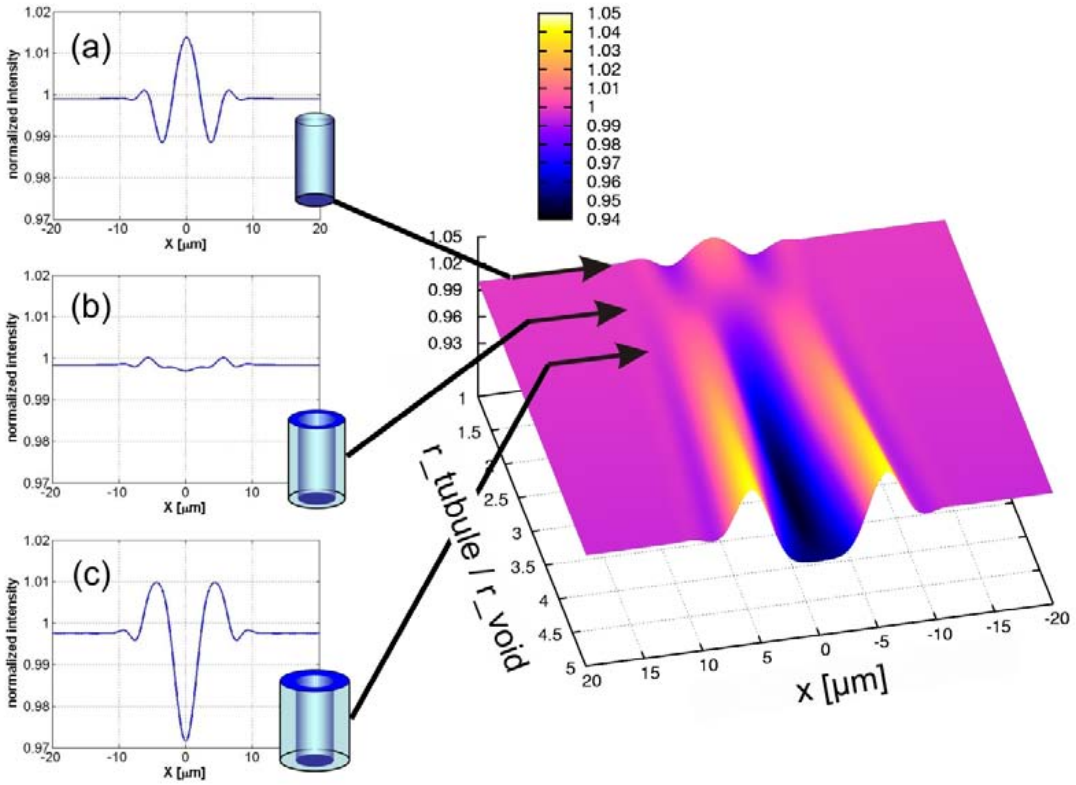

Figure 3.37: Simulation of the evolution of the interference pattern of a tubule as a function tubule/void radii ratios at $d = 433\,\mathrm{mm}$. The r_{tub}/r_{void} ratio is calculated from 1 (corresponding to no PTD) to 5 (thickest PTD observed from SEM images, see Fig. 3.36d). Three characteristic line profiles are plotted for ratios of (a) 1, (b) 1.67 and (c) 2.5. With no PTD surrounding the void (a) a bright interference peak forms at the tubule centre while tubules with a very thick PTD (c) will cause a dark central interference. Note that for a critical ratio $r_{tub}/r_{void} \approx 1.67$ the interference pattern almost vanishes (b).

profiles for $d = 433\,\mathrm{mm}$ and for a void radius $r_{void} = 0.8\,\mu\mathrm{m}$. The results obtained for tubular radii ranging from $0.8\,\mu\mathrm{m}$ to $4.0\,\mu\mathrm{m}$ are presented in the form of a pseudo-3D surface plot. Note the resemblance to the analytical results of propagation of a (x, z) plane based on eq.

3.5, shown in Fig. 3.34c. When there is no PTD ($r_{tub} = r_{void} = 0.8\,\mu\mathrm{m}$) the void focuses the X-rays, forming a central peak. This is emphasized in the line profile (a) redrawn in the inset on the left hand side of Fig. 3.37. As the thickness of PTD increases, focusing is reduced and at some critical thickness, the interference patterns vanish and no contrast is visible. The line profile is just about flat (Fig. 3.37b). This occurs at $r_{tub} = 1.67 \times r_{void}$ which is the critical ratio of void to tubule thickness, when $25\,\mathrm{keV}$ X-rays are used. Tubules of this diameter and thickness do not show detail in the reconstructed Fresnel-propagated tomograms due to a cancellation of the constructive and destructive interference contributions. By increasing the PTD thickness further (Fig. 3.37c calculated for $r_{tub} = 2.5 \times r_{void}$) an inversion of the effects of constructive and destructive interference is seen. Thus for thick PTD, a central dark minimum surrounded by bright rings is observed. Simulations of propagation through both smaller and larger void radii (well within the range observed from SEM pictures) revealed patterns that were not significantly different from those seen in Fig. 3.37. Thus tubules with none or little PTD always appear as brighter spots surrounded by dark bands while tubules with radii of $1.65 - 1.7$ times the radius of the void show negligible contrast and tubules with even thicker PTD sheaths always appear as dark spots surrounded by bright circles.

The effect of increasing the propagation distance can be seen by the pseudo-3D projection shown in Fig. 3.38. When $r_{tub} = r_{void}$, no PTD exists and the resulting interference patterns at distances up to $1.2\,\mathrm{m}$ are shown in Fig. 3.38a. In the absence of PTD the tubule functions as a focusing lens and increasing the propagation distance only highlights this effect. For tubules with thick PTD, i.e. $r_{tub} > 1.7 \times r_{void}$, we observe a constant defocusing behaviour of the tubule, independent of the propagation distance. Fig. 3.38b shows the results for $r_{void} = 0.8\,\mu\mathrm{m}$ and $r_{tub} = 2.4\,\mu\mathrm{m}$. At propagation distances between 0 and $0.2\,\mathrm{m}$ a strong increase in the signal amplitude is observed and for propagation distances > $0.2\,\mathrm{m}$ the effect of propagation is basically to spread out the interference fringes (see line plots Fig. 3.38c-e). Interference patterns obtained for tubules with $r_{tub} \approx 1.67 \times r_{void}$ (data not shown) show complex shapes in the simulations. They appear as very small fluctuations of the amplitudes at increasing propagation distances with extremely low contrast and they are practically not detectable in experimental tomograms. A typical cross-section of a Fresnel-propagated tomogram is shown in Fig. 3.39a. The distribution of structures is in strong contrast to the scanning electron images of the microstructure in a polished sample (cf. Fig. 3.36). The primary difference arises from the effects of constructive and destructive interferences (both corresponding to voids in the tubules) that appear due to propagation. To fully interpret the results of simulation, the SEM image shown in Fig. 3.36a was numerically propagated, to obtain a virtual Fresnel-propagated cross-section SEM image in Fig. 3.39b. This was done by assigning complex refractive indices according to the grey values corresponding to tissue densities in dentin (PTD, water-filled void and intertubular matrix) as provided by table 3.6. Figure 3.39b was thus obtained by Fourier transforming a complex map derived from Fig. 3.36a, multiplying by the Fresnel-propagator, inverse transforming and calculating the squared modulus. The detector resolution was taken into account by filtering the intensity image with a Gaussian kernel.

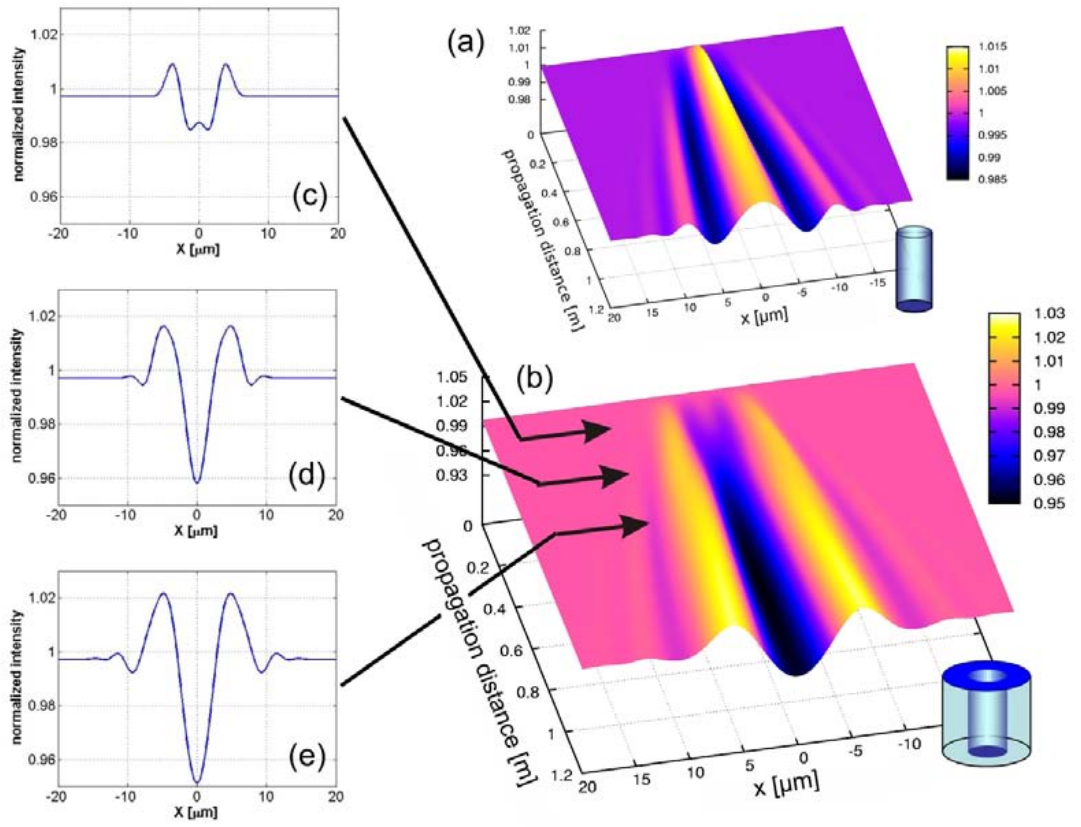

Figure 3.38: Simulated Fresnel propagation of tubules at various sample detector distances $d = 0$ to $1.2\,\mathrm{m}$. The two graphs (a) and (b) show the effect the propagation distance has on the measured interferences. Graph (a) shows the evolution of contrast produced by a simple void of $r_{void} = 0.8\,\mu\mathrm{m}$ while in (b) a PTD sheath of $1.6\,\mu\mathrm{m}$ thickness was added ($r_{tub}/r_{void} = 3$). The three plots on the left show explicitly the interference patterns at (c) $d = 144\,\mathrm{mm}$, (d) $d = 433\,\mathrm{mm}$ and (e) $d = 720\,\mathrm{mm}$.

Note the remarkable similarity to Fig. 3.39a, which shows a slice through a reconstructed Fresnel propagated tomogram of dentin from the adjacent area in the tooth. Areas of constructive and destructive interferences appear in some areas of the propagated SEM image, while in other areas contrast is lost.

Finally, the mean distance between the center of tubules must be kept in mind. This is important because imaging dentin beyond a certain propagation distance will cause the fringes to overlap, forming complex interferences. As a result structural details will become obscured, as can be seen for example when comparing tomograms recorded at short and long propagation distances in Fig. 3.40. Notice how the same region in tomographic datasets obtained at different propagation distances ($d = 144\,\mathrm{mm}$, $433\,\mathrm{mm}$ and $720\,\mathrm{mm}$) reveals similar features, which appear to grow. The spreading of the interference patterns is seen to exceed the mean distance between the tubules, resulting in reduced visibility and blurring. The distance at which tubules can be visualized best is therefore a compromise between tubule size and intertubular distance,

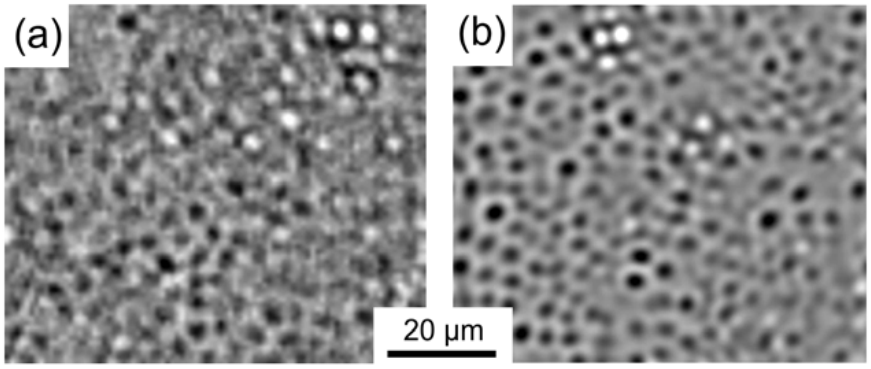

Figure 3.39: Slice across a Fresnel propagated tomogram compared with a propagated SEM image. (a) A magnified region from a recorded Fresnel propagated micro tomogram $\approx 0.5\,\mathrm{mm}$ below the DEJ (experimental data) shows a striking similarity to the simulated picture (b) obtained by virtual Fresnel propagation of the SEM image from Fig. 3.36. Both pictures correspond to a propagation distance of $d = 433\,\mathrm{mm}$.

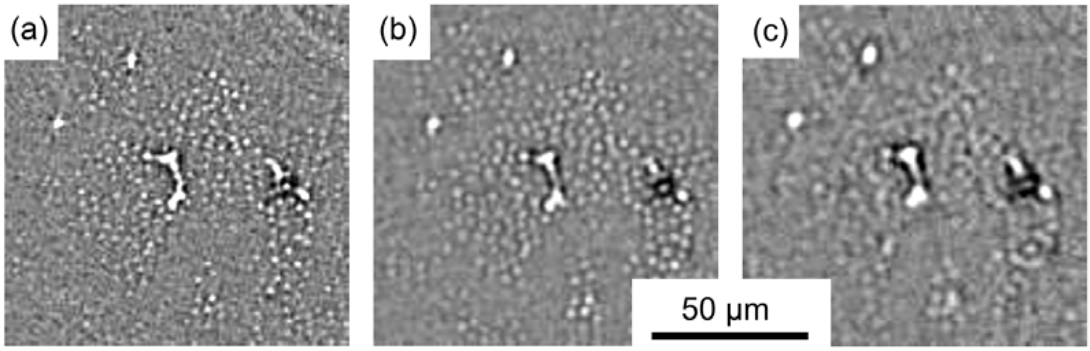

Figure 3.40: The effect of increasing propagation distance on image quality. Identical regions from Fresnel-propagated micro tomograms of dentin showing a close packing of tubules. The images recorded at (a) $d = 144\,\mathrm{mm}$ and (b) $d = 433\,\mathrm{mm}$ reveal clear details of the microstructure. At $d = 720\,\mathrm{mm}$ (c) tubules lose detail in the image due to the overlapping interference patterns.

for different depths of dentin.

Discussion: Due to interference in quasi-coherent X-ray beams, the 3D distribution of tubules can be visualized in two forms: bright *spots* surrounded by dark rings, when the PTD is absent or is thin ($r_{tub} \leq 1.5 \times r_{void}$) or dark *spots* surrounded by bright rings when the PTD thickness is substantial ($r_{tub} \geq 2 \times r_{void}$). Tubules where $r_{tub} \sim 1.67 \times r_{void}$ show no features when coherent $25\,\mathrm{keV}$ X-rays are used for imaging. Thus the three-dimensional shape of the tubules and deviations of the tubule design can be mapped within the bulk. Interference fringes originating from features only 1 to $2\,\mu\mathrm{m}$ large, which is below the resolution of the system, are clearly observable in the Fresnel-propagated reconstructed tomograms. However, this is only true as long as patterns from neighbouring structures do not overlap. At large ($> 0.5\,\mathrm{m}$) dis-

tances, dentin features touch and overlap (Fig. 3.40c) rendering such images less informative. Effects of thickness and structure of tubules in dentin on the tomographic image were considered by comparison between an analytical model, numerical simulations of propagation and real measurements of tomograms of dentin microstructure. The enhancing effects of propagation, namely increased contrast of tubules and concomitant magnification of the lateral dimensions of features in the reconstructed tomograms, facilitate exploration of the subtle microstructure variation, as well as the distribution of defects. The 3D images indicate that the tubules appear denser and thicker at increasing distances beneath the enamel. This is in notable accord with other reports of stiffening and hardening of the microstructure [Zas06, Cra59, Wan98] which can be explained by both increased density and thickness of the PTD. From approximately $200\,\mu\mathrm{m}$ beneath the enamel cap and deeper in, clear interferences patterns are seen, many with dark centers. However, clusters of dark spots surrounded by white rings are seen in some areas, whereas clustered white spots surrounded by dark rings are seen in other areas. Further analysis is still needed to fully characterize the distribution of the PTD and tubule thickness in teeth.

3.2.2 Time-median 3D imaging of water immersed tooth dentin

Following the previously described test measurements and simulations, beamtime was allocated at the ESRF/ID19 beamline for high-resolution Fresnel-propagated tomography of human tooth dentin. A method for obtaining high-quality and low-noise 3D images of this material is introduced in appendix B.2.4. In order to remove stray intensities from bubbles that appear and move randomly in the water surrounding the dentin, three sequential tomography scans are recorded under identical experimental conditions. For each projection angle θ, the three corresponding radiographs are numerically aligned by means of image cross-correlation. Improved projection images are then obtained by calculating the median values of matching pixels in the three aligned radiographs [Zab07a].
Fig. 3.41 shows two high-resolution ($\Delta x = 0.7\,\mu\mathrm{m}$ pixel size at $R \approx 1\,\mu\mathrm{m}$ spatial resolution using a $12\,\mu\mathrm{m}$ thin LAG:Eu screen) projection images of a cylindrical water immersed sample of tooth dentin. While the first is an experimentally recorded radiograph, the second image (Fig. 3.41c) represents the outcome of the time-median filter applied to three radiographs that were recorded during repeated $180°$ scans. An enlarged view (inset Fig. 3.41b) reveals the enhanced contrast of the dentinal tubuli and the silhouettes of randomly appearing and moving bubbles both highlighted by Fresnel-propagation (the images were recorded at $d = 180\,\mathrm{mm}$ sample-detector distance). Unlike Fig. 3.41b the closer view onto the time-median image (inset Fig. 3.41d) only shows the tubules whereas stray intensities caused by bubbles are almost completely removed. The effect of the time-median filter onto the reconstructed 3D data is seen in Fig. 3.42 where an axial slice - reconstructed from 1500 radiographic projections - is shown for the "conventional" data (a) and for the improved data which combines three convential scans (b). The difference of Fig. 3.42a and b is shown in Fig. 3.42c to highlight the

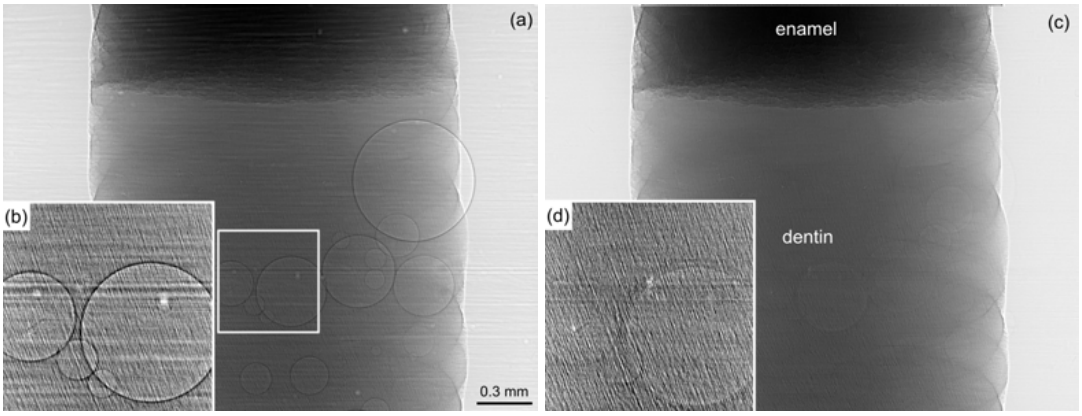

Figure 3.41: Fresnel-propagated projection image of human tooth dentin recorded at the ESRF/ID19 beamline. (a) Conventional radiograph (the inset (b) shows an enlarged region where bubble silhouettes obscure the structure); (c) Improved projection constructed from the median values of matching pixels in three radiographs recorded during repeated scans. (d) Inset showing the same region as (b). Note most of the stray intensities caused by bubbles have been removed.

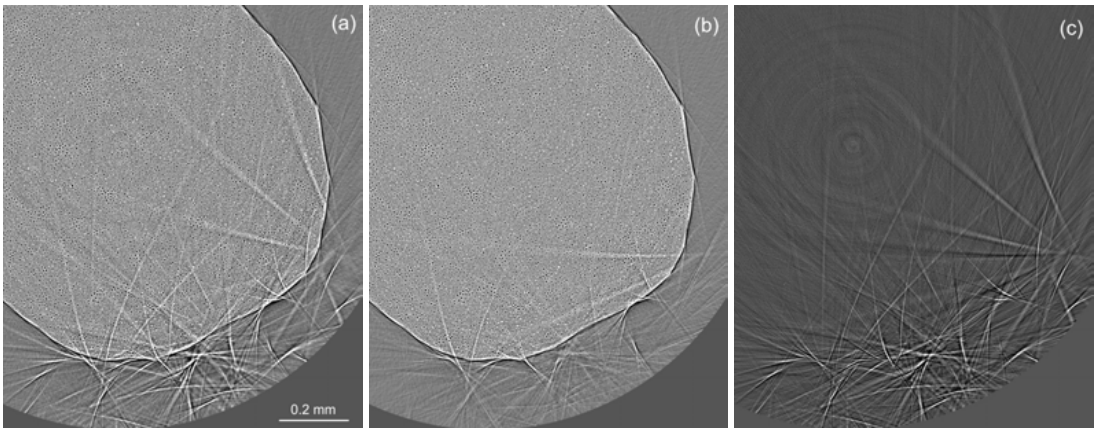

Figure 3.42: Axial slice reconstructed (a) from conventional radiographs (note the streak artifacts caused by the bubble silhouettes in Fig. 3.41a) and (b) from improved projection images. (c) The difference image (a-b) shows the artifacts that were removed by the time median filter.

artifacts that were removed by this non-linear filter.

Each radiograph represents $t_{exp} = 0.5\,\mathrm{s}$ exposure to a very high flux ($\sim 10^{12}\,\mathrm{Ph/mm^2/s}$) of $22\,\mathrm{keV}$ X-rays. Due to the fast readout ($\sim 13\,\mathrm{ms}$) of the ESRF-Frelon camera, complete scans are recorded in $14\,\mathrm{min}$, hence not more than $42\,\mathrm{min}$ are needed to record the 3 tomograms which are necessary for the time-median imaging. Attempts were made to reduce the acquisition-time even further by lowering the exposure time to $t_{exp} = 0.1\,\mathrm{s}$. An enlarged region on an axial slice is shown for a conventional reconstruction from one single scan (Fig. 3.43a) and for the time-median reconstruction (Fig. 3.43b) using three repeated scans. The

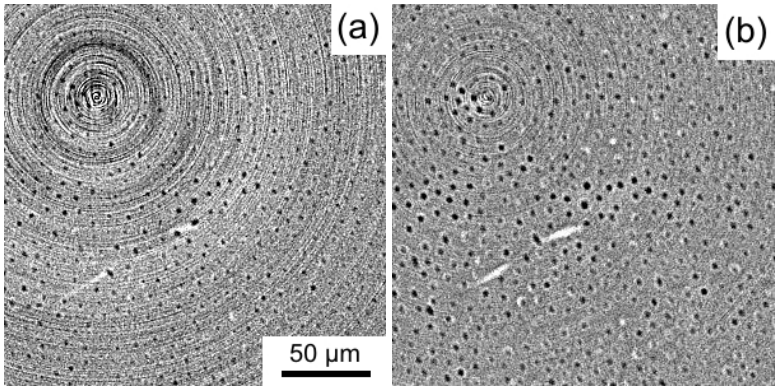

Figure 3.43: Enlarged region of an axial slice reconstructed from 1500 "high-speed" radiographs ($t_{exp} = 0.1\,\mathrm{s}$). (a) Conventional tomography; (b) Reconstruction from time-median images employing three repeated scans. Following each scan small (x, y)-shifts were applied to the sample in order to reduce the ring artifacts seen in (a). Note that most features show a dark central intereference peak and only few bright spots are seen indicating thick PTD sheaths for most of the tubules in the imaged dentin region.

improvements in terms of signal-to-noise ratio and artifact reduction are striking. Unlike the conventional tomogram where the dentinal tubuli (represented by their appropriate interference fringes) appear obscured by image noise and ring artifacts, the same image but reconstructed from improved projections reveals the spatial arrangement of the tubules as well as intensity variations in the interference lobes that were hardly visible in Fig. a. While the improved signal-to-noise ratio is due to the better photon statistics, removal of the ring artifacts is obtained by slightly shifting the sample after each of the three scans, by $10 - 20$ pixels in the x- and/or y-direction. During the numerical alignment which preceeds time-median filtering, small sample shifts are reversed. Consequently, defects on the CCD and/or scintillator screen - commonly associated to ring artifacts due to their fixed position in the images - are removed from the improved radiographs. The effect of changing the propagation distance is seen in Fig. 3.44. The simulations shown in the previous subsection (Fig. 3.38) are very well confirmed by these high-resolution images. The circular interference fringes of the tubules appear both enhanced and widened at larger propagation distances, whereas images taken at shorter values of d seem to converge towards the *real* size and shape of the tubules (see Fig. 3.36a for comparison). Yet the conclusion that Figs. 3.36a and 3.44a are equivalent is wrong. Indeed Fig. 3.44a is entirely the result of Fresnel-propagation. Although most tubules resemble dark voids surrounded by bright sheaths, some show an inverse contrast as predicted by simulations shown in Fig. 3.37. An inversion of the tubule's contrast due to an increase of d is not observed.

Note that unlike the previous pictures, Fig. 3.44a and b show the results of time-median images constructed from five repeated scans, recorded with $\Delta x = 0.35\,\mu\mathrm{m}$ pixel size and $R \sim 0.6\,\mu\mathrm{m}$ resolution which is the best quality available to date. Since there was no such image available for $d = 180\,\mathrm{mm}$, an inset is shown with Fig. 3.44c to allow for comparison between

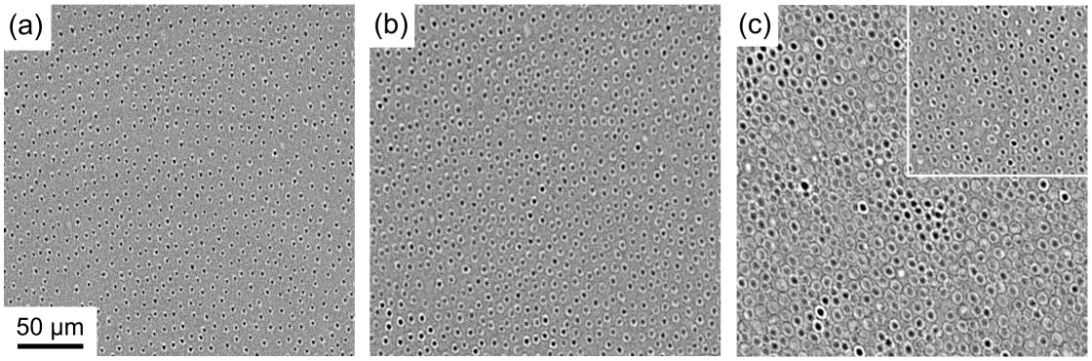

Figure 3.44: Changes in the 3D interference signal of the tubules due to increasing sample-detector distance: (a) *near-field* propagation image recorded at $d = 50\,\mathrm{mm}$; (b) $d = 100\,\mathrm{mm}$, both (a) and (b) were recorded with $\Delta x = 0.35\,\mu\mathrm{m}$ pixel size and $R \sim 0.6\,\mu\mathrm{m}$ resolution; (c) $d = 180\,\mathrm{mm}$ with $\Delta x = 0.7\,\mu\mathrm{m}$ pixel size and $R \sim 1.0\,\mu\mathrm{m}$ resolution (the inset shows a part of the same axial slice but recorded at $d = 100\,\mathrm{mm}$ to allow for a better comparison, since there was no record of the slice shown in (a) and (b) at $d = 180\,\mathrm{mm}$).

identical slices at $d = 100\,\mathrm{mm}$ and $d = 180\,\mathrm{mm}$ (both recorded with $\Delta x = 0.7\,\mu\mathrm{m}$ pixel size and $R \sim 1.0\,\mu\mathrm{m}$ resolution and using three repeated scans to construct improved projection images).

3.2.3 3D image analysis and phase-retrieval

To characterize the orientation and density of the tubules in bulk samples, a 3D Fourier analysis method was developed in the framework of this thesis. Small cubic subvolumes $o(x, y, z)$ of typically 128 pixel length are cut from the reconstructed 3D Fresnel-propagated images of tooth dentin. A three-dimensional fast Fourier transform $\hat{o}(f_x, f_y, f_z)$ of the sub-cubes is computed [Fri05] as shown for an example in Fig. 3.45. Note that f_x, f_y and f_z are the spatial frequencies in 3D reciprocal space, conjugates to x, y and z. In such a small subvolume the tubules are characterized by a quasi-parallel orientation and a random, homogeneous distribution in the bulk material (the inset in Fig. 3.45d shows a typical axial slice through a (128 pixel)^3 cube of tubular dentin. As can be seen from Fig. 3.45a-c the average orientation vector of the tubules can be easily found by binarizing the 3D FFT's modulus and calculating the major axis of inertia of the resulting ellipsoid. An oblique plane $\hat{p}(u, v)$ normal to this axis is then cut through the reciprocal data (Fig. 3.45d). The result shows a striking similarity to small-angle scattering data of nanometer-sized structures. However, in addition to the tubules structure factor the reciprocal intensities in Fig. 3.45 contain information about the complex Fresnel-propagator. A one-dimensional intesity $\hat{p}(\rho)$ (with $\rho = \sqrt{u^2 + v^2}$) is calculated from the 2D cut in Fig. 3.45d by averaging a large number (typically 200) of radial profiles corresponding to different polar angles. Fig. 3.46 shows two such radial intensity profiles calculated from quasi identical subvolumes which correspond to records of the same sample taken at different sample-detector distances ($d = 84\,\mathrm{mm}$ and $113\,\mathrm{mm}$). The effect of

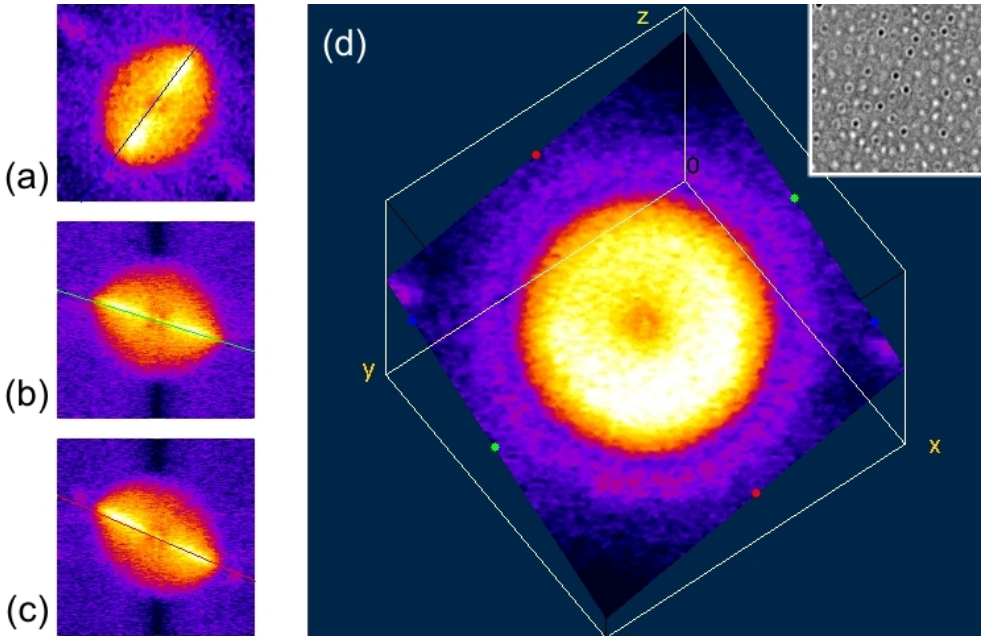

Figure 3.45: Three-dimensional Fourier transform of a (128 pixel)^3 cubic subvolume of dentinal tubuli (recorded with $\Delta x = 0.7\,\mu\mathrm{m}$ pixel size and $R \sim 1.0\,\mu\mathrm{m}$ resolution at the ESRF/ID19 beamline. (a-c) Frontal, axial and sagital slice through the modulus of the 3D FFT. (d) oblique cut perpendicular to the axis of rotational symmetry of the tubules.

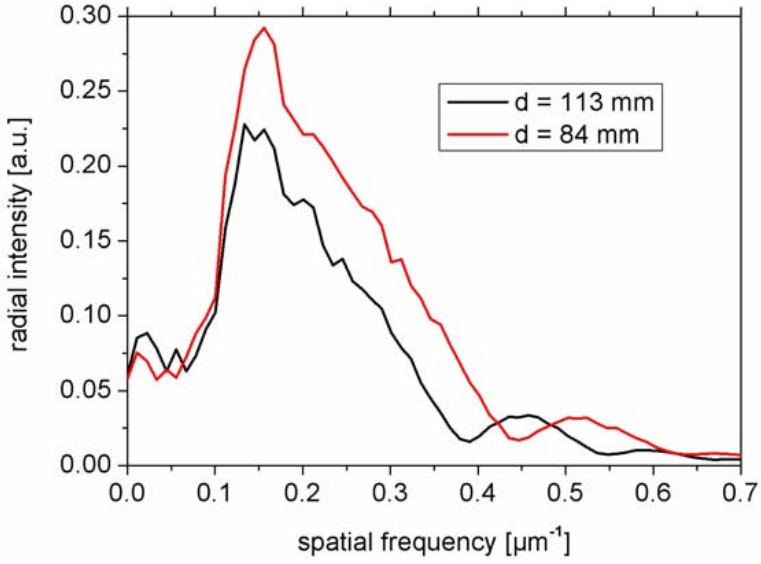

Figure 3.46: Radial intesity profiles calculated from oblique cuts through the 3D Fourier transform of a (128 pixel)^3 subvolume. of dentin measured at $d = 84\,\mathrm{mm}$ and $113\,\mathrm{mm}$. Note that the second peak ($0.51\,\mu\mathrm{m}^{-1}$ for $d = 84\,\mathrm{mm}$) shifts towards lower frequencies when d is increased ($0.43\,\mu\mathrm{m}^{-1}$ for $d = 113\,\mathrm{mm}$), a result of oscillations in the contrast transfer function which depend on d.

increasing the propagation distance is obviously a shift of the diffraction signal $\hat{p}(\rho)$ towards lower spatial frequencies (written in terms of reciprocal micrometers). A maximum is observed at $\rho \approx 0.15\,\mu\mathrm{m}^{-1}$ for the two distances. The inverse of the peak frequency corresponds to the average intertubular distance $\langle r \rangle \approx 6.7\,\mu\mathrm{m}$ and is invariant to the propagation distance d. Note that this value is slightly smaller than estimated from the electron microscope ($9\,\mu\mathrm{m}$ for Fig. 3.36a), probably the result of an increase in tubule density further below the dentin enamel junction (DEJ).

In addition to the average inter-distance between tubuli, Fig. 3.46 shows the highest damping of the signal: $\hat{p} \approx 0$ at $\rho \approx 0.45\,\mu\mathrm{m}^{-1}$ and $0.64\,\mu\mathrm{m}^{-1}$ for $d = 84\,\mathrm{mm}$, whereas the minima appear shifted at $d = 113\,\mathrm{mm}$. For the longer distance hardly any signal is observed at $\rho \approx 0.38\,\mu\mathrm{m}^{-1}$ and $0.55\,\mu\mathrm{m}^{-1}$. These values coincide with the minima of the contrast transfer function (CTF, section B.3.1) $\sin(\pi\lambda D\rho^2)$ for pure phase objects. Due to the oscillatory shape of the CTF, spatial frequencies which correspond to $\rho_n = \sqrt{n/(\lambda D)}$ (with $n = 0, 1, 2, \ldots$) are not visible in the Fresnel-propagated images. Note that this phenomenon is the reason for using mulitiple distances to retrieve phase maps from Fresnel-propagated projection images [Zab05]. At $\lambda = 0.56\,\text{Å}$ ($E = 22\,\mathrm{keV}$) and $d = 84\,\mathrm{mm}$ the CTF is zero at $\rho_1 = 0.46\,\mu\mathrm{m}^{-1}$ and $\rho_2 = 0.65\,\mu\mathrm{m}^{-1}$. At $d = 113\,\mathrm{mm}$ the zeros are at $\rho_1 = 0.40\,\mu\mathrm{m}^{-1}$ and $\rho_2 = 0.56\,\mu\mathrm{m}^{-1}$, respectively. Note that these values are slightly smaller than those observed in Fig. 3.46 and a perfect match is found at $E = 21.3\,\mathrm{keV}$ indicating a slight misalignment of the multilayer monochromator.

Consequently, at least two propagation distances must be used for this analysis method. Note that the maximum sampled frequency in two curves of Fig. 3.46 is given by the Shannon theorem $\rho_{max} = 1/(2\Delta x) \approx 0.7\,\mu\mathrm{m}^{-1}$. Deconvolution with the CTF and the detector blurring is a complicated procedure which is why this method was only used to investigate qualitatively the changes in tubule density along an axis perpendicular to the DEJ surface. Fig. 3.47 shows five diffraction curves $\hat{p}(\rho)$ calculated for (128 pixel)^3 sub-cubes that were cut at different depths below the DEJ ranging from $0.11\,\mathrm{mm}$ to $1.10\,\mathrm{mm}$. As observed from SEM pictures, very close to the DEJ ρ_{max} is shifted to lower spatial frequencies ($0.13\,\mu\mathrm{m}^{-1}$) compared to the *deep dentin* ($0.16\,\mu\mathrm{m}^{-1}$). For this particular sample of dentin this shows that the average intertubular distance is $\sim 7.7\,\mu\mathrm{m}$ underneath the DEJ and $\approx 6.3\,\mu\mathrm{m}$ below. Furthermore the overall signal becomes stronger at increasing depth below the DEJ. This is observed for the low and the higher spatial frequencies. Inspection of the corresponding axial slices (shown in Fig. 3.47) confirms that the increase in reciprocal signal strength occurs along with stronger pronunciation of the tubules' interference fringes. SEM images and the propagation simulations reported in the previous subsection indicate that the peritubular dentin (PTD) right underneath the DEJ is of lower density than the deep dentin PTD. For the latter the changes indicated by Fig. 3.47 are possibly due to an increase of PTD thickness but more data is required to prove this assumption.

Phase-retrieval was tested on the structure of dentin, whereby approximate maps $\phi(x, y, \theta)$ were calculated for each projection angle using a combined iterative algorithm (appendix

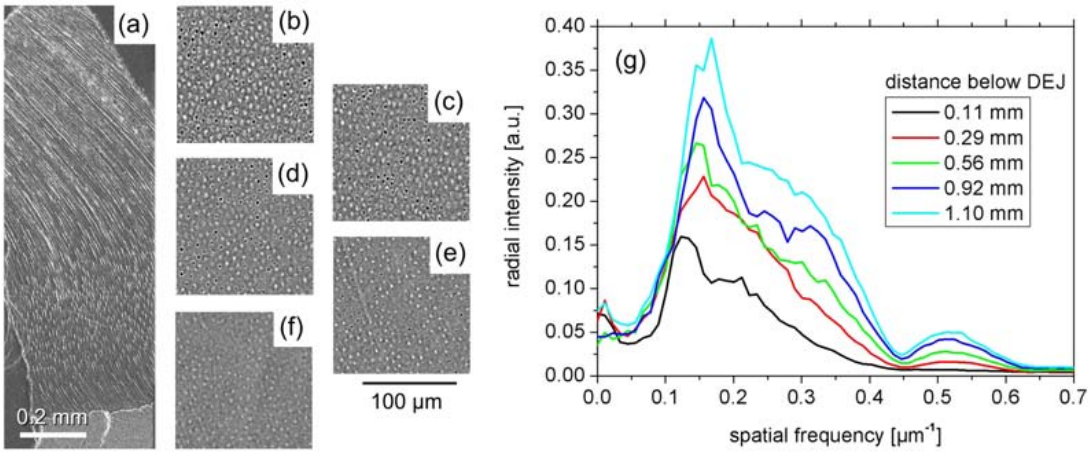

Figure 3.47: Fourier analysis of changing tubule density with increasing depth below the DEJ surface. (a) A frontal view onto the sample of dentin reconstructed from Fresnel-propagated radiographs taken at $d = 84\,\mathrm{mm}$ sample-detector distance reveals the tubular microstructure. (b-f) Small axial slices of the same data represent the tubular structure in real space at (b) $1.10\,\mathrm{mm}$, (c) $0.92\,\mathrm{mm}$, (d) $0.56\,\mathrm{mm}$, (e) $0.29\,\mathrm{mm}$ and (f) $0.11\,\mathrm{mm}$ below the DEJ surface. (g) The five corresponding diffraction plots show the radial intensity in reciprocal space.

B.3.3) to process four tomographic datasets recorded at increasing sample-detector distances $d = 15\,\mathrm{mm}$. $48\,\mathrm{mm}$, $81\,\mathrm{mm}$ and $113\,\mathrm{mm}$. A reconstructed axial slice of this holotomography is shown in Fig. 3.48. The result of the phase retrieval appears rather poor which is why Fresnel-propagated images must be preferred. Apparently the algorithm does not manage to find a unique solution for the Fresnel interference rings of dentinal tubuli. This is seen when some tubules appear as white and some as black spots, whereas a black void surrounded by a white sheath would be the correct solution. Most likely, phase-retrieval does not work properly when the feature size is too close to the resolution limit of the imaging system. Consequently, Fresnel-propagated 3D images recorded at $d = 50$ to $150\,\mathrm{mm}$ are best suited for the study of dentin tubular microstructure.

Short summary

Unlike conventional absorption μCT, where the micrometer-sized dentinal tubules cannot be distinguished from the image noise (cf. appendix B.2, Fig. B.11), Fresnel-propagated X-ray imaging is capable of sufficiently enhancing the tubules signal. 3D images recorded of water-immersed tooth dentin could be highly improved by time-median averaging three sequential μCT scans. With this new visualization method for wet biomaterials, image noise is strongly reduced and the destructive effects of bubbles in the water surrounding the sample are almost completely removed. Simulations of X-ray propagation through a single tubule revealed that the interference signal stored in the Fresnel-propagated datasets contains additional information about density and thickness of the peritubular dentin (PTD) surrounding the hollow

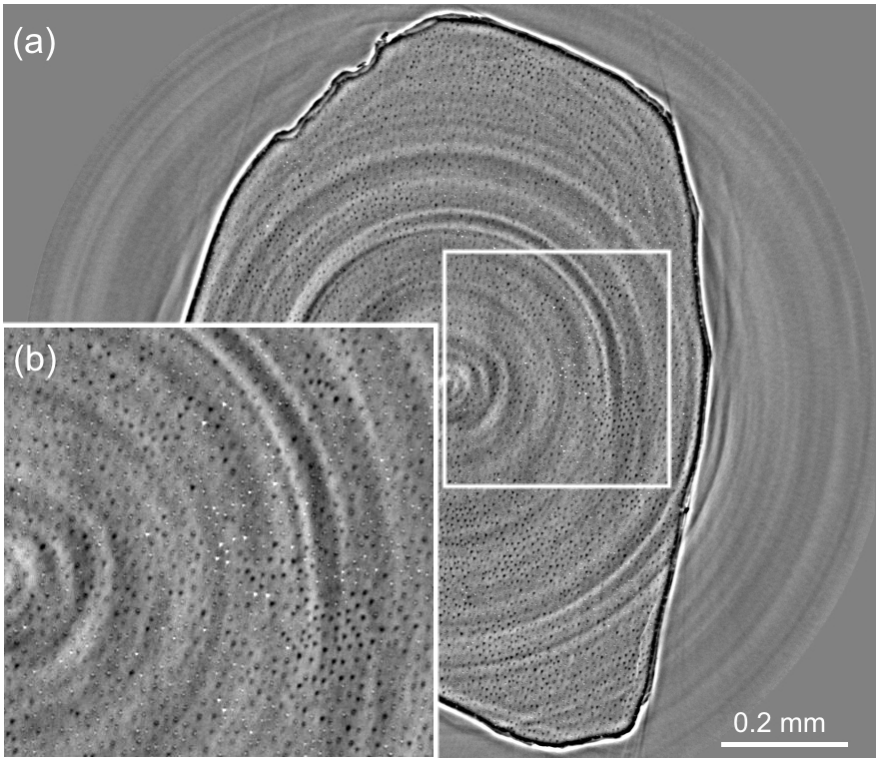

Figure 3.48: Holotomography of tooth dentin using four sample-detector distances ($d = 15\,\mathrm{mm}$. $48\,\mathrm{mm}$, $81\,\mathrm{mm}$ and $113\,\mathrm{mm}$). (a) Axial slice with enlarged inset (b).

tubules. Dark interference minima indicate a thick PTD sheath, while bright maxima orginate from voids that are surrounded by only little or no PTD. Particularly underneath the DEJ (over a depth of $\approx 100\,\mu\mathrm{m}$) hardly any sign of PTD is found which is in accordance with SEM measurements. Towards the lumen the PTD density/ thickness increases continuously. The twisted "s-shape" of the tubules - sililar to a spring - in the DEJ near region followed by a more or less straight orientation towards the lumen indicates graded mechanical properties (soft elastic zone underneath the DEJ, hard stiff zone towards the lumen) which were indeed measured by other methods [Zas06]. A 3D Fourier analysis method was successfully developed to quantify the microstructural changes in the PTD density/ thickness as well as in the interdistance between the tubules. Further work will be carried out to separate those contributions which are intrinsic to Fresnel-propagation, i.e. to the contrast transfer function, from those due to the dentin structure. With an integral measurement set of multiple enamel/ DEJ/ dentin samples extracted from different teeth and from different sides of each tooth a new attempt to create a realistic 3D mechanical model of tooth functioning will be made.

3.3 Natural rock

Introduction: The aim of this part of the work was to obtain new insight into the formation and propagation of cracks in natural rocks. Due to their strongly heterogeneous microstruc-

ture, experimental and analytical characterizations of the elastic properties and compressive strength of rocks often do not yield reproducible results. In other words, the ductility and the bulk behavior under stress are strongly affected by the local distribution of flaws, fossils, inclusions, cavities, grain boundaries and microcracks inside the rock. Griffith showed that the resulting fracture processes in such an inhomogeneous material are mainly controlled by micro-flaws [Gri24]. Consequently, crack initiation, propagation and growth are preferably studied on the micrometer-scale in order to better understand macroscopic fracturing. On the other hand, rock fracture mechanics considers cracks ranging from micrometers to a few kilometers [Atk87]. There exist three basic modes of crack tip displacement: mode I - opening or tensile mode, where the crack surfaces move directly apart, mode II - sliding or in-plane shear mode, where the crack surfaces slide over one another in a direction perpendicular to the leading edge of the crack and mode III - tearing or anti-plane shear mode, where the crack surfaces move relative to one another in parallel to the leading edge of the crack. These three modes result in kinematic sequence: 1. Tensile mode I cracks are generated at randomly distributed micro-flaws. These tensile cracks are almost parallel to the direction of maximum stress. 2. Shear (wing) cracks start from the tips of tensile cracks and grow along a curvilinear path. 3. Fracture occurs by coalescence of tensile and wing cracks.

It is well known that cracks can be described as curved surfaces in three dimensional space, yet most microscopic investigations on fracturing in rocks were limited to the analysis of thin sections [Jan01, Moo95]. For a long time the appropriate 3D imaging technology has not been available. First volumetric crack images were obtained from materials that are transparent to visible light. Numerous investigations on the fracture of glass [Bie67, Hoe65, Ger94], resin (e.g. poly-methyl-meta-acrylate) [Dys95, Dys03, Hor85, Can90] and ice [Sch99] were reported. These transparent materials allow for the study of fracture processes while controlling the concentration of ab initio defects in the samples. Cross-sectional images of fractured gypsum samples were studied extensively by Bobet and Einstein 1998 [Bob98] and Lajtai [Laj74] to model a representative variety of brittle rocks. With X-ray tubes are becoming a standard tool in geophysical laboratories, the amount of research on the three-dimensional distribution of grains and cavities in natural rock increased significantly over the past ten years [Ket05, Hir03, Oht01, Ver03]. In addition to natural rocks, X-ray computed tomography (CT) was applied to study many “rock-like” materials such as mortar and concrete [Lan03, Ota03]. The number of reports increased along with the highest available resolution of the method [Des06]. X-ray CT was shown to be particularly useful for the analysis of the hierarchal size distribution of pores and minerals in rocks because this technique has the potential to visualize details ranging over many orders of magnitude on the length scale (from $0.5\,\mu\mathrm{m}$ to $0.5\,\mathrm{m}$). Ultrasonic techniques are sometimes used to obtain additional information on the fracture processes [Zan00]. The number of reports on 3D imaging of natural rock, whereby mineral phases as well as cracks were analyzed, increased with neutron radiography and tomography becoming available at cold and/or thermal neutron sources [Bas04, Lun03, Win02]. Typical mineral rock constituents (e.g. different silicates such as quartz, feldspars, micas, pyroxene,

amphibole) are highly transparent to neutrons, thus allowing to record projection images of relatively large samples (1 to 10 cm). Still, the maximum spatial resolution of neutron tomography (50 µm) is not capable of imaging the very small porosity known inherent to natural rocks [Fre95]. Similarly, the resolving power of common X-ray tomographs is limited to some tenths of a millimeter. Therefore, 3D imaging of the mineral and crack distribution in rock with micrometer details was restricted to the users of hard X-ray beamlines, available on a few synchrotron facilities throughout the world. Reports on such experiments are still rare [Mat03, Len03, Nak04, Bes06, Lan06], and these report on finest details of 10 to 20 µm size.

3.3.1 Cracking - Absorption CT

The first experiment on rocks at BESSY/BAM*line* involved absorption CT ($\Delta x = 3.6\,\mu\mathrm{m}$ pixel size) with a rather moderate spatial resolution ($R \sim 10\,\mu\mathrm{m}$) to visualize and analyze pores and cracks in two types of sedimentary rock, before and after mechanical compression: A Carboniferous greywacke was selected due to its heterogeneous distribution of various minerals and grain sizes, and a Triassic limestone which is characterized by a very homogeneous fine-grained microstructure was chosen for comparison.

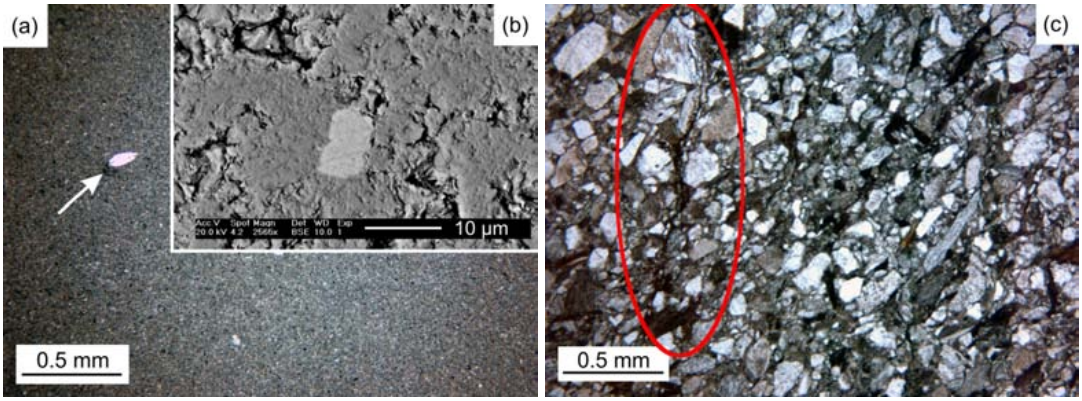

Figure 3.49: (a) Microscopic image showing a cross-sections of limestone (the arrow indicates a sparitic shell included in the fine clay-matrix). The inset (b) shows a magnified scanning (backscattered) electron microscopy image of the same limestone revealing µm-sized inter-granular porosity and pyrites (bright contrast) of $\approx 10\,\mu\mathrm{m}$ size. (c) Microscopic image of greywacke showing various mineral grains of different sizes (quartz, feldspar and mica) ranging from 10 µm to 0.5 mm. An old "healed" crack that is filled with (opaque) ore minerals is indicated by the red ellipse.

The greywacke came from a core drilling near Waldeck and the limestone from the vicinity of Berlin, both in Germany. Fig. 3.49 shows two microscopic images of thin sections of the two investigated rocks. The cutting plane was chosen in such a way that the direction of maximum stress (applied to cylindrical samples of the same material) would lie in the plane. According to Folk the limestone can be classified as a micrite and after Dunham as a mudstone [Fol59, Dun62]. It is characterized by a homogeneous distribution of grains smaller than 5 µm

and contains few small sparitic shells. The inset (Fig. 3.49b) shows an electron microscopic image of the fine limestone grains revealing micrometer-sized inter-granular porosity. Energy dispersive X-ray analysis further revealed that small pyrites are randomly distributed over the fine limestone matrix (e.g. the bright grain in the middle of Fig. 3.49b).
The greywacke consists of angular and round grains embedded in a compact, fine clay matrix. Grain sizes of the mineral constituents range from $10\,\mu\mathrm{m}$ to $0.5\,\mathrm{mm}$. Consequently, greywacke has a completely different fracture behavior compared to limestone. The minerals in greywacke are mostly mono- or polycrystalline grains of quartz and fragments of igneous and/or sedimentary rocks. Few feldspars and mica (mostly biotite) are found and this rock can thus be classified as a lithic greywacke (after [Fol74]). A "healed" crack filled with opaque ore minerals is marked by an ellipse in Fig. 3.49c. Such healed cracks indicate that the greywacke had fractured earlier and the resulting cavities were filled with iron oxides after. From fracture tests it was observed that when compressive stress is applied more or less parallel to the orientation of the healed cracks, new cracks develop alongside this "preferred" orientation.
Preparation of samples for deformation and micro-tomography was relatively simple. For each material small cylinders of $\approx 6.6\,\mathrm{mm}$ in diameter and $10\,\mathrm{mm}$ height were cut out of the bulk material using a diamond core drill. This cylinder size was chosen to allow the samples to fit into the field of view of the detector array at the same time allowing the visualization of details of at least $10\,\mu\mathrm{m}$ size. Larger samples would require X-rays of higher energies ($E > 100\,\mathrm{keV}$) in order to guarantee a sufficient translucency of the material. Since these energies are not available at BESSY/BAM*line* the sample diameter was limited to $7\,\mathrm{mm}$ at most.

Experimental: Three cylinders of each material were selected and complete tomograms were acquired of their initial microstructure. Then the samples were axially loaded to different percentages of the average maximum strain $\langle\epsilon_{max}\rangle$ (as determined from a number of different test samples): 60% (samples G1, and L1), 80% (samples G2 and L2) and 90% (sample G3 and L3). Strain-controlled uniaxial compression was applied at constant speed ($0.1\,\mathrm{mm/min}$) to the dry samples that were placed between the two loading plates of an universal testing machine (UP25) without any additional confining pressure. After compression the samples were unloaded and repositioned on the tomography stage where a second record of every sample was taken. Note that because the tomograms were recorded from the unloaded samples, effects due to elastic deformation cannot be observed in the images. In order to characterize the overall course of plastic deformation, i.e. the average maximum strain $\langle\epsilon_{max}\rangle$ and the average uniaxial compressive strength $\langle\sigma_{max}\rangle$, six additional test cylinders of each rock were compressed until fracture occurred. The measured stress-strain curves for limestone and greywacke are depicted in Fig. 3.50a and b along with photos of a fractured sample of each material. While all limestone samples split into many columns, for greywacke a single oblique fracture was observed during these tests whereby the sample split into two pieces. The average uniaxial compressive strength $\langle\sigma_{max}\rangle$ and the average maximum strain $\langle\epsilon_{max}\rangle$ were calculated from these tests. $\langle\epsilon_{max}\rangle$ is indicated in the graphs by vertical dotted lines,

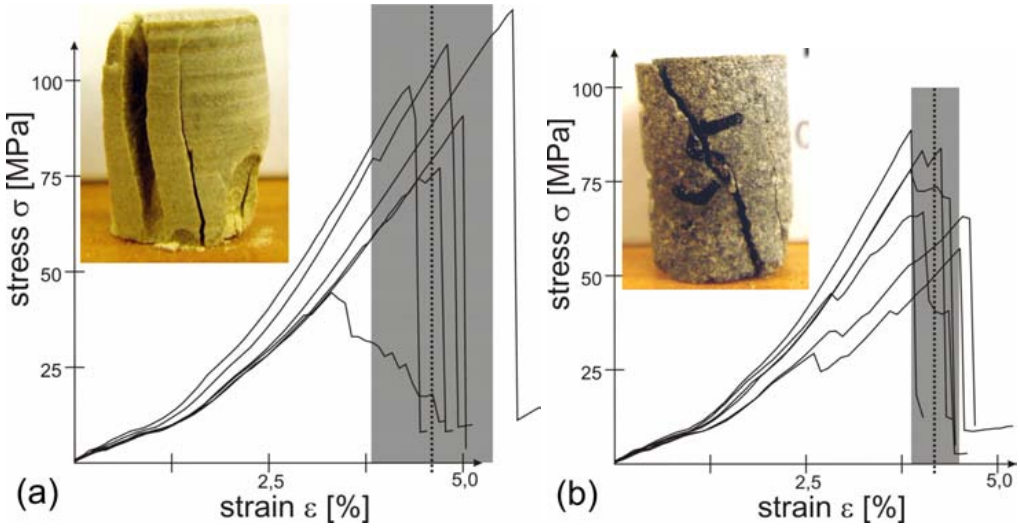

Figure 3.50: Stress-strain curves obtained from fracture tests on small cylinders of (a) limestone and (b) greywacke. The dashed lines indicate the average maximum strain and the gray bars mark the scattering of the individual values. The insets show photos of fractured greywacke and limestone samples. Note the multi-columnar fracture of the limestone in contrast to the single oblique fracture of the greywacke.

whereas the scatter of $\langle \epsilon_{max} \rangle$ is marked by gray bars (Fig. 3.50). The deformed samples had a length-to-diameter ratio ranging from 1.4 to 1.7. The measured average maximum strain and strength were corrected for the different ratios by using the shape correction given in [Pel93]. For greywacke $\langle \sigma_{max} \rangle = 74 \pm 10\,\mathrm{MPa}$ was found (mean value $\pm$ standard deviation) and for limestone $\langle \sigma_{max} \rangle = 87 \pm 26\,\mathrm{MPa}$. These values correspond reasonably well to those given in [Pel93] (greywacke: mean value $81\,\mathrm{MPa}$, limestone: mean value $105\,\mathrm{MPa}$). As can be seen from the stress-strain curves the scatter of the σ_{max} values was very pronounced especially for the limestone samples. This appears to contradict the fine homogeneous microstructure. Inclusions (sparitic shells as seen in Fig. 3.49a) are probably responsible for the strong variation in material strength. Some deformation curves show non-linear "kinks" prior to peak stress, indicating partial relaxation due to the formation of cracks or collapse of pores inside the samples. Furthermore, these kinks might be related to tiny irregularities in the sample shape. From Fig. 3.50 it is also seen that the values of maximum strain ϵ_{max} scatter less than the compressive strength. The tests on limestone yielded $\langle \epsilon_{max} \rangle = 4.6 \pm 0.7\%$, whereas the greywacke samples attained $\langle \epsilon_{max} \rangle = 4.2 \pm 0.2\%$. Strain-controlled deformation was applied to the samples that were used for tomography, according to the values of $\langle \epsilon_{max} \rangle$.

Data processing: Because of the limited vertical size of the X-ray beam ($E = 33\,\mathrm{keV}$), three tomograms (900 projection angles each) were recorded at different heights to cover the entire sample volume. In a first step these three recorded sections are assembled into one dataset. Fig. 3.51a and b depict how the different parts of sample G3 are aligned while Fig. 3.51c illustrates

the different microstructural constituents in this material by coloring cracks and ore-minerals and setting low density minerals transparent. The total analyzed volume per sample was ca.

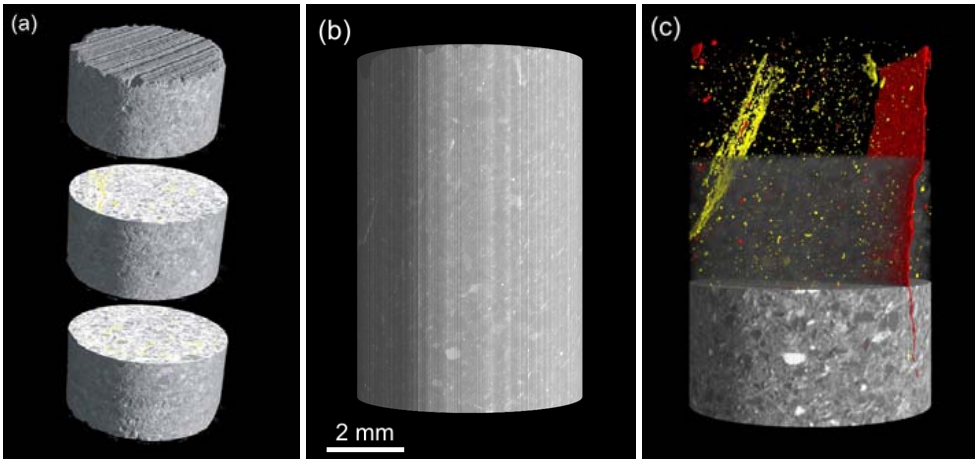

Figure 3.51: 3D images of sample G3: (a) Virtual assembly of three tomograms of G3 that were recorded to map the entire height of the sample. (b) $2 \times 2 \times 2$ binning is applied to the complete dataset which is further converted into 8-bit data in order to reduce the computer memory required for image analysis. (c) Reconstruction of linear absorption coefficients allows to distinguish grains and phases in the greywacke. In red: porosity and a macro-crack forming after strong deformation; In yellow: dense mineral particles reveal a healed crack with an orientation similar to the new crack.

$0.5\,\mathrm{cm}^3$, representing a virtual three-dimensional space of $2037 \times 2037 \times 2500$ pixels. For some parts of the image analysis, data reduction was convenient to relax the requirements for computer memory. Therefore, $2 \times 2 \times 2$ binning was applied to the 3D images, thus reducing the number of voxels by a factor of 8 without compromising information that is required for 3D image analysis.

Results: Tomographic records were taken of three limestone (L1-3) and greywacke (G1-3) samples before and after deformation which aimed at reaching 60%, 80% and 90% of the average maximum strain $\langle \epsilon_{max} \rangle$ (cf. Fig. 3.50). 3D image analysis was applied to characterize porosity $n = (\sum_j V_j)/V_s$ (the sum over all pore volumes V_j normalized by the total sample volume V_s) and pore density N (number of pores per mm^3) for each record. The results are listed in table 3.7 along with sample dimensions, strain (ϵ) and stress (σ) values. The strongest deformation was applied to the samples G3 and L3. For G3 a strong increase in total porosity is observed, which is related to the formation of a "macroscopic" crack (shown in Fig. 3.51c). For the deformed limestone samples an increase both in porosity and pore density is found, compared to the undeformed samples. This effect is particularly pronounced for sample L3. The increase of porosity in L3 is not as strong as in G3 but visual inspection of the 3D images of L2 and L3 (after deformation corresponding to 80% and 90% of $\langle \epsilon_{max} \rangle$) reveals that "small" cracks were initiated in both samples (Fig. 3.52). No change in porosity is observed

sample	dimensions [mm^3]	ϵ [%]	σ [MPa]	n_i [0.1%]	n_f [0.1%]	N_i [mm^{-3}]	N_f [mm^{-3}]
G1	$7.3 \times 7.3 \times 9.0$	2.78	34	0.25	0.18	-	3.3
G2	$7.3 \times 7.3 \times 8.9$	3.34	81	0.62	0.64	7.0	9.8
G3	$7.3 \times 7.3 \times 8.8$	3.87	79	0.32	3.61	17.0	9.5
L1	$7.3 \times 7.3 \times 6.0$	2.54	27	0.027	0.041*	3.01	4.53
L2	$7.3 \times 7.3 \times 9.2$	3.58	53	0.024	0.042*	2.57	3.81
L3	$7.3 \times 7.3 \times 9.2$	4.06	87	0.048	0.24*	7.62	46.39

Table 3.7: Porosity n calculated by means of 3D image analysis of the deformed (subscript 'f') and the undeformed (subscript 'i') samples of greywacke (G1-3) and limestone (L1-3). The pore density N in sample G1 could not be determined due to strong image noise. *After compression small pieces of the samples L1-3 had splintered off the edges and the corresponding (artificially enlarged) void spaces were excluded by applying a size filter.

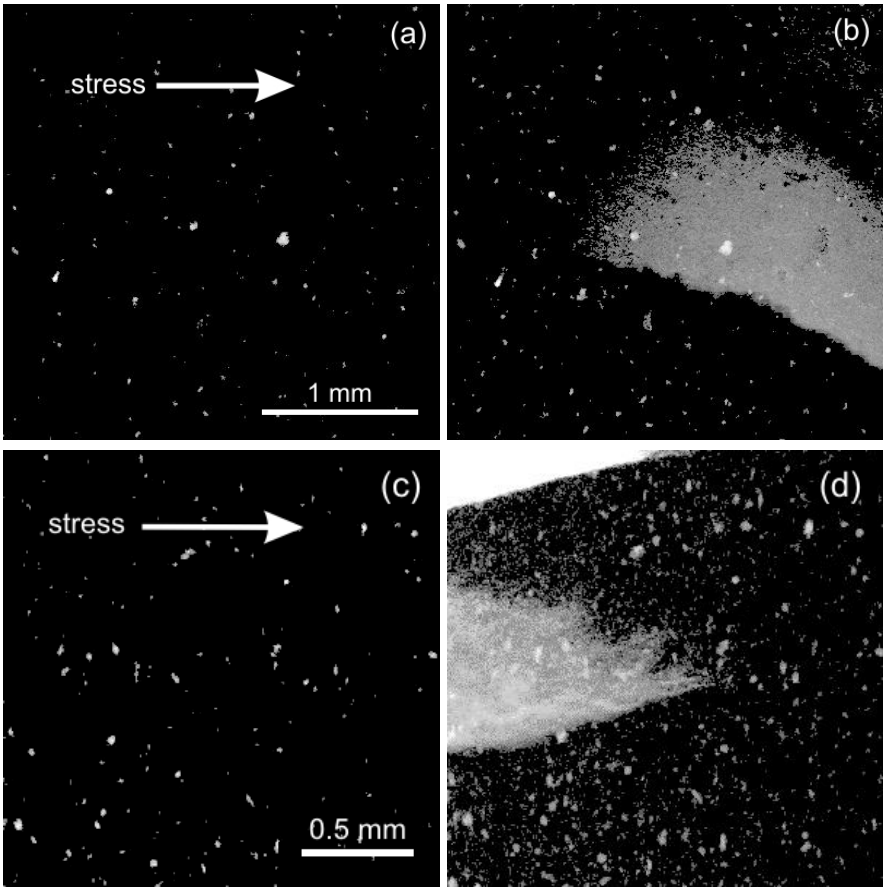

Figure 3.52: Virtual projection of pores in a small section at the bottom of the sample L2 (a) before and (b) after deformation causing the formation of a small crack. Top edge of sample L3 (c) before and (d) after deformation and cracking.

after deformation of sample G2 and a slight decrease of porosity is found after deformation of G1. Note that the image data of the undeformed sample G1 was corrupted by strong image noise and the pore density n is therefore not shown in table 3.52. Nevertheless the porosity in G1 could be estimated after filtering the smallest particles that were presumably artificial results of this noise. The uncertainty for the porosity values in the other datasets is smaller than 20%. In order to further characterize porosity and pore density the distributions of shape

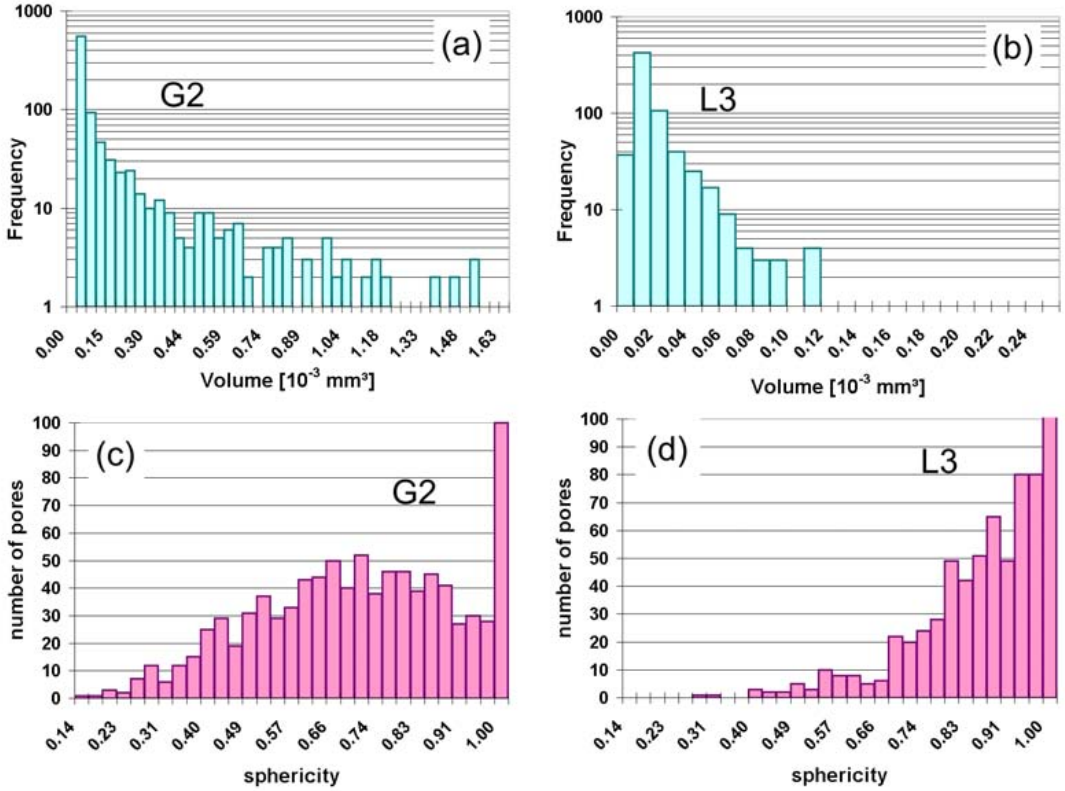

Figure 3.53: (a + b) Histograms showing the distribution of pore volume in undeformed (a) greywacke and (b) limestone. (c + d) Distributions of pore shape (sphericity) calculated for (c) greywacke and (d) limestone (a value of 1 corresponds to a spherical pore).

and size of the individual pores were calculated for each of the greywacke and the limestone samples. Fig. 3.53a-d shows histograms of pore volume and shape. The latter is characterized by the shape factor F. Obviously the pores in limestone are smaller (Fig. 3.53b and d) and appear "rounder" than those present in greywacke (Fig. 3.53a and c). Fig. 3.53d shows the number of pores to increase steadily towards $F = 1$ (value for a sphere). Comparison with high-resolution SEM pictures (Fig. 3.49c) shows that this trend towards a round shape is at least partially an artifact of the 3D analysis procedure, whereby very small objects always produce an F close to unity. In the samples G1-3 larger pores of irregular, non-spherical shape are found (Fig. 3.53c shows a peak at $F \sim 0.75$) and a significant amount of very small pores characterized by a second peak at $F = 1$. Note that the factor F is not a unique description of

the pores' shape. Therefore, these quantitative results were compared to 2D projection images of the entire porosity (e.g. Fig. 3.52). A binary image of the porosity (pores are represented by voxel values of 1 while the rest of the virtual volume is set to zero) is projected along one coordinate axis (x, y or z). Such a projection image of the porosity in sample G2 is shown in Fig. 3.54 along with an enlarged view (b) revealing a large variety of pore sizes and shapes.

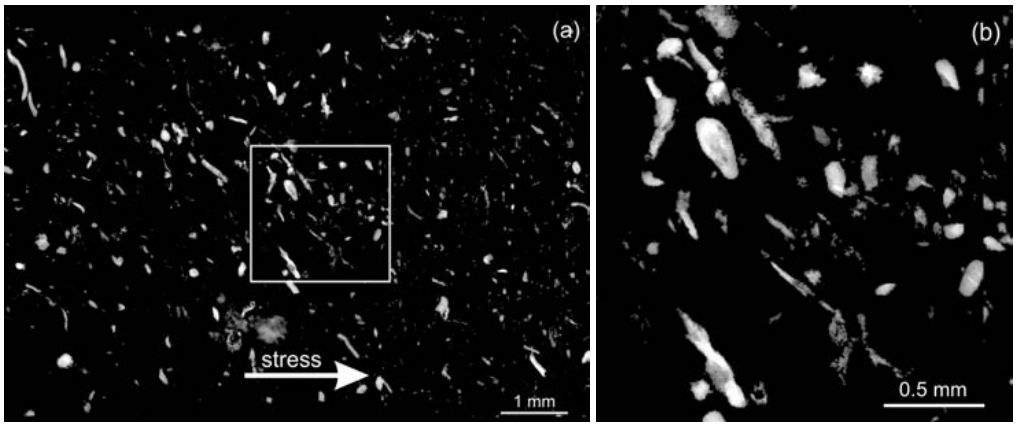

Figure 3.54: (a) Virtual projection of the pore space in the second greywacke sample. (b) The magnification reveals elongated pores that seem to follow a general orientation of the mineral. Randomly oriented oblate and angular pores are observed as well.

For the greywacke sample G3, formation of a "macroscopic" crack was observed after application of a strong deformation corresponding to 90% of the average maximum strain. Fig. 3.55a and b show a sagital slice through the G3 datasets in the initial and deformed state. Similar to the analysis of thin sections under the microscope one can index intragranular cracks (dividing mineral grains), grain-boundary cracks (following the outline of a particular mineral) and inter-granular cracks (traversing the inter-granular matrix). This concept of two-dimensional crack-classification is shown in Fig. 3.55c. Obviously the macro-crack in G3 is composed of many microcracks of well defined orientation. A sagital slice along the entire sample length, a binary image of the crack and a rose-diagram calculated from the orientation of these microcracks are shown in Fig. 3.56. To calculate Fig. 3.56c, the binary image of the crack (b) is manually segmented into small straight sections. For the latter the orientation angle α with respect to the direction of applied stress (vertical image axis) is calculated. The rose-diagram is a circular histographical plot of α, whereby the radius of the black bars corresponds to frequency. Although the complete crack is tilted by $\approx 10°$ with respect to the direction of maximum compression, the orientation of individual tensile cracks with this direction is quasi-parallel. On the other hand, orientation of the shear cracks (labeled "wing cracks" in Fig. 3.55c) which are inter-connecting the tensile cracks ranges from $20°$ to $40°$.

In addition to this 2D "section-analysis" the three-dimensional nature of the data allows for a volumetric analysis of the crack. In order to quantify its shape, total size and orientation, the macro-crack is binarized and separated from the smaller isolated pores in the sample volume. This procedure requires a special type of binarization based on a region growth algorithm and

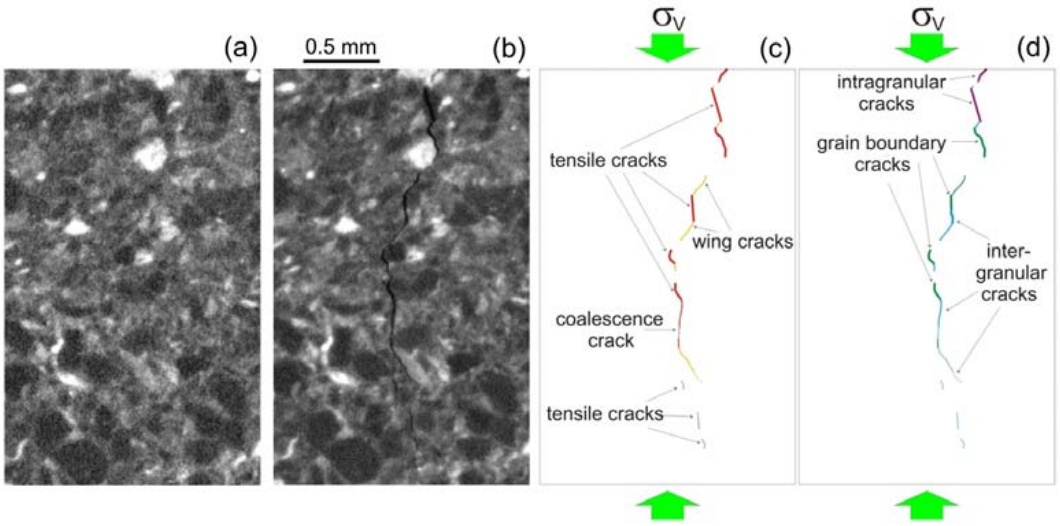

Figure 3.55: Sagital slice through the 3D data (a) before and (B) after deformation /formation of a macro-crack in sample G3. (c) The macro-crack is decomposed into tensile cracks, parallel to the deformation, oblique wing-cracks and coalescence cracks. (d) These microcracks either run through (intra-granular), alongside (grain-boundary) or between (inter-granular) individual mineral grains.

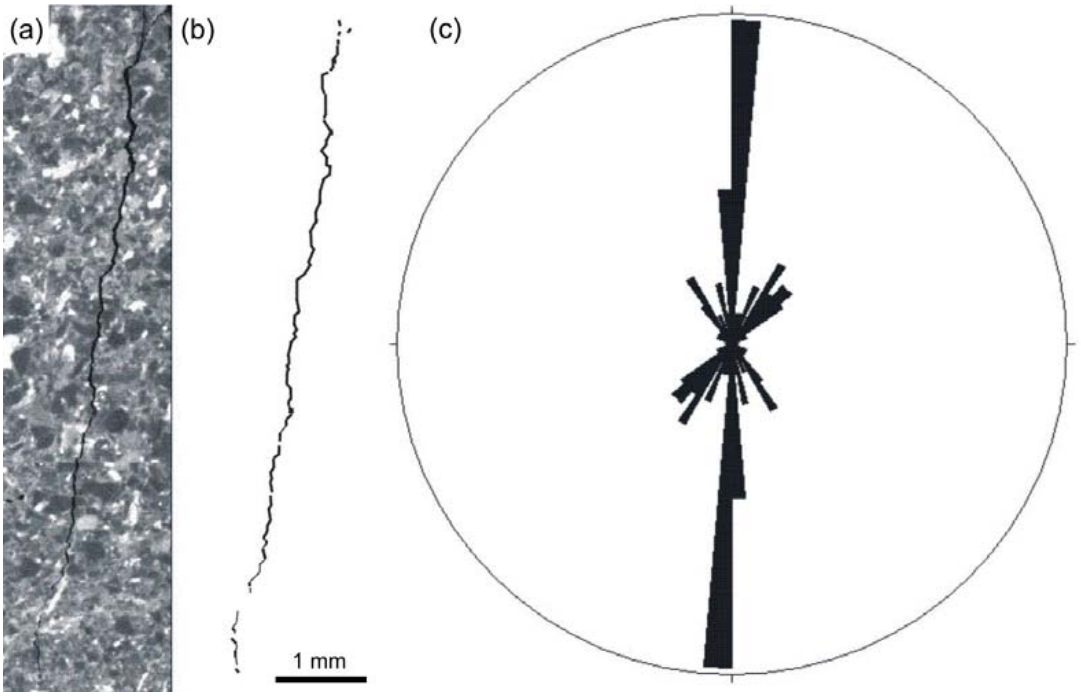

Figure 3.56: 2D orientation analysis of the macro-crack in sample G3. (a) Sagital slice (perpendicularly to the crack plane and parallel to the crack propagation) showing the complete crack. (b) Binary image of the crack. (c) Rose diagram of crack orientation.

the application of a size filter that grants survival only to the largest objects in the sub-volume

containing the crack. Counting the remaining voxels yields a crack volume of $0.15\,\mathrm{mm}^3$. Fig. 3.57a shows a plane that is fitted to the crack. The normal vector of this crack-plane coincides with the minor axis of inertia of the crack (for details see section 2.2). The crack-"topography" (normal crack-to-plane distance) is shown in Fig. 3.57b.

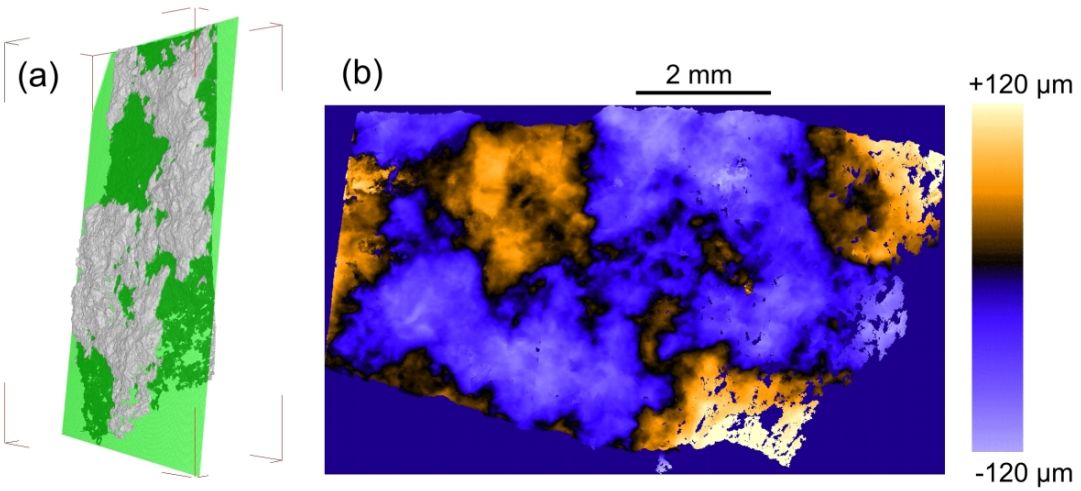

Figure 3.57: (a) The quasi-planar macro-crack is projected onto the plane perpendicular to its major orientation axis. (b) A "topography" view is calculated from the distance of each voxel (belonging to the crack) normal to the plane (red: above, green: below the plane). For points where more than one crack voxel is found normal to the crack plane, (b) shows the average distance.

The standard deviation of the crack-to-plane distance equals $\pm\ 52\,\mu\mathrm{m}$ and can be compared to the length ($\sim 8.6\,\mathrm{mm}$) along the direction of crack-propagation) and width ($\sim 5.0\,\mathrm{mm}$) of the crack, stating that it is quasi-planar on a macroscopic scale. In order to visualize the local thickness of the crack, the crack voxels lying on given a line perpendicular to the crack plane are counted, and this is repeated for the entire crack area. The resulting thickness-projection onto the crack-plane is depicted in Fig. 3.58a. The macro-crack shows a wedge-shaped thickness profile along the direction of maximum compression with a opening of $\sim 100\,\mu\mathrm{m}$ at the top and $\sim 7\,\mu\mathrm{m}$ at the bottom. Small microcracks probably extend further into the sample but are not detected due to the limited resolution of the imaging system. Figure 3.58a contains few image artifacts ("bright clouds", marked by arrows) caused by low density mineral grains that were partially connected to the crack and can thus not be fully separated from the latter by the binarization algorithm.

In order to analyze the mineral constituents in the area of crack propagation, the records of the sample G3 before and after were combined. The two datasets were spatially aligned in the Euclidean coordinate system, and a box is cropped around the matching regions where the crack formed during deformation. Masking this region in the undeformed sample with the binary image of the crack in the deformed sample yields a three-dimensional volume showing the mineral structure previous to fracturing. Projecting this data along lines perpendicular to

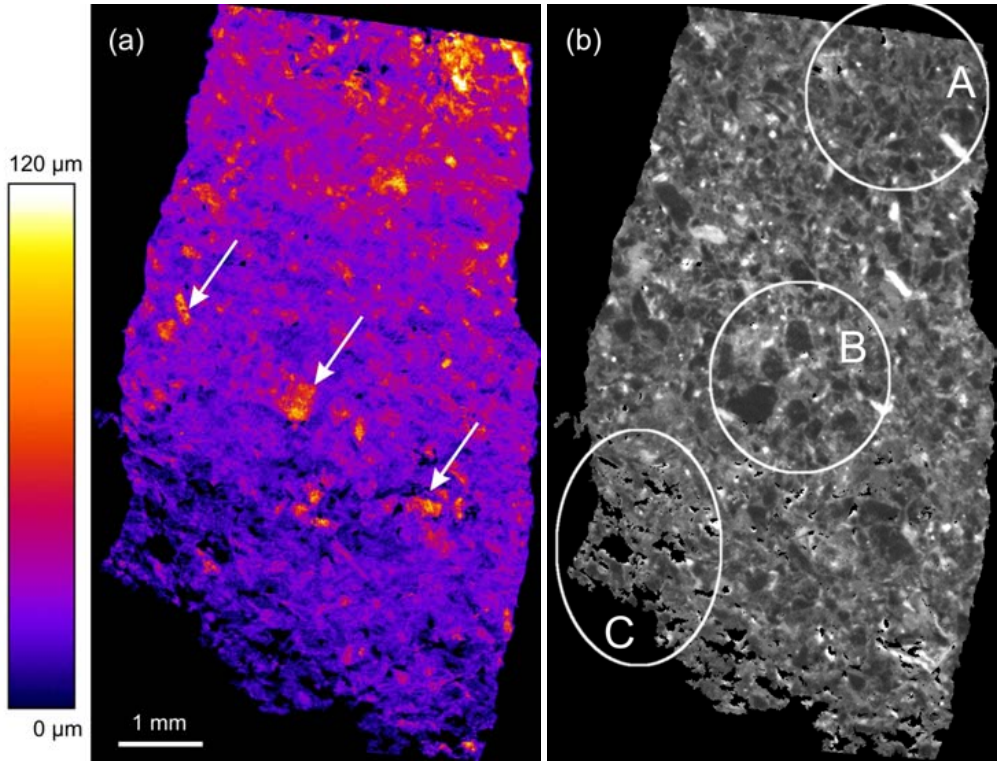

Figure 3.58: (a) The thickness of the crack is projected onto the crack-plane. Some artifacts appear (white arrows) due to mineral particles of low density (dark appearance in (b)) that are artificially counted as pores. (b) The projected map of the G3 microstructure in its undeformed state masked by the binary crack image of the matching structure after deformation and normalized by the crack thickness (A: region of intra-granular cracks, B: inter-granular cracks and C: grains that appear to be spared by the fracture).

the crack plane and normalizing the resulting image by division with the crack thickness (Fig. 3.58a), a map of the mineral constituents that were traversed by the crack is obtained (Fig. 3.58b). Dense feldspars (bright) and less dense quartz (dark) indicate where intra-granular- and/or grain-boundary cracks have developed. In the center of Fig. 3.58b large quartz grains of low density (marked "A" in Fig. 3.58b) were apparently split by microcracks while in other regions (B) the density of inter-granular cracks is higher (appearing more or less homogeneous in gray). The crack tip (lower part of Fig. 3.58b) features mostly inter-granular microcracks whereas larger grains have been spared by the fracture (C).

The analysis is completed by calculating projections of the total porosity, similar to Fig. 3.54 before and after formation of the macro-crack in the sample G3 (Fig. 3.59a and b). In the limestone samples L2 and L3 somewhat smaller cracks formed after compression on the top and bottom sample edges respectively (cf. Fig. 3.52a and b). The crack in L2 is approx. $2.0\,\mathrm{mm} \times 1.0\,\mathrm{mm}$ in size and shows a very ragged shape except where it runs along the cylinder surface. The topography is quasi-planar and tilted by approx. $8°$ with respect to the direction of maximum compression. The crack in sample L3 is even smaller (approx. $1.2\,\mathrm{mm} \times 0.6\,\mathrm{mm}$) with

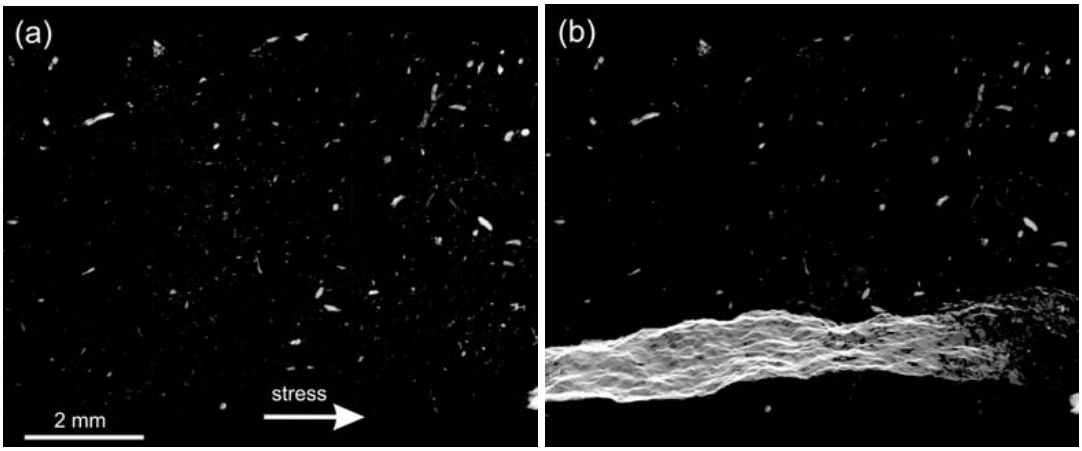

Figure 3.59: Virtual projection of the pores in the third greywacke sample before (a) and after (b) uniaxial compression causing formation of a macroscopic crack. It can be seen from (b) that crack formation and propagation occurred independently of the pre-existing porosity distribution in the sample.

a similar orientation. These cracks were too small to allow their decomposition into tensile and wing cracks. Larger fragments had splintered off the cylinder edges after deformation of all three limestone samples.

Discussion: The fine homogeneous microstructure of limestone and the strongly inhomogeneous arrangement of various mineral grains in greywacke leads to a different behavior of these two materials under stress. The 3D characterization of a macro-crack in sample G3 and observations of smaller cracks forming in the limestone samples L2 and L3 are in good agreement with the common theories of crack nucleation and propagation where it is assumed that cracks nucleate at micro-flaws which are randomly distributed in the material. Such flaws could be pores, weak mineral phases, microcracks and/or grain boundaries.
The striking correspondence of the macroscopic crack in the deformed sample G3 and numerous dense iron-oxide-filled spaces (associated with old "healed" cracks) proves that the bulk material has a preferred orientation for cracking. Both the old healed and the new crack appear almost parallel although on opposite sides of the sample cylinder. The total angle of crack orientation ($\sim 10°$) results from quasi-parallel tensile that are inter-connected via oblique wing cracks. At the tip of the macro-crack individual tensile microcracks are observed (Fig. 3.55 and 3.59b). From the 2D slice in Fig. 3.55 a kinematic sequence can be interpolated whereby crack propagation and growth occurs via mode I tensile and mode II shear cracks.
In fracture mechanic penny-shaped microcracks are most commonly used to model flaws in brittle materials [Ger94, Dys03, Ada78, Can90]. Observation from the undeformed greywacke samples revealed pores of various shapes and sizes that do not correlate with crack propagation in G3. The kinks in the stress-strain curves from the fracture tests on greywacke and limestone (cf. Fig. 3.51) indicate furthermore that spontaneous cracking is more probable for samples

of such small dimensions than the quasi-continuous built-up of a macro-crack. In fracture mechanics a process zone of circular spread (when extrapolated from 2D sections [Atk87]) is associated with the non-linear propgation of crack tips. As can be seen in Fig. 3.57, 3.58 and 3.59b coalesced or isolated microcracks are directly located in the plane and at the tip of the propagating crack. Fig. 3.59 shows the crack in G3 to form in an area of particularly low porosity. However this statement must be restricted to pores of $10\,\mu\mathrm{m}$ size or larger, whereas smaller pores could indeed contribute to the cracking (e.g. numerous micron-sized pores were observed in SEM images of the grain boundaries in greywacke and limestone). Propagation of the crack supposedly occurs along grain boundaries, mineral cleavage planes and the fine intergranular matrix in greywacke. An image of the undeformed microstructure that was traversed by the crack does not appear much different from an arbitrary cross-section through the material. Attention must be paid to the parts of the crack that coincide with the boundary between two grains of different mineral constituents: In these places Fig. 3.58b probably shows ambiguous information. "Opening" of the crack is observed at the front tip of propagation that is presumably formed by tensile cracks which are inter-connected via wing cracks that are too thin to be detected by the imaging system.

Statistical analysis of the porosity in the sample G2 and L2 showed pores of various sizes and shapes in greywacke and small round pores in limestone. Electron microscopy revealed the latter to be part of a larger network of intergranular porosity which is not imaged due to the limited spatial resolution of the X-ray detector system. It is important to note that values for the total porosity in these materials, which are found in literature and are measured by other methods (e.g. mercury intrusion or scanning electron microscopy) indicate a larger porosity than what is calculated from the tomographic data. A reasonable explanation for this discrepancy is that an important part of the pores is smaller than the resolving power of the system, i.e. $\leq 10\,\mu\mathrm{m}$ in size. In addition very large pores (mm- or even cm-sized) were excluded by cutting the sample cylinders out of homogeneous and compact regions in the rock.

Compared to greywacke the formation of cracks in limestone supposedly takes place on a smaller scale (see Fig. 3.52) in accordance with the very fine-grained microstructure that characterize this material. A systematic increase in the limestone porosity is observed after compression and from these observations one could hypothesize that the deformation energy applied to limestone yields the formation of new micropores preceding the formation of larger cracks, while stress applied to greywacke is likely to build up without the appearance of new micropores and fracture occurs in the form of a large macro-crack. The tomography data shows that the typical multi-columnar fracture of the limestone samples starts at the cylinder edges with mm-sized cracks preceding the breaking of small splinters. According to Germanovich et al. [Ger94] a low concentration of micro-flaws causes splitting (columnar fracture). High concentration of simultaneously growing microcracks results in initiation of new, growing cracks localized in a narrow band inclined to the direction of maximum compression, causing oblique (shear) rock fracture. The macro-crack observed in G3 coincides very well with this description. The 3D-model of Healy et al. [Hea06] indicates that shear fractures in brittle rock

form through the interaction and coalescence of many sub-parallel tensile microcracks. The authors considered the elastic stress field around finite oblate spheroids which will promote en echelon tensile 3D interactions with neighboring cracks under an maximum angle of 26°. The rose diagram in Fig. 3.56c reveals that shear cracks in G3 inter-connect tensile cracks and are orientated $\approx 20°$ to $40°$ with respect to the latter. Although these findings agree remarkably well with the literature, these values exceed the limits predicted by Healy et al. In their model they used a different material assuming interacting tensile cracks of fixed location and shape. Crack nucleation and propagation are neglected which provides a possible explanation for the difference between the experimental data and their model.

3.3.2 Cracking - Fresnel-propagated CT

For the study reported in the previous subsection, dealing with cracking in natural greywacke and limestone, absorption μCT was applied yielding a relatively poor resolution of $R \approx 12\,\mu\mathrm{m}$. A spatial correlation between (initial) porosity in the unloaded state and cracks developing during mechanical compression was missing. Nevertheless evidence was found that there exists a preferred orientation for crack-propagation in the greywacke as could be seen from the new and the old *healed* cracks. Yet, significant microstructural details (as seen in SEM images) could not be resolved by the method: e.g. intergranular porosity and grain boundaries. Fresnel-propagated X-ray imaging was therefore applied to improve the signal-to-noise ratio (SNR) and to visualize pores and grains that were not visible in 3D images of $\mu(x, y, z)$. Fig. 3.60 shows twice the same reconstructed axial slice of greywacke: An absorption tomogram recorded at $d \approx 10\,\mathrm{mm}$ sample-detector distance and the same slice reconstructed from Fresnel-propagted images ($d \approx 1.12\,\mathrm{m}$).

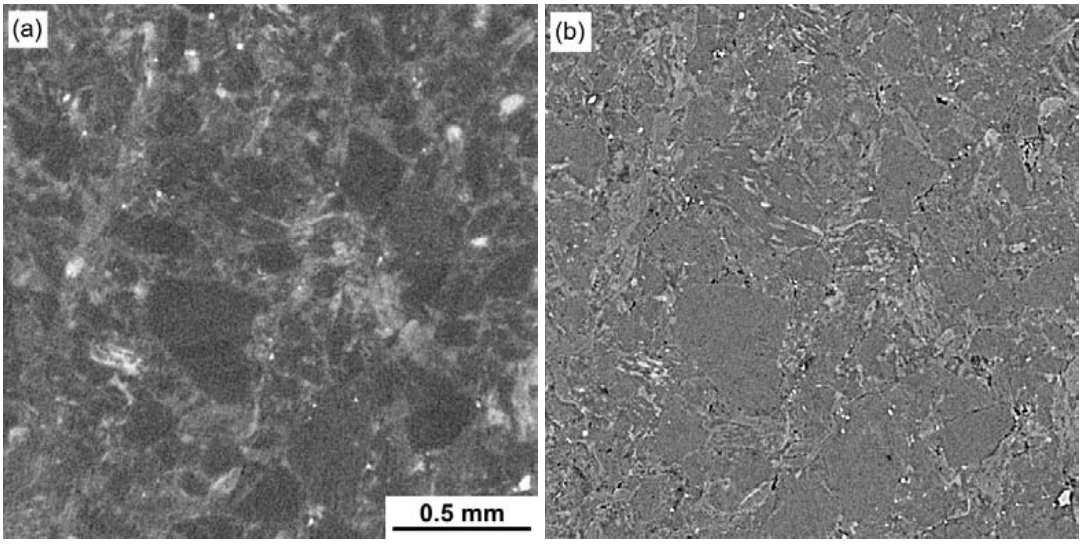

Figure 3.60: Details in μCT images recorded at different propagation distances: (a) absorption regime $d = 10\,\mathrm{mm}$, (b) $d = 1.12\,\mathrm{m}$ ($E = 33\,\mathrm{keV}$, $\Delta x = 3.6\,\mathrm{microm}$).

Both datasets were recorded with the X-ray macroscope ($\Delta x \approx 3.6\,\mu\mathrm{m}$ effective pixel size and $R \approx 6-8\,\mu\mathrm{m}$ resolution, using a $22\,\mathrm{microm}$ thin CWO scintillator) at $E = 33\,\mathrm{keV}$ energy. The SNR of the absorption data is rather poor. Although the angular grains of Feldspar can be distinguished from the fine clay-like matrix no intergranular porosity is detected in Fig. 3.60a. When Fresnel-propagation is applied the visibility of micron-sized details in the intergranular region is improved significantly. Particularly in the intergranular region numerous features (appearing either dark or bright in Fig. 3.60b) are revealed due to edge-enhancement at the material interfaces. Comparison with SEM pictures indicate that the bright features are small inclusions of ore minerals, whereas the dark features in Fig. 3.60b coincide with micropores. Simulations (see section 3.2.1) have shown that Fresnel-propagated images of micropores appear enhanced and magnified with increasing propagation distance due to formation and spreading of the appropriate interference fringes. For mechanical reasons the sample cylinders had to be of $6-7\,\mathrm{mm}$ in diameter at least. The full length of the z detector-translation was therefore used to produce a significant phase contrast effect in the recorded radiographs. Additionally the SNR and hence the material contrast is highly improved when Fresnel-propagated hard X-ray images are recorded for this type of material (i.e. $\delta >> \beta$).
During beamtime at BESSY/BAM*line* , tomograms of different types of rock were recorded in phase contrast mode, before and after the samples experienced increasing successive mechanical load. Similar to the work described in the previous subsection, unconfined uniaxial compression experiments were carried out after each tomography scan on an universal testing machine. Cylindrical samples were prepared from three important types of rock: a) Granite as a typical intrusive, felsic, igneous rock; b) Basalt as an extrusive volcanic rock and c) Greywacke which is a texturally-immature sedimentary rock.

Preliminary studies: Repeated fracture tests as well as a detailed petrographic analysis of the rocks preceded the synchrotron experiment. Fig. 3.61 shows a polished thin section of granite in transmitted light (a) and between *crossed Nichols* (b, the polarizer is perpendicular to the analyzer). Granite is mainly composed of quartz (SiO_2, "Q" in Fig. 3.61a, density $\rho = 2.65\,\mathrm{g/cm^3}$) with grains of feldspar ($\rho \approx 2.5-2.8\,\mathrm{g/cm^3}$) and mica ($\rho \approx 2.7-3.3\,\mathrm{g/cm^3}$) embedded into the matrix. Feldspars are prone to weather and can be easily distinguished from the quartz due to their high degree of corrosion. There are three main types of feldspar ("F" in Fig. 3.61a) which are expressed in terms of their endmembers: $NaAlSi_3O_8$ (albite), $KAlSi_3O_8$ (K-feldspar, e.g. a microline (M) is seen in Fig. 3.61b) or $CaAl_2Si_2O_8$ (anorthite). Solid solutions between K-feldspar and albite are called alkali feldspar whereas solutions between albite and anorthite are called plagioclase (only limited solid solution occurrs between K-feldspar and anorthite). The micas found in this particular granite were mostly biotites (marked "B" in Fig. 3.61a) with the approximate chemical formula $K[Mg,Fe]_3AlSi_3O_{10}[F,OH]_2$. Dense opaque inclusions were observed in some biotites: These are probably zircons ($ZrSiO_4$, $\rho \approx 3.9-4.2\,\mathrm{g/cm^3}$) which are commonly found in igneous rocks as primary crystallization products.

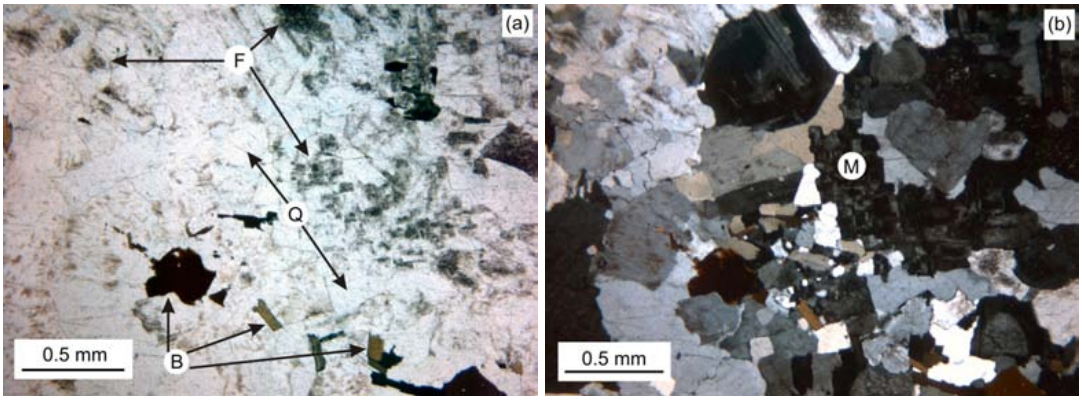

Figure 3.61: Light microscopy of a thin section of granite: (a) transmitted light (F: feldspar, Q: quartz, B: biotide (common mica)), (b) crossed Nichols (M: microline).

Table 3.8 lists the sample dimensions, compressive stress σ_c (values were normalized to compensate for different height-to-diameter ratios) and strain ϵ measured from repeated loading and single fracture tests on granite (labeled "T"). From the cyclic compression tests (whereby

sample	diameter [mm]	height [mm]	σ_c [MPa]	ϵ [%]	event
T1*	6.86	10.17	43.22	2.47	-
T1*	6.86	10.17	50.82	2.89	-
T1*	6.86	10.17	56.05	2.82	-
T1*	6.86	10.17	67.58	3.46	-
T1*	6.86	10.17	81.72	3.96	fracture
T3	6.96	10.16	67.32	4.34	fracture
T4	7.05	9.48	58.17	3.26	fracture
T5	7.14	9.40	49.61	3.04	-
T5	7.14	9.40	55.02	3.12	-
T5	7.14	9.40	58.78	3.23	-
T5	7.14	9.40	90.52	4.47	fracture
T6	6.96	9.86	63.90	4.51	fracture
T7	7.31	9.50	39.95	3.64	fracture
T8	7.05	9.75	41.60	3.54	fracture

Table 3.8: Compression tests on cylindric samples of granite. To the samples T1 and T5 increasing load was applied repeatedly whereas T3, T4, T6, T7 and T8 were single compression tests. *) Tomographic datasets were acquired during compression experiments on T1 during beamtime at BESSY/BAM*line* in January 2006.

increasing load was applied repeatedly until fracture occurred) revealed an average strength of $\langle\sigma_{cyclic}\rangle = 86.12 \pm 4.4\,\mathrm{MPa}$ and an average strain at fracture of $\langle\epsilon_{cyclic}\rangle = 4.22 \pm 0.25\%$. Slighly lower values were found for the single fracture tests: $\langle\sigma_{single}\rangle = 54.2 \pm 11.4\,\mathrm{MPa}$

and $\langle \epsilon_{single} \rangle = 3.86 \pm 0.48\%$. The sample T1 was used for the BESSY experiment in January 2006 (results shown later on).

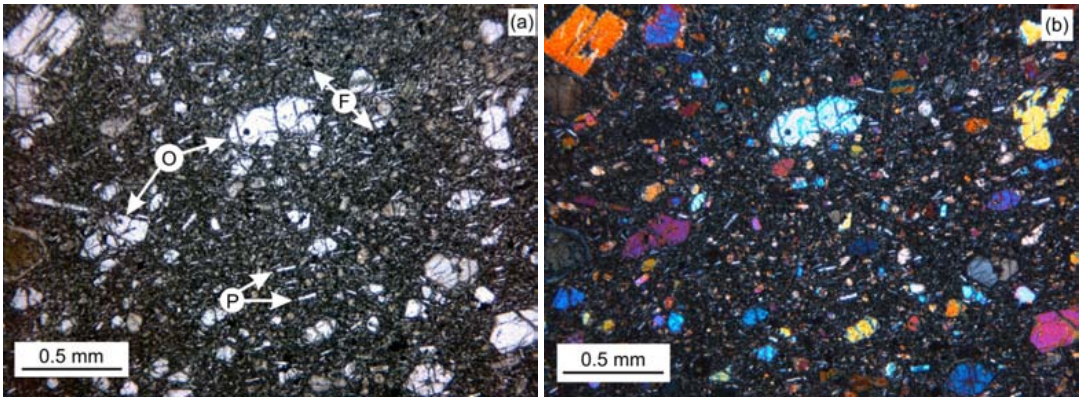

Figure 3.62: Light microscopy of thin sections of basalt: (a) shining-through light (O: olivine, P: plagioclase, F: ore minerals containing iron), (b) crossed Nichols.

Light microscopy images of a thin section of basalt are shown in Fig. 3.62. The largest grains in this particular basalt are olivines ("O" in Fig. 3.62a) with the chemical formula [Mg,Fe]$_2$SiO$_4$ and density $\rho \approx 3.27 - 3.37\,\mathrm{g/cm^3}$. Olivines with a Mg-endmember are called forsterite while those with a Fe-endmember are called fayalite. Obviously these minerals are prone to anisotropic corrosion processes which gives rise their *ripped* shape which is seen in Fig. 3.62. Small band-shaped grains of plagioclase (albite and anorthite) are marked "P" in Fig. 3.62a. Small opaque grains of dense ore minerals, probably magnetite (Fe$_3$O$_4$, $\rho \approx 5.18\,\mathrm{g/cm^3}$) and/or ilmenite (FeTiO$_3$, $\rho \approx 4.5 - 5.0\,\mathrm{g/cm^3}$), were observed under the microscope as well as in the X-ray images. A detailed EDX (energy dispersive X-ray analysis) further revealed the presence of pyroxenes (silicate minerals) of high calcium content in the basalt. Fig. 3.63 shows a backscattered electron SEM image of the basalt (a) as well as a EDX map of the same region (b). The ore minerals (bright signal in the backscattered electron image) were thus identified as ilmenite due to their high content in titanium and iron. K-feldspar was found in the matrix surrounding the angular plagioclase grains. All these findings are in full agreement with the mineral constituents commonly observed in igneous rocks like basalt. Table 3.9 lists the sample dimensions, compressive stress σ_c and strain ϵ, measured from repeated loading and single fracture tests on basalt (labeled "B"). The cyclic compression tests revealed an average strength of $\langle \sigma_{cyclic} \rangle = 299 \pm 117\,\mathrm{MPa}$ and an average strain at fracture of $\langle \epsilon_{cyclic} \rangle = 8.2 \pm 2.4\ \%$. The strong scattering of the average values is due to sample B4 which was used for the BESSY experiment in August 2006 and which broke much *earlier* than the samples B3 and B5 when increasing repeated load was applied. Similar to granite, lower average values were found for the single fracture tests: $\langle \sigma_{single} \rangle = 200 \pm 35\,\mathrm{MPa}$ and $\langle \epsilon_{single} \rangle = 6.55 \pm 0.26\%$.

A microscopy image of greywacke in shining-through light was already shown in Fig. 3.49c and Fig. 3.64a indicates the mineral constituent in the same image but taken between crossed

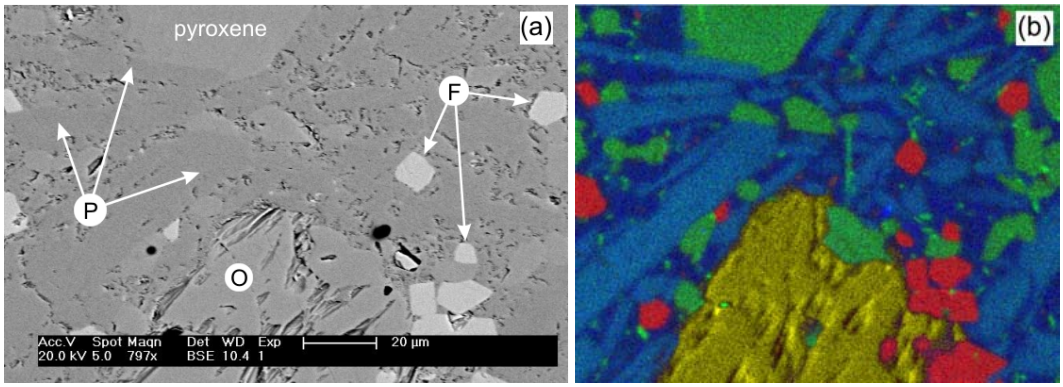

Figure 3.63: Scanning electron microscopy on basalt: (a) backscattered electron image (O: olivine, P: plagioclase, F: ore minerals containing iron), (b) EDX map with the majority elements in colors (red: Ti and Fe (ilmenite), green: Ca, Si (pyroxene), dark blue: Al, Si, K (K-feldspar), bright blue: Al, Si, Ca (anorthite), yellow: Mg, Fe, Si (olivine)).

sample	diameter [mm]	height [mm]	σ_c [MPa]	ϵ [%]	event
B1	6.68	9.90	164.64	6.29	fracture
B3	6.86	9.45	267.88	8.43	-
B3	6.86	9.45	303.65	8.78	-
B3	6.86	9.45	341.70	9.60	-
B3	6.86	9.45	357.93	9.94	fracture
B4*	6.00	9.85	78.94	3.39	-
B4*	6.00	9.85	75.15	3.13	crack
B4*	6.00	9.85	135.81	4.88	fracture
B5	5.97	8.88	163.98	5.27	-
B5	5.97	8.88	194.35	5.90	-
B5	5.97	8.88	213.58	6.25	-
B5	5.97	8.88	402.19	9.86	fracture
B6	6.18	8.89	234.50	6.81	fracture

Table 3.9: Compression tests on cylindric samples of basalt. To the samples B3, B4 and B5 increasing load was applied repeatedly whereas B1 and B6 were single compression tests. *) Tomographic datasets were acquired during compression experiments on B4 during beamtime at BESSY/BAM*line* in August 2006. The second loading cycle was interrupted after hearing the sample *crack*.

Nichols. The different mineral constituents were identified by EDX analysis as shown in Fig. 3.64b along with the corresponding backscattered electron image (c). The fine compact matrix of this sedimentary rock contains a great variety of minerals. Among these the most prominent are mono- (Q) and polycrystalline (P) grains of quartz, biotites (B) as well as fragments of magmatic (M) and sedimentary (S) rock. Samples were cut from the same bulk material

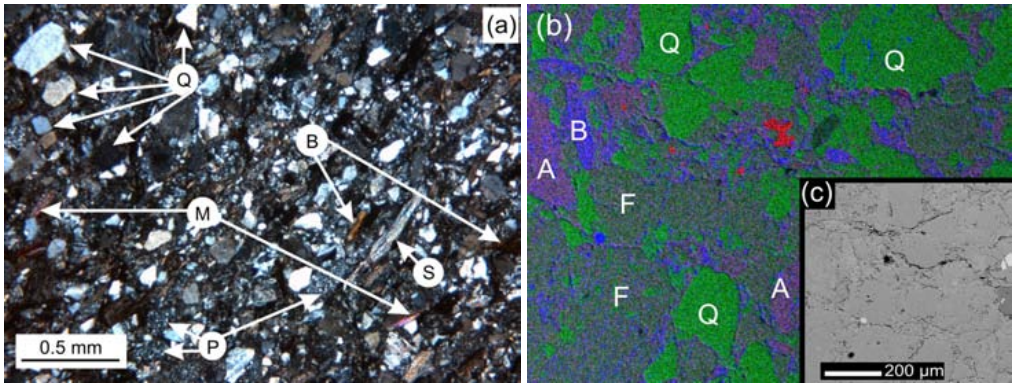

Figure 3.64: (a) Light microscopy image between crossed Nichols (Q: monocrystalline quartz, P: polycrystalline quartz, B: biotite, M: fragments of magmatic rock, S: sedimentary rock). (b) EDX analysis reveals Q: quartz (green Si), B: biotite (blue Fe) and plagioclase A: albite (green Si, magenta Al) and F: anorthite. Some Ca-precipitates are depicted in red. The inset (c) shows the corresponding backscattered electron image.

as those reported in the previous section. *Healed* cracks filled with ore minerals (probably magnetite) were commonly observed in thin sections perpendicular to the loading direction. The EDX map shows iron content in biotite as well as in intergranular spaces between grains of quartz and plagioclase (A and F in Fig. 3.64b). This particular lithic greywacke of the Carboniferous period (≈ 360 million years ago) was extracted near Waldeck (Germany).
Table 3.10 lists the sample dimensions, compressive stress σ_c and strain ϵ, measured from repeated loading and single fracture tests on greywacke (labeled "G"). The cyclic compression tests revealed an average strength of $\langle \sigma_{cyclic} \rangle = 62 \pm 22\,\mathrm{MPa}$ and an average strain at fracture of $\langle \epsilon_{cyclic} \rangle = 2.67 \pm 0.34\%$. As expected, lower average values were found for the single fracture tests: $\langle \sigma_{single} \rangle = 48 \pm 9\,\mathrm{MPa}$ and $\langle \epsilon_{single} \rangle = 2.75 \pm 0.34\%$. Note there is a discrepancy between the latter and the fracture tests on greywacke that were reported in the previous section ($\langle \sigma_{single} \rangle = 59 \pm 15\,\mathrm{MPa}$ and $\langle \epsilon_{single} \rangle = 4.23 \pm 0.24\%$) where the average strain at fracture was much higher. This effect is probably related to the top and bottom surface of the test cylinders which was roughly cut for the *old* tests but properly polished for the new tests.

Results from Fresnel-propagated tomography on greywacke: Two cylindrical samples of greywacke, "G2" and "G3" (see table 3.10), were deformed repeatedly reaching 86% and 97% of the average maximum strain at fracture $\langle \epsilon_{cyclic} \rangle$ respectively. Tomographic scans of the samples were acquired before and after each loading cycle. Fig. 3.65 shows the stress-strain curves for the two experiments (the numbers $1, 2, \ldots$ indicate the loading cycle). Sample G2 was used for experiments in January 2006 ($E = 33\,\mathrm{keV}$ and $\Delta x = 3.6\,\mathrm{microm}$). Increasing load was applied twice until the rock fractured during the third deformation. One oblique crack developed during the first and grew during the second compression. Fig. 3.66 shows a thickness projection of the pore space belonging to this crack after the first two load cycles. The connected porosity of the crack was found by *region-growth* threshold binarization [Kir04]

sample	diameter [mm]	height [mm]	σ_c [MPa]	ϵ [%]	event
G2*	5.75	9.70	40.96	2.13	-
G2*	5.75	9.70	47.41	2.30	-
G2*	5.75	9.70	49.30	2.30	fracture
G3**	5.50	9.65	39.74	2.92	-
G3**	5.50	9.65	44.70	2.59	fracture
G4	5.64	9.72	63.07	2.66	fracture
G5	5.86	9.77	42.87	2.67	fracture
G6	5.86	9.31	42.07	2.37	fracture
G7	5.41	9.65	33.87	2.21	-
G7	5.41	9.65	39.87	2.08	-
G7	5.41	9.65	45.02	2.23	-
G7	5.41	9.65	55.73	2.57	fracture
G8	5.53	9.41	39.68	1.82	-
G8	5.53	9.41	44.13	1.81	-
G8	5.53	9.41	51.93	1.99	-
G8	5.53	9.41	98.39	3.24	fracture
G9	5.53	9.12	43.20	3.29	fracture

Table 3.10: Compression tests on cylindric samples of greywacke. To the samples G2, G3, G7 and G8 increasing load was applied repeatedly whereas G4, G5, G6 and G9 were single compression tests. *) sample G2 was used for experiments in January 2006, **) sample G3 in August 2006.

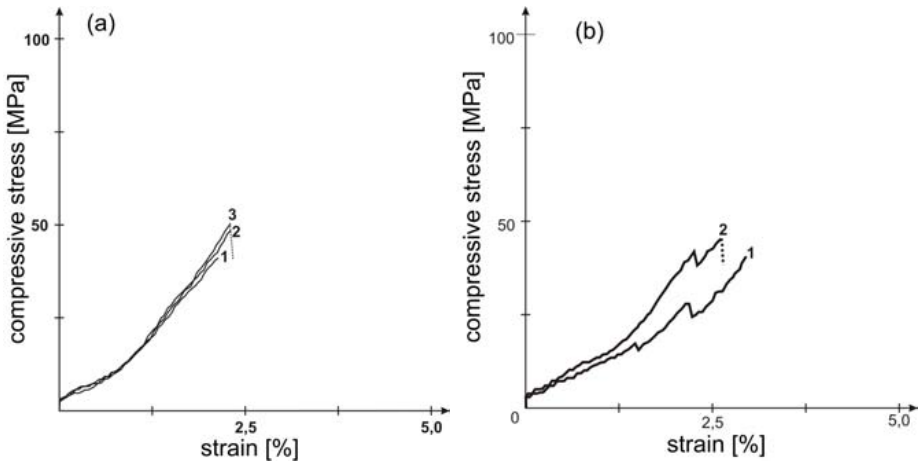

Figure 3.65: Stress-strain diagrams recorded for cyclic deformation during experiments at BESSY/BAM*line* : (a) sample G2 broke during the third, (b) sample G3 during the second loading cycle (stress release due to fracture is indicated by a dashed line).

followed by size-filtering of the smaller pores that do not belong to the main crack. Orienta-

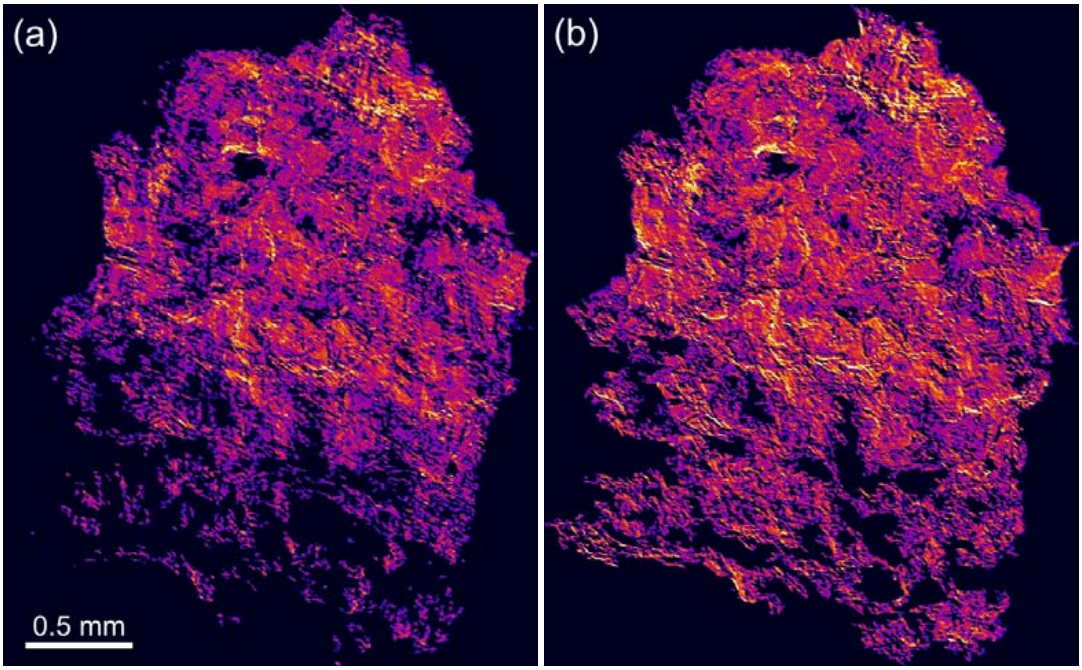

Figure 3.66: Thickness projection of the porosity belonging to the crack which formed during compression of G2. (a) Crack after the first and (b) after the second load cycle.

tion of the crack with respect to the direction of load (vertical axis), i.e. the *crack-plane*, was found by calculating the eigenvalues and vectors of the corresponding inertia ellipsoid (for a detailed explanation of this method see section 2.2). Fig. 3.66 was obtained by projecting the binary crack volume onto the plane normal to the major inertia axis. Unlike the absorption tomography study, the Fresnel-propagated 3D images clearly show the large crack to build up by coalescence of small microcracks (ca. $10 \times 20\ \mu m^2$ in size) which form a network at the crack tip and appear elongated in the direction perpendicular to crack propagation. The porosity in the unloaded sample (without application of a size filter) when projected onto the crack-plane as well as the topography (average distance of each *crack voxel* normal to the crack-plane) of the crack in its final stage are shown in Fig. 3.67

In order to analyze the porosity in the initial microstructure the volume representing the latter was masked with the binary crack volume obtained from the rock after application of the second load. Although the datasets were approximately matched by x-, y- and z translations, a finite tilt/deformation of the loaded rock with respect to the unloaded rock required expansion of the binary mask by $\pm\ 75\,\mu\mathrm{m}$ in order to map the entire space where the crack formed. The same mask was applied to an arbitrary region inside the unloaded sample, revealing that the crack formed in a region of particularly low porosity. This fact, although in agreement with findings from absorption μCT, is somewhat surprising because one would expect the crack to propagate along the pre-existing pores in the material. Even with the highly improved visibility of micron-sized pores in the phase-contrast data, the contrary appears to be the case.

The sample G3 was investigated during beamtime in August 2006. Unfortunately only one

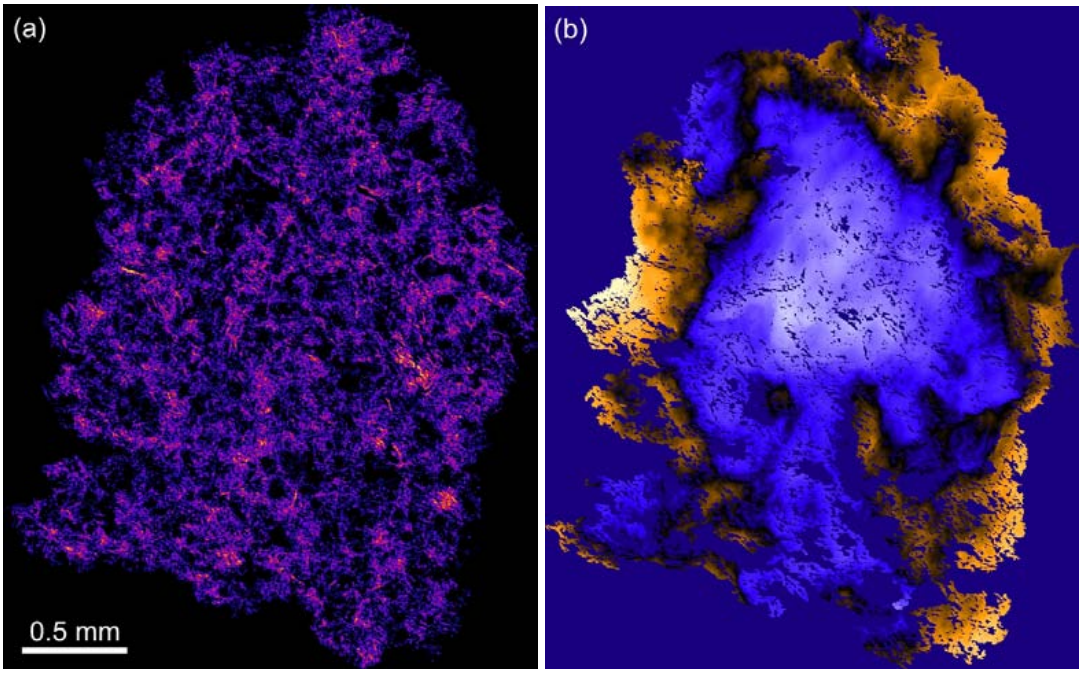

Figure 3.67: (a) Initial porosity in greywacke prior to the application of mechanical load (Color range from 0 to $40\,\mathrm{microm}$ projected pore thickness). (b) Topography of the crack in its final state (after second loading, color range from $-216\,\mu\mathrm{m}$ to $+252\,\mu\mathrm{m}$).

loaded state was recorded because the sample already broke during the second compression. Projected crack thickness and crack topography are depicted in Fig. 3.68. There are discontinuities the crack topography seen in the upper part of Fig. 3.68c. Bifurcation of the crack occurred on the top surface of the cylinder and parts of the sample splintered off during the loading. Consequently crack thickness is artificially increased in these regions (cf. Fig. 3.68a) and the exact distance to the crack-plane cannot be determined unambiguously. Focusing onto the lower part of the crack a vertically wedge-shaped course of the crack is found, eventually interrupted by micron-sized scar-shaped discontinuities in the crack thickness (shown in the inset Fig. 3.68b). A view onto the initial greywacke microstructure masked by the crack-volume and projected onto the crack-plane is shown in Fig. 3.69a along with a sagital slice through the loaded sample perpendicular to the crack (Fig. 3.69b-d). Both pictures clearly reveal a correlation between *new* crack propagation and *old* healed cracks which appear as bright lines in the tomographic data due to their dense iron-oxide filling. A significant part on the right hand side of Fig. 3.69a shows the bright iron oxide filling of a healed crack. This indicates that the region of crack propagation coincided with an old healed crack. The sagital view onto the crack confirms this correlation while the enlarged insets (Fig. 3.69b an c) reveal that the new crack did not always propagate along the iron-oxide filling of the old cracks. Particularly at the lower tip crack propagation seems to be *deflected* and the crack turns into the opposite direction away from the old healed cracks. Similar to the sample “G2”, the masked region of crack-propagation in the unloaded sample shows particularly few pores compared to other

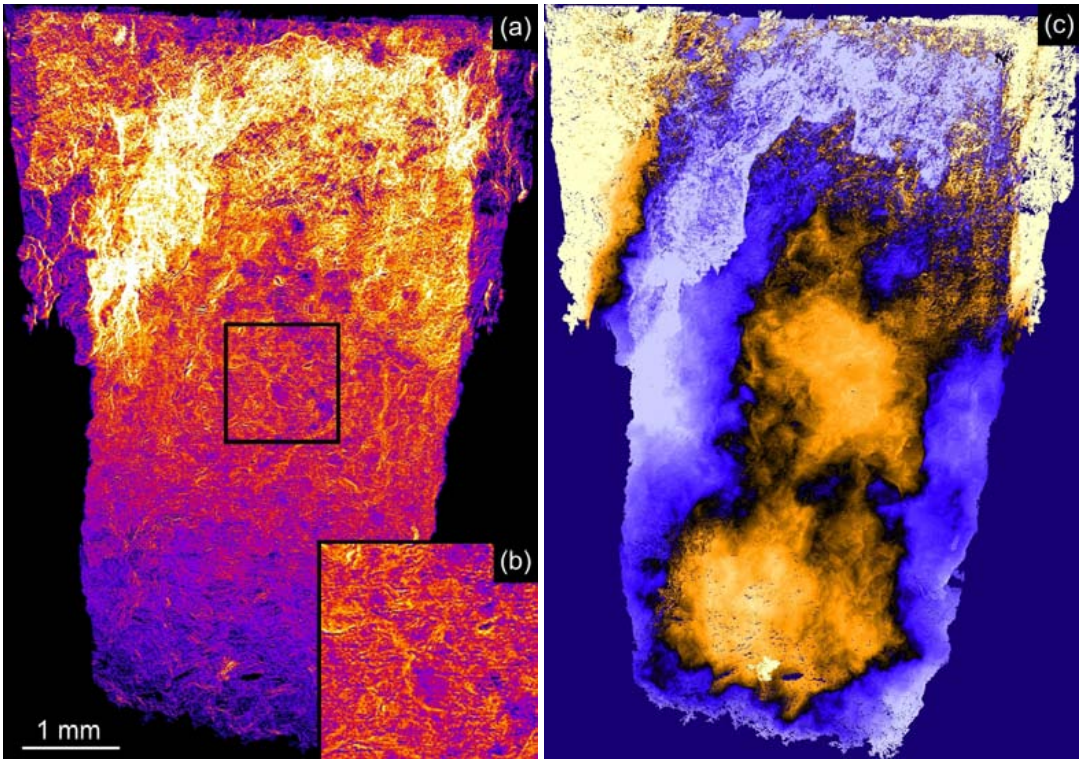

Figure 3.68: Crack in sample "G3": (a) Thickness projection (color range from 0 to $80\,\mu\mathrm{m}$), (b) The enlarged inset reveals scar-shaped discontinuities in the pore volume, (c) Topography of the crack (color range from $-216\,\mu\mathrm{m}$ to $+252\,\mu\mathrm{m}$).

regions of the same size in the sample.

In order to learn more about the local strain that led to cracking of this greywacke, 2D deformation maps were calculated from Fig. 3.69d and the corresponding slice of the unloaded sample. The algorithm which was used to calculate local deformation vectors is very similar to the one used for the analysis of thixotropic flow in semi-solid metals (see section 6.2.3). Following manual (x, y, z)-alignment of the deformed and undeformed sample, a sagital (y, z)-slice quasi-perpendicular to the crack is cut from both datasets (during filtered back-projection the datasets were pre-aligned so that the crack was approximately parallel to the x-axis). A virtual grid of 32 pixels spacing in y- and z-direction is superimposed onto the two slices and small squared templates of 64 pixel side length are cut around each point on the grid. Each pair of corresponding templates from the deformed and the undeformed sample is matched by Fourier image cross-correlation and three deformation maps are generated from the resulting displacement-vectors: y, z and the modulus $\sqrt{y^2 + z^2}$. In order to reduce the uncertainty of the image cross-correlation, a 3×3 median filter was applied to the deformation maps which are shown in Fig. 3.70.

Most of the deformation appears to occur along the y-axis, perpendicular to the direction of load. The y-deformation is reversed (transition from black to white) along a horizontal line in the upper part of Fig. 3.70a indicating that the top and lower parts were gliding into oppo-

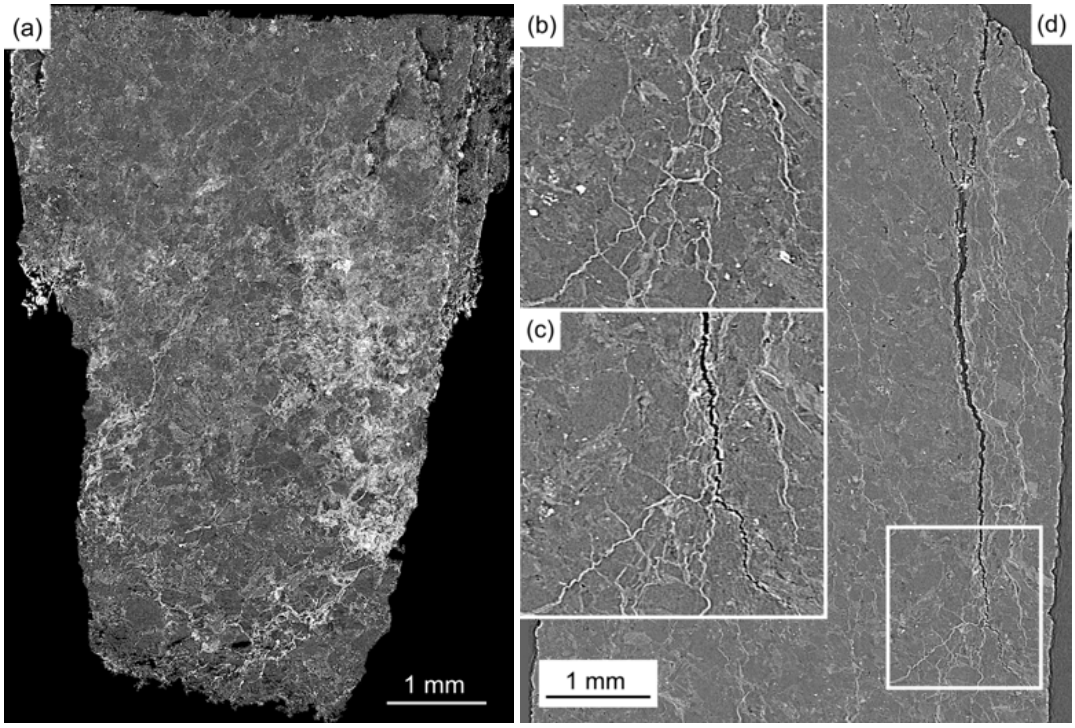

Figure 3.69: Initial microstructure in greywacke before loading: (a) The unloaded sample is masked with the binary crack volume from the loaded sample and average gray values representing the region of crack propagation are projected onto the crack-plane. (b-d) Sagital slice through the cracked sample: The insets (b) and (c) show an enlarged region (white square in (d)) before (b) and after (c) cracking.

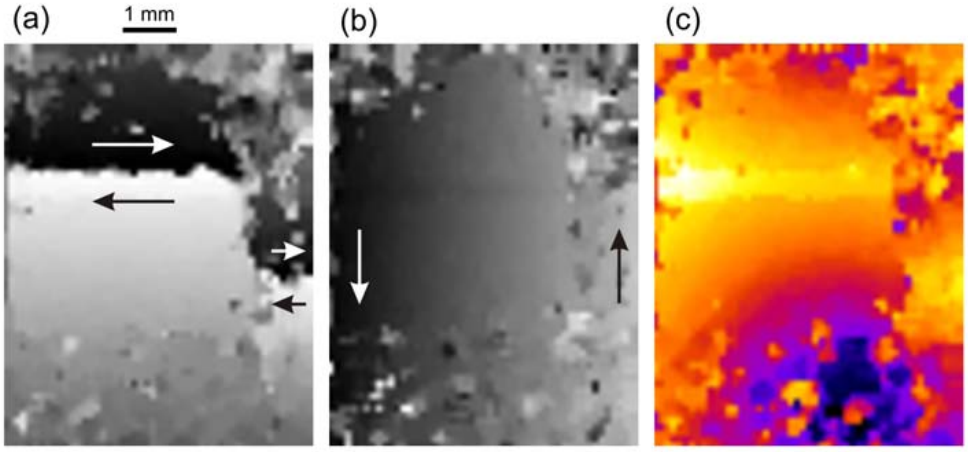

Figure 3.70: Deformation maps calculated on a (y, z) raster of 32 pixels spacing (template size 64×64 pixels, i.e. $230 \times 230\,\mu\mathrm{m}^2$) for corresponding sagital slices through the loaded (Fig. 3.69d) and the unloaded sample: (a) y-displacement, (b) z-displacement (gray scale from $-115\,\mu\mathrm{m}$ (black) to $+115\,\mu\mathrm{m}$ (white)). (c) Modulus of the displacement vector (color scale from 0 (black) to $160\,\mu\mathrm{m}$ (white)).

site directions. This *horizontal fracture* is interrupted at the exact position where the vertical crack developed, and continues beyond the crack but further down the z-axis. This discontinuity (z-step) of the y-deformation follows precisely the course of the vertical crack which is depicted in Fig. 3.69d. The z-deformation map shows a horizontal gradient which is not surprising since the two samples were slightly tilted with respect to each other. The modulus of the deformation vector (Fig. 3.70c) is maximal over the horizontal *gliding plane* and shows a radial increase around a (black) point in the lower right part of the map. Such a minimum in the modulus of the displacement vector is however not related to real deformation but most probably the result of a small sample tilt which occurred around this particular point.
Calculating deformation maps works well if the two samples are perfectly aligned and no deformation occurs along the x-axis. More sophisticated algorithms have been tested recently with success to obtain 3D deformation maps from tomographic data [Bes06]. Unlike in-situ experiments, the different datasets presented in this work were slightly misaligned and tilted with respect to each other, inducing uncertainties in the image cross-correlation. Also the maximum displacement that could be found is limited to half the size of the templates (i.e. $115\,\mu\mathrm{m}$), which is why outer parts of the maps in Fig. 3.70 show random values.

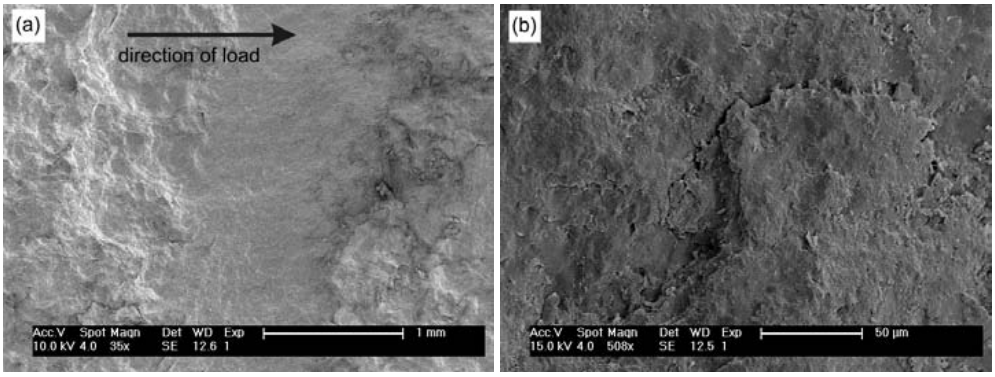

Figure 3.71: High-resolution SEM pictures of the fractured surface of sample G3.

The remanents of the broken sample G3 were recovered and high-resolution SEM images of the fractured surface could be recorded. Fig. 3.71 shows two representative backscattered electron pictures recorded at different magnifications: An overview of the fracture surface (Fig. 3.71a) reveals that crack propagation was quasi-planar over approx. $1\,\mathrm{mm}$ length where roughness of the crack appears much smaller than elsewhere. This rather smooth part of the surface might coincide with an old healed crack as seen in Fig. 3.69a. The enlarged SEM picture (Fig. 3.71b) shows leaflet-shaped structures on the flat crack surface indicating that cracking occurred along a preferred crystallographic cleavage plane of the corresponding mineral.

Fresnel-propagated tomography of basalt: Basalt is the strongest rock that was investigated during this work (see table 3.9). Its strength was estimated from cyclic compression

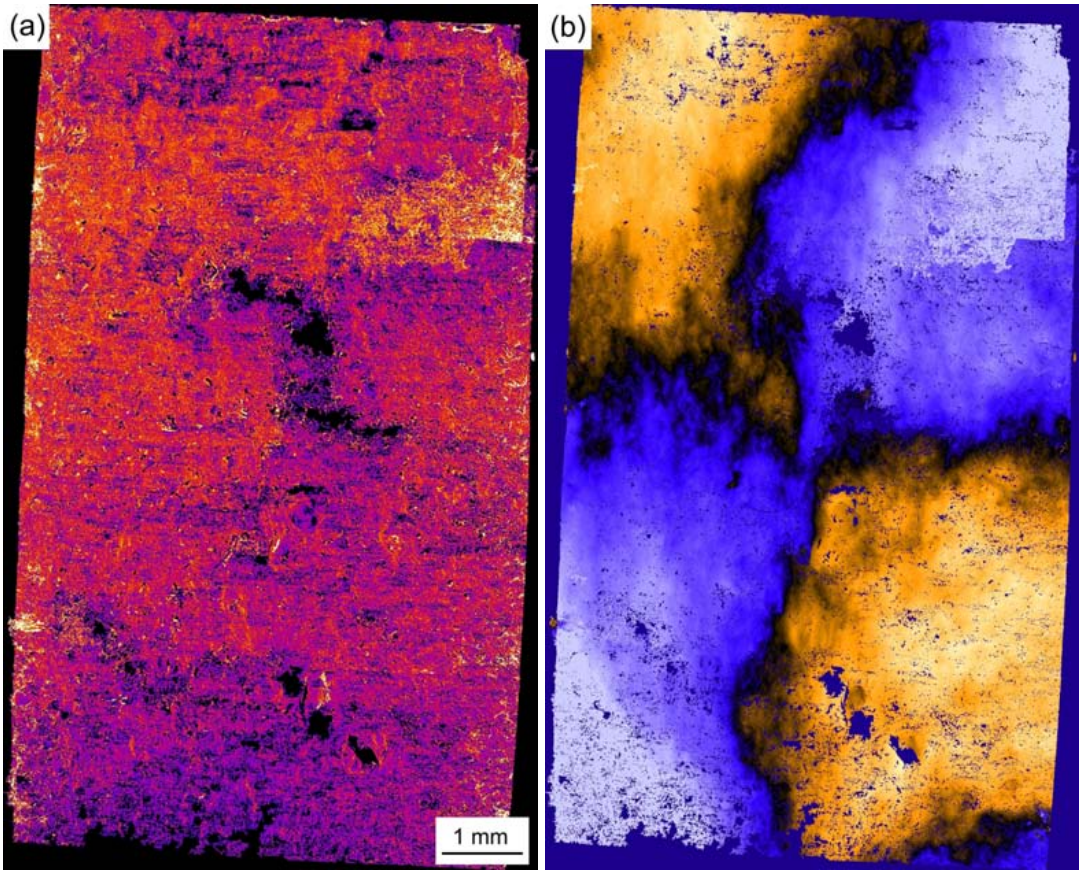

Figure 3.72: Crack in the basalt sample: (a) thickness (color scale from 0 to 40 µm) and (b) topography of the crack (color scale from −288 µm to 324 µm).

tests to yield 350− 400 MPa at an average strain at fracture of almost 10%. During beamtime in August 2006 the basalt sample B4 already started to crack while load was applied for the second time and before reaching 5% of strain. Tomography revealed that the sample was almost completely cut apart by a very thin slightly twisted crack. The basalt broke during the third compression. The projected maps of crack thickness and crack topography after the second load cycle are shown in Fig. 3.72. While Fig. 3.72a reveals a quasi homogeneous thickness of 10 to 15 µm of the crack, the topography view (Fig. 3.72b) clearly illustrates the twisted course of the propagating crack. After the second compression the material was only held together by some few mineral grains that are seen as black areas in Fig. 3.72a. Crack bifurcation occurred in some regions seen in the upper right part of Fig. 3.72a where the crack thickness is artificially increased. Consequently discontinuities are observed for the same regions in the crack topography view.

Masking the *uncracked* dataset recorded before the second loading with the corresponding pore volume of the crack yields a 2D representation of the basalt microstructure that was traversed by the crack. Probably due to the small size of the intergranular pores (see Fig. 3.63a) almost no porosity could be detected in the uncracked basalt sample. Fig. 3.73 shows the pro-

jection of the masked (uncracked) microstructure of B4 after the first compression (a) as well as a sagital slice (perpendicular to the crack) of the cracked sample (b). The enlarged insets

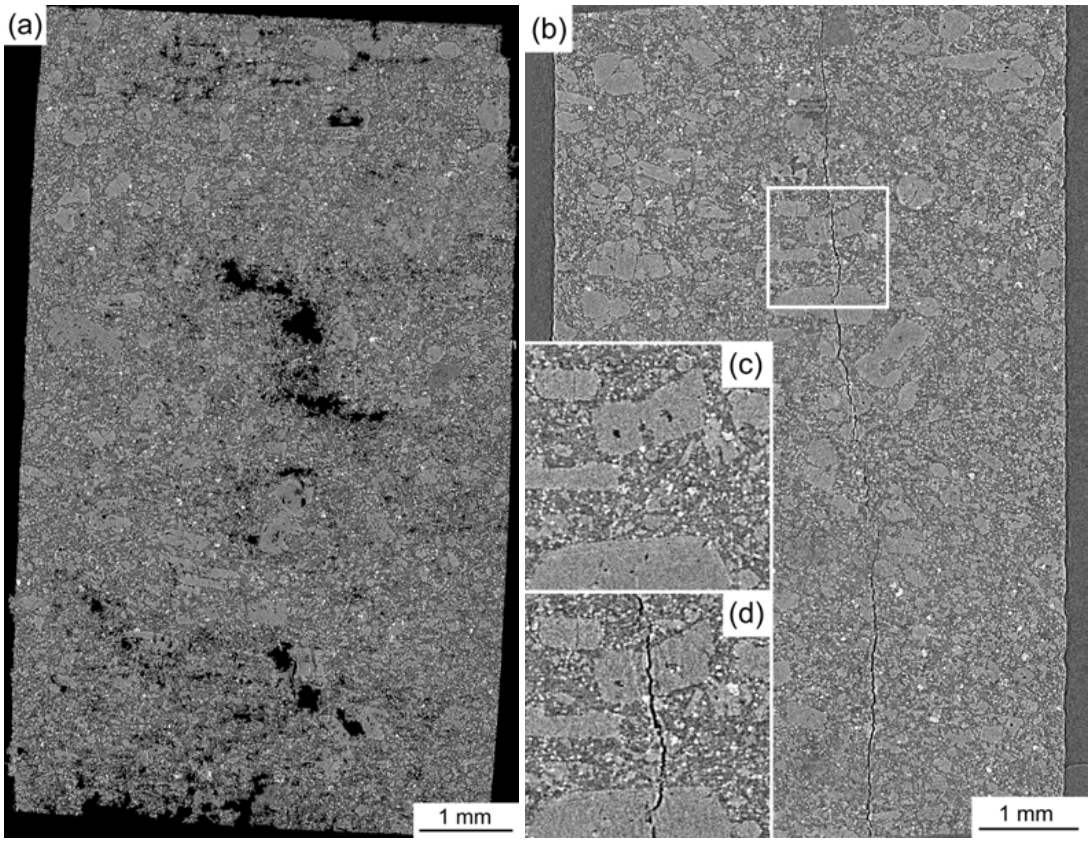

Figure 3.73: Microstructure in sample B4 before second load cycle: (a) Masking the 3D image with the binary crack yields reveals the microstructure where crack propagation took place. (b) Sagital slice through the cracked sample. Insets (c) and (d) show an enlarged region before and after cracking.

highlight a small region in this sagital slice (marked as white square in Fig. 3.73b) before and after cracking (Fig. 3.73c and d). The crack appears to traverse indiscriminately matrix and olivines as seen from the corresponding microstructure in the uncracked sample. Fig. 3.73a does not reveal a particular concentration of ore minerals or olivines that might have favored crack propagation in these parts of the rock.

2D deformation maps were calculated by comparing sagital slices of sample B4 before and after cracking. Due to a high spatial correlation between the two datasets, uncertainties in the determination of the local displacement vectors (appearing as random values in the deformation maps) were almost completely avoided and unlike for sample G3 no median filter was applied. Results are shown in Fig. 3.74. Similar to the greywacke sample G3 a horizontal fracture is found in the basalt, invisible in the tomoraphic images but clearly seen as an opposite displacement in the x-direction (Fig. 3.74a). Although the event of cracking was induced and measured in a single step the deformation maps reveal two sequential events: (a) horizon-

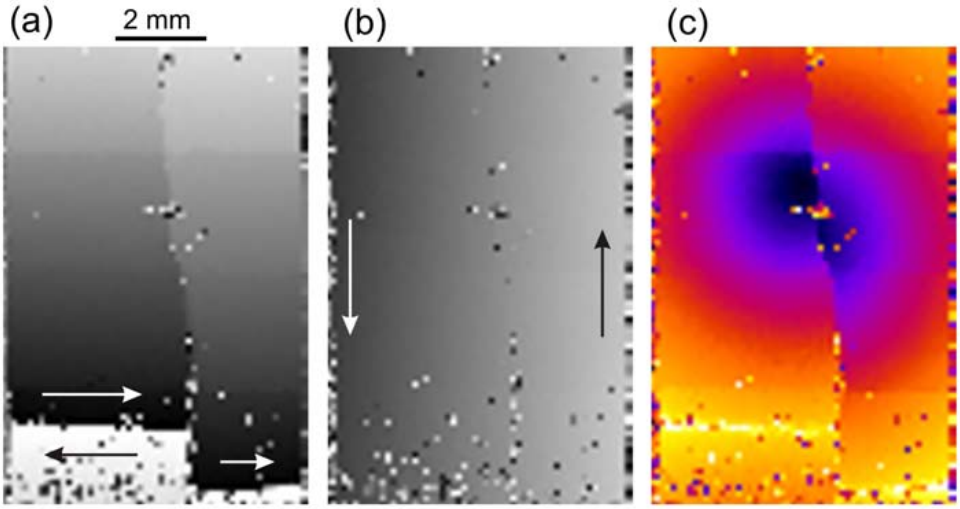

Figure 3.74: Deformation maps calculated on a (y, z) raster of 32 pixels spacing (template size 64×64 pixels, i.e. $230\times\ 230\,\mu\mathrm{m}^2$) for corresponding sagital slices through the cracked d) and uncracked sample B4: (a) y-displacement, (b) z-displacement (gray scale from $-115\,\mu\mathrm{m}$ (black) to $+115\,\mu\mathrm{m}$ (white)) and (c) Modulus of the displacement vector (color scale from 0 (black) to $160\,\mu\mathrm{m}$ (white)).

tal deformation along a *gliding-plane* perpendicular to the loading direction and (b) vertical fracture and cracking seen as a discontinuity (step) in the horizontal deformation as well as in the map of $\sqrt{\Delta y^2 + \Delta z^2}$. The circular minimum (black) in Fig. 3.74c results from a slight tilt of the two datasets and is not related to real deformation. The same tilt leads to a horizontal gradient in Fig. 3.74b.

High-reolution SEM images of recovered fracture surface after breaking sample B4 are shown in Fig. 3.75. Similar to greywacke the fracture surface was rather smooth on a macroscopic scale but unlike sample G3, the fracture surface of B4 is characterized by *side-cracks* perpendicular to the main crack as well as a rich variety of fractured grains of different minerals. Fig 3.75a-c shows a zoom onto fragments of plagiclase that appear scattered all over the fracture surface. The highest magnification (Fig. 3.75c) reveals sub-micron sized details of the fracture endings. Bifurcation of two crack planes as well as the formation of perpendicular side-cracks is seen in Fig. 3.75d. A zoom onto the clamshell-like fracture through an olivine reveals sub-micron cracks forming at corroded interfaces inside the mineral.

Fresnel-propagated tomography of granite: During BESSY/BAM*line* experiments in January 2006 increasing load was applied repeatedly to the sample "T1" (see table 3.8) reaching almost 4% compression until the sample broke during the fifth test. Tomography datasets were acquired before and following each compression. Fig. 3.76 shows the stress strain diagrams for the basalt (B4 see previous paragraph) and the granite T1. Cracks in T1 were already visible after the third compression. During the fourth test, tiny bits splintered off the edges but the sample remained stable until complete fracure occurred during the last compression. Thick-

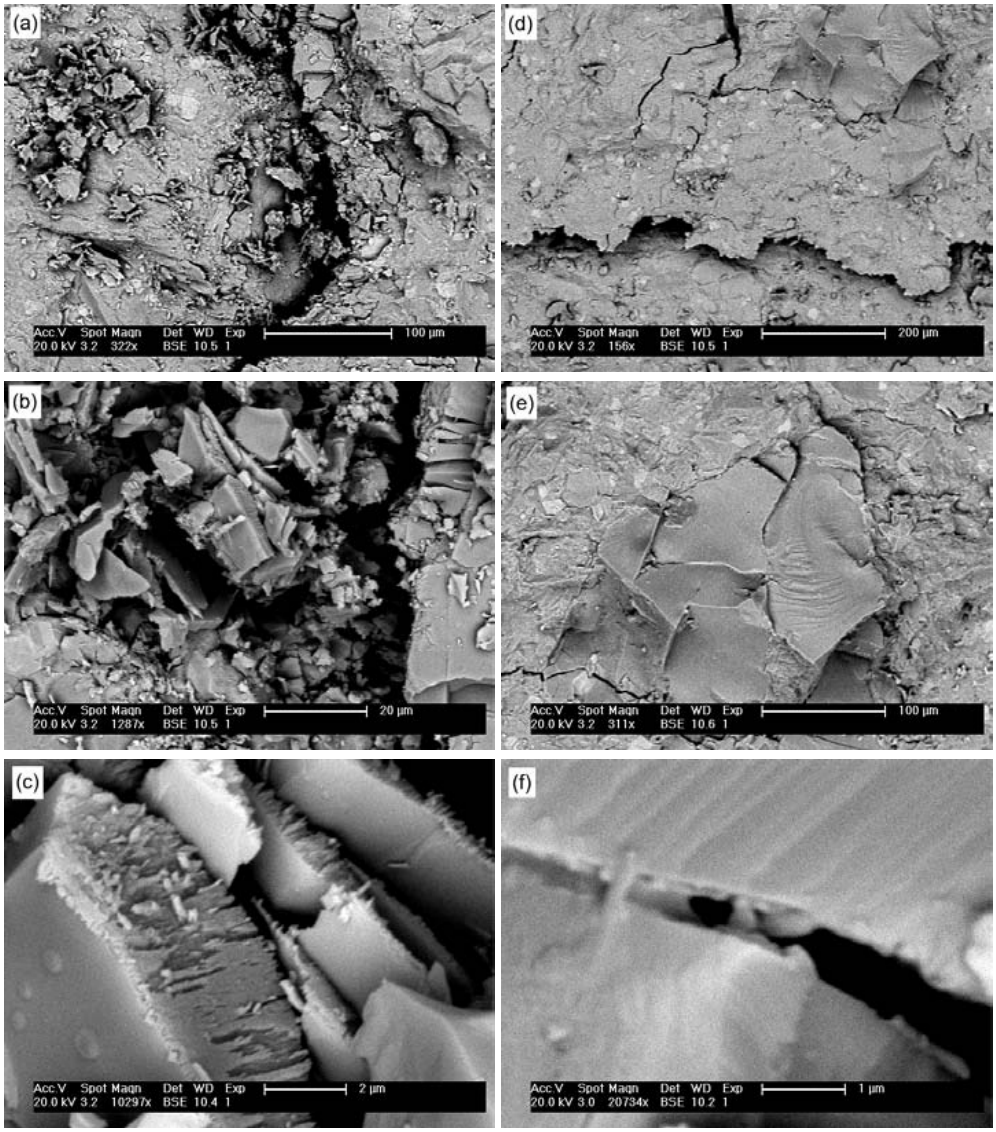

Figure 3.75: High resolution SEM views onto the fracture surface of the sample B4.

ness and Topography of the pore space corresponding to the crack were projected onto the crack plane as shown in Fig. 3.77 Obviously multiple cracks developed and splinters broke off during the fourth compression in the upper half of the sample along with one thin crack, newly forming in the lower part. The corresponding porosity in the same region before the fourth test shows that the cracks in granite developed from inside the sample and not from the edges as it was observed for greywacke and basalt. The very inhomogeneous distribution of dense minerals (quartz, biotites, etc.) and possibly the sponge-like highly corroded feldspars (seen as *bright-clouds* in Fig. 3.77a and c) gave rise to strong deformations inside the sample leading to grain-boundary cracking. A sagital slice perpendicular to the crack is shown for T1 after the third (Fig. 3.78a) and after the forth compression test. Enlarged insets show the regions were new cracks developed before and after application of load. Crack propagation clearly occurred

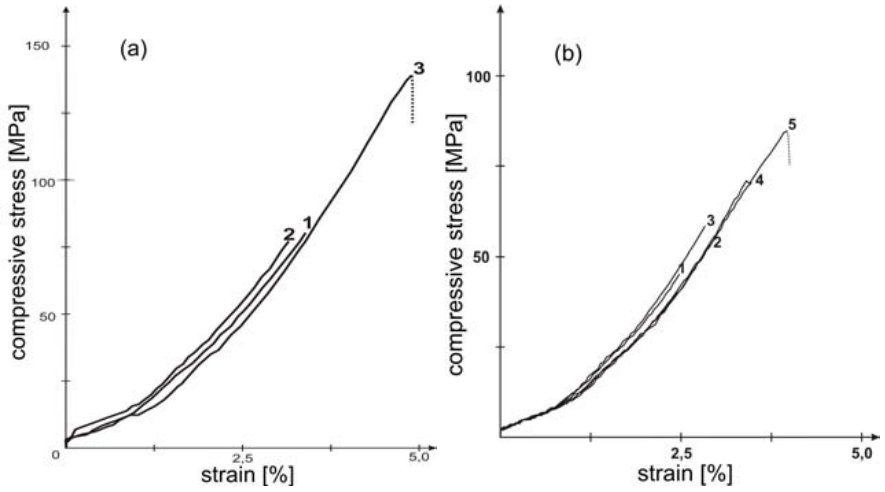

Figure 3.76: Stress-strain diagrams of basalt B4 (a) and granite T1 (b).

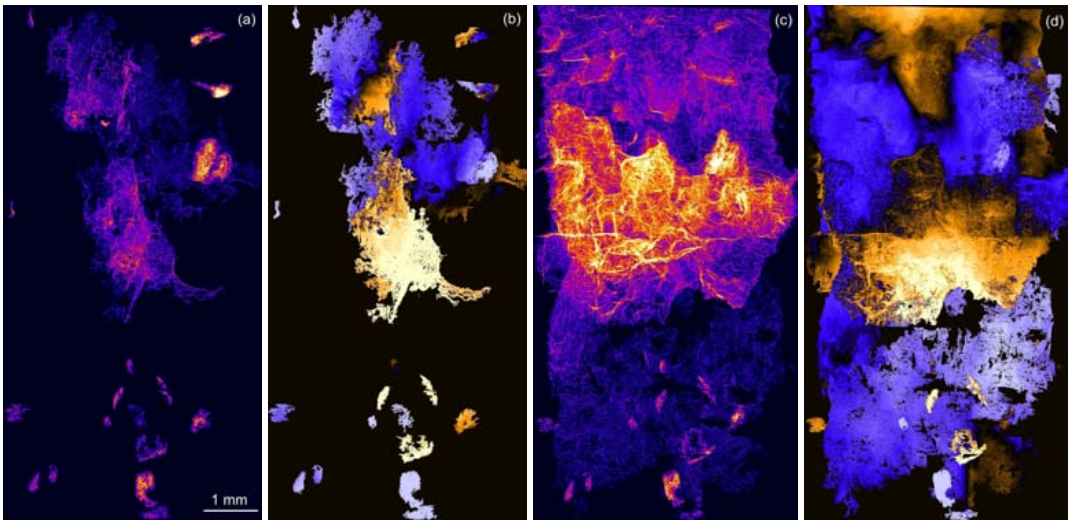

Figure 3.77: Development of cracks in the granite T1 during the third (a,b) and forth (c,d) compression test. (a+c) Thickness of the corresponding pore space projected onto the crack plane (color scale from 0 to $120\,\mu\mathrm{m}$), (b,d) topography view (average distance of the *crack-voxels* normal to the crack-plane (color scale from $-612\,\mu\mathrm{m}$ to $+576\,\mu\mathrm{m}$).

along the grain boundaries of the quartz grains and other minerals in the granite. Two datasets, one reacorded before and the other after a compresseion test could be well matched on one side of the developing crack while they appears misaligned on the other side (see insets in Fig. 3.78). A strong deformation inside the sample as seen from the deformation maps of B4 and G3 is probably the reason for this mismatch. Calculating the local deformation vectors for the 2D slices shown in Fig. 3.78 was not feasible due to the fact that anisotropic deformation occurred over wide regions in the 3D image. As seen in Fig. 3.77d the crack in T1 was much *rougher* than cracks in B4 and G3.

SEM images of the broken sample T1 are shown in Fig. 3.79. The backscattered electron view

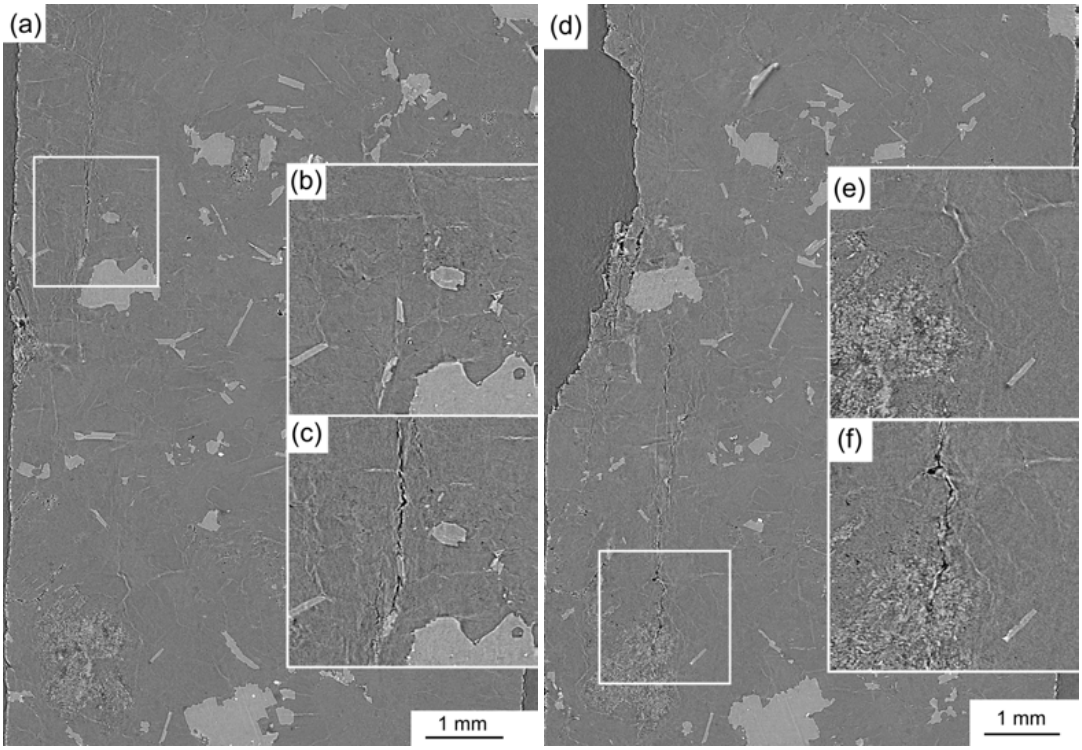

Figure 3.78: Sagital view into the sample T1 after the (a) third and (d) forth compression test. Magnified insets in (a and d) show regions where cracks developed before (b and e) and after (c and f) the third and the forth compression respectively.

onto the fracture surface of the granite also shows a much rougher topography than what was observed from similar views onto the fracture surfaces of B4 and G3. Magnified images (Fig. 3.79b-d) show intra-granular as well as intra-granular micro-cracks of random orientation in the broken material. Large stacks of sub-micron thick mineral platelets stand out of the fracture surface. When they are aligned perpendicular to the loading direction These stacks have an extremely high strength and do not break during compression.

3.3.3 Basalt - Holotomography

To investigate microporosity in the basalt rock on a smaller scale than that was shown in the previous subsection, three complete tomographic datasets were recorded at increasing sample-detector distances ($d = 15\,\mathrm{mm}$, $162\,\mathrm{mm}$ and $464\,\mathrm{mm}$) with the X-ray macroscope at BESSY/BAM*line* . 900 projection images of $\Delta x = 1.6\ \mu m$ pixel size and $R \sim 3 - 4\ \mu m$ resolution were acquired at each propagation distance using a $22\,\mu\mathrm{m}$ thin CWO scintillator screen ($E = 28\,\mathrm{keV}$). Figure 3.80 shows axial slices reconstructed from (a) the absorption, (b) the Fresnel-propagated and (c) the holotomography data along with a 3D rendering of the latter (d). The holotomoaphy was reconstructed using the CTF method presented in appendix B.3.1. The absorption data was used for normalization of the two Fresnel-propagated datasets prior to application of the phase-retrieval algorithm. The small dense ilmenites are well ob-

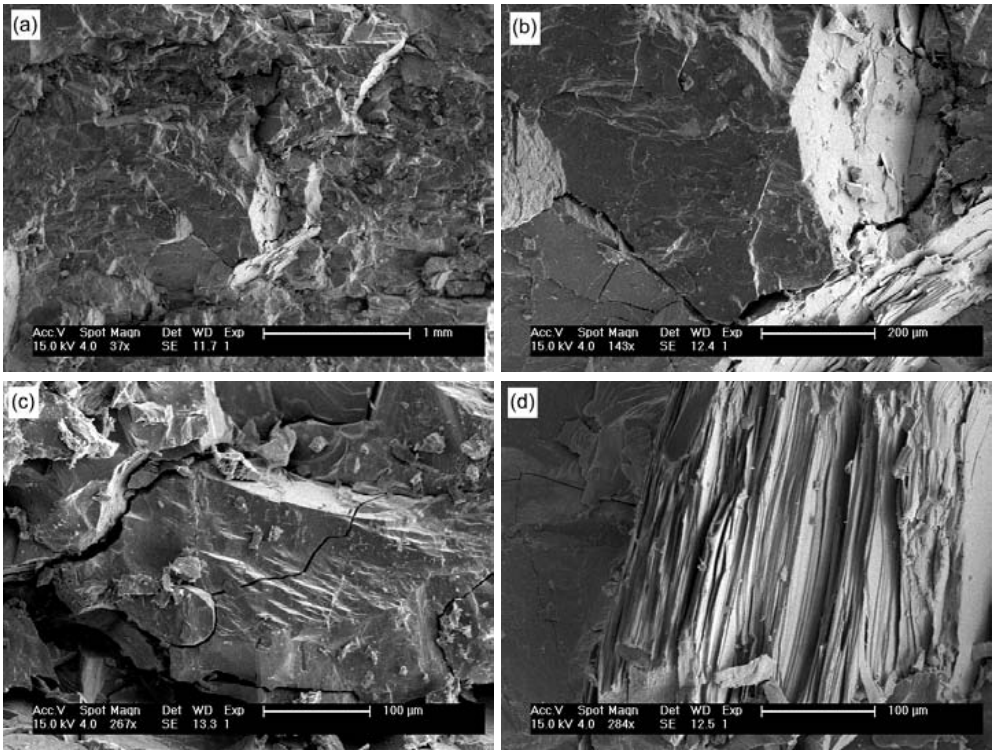

Figure 3.79: Backscattered electron SEM images of the fracture surface of sample T1.

served (dark particles) in the absorption image (Fig. 3.80a), pyroxenes are imaged as well due to their high calcium content. The outline of the latter appears enhanced in the Fresnel propagated tomogram but it requires holotomography to see the faint density difference between a large olivine in the center of Fig. 3.80c and the surrounding feldspars. Insets show intensity profiles calculated along the white line in Fig. 3.80a for the three imaging modes. A 3D rendering of the holotomography is depicted in Fig. 3.80d. Despite the improved visibility of the detailed microstructure only few micropores are observed in these images (bright spots in Fig. 3.80c). To observe the latter higher image resolution is required.

Short summary

X-ray μCT was applied to study the microstructure of various natural rocks before and after mechanical compression. Cracks were initiated in the small cylindrical samples by unconfined uniaxial compression. For some samples two or more steps of crack growth/ propagation could be measured in three dimensions before fracture occurred. The non destructive virtue of the μCT allows for comparison between the initial microstructure and the different deformation steps. 3D image analysis algorithms were developed to calculate orientation and to map thickness and shape of each crack. A dedicated 2D software was developed to quantify deformation and orientation of the individual tensile- and shear-cracks perpendicular to the crack plane. In addition to the absorption tomography, Fresnel-propagation is capable of enhancing

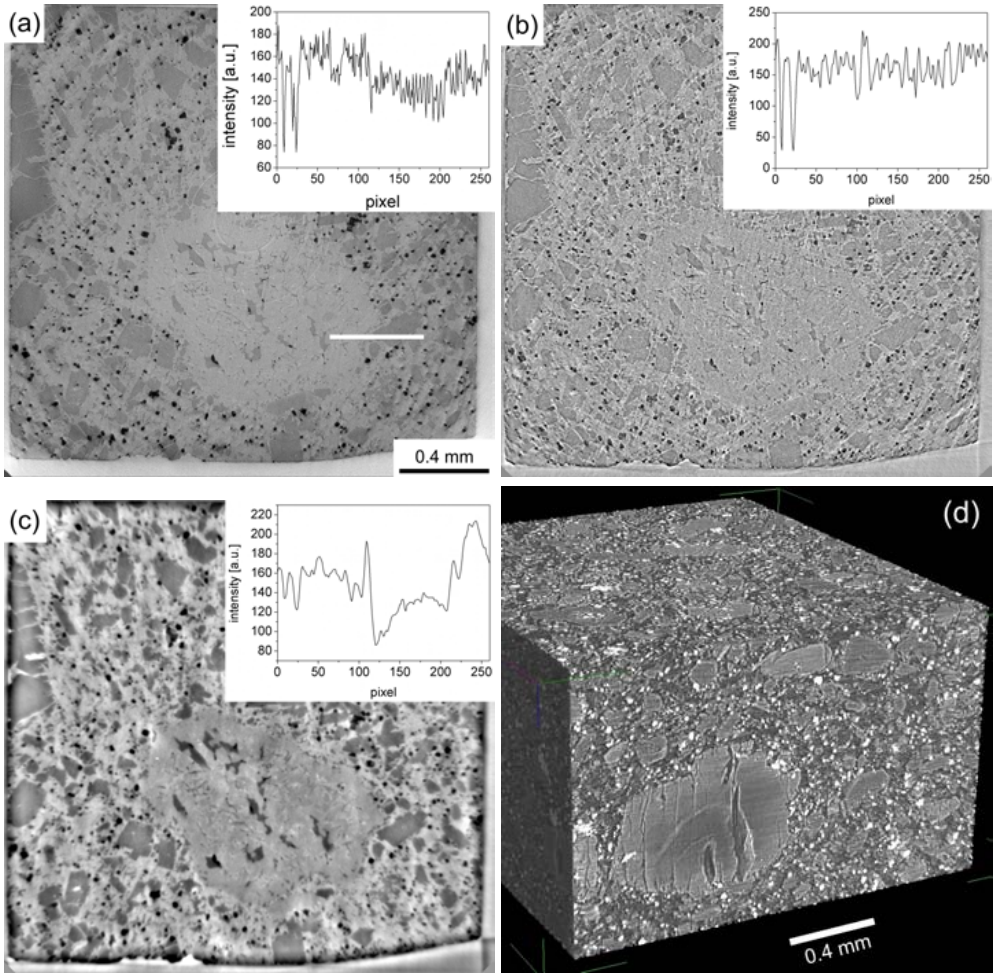

Figure 3.80: (a-c) Tomographic axial slice of basalt in (a) absorption ($d = 15\,\mathrm{mm}$), (b) Fresnel-propagated ($d = 464\,\mathrm{mm}$) and (c) holotomography ($d = 15\,\mathrm{mm}$, $162\,\mathrm{mm}$ and $464\,\mathrm{mm}$) imaging mode. Insets show a linear intensity profile calculated along the white line drawn in (a). (d) 3D rendering of the holotomography data.

the signals of micropores and inclusions (ore minerals), thus allowing for the comparison between initial inter-granular microporosity (which is hardly visible in absorption tomography) and cracks which form later during deformation. Particularly for greywacke a preferred direction for crack propagation/ formation is found to coincide with old healed cracks, whereas the initial microporosity is shown not to initiate cracking. The crack shapes in basalt, granite and greywacke showed significant differences in the fracture behavior of these rocks in agreement with SEM pictures of the fractured samples. While a single twisted crack was observed to split almost instantaneously the basalt, granite and greywacke developed one or more oblique cracks which started small and grew during further deformation. Cracks in greywacke started from the top and/or bottom of the test cylinders whereas granite developed cracks from the inside of the material. Holotomography was tested on a sample of basalt, yielding excellent information about the microstructural distribution of the main constituents: olivines, ilmenites

and pyroxenes. This method beholds great potential for 3D granular analysis of rock and other rock-like materials. Further experiments are planned, using Fresnel-propagation and holotomography to study deformation and cracking of rocks in situ.

3.4 Further studies

3.4.1 Time-resolved radiography of Al-Ge32 alloy

For the production of high quality light weight metallic components semi-solid casting is the preferred process [Fle91] due to very good die-filling and a fine equiaxed microstructure which characterizes the cast components. During thixo- or rheocasting, pre-alloyed material is commonly heated to a temperature above the solidus and below the liquidus line resulting in the coexistence of solid and liquid volume fractions in the feedstock material. For binary alloys the solid phase is enriched with the majority element and characterized by particle-agglomerates which are continuously subject to a morphological transformation: coarsening. For higher solid volume fractions ($g_S > 0.3$) these agglomerates start to build continuous connections. When the semi-solid mixture is injected with high pressure into the die, a spontaneous drop in the flow resistance of the alloy is observed due to shear forces which break apart the solid agglomerates (thixotropy). Joly and Mehrabian [Jol76] were the first ones to observe the apparent viscosity of a semi-solid Sn-Pb15 alloy decreasing by many orders of magnitude. Commonly variations from 10^7 to $10^{-1}\,\mathrm{Pa{\cdot}s}$ are observed for shearing rates ranging from 10^{-4} to $10^3\,\mathrm{s}^{-1}$ [Mod99, Lax80]. Hydrodynamics provide a linear relationship between the applied shear stress τ and the resulting shear rate $\dot{\gamma}$ in a liquid

$$\tau = \eta \cdot \dot{\gamma} \tag{3.6}$$

For Newtonian liquids the coefficient η, i.e. the apparent viscosity, does not depend on $\dot{\gamma}$. For a suspension of solids one has to replace η by a dimensionless effective viscosity which depends on the volume fraction of the solid particles [Que77]. Furthermore semisolid slurries exhibit pseudo-plasticity, in other words shear thinning (thixotropic) behavior and the apparent viscosity is - for a wide range of shear rates (10^{-3} - $10^3\,\mathrm{s}^{-1}$) - well described by a power law:

$$\eta = K \cdot \dot{\gamma}^{n-1} \tag{3.7}$$

Where $\dot{\gamma}$ is the shear rate, n the power-law index (note that $n = 1$ for newtonian fluids and $n < 1$ for shear thinning) and K the *consistency* [Fle91]. Based on equation 3.7 many empirical and theoretical models have been developed (for a review see [Fan02]), some of which consider the particle shape and agglomeration as fundamental parameters determining the shear thinning properties of the mixture. Because n and K depend strongly on the initial microstructure of the feedstock material it is difficult to include this thixotropic behavior into flow simulations of the industrial casting process. For optimal casting results a fine equiaxed microstructure is required while non-equiaxed structures (characterized by anisotropic dendrites) are known to deteriorate the rheological properties of the semi-solid slurry. In order to parameterize flow simulations, a relationship between the industrial thixomolding and the results from viscosity measurements in the rheometer is constructed by comparing microscopic images of plane sections that are cut from quenched samples representing these two processes.

Flow simulations are used to optimize the die geometry for homogeneous filling.
Since the experimental conditions do not allow direct observation of the solid particle flow in the die, only little is known about the behavior of the semi-solid skeleton when it is injected into a thin cavity at high pressure. Current state of the art X-ray radioscopy allows to directly visualize the semi-solid microstructure and its flow *in situ*. Here in situ observations of slow and fast injection processes of semi-solid Al-Ge32 alloy are reported. In the framework of the diploma thesis of Antonio Rueda - which was supervised by the author - an experimental setup for in situ flow observation of semi-solid alloys was constructed and assembled at BESSY/BAM*line* [Rue06]. Experimental beamtime was used twice, during multi-bunch and single-bunch mode, for the study of slowly moving slurry. During joint ANKA/HMI experiments at the ESRF/ID19 beamline in late 2006, additional high-speed experiments were carried out, employing the same setup while replacing the slow CCD with a high-speed CMOS detector (mentioned in section A.2). Photos of the experimental setup are shown in Fig. 3.81. A linear (Huber) motor is mounted vertically onto a frame of aluminum bars. This motor

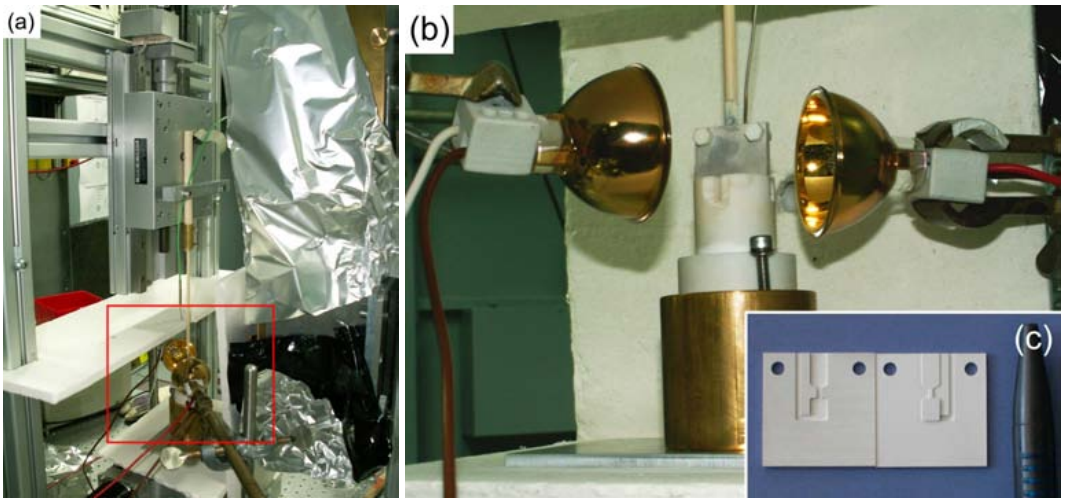

Figure 3.81: Photos of the experimental setup for in situ X-ray radioscopy of semi-solid flow. (a) A motor slowly moves down a stamp, pushing semi-solid slurry into a thin cavity between two boron nitride plates. (b) Magnified view onto the BN plates and the heating lamps. The inset (c) shows the flow profile that was machined into the two BN plates.

moves down a thin ceramic piston to push semi-solid Al-Ge32 alloy through a thin channel which is machined into two boron nitride (BN) plates (Fig. 3.81c). For continuous heating, the $1\,\mathrm{mm}$ thick BN plates are placed in the focus of two heating lamps (Osram Xenophot 64635 HLX, $150\,\mathrm{W}$) as shown in Fig. 3.81b.
Most experiments reported in the following were carried out at a temperature of $T \approx 460\,^{\circ}\mathrm{C}$ to yield a solid volume fraction of the Al-rich particles of $g_S \approx 0.47$. Grain refinement was used to create a heterogeneous dispersion of nucleation sites: 4 wt.% of commercial Al-Ti5-B grain refiner (KBM Affilips, Netherlands) were therefore added to the pure elements (>99.99%) prior to levitation melting and casting of an ingot in the cold furnace. Thin foils

(0.4 mm) of 3 mm × 3 mm size were cut from the ingot to fit into the cavity between the two BN plates. Different channel geometries were machined into three sets of BN plates. Unfortunately, a hand-made cavity had to be used during the first experiment (multi-bunch mode) at BESSY/BAM*line* because no spares were available after the first BN sample holder broke during experimental preparations. For the second experiment (single-bunch mode) BN plates with a 3 mm wide and 0.4 mm thin sample cavity leading into a 1 mm wide and 0.1 mm thin channel terminated by a larger recipient and a ventiduct for pressure balance. Temperature was monitored my a thermocouple placed close to the flow channel. For the ESRF/ID19 experiment similar geometries were used (shown in Fig. 3.81c) with a slightly shorter and thicker (0.2 mm) channel. Fig. 3.82 shows a schematic drawing of this experiment. An overview

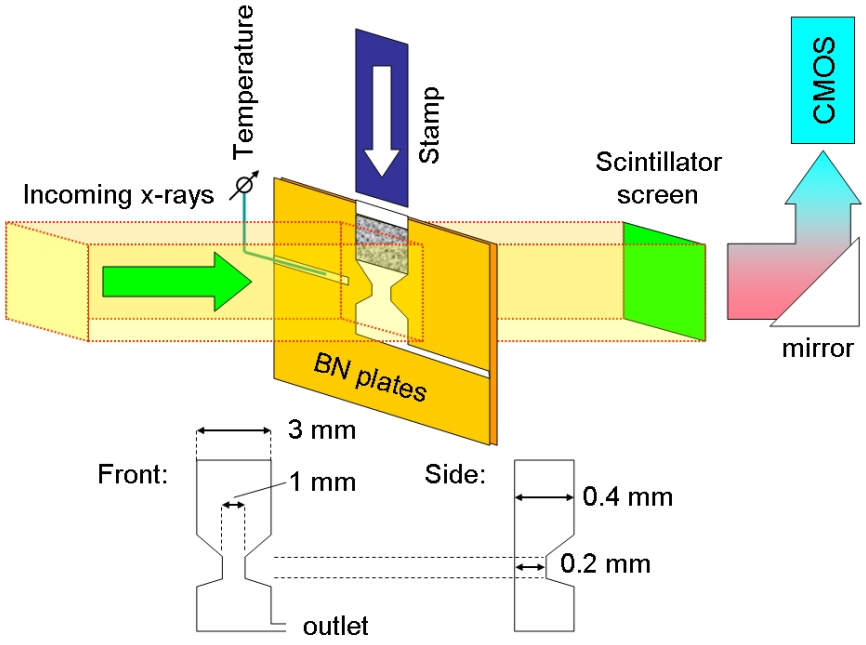

Figure 3.82: Schematic drawing of the in situ radioscopy using a CMOS camera.

over the samples and experiments carried out during the three beamtimes, showing sample thickness a, piston speed v, temperature T, measurement time t and frame rate r is given in table 3.11. The first tests at Bessy (MB1-5) were only partially successful which is why they are only briefly described here. The X-ray macroscope (cf. section A.2) was used to acquire radiographs with an effective pixel size $\Delta x = 1.6\,\mu\text{m}$ and spatial resolution $R \sim 6-7\,\mu\text{m}$ (YAG:Ce scintillator). The X-ray energy was set to $E = 25\,\text{keV}$ for all experiments.

For the analysis of the radiographic data an algorithm was developed using local image cross-correlation whereby a virtual rectangular grid of 64 pixel spacing was superimposed onto each image in a radioscopic sequence. For each square element (64×64 pixels in size) on this raster the vertical (Δy) and horizontal (Δx) displacements were calculated with respect to the same element in the previous image. Eventually a *time-median* was applied to the resulting sequence of displacement-maps. The first experiment MB1a was meant to represent a very

sample	a [mm]	v [µm/s]	T [°C]	t [min]	r [fps]
MB1a*	0.4	0.6	460	26.6	0.19
MB1b*	0.4	1.2	460	13.3	0.19
MB2	0.4	1.0	460	18.3	0.19
MB3	0.4	10	420	6.4	0.19
MB4	0.4	10	460	8.0	0.19
MB5	0.4	10	500	9.5	0.19
SB1	0.4	8	466	13.3	0.19
SB2	0.4	8-80	460	19.6	0.25
SB3	0.4	5	460	19.0	0.28
SB4	0.4	5	460	26.7	0.29
SB5	0.4	5	490	26.7	0.29
SB6	0.4	10	500	26.7	0.29
ES1	0.4	2 cm/s	470	0.075	66.7

Table 3.11: Samples measured in multi-bunch (MB1-5) and single-bunch (SB1-6) beamtime at BESSY/BAM*line* and at the ESRF/ID19 (ES1): Sample thickness a, piston speed v, temperature T, measurement time t and framerate r. *The same sample was used for experiment MB1a and MB1b only changing the speed of the piston which was driven *step-by-step* for this first test (for the following experiments continuous motion was applied).

slow piston speed of $\sim 0.6\,\mu\mathrm{m/s}$. Fig. 3.83a and b show radiographs taken at the beginning ($t_1 = 0$) and at the end of MB1a ($t_2 = 27\,\mathrm{min}$) respectively. A two-dimensional map of the maximum displacement amplitude $A = \sqrt{\Delta x^2 + \Delta y^2}$ (MDA) is calculated over the whole sequence (after application of a time median over three sequential images) as depicted in Fig. 3.83c. This map was compared to the maximum flow in the x- and y-direction and motion was

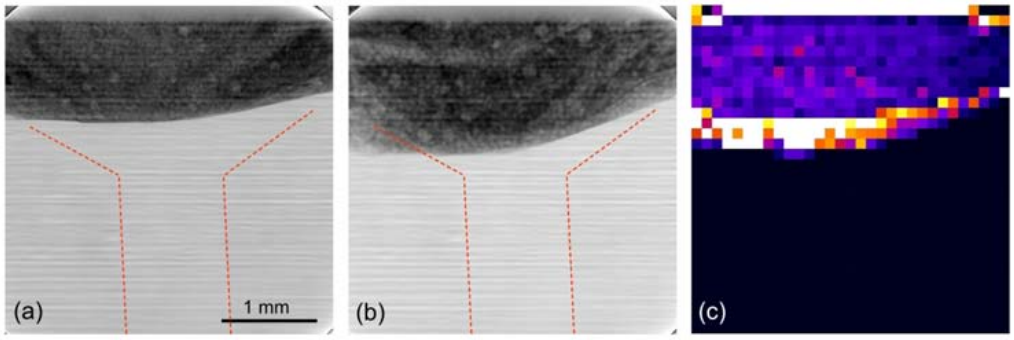

Figure 3.83: First (a) and last (b) radiographic image of sequence MB1a. (c) Maximum displacement amplitude $A = \sqrt{\Delta x^2 + \Delta y^2}$ (MDA) map calculated from image cross-correlation. Colors represent values of $A = 0$ (black) to $A_{peak} = 0.9\,\mu\mathrm{m/s}$ (white).

found to occur mainly vertically. Peak values of $A_{peak} = 0.9\,\mu\mathrm{m/s}$ are observed at the lower edge of the sample whereas hardly any motion is detected in the upper part ($A \leq 0.1\,\mu\mathrm{m/s}$).

This motion was too slow to observe the semi-solid slurry entering the thin channel below the sample cavity, therefore the piston speed was doubled for experiment MB1b while the same sample was kept in the BN sample holder. A radiography an the beginning and the end of this second sequence are shown in Fig. 3.84a and b respectively while the corresponding map of maximum displacement A is seen in Fig. 3.84c. Despite the faster piston speed the peak

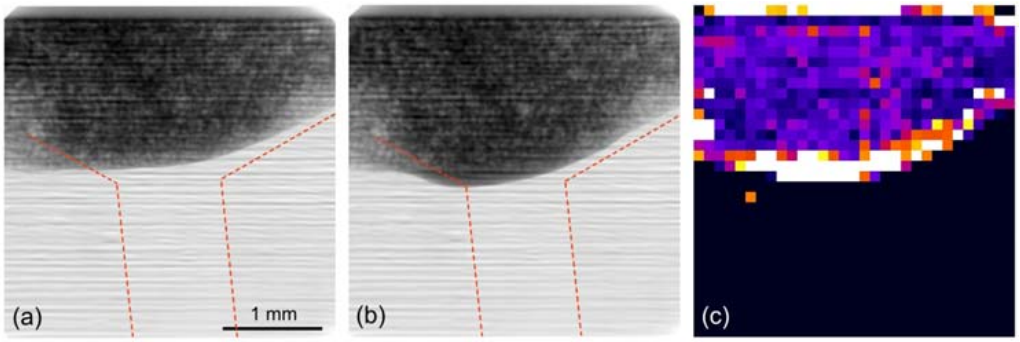

Figure 3.84: First (a) and last (b) radiographic image in sequence MB1b. (c) MDA map. Colors represent values of $A = 0$ (black) to $A_{peak} = 0.9\,\mu\mathrm{m/s}$ (white).

motion remained $A_{peak} = 0.9\,\mu\mathrm{m/s}$ (at the lower edge of the semi-solid slurry) and the total measurement time was too short to observe filling of the flow channel. A new AlGe32 foil was inserted for experiment MB2 to represent very fast piston speed. The experiment is represented by two radiographs taken at the start and at the end of MB2 shown along with the MDA map in Fig. 3.85a-c. This time, motion of the entire sample is observed featuring a horizontal

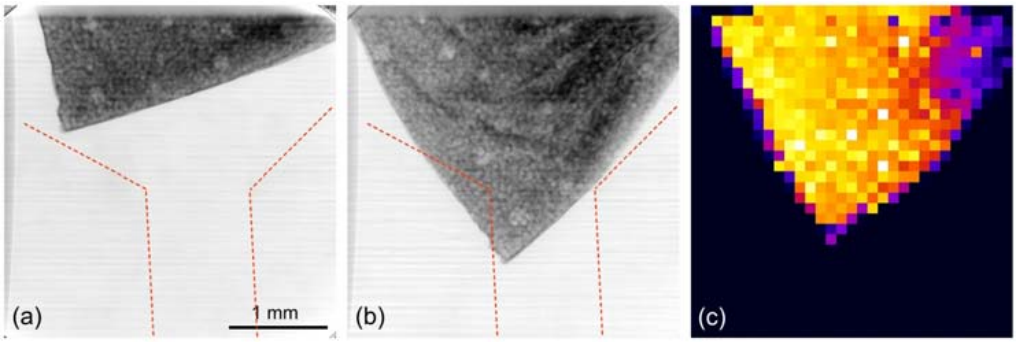

Figure 3.85: First (a) and last (b) radiographic image in sequence MB2. (c) MDA map. Colors represent values of $A = 0$ (black) to $A_{peak} \approx 11\,\mu\mathrm{m/s}$ (white).

velocity gradient with a peak displacement of $A_{peak} \approx 11\,\mu\mathrm{m/s}$ on the left hand side of Fig. 3.85c. Unfortunately the sample was too small to fill cavity which was larger than $3\,\mathrm{mm} \times 3\,\mathrm{mm}$ due to the fact that it had been prepared manually.

The series MB3-5 represent a constant piston speed ($v = 10\,\mu\mathrm{m/s}$) and varying temperature, i.e. decreasing solid volume fraction of the slurry from MB3 to MB5. Bigger sample foils were prepared to allow for good filling of the flow channel. Fig. 3.86a and b show the first and last radiograph of the sequence MB3 which corresponds to the lowest temperature $T =$

420 °C. The MDA map is depicted in Fig. 3.86c. Although more semi-solid slurry was pushed

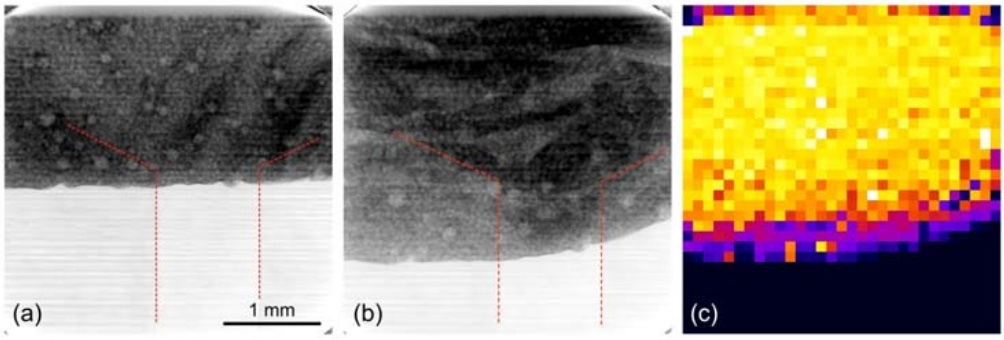

Figure 3.86: First (a) and last (b) radiographic image in sequence MB3. (c) MDA map. Colors represent values of $A = 0$ (black) to $A_{peak} \approx 11\,\mu\mathrm{m/s}$ (white).

into the channel, penetration of the latter is only observed in terms of thickness, in other words the darker parts of the sample silhouette in Fig. 3.86b show the outline of the channel (indicated by a dashed line in Fig. 3.86a) whereas the regions where material unexpectedly went into the gap between the BN plates appear bright. A maximum displacement amplitude of $A_{peak} \approx 11\,\mu\mathrm{m/s}$ was found in the upper parts of the Fig. 3.86c whereas the motion appears to slow down when the material reached the channel (lower part).

Fig. 3.87a and b show the first and last radiograph of sequence MB4. The MDA map is depicted in Fig. 3.87c (time-median over 3 images) featuring peak values of $A_{peak} \approx 11\,\mu\mathrm{m/s}$. Similar to MB3 semi-solid material went into the gap between the BN plates. This motion

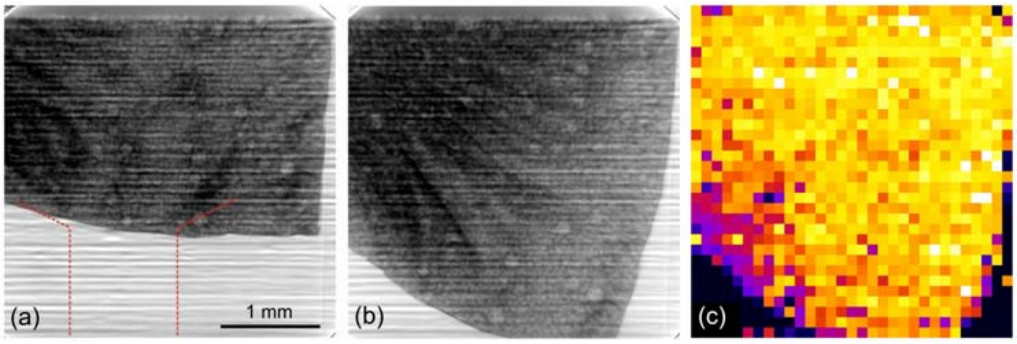

Figure 3.87: First (a) and last (b) radiographic image in sequence MB4. (c) MDA map. Colors represent values of $A = 0$ (black) to $A_{peak} \approx 11\,\mu\mathrm{m/s}$ (white).

was surprisingly found to be faster that the motion of the slurry at the entry of the flow channel (indicated by dashed line in Fig. 3.87a) where it appears to slow down. The rise in temperature does not show to have a significant effect.

Fig. 3.87a and b show the first and last radiograph of sequence MB5 ($T = 500\,°\mathrm{C}$), whereas the MDA map is depicted in Fig. 3.87c. As can be seen from Fig. 3.88b, strongly increased temperature led to a partial success with a maximum displacement map showing flow speeds of $A_{peak} \approx 11\,\mu\mathrm{m/s}$ indicating a parabolic speed profile around the main channel (appearing

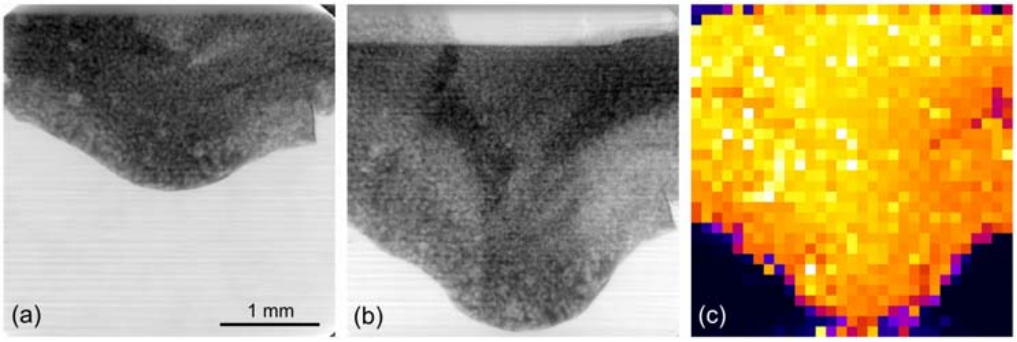

Figure 3.88: First (a) and last (b) radiographic image in sequence MB5. (c) MDA map. Colors represent values of $A = 0$ (black) to $A_{peak} \approx 11\,\mu\mathrm{m/s}$ (white).

as dark silhouette in Fig. 3.88b).
For the single-bunch beamtime at BESSY/BAM*line* (characterized by a reduced ring current of $25\,\mathrm{mA}$ instead of $250\,\mathrm{mA}$) precisely machined BN plates were used instead of manually prepared ones yielding striking improvements in flow control. Radiographs of the sequence SB1 at $t = 11\,\mathrm{min}$ and $t = 13\,\mathrm{min}$ are shown in Fig. 3.89a and b along with the MDA map (c). The liquid is observed to separate from the solid particles agglomerates, forming a *liquid*

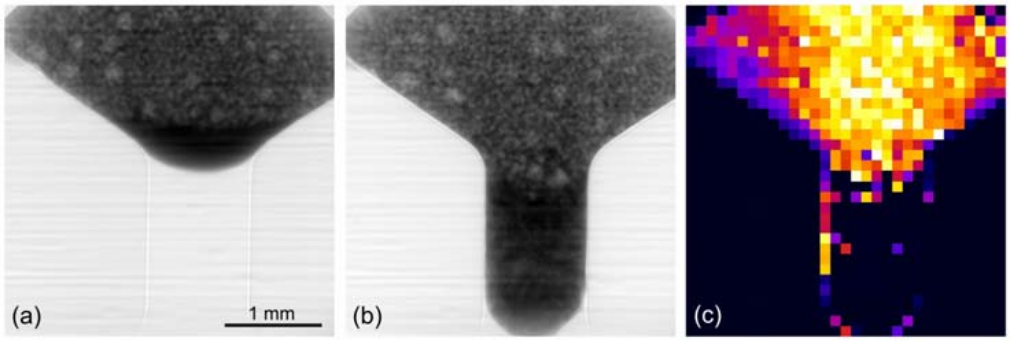

Figure 3.89: Radiographic images of sequence SB1 taken at $t = 11\,\mathrm{min}$ (a) and $t = 13\,\mathrm{min}$ (b). (c) MDA map. Colors represent values of $A = 0$ (black) to $A_{peak} \approx 10\,\mu\mathrm{m/s}$ (white).

front and penetrating the flow channel much faster than the Al-particles which remain at the entrance where the channel thickness decreases from $0.4\,\mathrm{mm}$ to $0.1\,\mathrm{mm}$. Solid and liquid follow the predefined geometry of the setup and do not penetrate the space between the two BN plates. Note that the displacement of the liquid front is so fast (estimated $22\,\mu\mathrm{m/s}$ from the radiographs) that it is not captured by the image cross-correlation and consequently, does not appear in Fig. 3.89c. The detection limit of the correlation is half the size of one element on the measurement grid, i.e. 32 pixel/frame $\approx 10\,\mu\mathrm{m/s}$ in x- and y-direction. Hence, the highest detected displacement amplitude is about 14 to $21\,\mu\mathrm{m/s}$ depending on the frame rate. Faster motion results in arbitrary values that are at least partially removed by the time-median filtering. Consequently, only the "slow" particle motion is seen in Fig. 3.89c revealing a funnel

shaped flow profile which shows increasing displacement amplitude towards the center of the cavity ($A_{peak} \approx 10\,\mu m/s$).
During experiment SB2 the piston was repeatedly moved up and down four times pushing the semi-solid slurry into the channel whereby the speed was increased step-wise from $v = 8\,\mu m/s$ to $v = 20\,\mu m/s$, $30\,\mu m/s$, $50\,\mu m/s$ and $80\,\mu m/s$ at constant working temperature at $T = 460\,°C$. Radiographs taken at $t = 6.6\,min$ and $t = 13\,min$ are shown in Fig. 3.89a and b along with the MDA map (c). The liquid front moving ahead of the solid particles was ob-

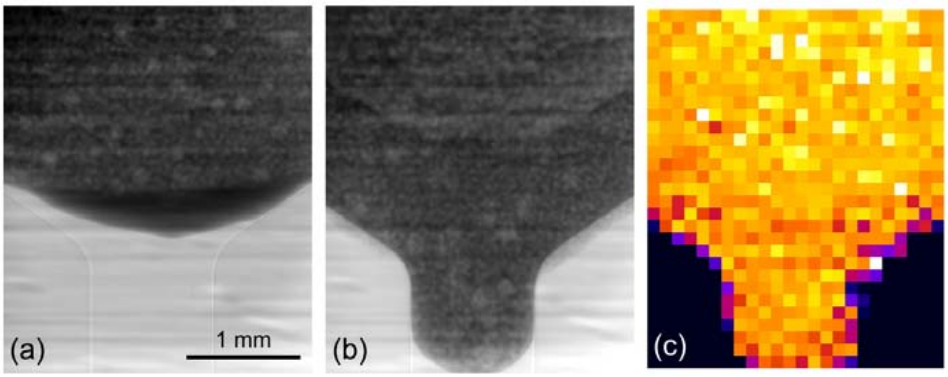

Figure 3.90: Radiographic images of sequence SB2 taken at $t = 6.6\,min$ (a) and $t = 13\,min$ (b). (c) MDA map ($A_{peak} \approx 17\,\mu m/s$).

served to withdraw from the channel when the piston is moved up again (suction). Therefore repeated pushing at increasing speed yielded a homogeneous filling of the flow channel with solid-liquid mixture (Fig. 3.90b). In contrast to the flow of the liquid melt and what would be expected from Bernoulli's principle (continuity equation) the particle movement slows down in the thin channel whereas faster motion is observed in the bigger sample cavity. Note that due to the high piston speed the peak values $A_{peak} \approx 17\,\mu m/s$ reach the limits of the method and higher velocities are probably not detected.
Fig. 3.89a-b shows three radiographs taken at a moderate piston speed of $v = 5\,\mu m/s$ during experiment SB3 at $t = 4.4\,min$, $t = 6.4\,min$ and $t = 19\,min$. The corresponding MDA map is depicted in Fig. 3.91d. The flow channel was fully filled during this experiment (the tip of the piston can be seen in the upper part of Fig.3.91c) revealing a very inhomogeneous motion of the agglomerated particles (Fig. 3.91a-d). Note that a time-median of radius 5 was therefore applied in order to reduce the strong scattering of the displacement vectors. The velocity of the liquid front preceding the solid particles was estimated from the radiographs to be $\sim 9\,\mu m/s$ in the channel. The calculated MDA of the particles shows peak values of $A_{peak} \approx 5.4\,\mu m/s$.
This experiment was repeated under identical conditions with a new sample (SB4). Three radiographs taken at $t = 9\,min$, $t = 16\,min$ and $t = 23\,min$ are shown in Fig. 3.92a-c, whereas the MDA map is depicted in Fig. 3.92d (again using a time median of radius 5). The flow of the liquid is seen to run ahead of the solid particles (estimated speed $15.9\,\mu m/s$). After the experiment the piston was withdrawn from the cavity and the liquid metal filling the lower

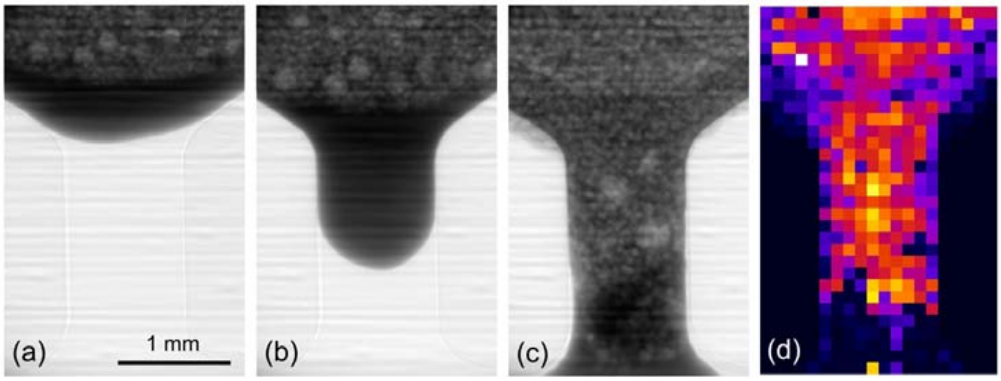

Figure 3.91: Radiographic images of sequence SB3 taken at $t = 4.4\,\mathrm{min}$ (a), $t = 6.4\,\mathrm{min}$ (b) and (c) $t = 19\,\mathrm{min}$. (d) MDA map ($A_{peak} \approx 5.4\,\mu\mathrm{m/s}$).

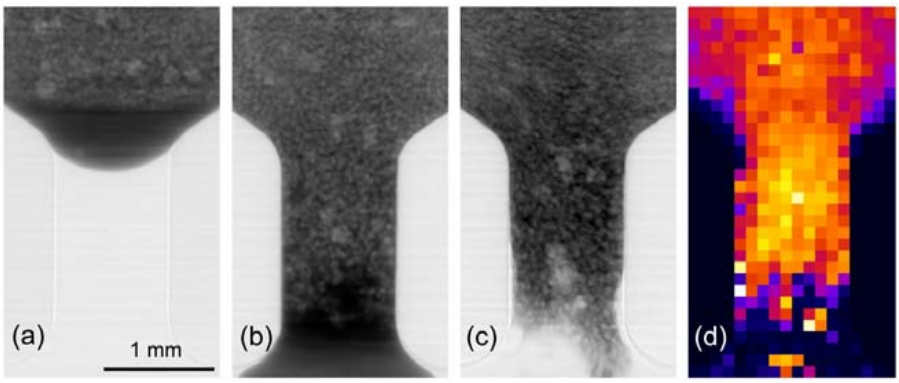

Figure 3.92: Radiographic images of sequence SB4 taken at $t = 4.4\,\mathrm{min}$ (a), $t = 6.4\,\mathrm{min}$ (b) and (c) $t = 19\,\mathrm{min}$. (d) MDA map ($A_{peak} \approx 5.4\,\mu\mathrm{m/s}$).

part of the flow channel was observed to withdraw leaving a dendrite branch of solid Al behind (Fig. 3.92c. This observation indicates that not only particle and liquid motion but also remelting and crystallization occur as a consequence of a strong concentration gradient of the constituent elements in the semi-solid slurry. Slight compaction of the Al-particle network is seen in the upper part of Fig. 3.92c. The MDA map shows velocities similar to SB3. ($A_{peak} \approx 5.4\,\mu\mathrm{m/s}$). This time the particle motion in the channel is slightly faster that outside (see Fig. 3.92d).

For the sequence SB5 the piston speed remained $v = 5\,\mu\mathrm{m/s}$ and temperature was raised to $T = 490\,°\mathrm{C}$. Three radiographs corresponding to $t = 5\,\mathrm{min}$, $t = 12\,\mathrm{min}$ and $t = 23\,\mathrm{min}$ are shown in Fig. 3.93a-c along with the calculated MDA map (Fig. 3.93d). Although particle motion is found to occur at similar speed the result is surprisingly different from the previous experiment. No liquid front is observed running ahead of the solid particles. The latter reach the middle of the flow channel then stop and pushing further only results in compaction of the solid phase. After 23 minutes the channel is almost entirely filled with aluminum (Fig. 3.93c). A rather homogeneous speed profile is observed for the particle motion which comes to a halt

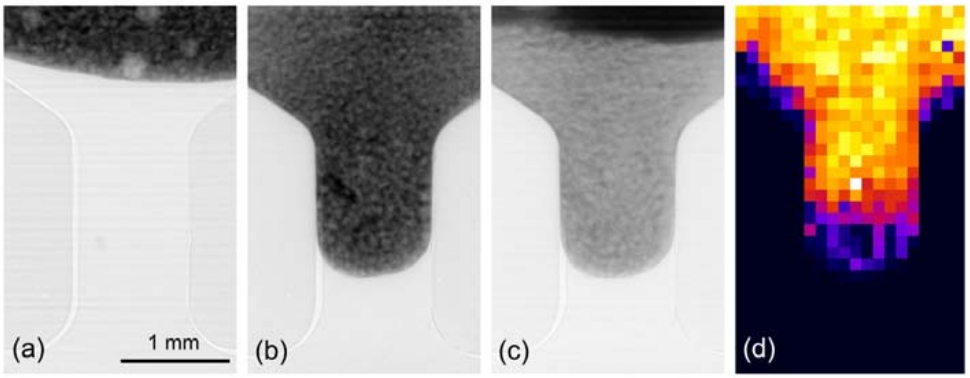

Figure 3.93: Radiographic images of sequence SB5 taken at $t = 5\,\mathrm{min}$ (a), $t = 12\,\mathrm{min}$ (b) and (c) $t = 23\,\mathrm{min}$. (d) MDA map ($A_{peak} \approx 5.4\,\mu\mathrm{m/s}$).

at the lowest position (time median of radius 5).
An intermediate result (SB6) could be produced by further raising the temperature to $T = 500\,°\mathrm{C}$ and increasing the piston speed to $v = 10\,\mu\mathrm{m/s}$. Fig. 3.94a-c show radiographs taken at $t = 5.5\,\mathrm{min}$, $t = 6.8\,\mathrm{min}$ and $t = 23\,\mathrm{min}$ along with the calculated MDA map (Fig. 3.94d). A moderate quasi-constant amount liquid precedes the particles which move at a peak velocity

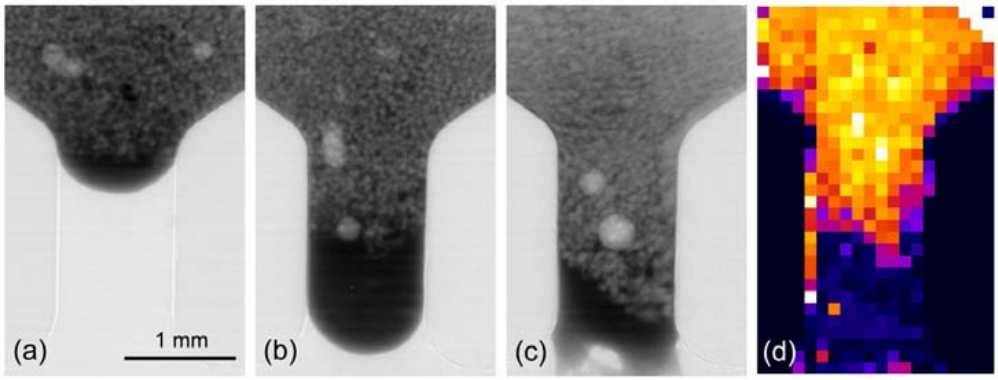

Figure 3.94: Radiographic images of sequence SB5 taken at $t = 5.5\,\mathrm{min}$ (a), $t = 6.8\,\mathrm{min}$ (b) and (c) $t = 23\,\mathrm{min}$. (d) MDA map ($A_{peak} \approx 11\,\mu\mathrm{m/s}$).

of $A_{peak} \approx 11\,\mu\mathrm{m/s}$. The the liquid is slightly faster progressing at an estimated speed of $18\,\mu\mathrm{m/s}$. Compaction of the solid phase mainly occurs in the upper funnel probably due to obstruction at the channel entrance (see Fig. 3.94c).
After each experiment the sample were cooled and if possible metallographic sections were prepared of the remanent AlGe32 alloy. Microscope images of the samples MB5, SB1, SB3, SB4, SB5 and SB6 are shown in Fig. 3.95. The large variety of microstructures, solid content and channel filling shows how strongly experimental conditions can influence the microstructure of cast components. MB5, SB1 and SB2 feature round globular Al-particles whereas a dense compressed matrix is observed in the samples SB5 and SB6. The structure of SB4 shows both globular particles in the lower part (corresponding to the thin channel) and com-

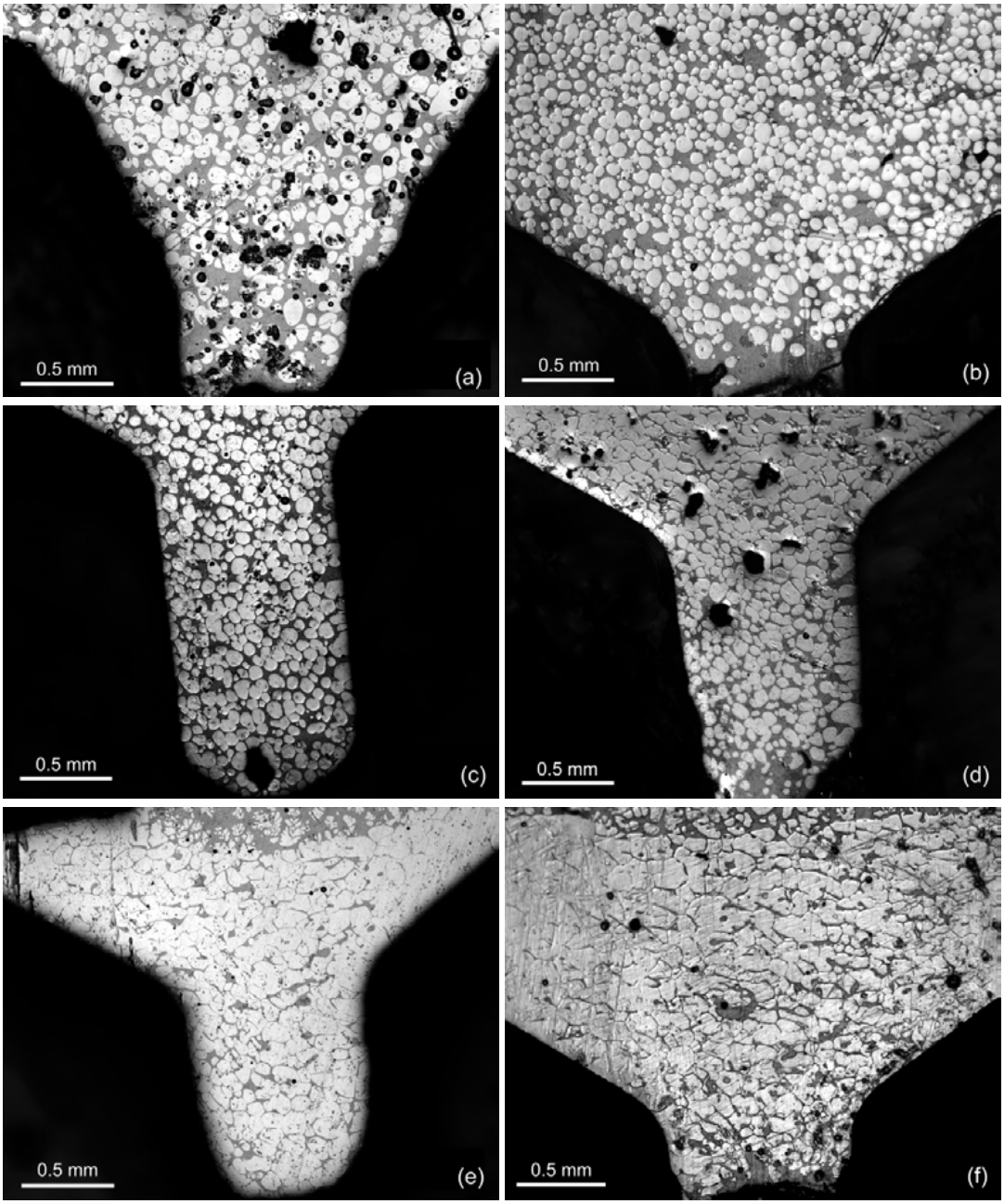

Figure 3.95: AlGe32 microstructure after the radioscopy experiments: (a) MB5, (b) SB1, (c) SB3, (d) SB4, (e) SB5 and (f) SB6.

pacted aluminum in the upper 'funnel' part.

During these 'slow' experiments at Bessy/BAM*line* de- and re-agglomeration of Al-particle clusters, commonly associated to the thixotropic effect, was not observed. Therefore an additional high-speed experiment was carried out with a PCO 1200hs CMOS camera at the ESRF/ID19 beamline. Due to the high X-ray flux a frame rate of $r = 67\,\mathrm{fps}$ was achieved employing a single double multilayer monochromator to select a photon energy of $E = 17\,\mathrm{keV}$

and using a GADOX converter screen ($\Delta x = 8.3\,\mu\mathrm{m}$ effective pixel size at $R \sim 15-20\,\mu\mathrm{m}$ resolution). The piston speed was $v = 2\,\mathrm{cm/s}$ (Newport linear stepping motor) and Fig. 3.96 shows four radiographs taken at $t = 1.155\,\mathrm{s}$, $t = 1.320\,\mathrm{s}$, $t = 1.455\,\mathrm{s}$ and $t = 1.815\,\mathrm{s}$. The

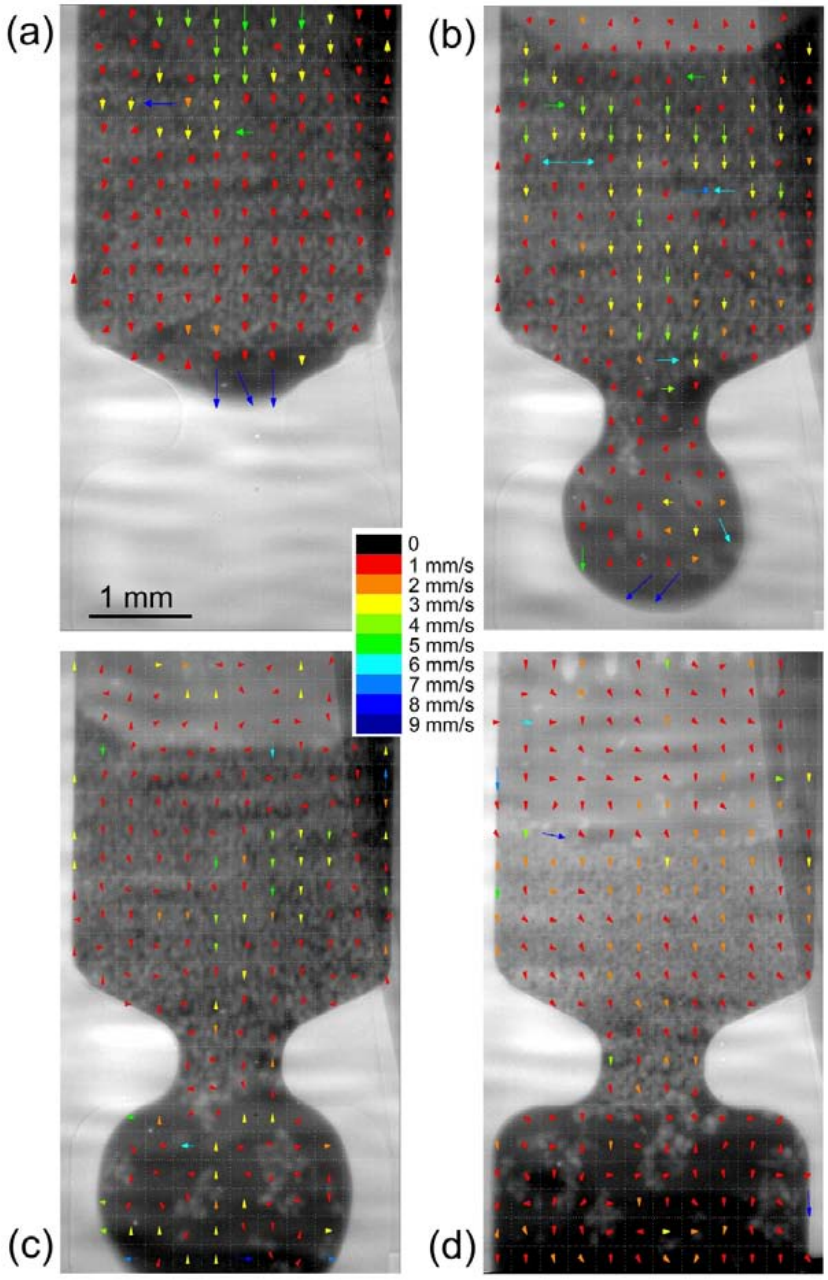

Figure 3.96: High-speed radiography images taken at (a) $t = 1.155\,\mathrm{s}$, (b) $t = 1.320\,\mathrm{s}$, (c) $t = 1.455\,\mathrm{s}$ (d) and $t = 1.815\,\mathrm{s}$.

virtual grid (32 pixel spacing) and the $(\Delta x, \Delta y)$ calculated displacement vectors are superimposed onto these images showing a maximum velocity of $9\,\mathrm{mm/s}$ (detection limit of the image cross-correlation). While a quasi-laminar vertical particle flow is observed in the sample cav-

ity (cf. upper part in Fig. 3.96b) reaching a maximum speed of $\sim 4\,\mathrm{mm/s}$ towards the middle and slowing down towards the borders, the particle motion almost comes to a halt at the entry of the $0.2\,\mathrm{mm}$ thin channel. First a liquid front is injected with high speed into this channel (a peak velocity of $\sim 13\,\mathrm{mm/s}$ is estimated from the radiographic images). Once a certain amount of liquid is filling the recipient (round droplet in Fig. 3.96b) small clusters of $10 - 20$ aluminum particles disconnect from the solid skeleton and shoot right through the channel into the recipient. The trajectory of these clusters is blurred due to their high speed (estimated from the radiographic images to $\sim 10\,\mathrm{mm/s}$). When the piston moves further down (Fig. 3.96c), agglomerates of Al-particles pile up in the thin channel hindering further clusters from traversing the channel. Meanwhile further liquid is injected causing a turbulent movement of the few Al-clusters in the recipient. In the final stage a net depletion of Al-Ge melt and compaction of Al-particles is seen in the sample cavity (Fig. 3.96d). Since no more liquid is injected in to the channel the turbulent motion of the Al-clusters in the recipient has stopped. These cluster however do not remain still but slowly float up along the recipient walls then re-agglomerate with the particles that were piled-up in the thin channel. The result of the process is a complete filling but a very inhomogeneous microstructure as can be seen from a metallographic section of the retrieved material (Fig. 3.97). Note that fine Al-particle crystallized in the recipient

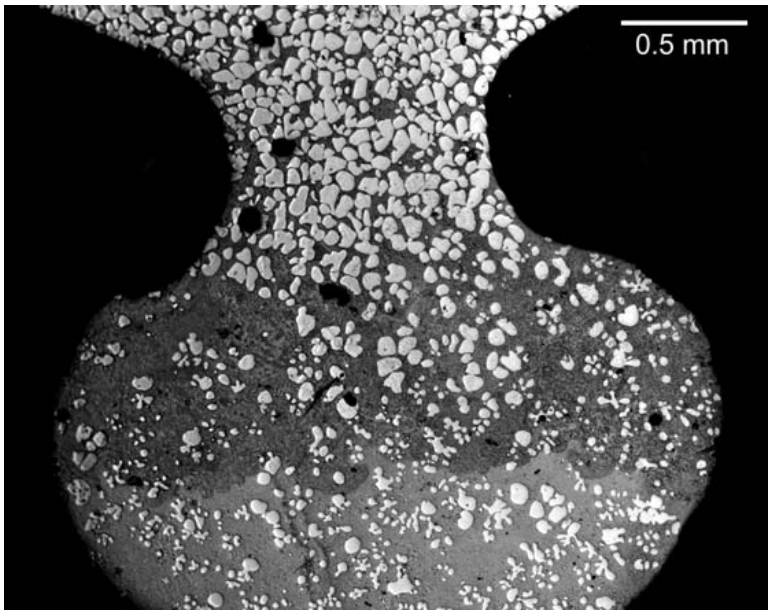

Figure 3.97: Metallographic section of the AlGe32 material retrieved from the high-speed injection experiment at ESRF/ID19.

during cooling of the sample (experiment took place at $470\,°\mathrm{C}$ while the solidus temperature is $T_s \approx 420\,°\mathrm{C}$).

Discussion: Variation of processing temperature and piston speed was tested for the *slow injection* regime using time-resolved radioscopy at BESSY/BAM*line* . During most tests a liq-

uid front preceded the progressing particle network leading to strong liquid/solid concentration gradients in the channel and recipient. Separation of liquid and solid could be partially avoided by raising the temperature but compaction of the Al-network was the immediate consequence. Finally the velocities of liquid and solid were observed to converge for a very particular piston velocity ($10\,\mu\mathrm{m/s}$) and temperature ($T = 500\,°\mathrm{C}$) but further studies are needed to prove whether such a ratio can also be found for lower temperatures in order to avoid compaction of the solid phase.

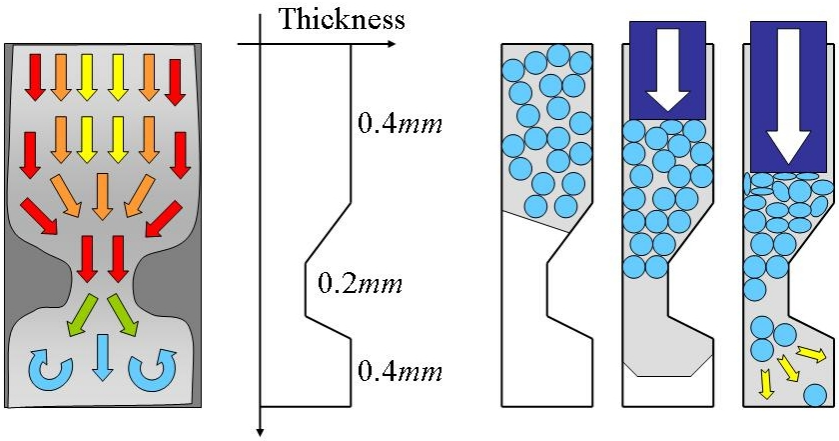

Figure 3.98: Schematic explanation of the semi-solid high-speed injection observed during beamtime at ESRF/ID19.

Unlike the slow injection experiments, the high-speed radioscopy data recorded at ESRF/ID19 clearly showed the de-agglomeration and re-agglomeration of solid Al-clusters. This observation strongly emphasizes that high-injection velocities are needed to produce this behavior which is associated with the thixotropic effect in semi-solid alloys. The results of the high-speed experiment are schematized in Fig. 3.98.

3.4.2 Porosity in single-crystal nickel-base superalloys

Modern generations of nickel-base superalloys contain a higher concentration of refractory elements in order to increase the working temperatures of turbine blades. A side effect is a stronger dendritic segregation during solidification, making an extensive homogenisation necessary. The porosity, concentrated on the interdendritic region increases during such a heat treatment. Afterwards not only irregular shaped solidification pores (S pores) but also spherical homogenisation pores (H pores) are observed [Epi02]. Modern superalloys are used at very high temperatures up to $1100\,°\mathrm{C}$ for long times. In the framework of a cooperation with the materials department at the technical university of Berlin, the formation of a third class of pores was investigated: Deformation pores (D pores) [Lin06]. D pore formation increases with temperature and creep time and is correlated to creep strain. This kind of material degradation has to be taken into account for high temperature/long term applications.

Materials and method: The investigated materials were 4 different single crystal superalloys, CMSX-6, SRR99, CMSX-4 and CMSX-10, grown by dendritic solidification in [001] direction. With increasing content of refractory elements (Mo, Ta, W, Re) higher temperatures for homogenisation are applied mostly combined with longer holding times (Tab. 3.12). Casting and heat treatment was performed by Doncasters Precision Casting, Bochum, Germany.

superalloy	Mo+Ta+Re+W [wt %]	Max. Temp [°C]	Total time [h]
CMSX-6	4.9	1280	10
SRR99	13.1	1303	5
CMSX-4	16.5	1303	9
CMSX-10	20.5	1366	20

Table 3.12: Single crystal superalloys with increasing concentration of refractory elements. Homogenisation of the dendritic segregation needs higher temperatures and longer times.

Creep tests were carried out on CMSX-4 at $T = 1100\,°\mathrm{C}$ constant temperature applying a continuous load in the [001] direction of the crystals ranging from 105 to $135\,\mathrm{MPa}$. Some of the tests were interrupted, others run until fracture in order to study the evolution of porosity during the creep process. Table 3.13 resumes samples and main results.

superalloy	T [°C]	load [MPa]	time [h]	porosity [%]	pores [mm^{-3}]	diameter [μm]
CMSX-6	-	-	-	0.05	1246	9.5
SRR99	-	-	-	0.16	5459	8
CMSX-4	-	-	-	0.17	3776	9.5
CMSX-10	-	-	-	0.30	2102	15
CMSX-4	1100	120	25	0.15	3032	9.5
CMSX-4	1100	120	150	0.17	6055	10.5
CMSX-4	1100	120	292	0.30	7845	11, 7
CMSX-4	1100	117	392*	0.33	11894	11.5, 7.5
CMSX-4	1100	135	149*	0.39	10840	12, 8
CMSX-4	1100	105	692*	0.20	3613	11

Table 3.13: Investigated superalloys, testing parameters, maximum of the sphericity distribution and porosity. *) Tests were run until fracture.

For tomography investigations bars of $0.5\times\ 0.5\,\mathrm{mm}^2$ cross section (in plane with the secondary dendrite arm directions [100] and [010]) and $14\,\mathrm{mm}$ length were cut along direction of the primary dendrite arms [001] (PDA). The sharp corners of the 100 surfaces were removed by electro polishing. X-ray tomograms with a resolution of $R \sim 1\ \mu m$ were recorded at the European synchrotron radiation facility (ESRF/ID19), Grenoble, France prior to the present

work. For each specimen a volume of approx. $0.5 \times 0.5 \times 1.0\,\mathrm{mm}^3$ was recorded at $E = 50\,\mathrm{keV}$ photon energy. After processing the tomograms (e.g. ring artifact filtering, see section B.2), each pore was addressed by its position and characterized by geometrical parameters. Analysis of this data allowed to correlate material, heat treatment and test parameters with those of the porosity.

Results: In a first step the porosity in four different undeformed and fully heat treated superalloys was measured. Fig. 3.99a shows the correlation between refractory element concentration and porosity along with the pores' volume partition as a function of the equivalent pore diameter a (Fig. 3.99b). The volume partition is the product of the pore volume V and the

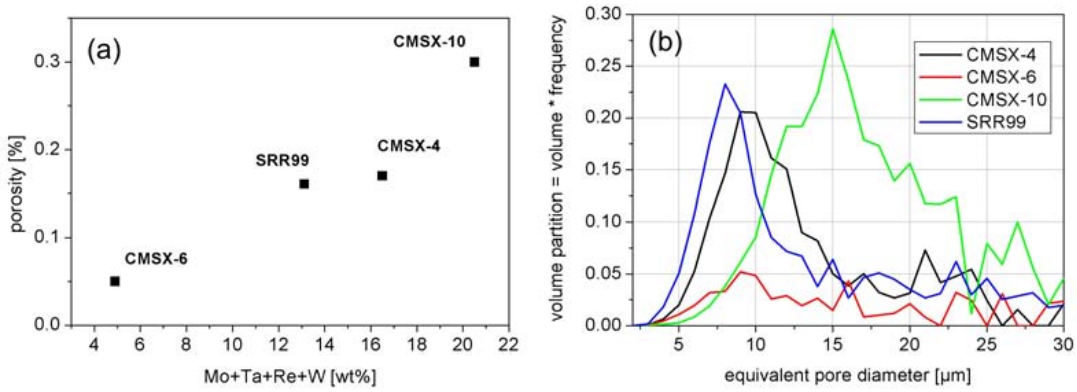

Figure 3.99: (a) Correlation between porosity and content of refractory elements. (b) Volume partition in standard heat treated (SHT) undeformed superalloys as a function of the equivalent pore diameter a.

number of pores with the equivalent pore diameter $a = \sqrt[3]{6V/\pi}$. Obviously the total porosity as well as the average pore size increase along with the concentration of refractory elements (Fig. 3.99a). The peaks in the volume partition between $a = 7\,\mu\mathrm{m}$ and $a = 15\,\mu\mathrm{m}$ (SR99 and CMSX-4) are identified as H-pores, those pores with larger diameters a are S-pores. It can be seen that the long term homogenisation results in an increase of H-porosity. These pores forms the most important porosity in superalloys with a high content of refractory elements (e.g. CMSX-10).

The influence of high temperature creep on porosity was investigated in CMSX-4, which was selected, because it is most commonly used in turbine blades. Fig. 3.100 shows the correlation between porosity and creep time (a), as well as between sphericity $F = 6V\sqrt{\pi/A^3}$ and creep time (b), for continuous creep deformation at $T = 1100\,°\mathrm{C}$ and $120\,\mathrm{MPa}$ constant load. The total porosity increases steadily reaching approx. twice the initial value until rupture occurs after $\sim 400\,\mathrm{h}$ creep time (Note that $117\,\mathrm{MPa}$ were applied for the longest deformation).

Fig. 3.100 shows the maximum values of the F distributions of the CMSX-4 samples, undeformed and creep deformed at $120\,\mathrm{MPa}$ and $117\,\mathrm{MPa}$. With increasing creep time the pores become more aspherical (note that $F = 1$ for a sphere and $F < 1$ for other shapes) approach-

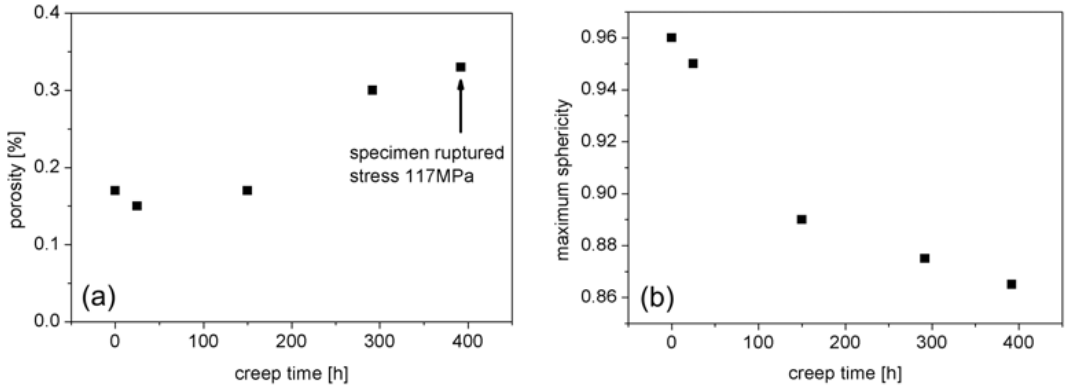

Figure 3.100: Increase of porosity during creep at 1100 °C. The points between 25 h and 300 h belong to interrupted creep tests at 120 MPa, the last one to a test run until rupture at 117 MPa. All specimens from one batch.

ing a sphericity value of $F \approx 0.86$.

More details about the pores' size and shape are observed in the volume partition and the sphericity distribution, depicted in Fig. 3.101a and b, respectively.

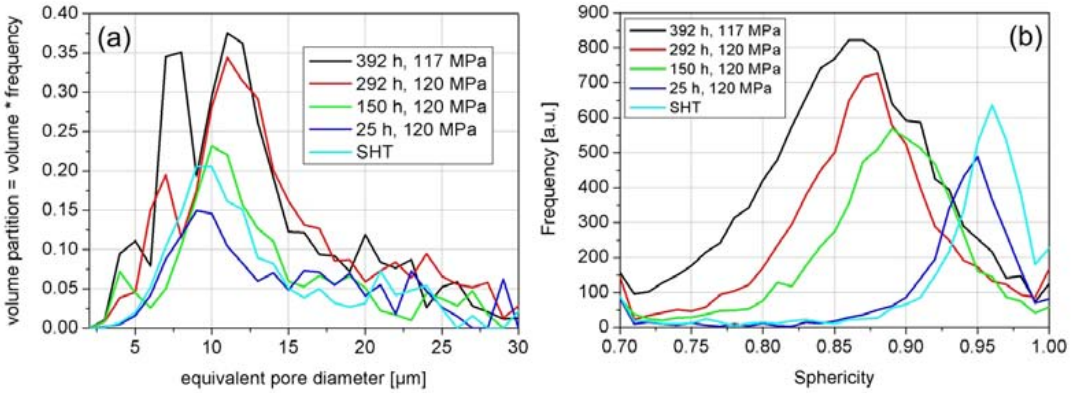

Figure 3.101: Change of the porosity in CMSX-4 during creep at $T = 1100$ °C. The 392 h specimen was loaded with 117 MPa, the other sample with 120 MPa. (a) Volume partition as a function of equivalent pore diameter a. (b) Sphericity F distribution.

The characteristic peaks in the pore volume partition both increase and shift towards larger pores. Consequently the increase of total porosity (Fig. 3.100a) comprises pore growth and pore generation. Note that a new class of small pores develops for long creep times. After 150 h a small peak can be recognised corresponding to pores of $a \approx 4\,\mu\text{m}$. After 292 h this peak is more pronounced and shifted to $a \approx 7\,\mu\text{m}$, whereas after 392 h a sharp peak is observed at $a \approx 8\,\mu\text{m}$ pore diameter. Meanwhile the volume partition of larger pores (seen as a broad peak at $a = 10-12\,\mu\text{m}$) is continuously increasing and slightly shifting towards larger diameters, thus contributing significantly to the increase of total porosity.

Undeformed CMSX-4 is mostly characterized by spherical pores ($F = 0.9-1.0$, H-pores) and

only few irregularly shaped pores ($F < 0.9$, S-pores) are observed in the sphericity distribution (Fig. 3.101b). During creep deformation the shape of the pores becomes more aspherical with increasing creep time. After $150\,\mathrm{h}$ the maximum of the sphericity distribution has clearly shifted towards smaller values $F < 0.9$. Presumably the round pores which characterize the undeformed sample are microscopically transformed approaching a more polyhedral shape. Comparing visually the tomography data of undeformed CMSX-4 with that of a specimen deformed at $1100\,^{\circ}\mathrm{C}$ and $117\,\mathrm{MPa}$ for $392\,\mathrm{h}$ confirms this assumption: The pores are changing their shape during creep deformation (cf. Fig. 3.102).

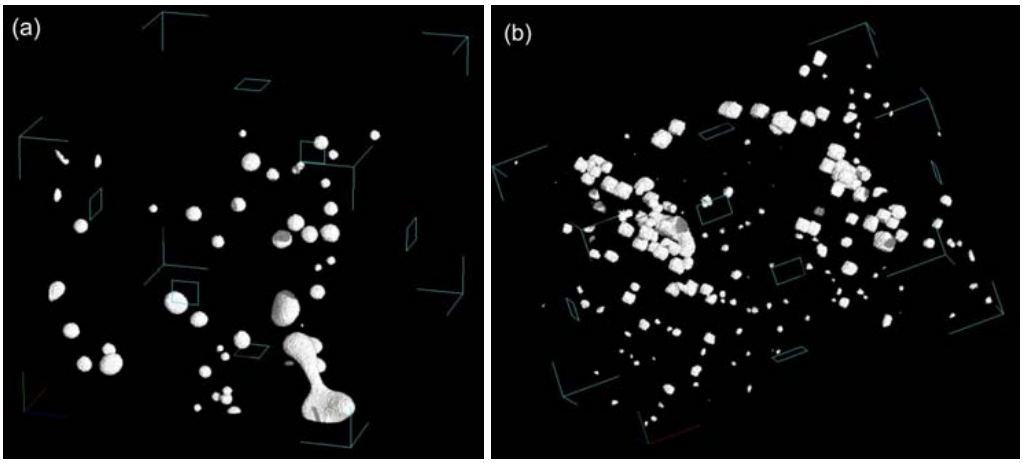

Figure 3.102: The shape of the pores changes from spherical pores after heat treatment to polyhedral pores after creep deformation. (a) CMSX-4 undeformed. (a) CMSX-4, $1100\,^{\circ}\mathrm{C}$, $117\,\mathrm{MPa}$, $392\,\mathrm{h}$. Dimension of the volumes: $295 \times 180 \times 210\,\mu\mathrm{m}^3$.

Next the spatial arrangement of the pores was analyzed. A frontal view onto the pores with the vertical axis coinciding with the primary dendrite arm (PDA direction) (Fig. 3.103a) indicates that the pores are arranged along the dendrites. Unfortunately the latter cannot be observed in absorption tomograms because the density contrast of this imaging technique is too weak. However, in scanning electron microscopy (SEM) neighboring dendrites can be distinguished due to a orientation mismatch of $\sim 1^{\circ}$ causing a sufficient intensity contrast [Bru97]. Comparing Fig. 3.103a with b and c reveals that the pores are highly localized at the low angle boundaries between dendritic subgrains. Calculating virtual projection images of the porosity along the PDA direction highlights this result (Fig. 3.104). The spatial distribution of the pores reflects surprisingly well the dendrite boundaries in undeformed samples of CMSX-10 (Fig. 3.104a) and CMSX-4 (Fig. 3.104b). During creep deformation the round pores in these regions are observed to transform into polyhedral pores (Fig. 3.104c and d). Before deformation the primary and secondary dendrite arms contain almost no porosity. After $150\,\mathrm{h}$ creep deformation at $1100\,^{\circ}\mathrm{C}$ and $120\,\mathrm{MPa}$, small pores start forming in these areas close to the dendrite boundaries. These pores will be referred to as D pores. Density and size of the D pores increases after $392\,\mathrm{h}$ deformation. Still their density drops towards the dendrite centers.

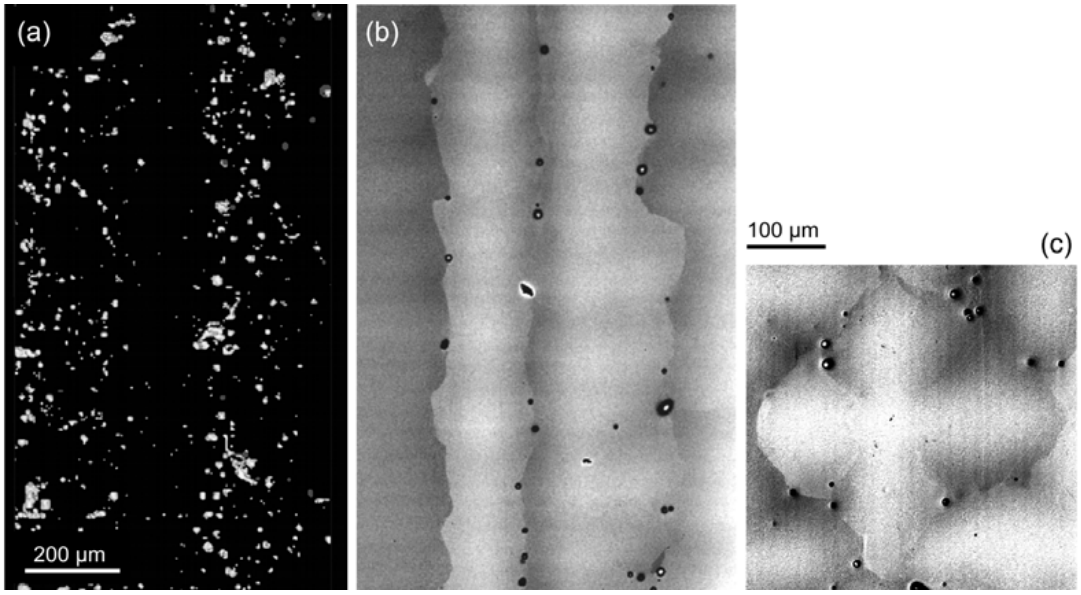

Figure 3.103: Porosity in CMSX-4: (a) Projection of the pores in CMSX-4, 1100 °C, 117 MPa, 392 h into the (100)-plane parallel to the PDA direction. (b+c) Dendritic structure in undeformed CMSX-4. SEM back scatter electron images of (100)-sections (b) and (001)-sections (c). The pores are placed mostly in the subgrain boundaries between the dendrites. Sharp contrasts: orientation contrast, smooth contrasts: material contrast.

Fig. 3.105 shows the volume partition of pores in strongly deformed fractured CMSX-4. The appearance of D pores seems to depend mostly on the applied creep stress. No sign of D pore formation is observed after 692 h when the material is deformed under relatively low stress (105 MPa), whereas a very pronounced volume partition of D pores is observed after 145 h deformation at higher creep stress (135 MPa). The same test (150 h creep time) but with slightly lower stress produces no D pores. For the 120 MPa sample, a very small peak in the volume partition around $a \sim 4\,\mu\mathrm{m}$ might indicate the beginning of D pore formation.

Discussion Solidification pores are known to exist in the interdendritic region of superalloys. However, little is known about the influence of high temperature creep on this porosity. While Sherry and Ai state, that no new pores are generated during creep [She90, Ai92], more detailed investigations from Komenda and Epishin lead to opposite conclusions [Kom97, Epi02]. In CMSX-4 an increase of small pores $a < 6\,\mu\mathrm{m}$ during creep at 950 °C was found [Kom97]. Generation of new pores during creep was confirmed for CMSX-4 and CMSX-10 by Epishin et al., who observed D pores of polyhedral shape [Epi02]. For CMSX-4 these pores have 110, for CMSX-10 100 facets. Polyhedral pores with 110 facets have been reported earlier by [She90] for SRR99 after 100 h of creep deformation at $T = 1050$ °C and 160 MPa creep stress.

Reasons for the generation of D-pores were discussed in [Epi04]. The raft formation during high temperature creep allows dislocation movement along the γ/γ'-interfaces perpendicu-

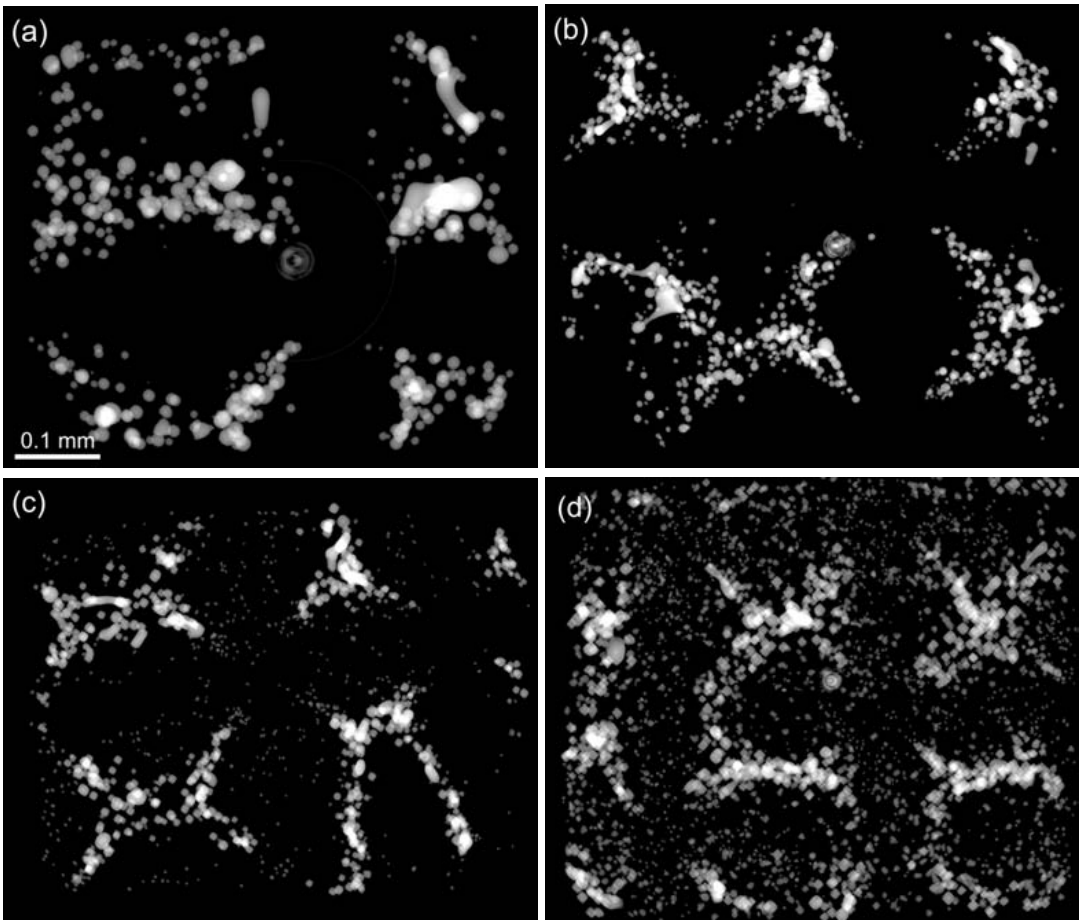

Figure 3.104: Axial projection of porosity onto (001)-plane perpendicular to the PDA direction in (a) CMSX-10 and (b) CMSX-4 superalloy. Formation of creep pores in CMSX-4 at 1100 °C: (c) 150 h, 120 MPa, (d) 392 h, 117 MPa.

lar to the stress direction but prevents dislocation climb parallel to the stress direction. This anisotropy of dislocation climb has the consequence that the vacancies generated in the interfaces are not absorbed by dislocations climbing in perpendicular directions. Plastic deformation and vacancy generation take part everywhere in the dendritic structure. However, D pore formation is mostly observed in the interdendritic area (cf. Fig. 3.104). This observation can be explained with the mosaic structure of the dendrites. Obviously crystalline defects supply a vacancy draining system towards the interdendritic area, where the increasing vacancy concentration leads to a condensation, observed as D pores. These crystalline defects act as nucleation centers and the fact that D pore formation is most pronounced at the centers of highest creep stress is in full agreement with this interpretation. For low creep rates the vacancies have enough time to diffuse to the subgrain boundaries and join the pre-existing S and H pores. With higher creep rate the vacancy generation rate increases along with the probability to meet other vacancies before reaching the interdendritic area.

This work revealed that pores in the undeformed samples are highly spherical. The transfor-

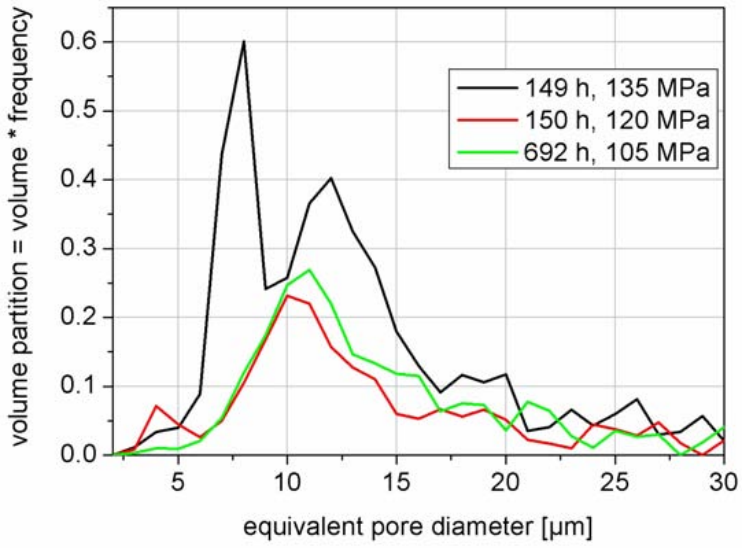

Figure 3.105: Pore size distribution in CMSX-4 specimens, creep ruptured at $T = 1100\,°\mathrm{C}$ under different creep stresses ($135\,\mathrm{MPa}$, $120\,\mathrm{MPa}$ and $105\,\mathrm{MPa}$).

mation of their shape (Figs. 3.102-3.101) takes part in course of the vacancy condensation during creep. Scanning electron microscopy images of high spatial resolution (SEM, Fig. 3.106) reveal further detail of this pore shape transformation. Very small pores are faced by

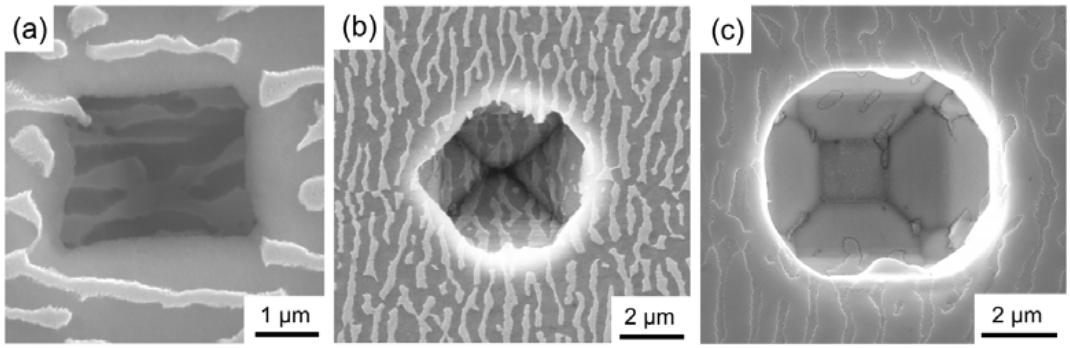

Figure 3.106: SEM images of polyhedral pores forming during creep deformation at $T = 1100\,°\mathrm{C}$. (a) CMSX-4 deformed for $292\,\mathrm{h}$ under $120\,\mathrm{MPa}$ creep stress; (b) CMSX-4, deformed for $150\,\mathrm{h}$ under $120\,\mathrm{MPa}$ creep stress; (c) CMSX-10 deformed for $200\,\mathrm{h}$ under $120\,\mathrm{MPa}$ creep stress.

100 surfaces (fig. 3.106a), bigger ones by 110 surfaces (fig. 3.106b). Fig. 3.106c shows, that both types of surfaces can be combined in one pore.

Pore analysis on the tomography data showed that the sphericity evolves towards $F = 0.86$ and the F distribution of the pores remains monodispersed (cf. Fig. 3.101). The statistical results from tomography can be interpreted by calculating the sphericity F for the particular geometries of individual pores that were observed in the SEM. Cubic pores (6 facets) were

associated to 100 surfaces , dodecaedrons (12 facets) to 110 surfaces and cubo-dodecaedron pores (18 facets) to mixed 100 and 110 surfaces. Although not observed in the SEM octahedral pores (8 facets, formed by 111 surfaces) were considered for the sake of completeness. Fig. 3.107 shows the correlation between the sphericity F and the reciprocal number of facets n^{-1}. Consequently the D pores that were observed in CMSX-4 to approach a sphericity $F = 0.86$

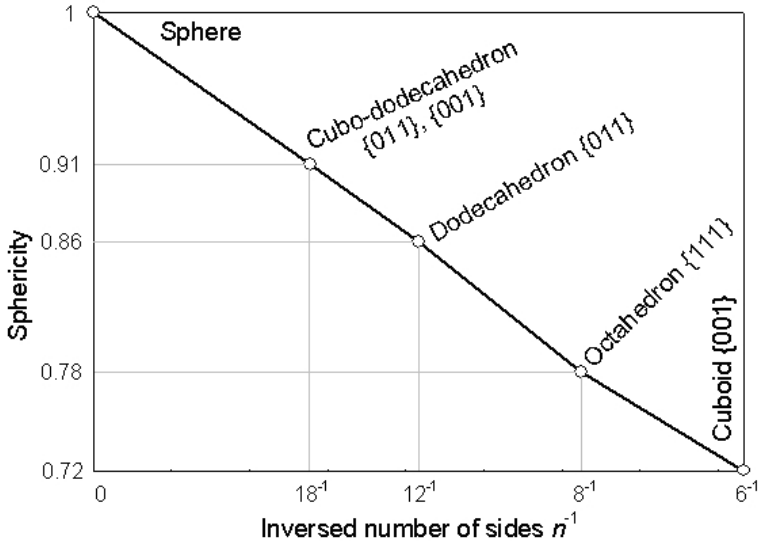

Figure 3.107: Decrease of sphericity F with the formation of polyhedral pores. Each polyhedron has ideal shape, i.e. its shape was optimized to give the maximal sphericity. For the sphere a face number $n = \infty$ is assumed.

would converge towards dodecahedral shape. Furthermore, Fig. 3.106a indicates that small round S pores first take a cubic shape before transform into dodecahedral D pores. According to Fig. 3.107 spheres would have to reduce their number of facets, whereas cubes have to increase n to reach $n = 12$. This interpretation is supported by the F distribution of the $392\,\mathrm{h}$ specimen in Fig. 3.101b, where pores of $F = 0.7$ to 1.0 are observed possibly including cubes and spheres.

Chapter 4

Conclusions and Outlook

The unique capabilities of X-ray imaging with partially coherent synchrotron light were successfully applied to study dynamical and static properties of various material systems. The coarsening kinetics in semi-solid aluminum-germanium alloy were analyzed and found to be in good agreement with classical theory. Based on sequentially acquired tomograms, new 3D characteristics of self-similar coarsening were defined. Additional experiments revealed significant differences between the coarsening of alloys with equiaxed and dendritic microstructures. Furthermore, a novel 2D radiography experiment was developed and applied to study ripening and flow in semi-solid metallic mixtures in situ. Fresnel-propagated imaging was applied to an engineering AZ91 alloy in order to enhance the particle-particle interfaces and to quantify the microstructural transformations taking place when high shearing rates are applied to semi-solid slurry. Three-dimensional particle parameters revealed that the transition from small dendrites to large globules takes place via discrete particle classes. In the limit of long shearing times, only one class - large globular particles - remains, and sphericity is found to increase for higher shearing rates. Phase imaging was developed at BAM*line* and applied to AZ91 alloys. Additional holotomograms were recorded of various Al-Si alloys as well as AZ91 during beamtime at ESRF/ID19. Holotomography showed to be the only technique, capable of accurately imaging the 3D microstructure in these alloys.

Time-median Fresnel-propagated imaging was developed to record the microstructure of human tooth dentin. Stray intensities, originating from bubbles that form when water is exposed to a high flux of hard X-rays, are mostly suppressed whereby the overall signal-to-noise ratio is improved. Detailed simulations and a priori knowledge about the tubules and their sheaths of peritubular dentin were combined to provide direct interpretation to the Fresnel-propagated images. Based on these simulations, the individual interference fringes, centered around each tubule, can be interpreted in terms of PTD thickness and density. Information from images recorded at various propagation distances can be combined to avoid vanishing contrast for a critical thickness of peritubular dentin. A 3D algorithm was developed, based on the fast Fourier-transformation, to analyze the orientation, density and characteristics of the tubules. With increasing distance from the dentin-enamel junction (DEJ) the size of the tubules as well as the thickness of their peritubular sheaths increase, whereas right underneath the DEJ a less denser packing of tubules is observed.

Application of absorption and Fresnel-propagated imaging to study crack formation in rocks revealed significantly different fracture-properties in limestone, basalt, granite and greywacke - the four types of rock that were tested in this work. Oblique fracture is observed in greywacke,

and quasi dynamic absorption tomography could relate cracking to the microstructure of this rock. Particularly old healed cracks which are filled with iron oxides were shown to align with the newly forming cracks. Consequently a preferred microstructural orientation was shown to favor crack propagation in this material. Classical theory of cracking was shown to apply on the micrometer scale where coalescence between tiny tensile cracks preceding fracture is observed in the Fresnel-propagated images. Limestone shows columnar fracture and developing cracks were found to (down)scale with the average grain size in sedimentary rocks. Further particularities of cracks in basalt and granite were revealed by X-ray Fresnel-propagated tomography and scanning electron microscopy. A single twisted crack developed in basalt whereas multiple cracks formed *inside* the granite. 2D deformation maps were calculated from the tomograms revealing macroscopic tensile and shear fractures in greywacke and basalt.

In the framework of user-operation and cooperation, some further projects were carried out during this thesis. Imaging the evolution of porosity in single-crystalline Ni-based superalloys, when the latter is exposed to high temperature creep deformation, revealed the existence of creep pores as well as the morphological transformation of round S-pores into cubic and/or octahedral pores. The capabilities of synchrotron radiation for the differential imaging of the iron content in insect organs was tested on a larva. Further measurements are scheduled to quantify the exact chemical sensitivity of this method.

By the end of this work, the imaging system and the processing software at BESSY/BAM*line* are fully operational and the above mentioned results reveal a large potential of these techniques, to provide further insight into metallic, rock-type and biomineralized materials. Future experiments on particle coarsening and deformation of semi-solid alloys are scheduled and will apply tomographic X-ray imaging to observe the 3D microstructure in situ. Large amounts of 3D data on tooth dentin, representing a large variety of teeth and local dentin structure in the latter, were acquired towards the end of this thesis and are likely to reveal many secrets about the functioning of teeth. Fresnel-propagated in vivo plant tomography and paleobiology are two more promising applications on the BAM*line* μCT that have recently been successfully tested.

Appendix A

Instrumentation

A.1 BESSY and the 7T-WLS hard X-ray source

BESSY was initially designed as a highly brilliant infrared /soft X-ray source generating a $200\,\mathrm{mA}$ electron multibunch current in the storage ring ($240\,\mathrm{m}$ in circumference). The construction of BESSY's first hard X-ray ($E > 10\,\mathrm{keV}$) beamline was first announced in 2001 [Gör01], three years after the synchrotron started operation. The BAM*line* was planned and set up by the federal institute for materials research and testing (BAM) and the federal office for engineering physics (PTB) as a multi-purpose beamline operating at a superconducting 7 Tesla wavelength shifter (WLS). The WLS was built at Novosibirsk and designed to produce a characteristic X-ray energy of $13.5\,\mathrm{keV}$, given the electron energy of the ring to be $1.7\,\mathrm{GeV}$. According to the layout two main optical elements were installed, namely a double multilayer monochromator (DMM) and a double crystal monochromator (DCM). While the PTB restricted its plans for the BAM*line* to primary calibration of detectors and optical components, the BAM was settling for a wider range of experimental end-stations: topography, micro-computed tomography (μCT), X-ray fluorescence analysis (XRF), total reflection X-ray fluorescence analysis (TXRF), diffraction (XRD), reflectometry and extended X-ray absorption fine structure (EXAFS). Since 2003 the μCT setup is operated and developed jointly by the BAM and the division for materials (SF3, Hahn-Meitner-Institute Berlin) [Rac07b].

A.1.1 The beamline and optical elements

The tomography setup is mounted and unmounted before and following each CT experiment ($35\,\mathrm{m}$ downstream of the source) whereas a 6-axis diffractometer is permanently installed in the experimental hutch (at $37\,\mathrm{m}$). Fig. A.1 shows a sketch of the BAM*line* with the two optical elements installed in the beam-path. The X-rays can be optionally deflected by a double multilayer mirror (DMM, at $19.3\,\mathrm{m}$) and/or by a double crystal monochromator (DCM, at $27\,\mathrm{m}$). According to Bragg's condition for X-ray diffraction by crystals [Bra13], the reflection angle θ of the first mirror sorts out a particular wavelength λ_B (respectively an energy), thus the polychromatic beam is monochromatized:

$$n\lambda = 2d\sin\theta \tag{A.1}$$

With d the periodic lattice spacing normal to the mirror surface and n an integer. λ_B is obtained for $n = 1$ but eq. A.1 also permits the reflection of higher harmonic wavelengths

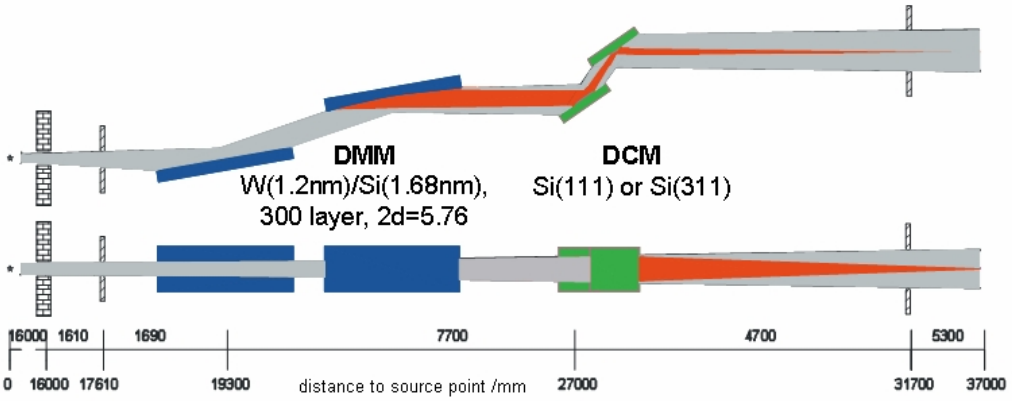

Figure A.1: The BAM*line* and its optical elements (DMM and DCM) [Gör01].

($n = 2, 3, \ldots$) which are unwanted and conventionally suppressed by slightly detuning the second DCM mirror. The energy resolution of the monochromators is defined by their angular acceptance (rocking curve) and $\Delta E/E$ is found approx. $1\% - 2\%$ for the DMM and $0.01\% - 0.02\%$ for the DCM.

For microtomography experiments it is impractical to use the DCM because of its low output flux. The energy resolution $\Delta E/E$ of the DMM is sufficient for quasi-monochromatic absorption and phase contrast imaging. Furthermore a flux density of the order $10^{10}\,\mathrm{Ph/mm^2/s}$ is required for such imaging experiments. The calculated and the measured photon flux density downstream of the DMM at the BAM*line* as a function of the X-ray energy (assuming an electron ring current of $200\,\mathrm{mA}$) is depicted in Fig. A.2. Note three characteristic drops in the flux

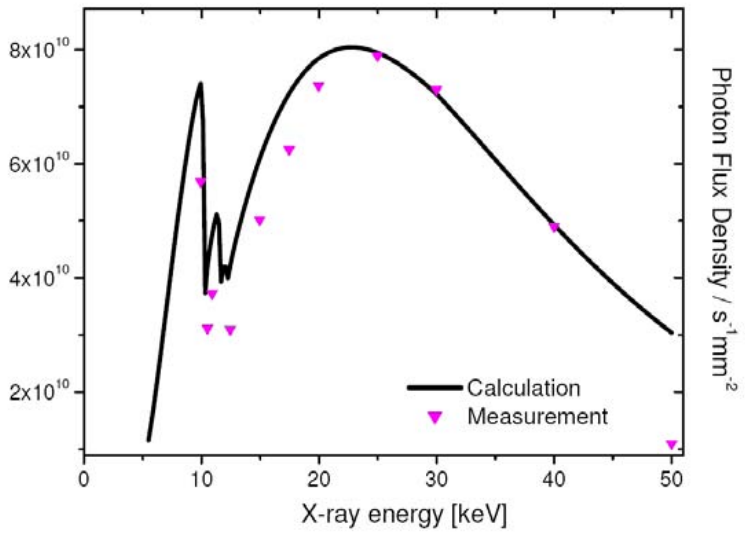

Figure A.2: Photon flux density of the BAM*line* DMM [Rac07b].

density at energies from $10\,\mathrm{keV}$ to $13\,\mathrm{keV}$. These drops are caused by X-ray absorption inside

the multilayer structure (L-absorption edges of thungsten). Each mirror comprises a stack of 300 double-layers ($a = 1.2\,\mathrm{nm}$ thungsten (high Z) and $b = 1.68\,\mathrm{nm}$ silicon (low Z)) with a corresponding thickness ratio $\gamma = a/(a+b) = 0.417$. This ratio is optimized to supress the second harmonic reflection (higher harmonics, $n > 3$, only make negligible contributions). The layers are deposited on a substrate (Si single-crystal, 100 plane) and the reflection of the super-lattice obeys eq. A.1 with $2d = 2(a+b) = 5.76\,\mathrm{nm}$. The DCM is not discussed in detail since it is only used for applications which require very high energy resolution (e.g. measurements of the X-ray absorption fine structure XAFS): Two pairs of silicon single crystals are available with different cutting planes (111 or 311). Both DMM and DCM can be operated in a *fixed-exit* mode. Horizontal beam focusing mechanics are included in the DCM, vertical focusing in the DMM: The second multilayer mirror is mounted on a meridional bending mechanism which can bend the mirror down to a radius of $1.5\,\mathrm{km}$ yielding a height of the focal line shorter than $0.5\,\mathrm{mm}$ for typical energies from $10\,\mathrm{keV}$ to $20\,\mathrm{keV}$. It has been shown [Rac07b] that the beam can thus be focused in order to increase the flux by a factor of approx. 10 without sacrificing spatial resolution. This statement is however only valid for absorption imaging, while phase contrast imaging requires a quasi-parallel beam of minimal divergence. The horizontal and vertical size of the available X-ray beam are limited by the dimensions of the multilayer top surface which is illuminated under very small angles ($\theta \approx 0.1\,^\circ$ to $1\,^\circ$). The horizontal beam size is thus limilted to approx. $40\,\mathrm{mm}$ for all mirror angles whereas the vertical beam size shrinks when higher X-ray energies are selected: typically a $11\,\mathrm{mm}$ heigh beam can be used at $E = 10\,\mathrm{keV}$ while at $E = 55\,\mathrm{keV}$ only $2\,\mathrm{mm}$ are available. In contrast to the DCM, the typical reflection angles of the DMM are close to the angle of total external reflection of the W-Si multilayer $\theta_T = \sqrt{2\delta}$ (where δ is the real decrement of the refractive index) which is proportional to the X-ray wavelength. As a result absorption filters have to be used in order to suppress the transmission of X-rays with $\lambda \geq 5\lambda_B$ by the DMM. When monochromaticity is not needed and very high flux is desired, the BAM*line* can also be operated in a windowless white-beam mode.

A.1.2 Conditions for coherent imaging

In addition to the requirements that are mandatory for recording high resolution X-ray attenuation maps, coherent imaging techniques such as phase contrast and holotomography bring about further demands to the beamline. Among these monochromaticity is the most fundamental, fortunately also the less stringent. Although the energy spread of the DMM is of the order of $1\% - 2\%$, imaging relatively thick ($1\,\mathrm{mm}$-$10\,\mathrm{mm}$) samples under quasi-coherent conditions is not a problem. This fact is surprising because the longitudinal coherence length $l_L = \lambda^2/\Delta\lambda$ is of the order $0.01\,\mu\mathrm{m}$. An intuitive explanation for the discrepancy between sample thickness and coherence length is that only the local phase modulations inside the sample, not the integral phase shift are causing the interference fringes which appear in phase contrast images [Clo97b].

Concerning spatial resolution there are upper and a lower limits for partially coherent imaging. The upper resolution limit is determined by the X-ray wavelength and the thickness t of the sample which causes an image blurring due to small angle scattering inside the sample given by $\sqrt{\lambda t} \approx 0.3\,\mu\mathrm{m}$ (for $t = 1\,\mathrm{mm}$ and $\lambda = 1\,\text{Å}$). An estimate for the minimum resolution can be obtained from the visibility of the fringes and was found approx. $10\,\mu\mathrm{m}$ during feasability studies in the framework of this thesis. The optical parameters of the BAM*line* microscope have been selected to cover the entire range between these two limits (cf. section A.2.6). The transverse coherence length l_T is determined by the angular divergence of the X-ray source which causes blurring when the wave is projected from the object to the detector plane. For two monochromatic plane waves of wavelength λ who propagate into divergent directions spreading an angle α, l_T is defined by the in-plane interference condition:

$$l_T = \frac{\lambda}{2\alpha} \tag{A.2}$$

The present case deals with a very small incoherent source which is situated very far from the object and the detector. Consequently the wave is only partially coherent and the angular divergence can be replaced by the lateral extension of the source $s = \alpha L$, with L the distance from the source to the object. The blurring of the image due to the finite source size is the projection of the source d/L, with d the distance from the object to the image plane. Due to the beam divergence, images are slightly magnified and one has to replace d by $D = dL/(d+L)$, which is called the propagation distance. On the BAM*line* $L \approx 35\,\mathrm{m}$ and the distance of the detector with respect to the sample $z_2 \approx 5\,\mathrm{mm}$ to $1.125\,\mathrm{m}$, hence the maximum propagation distance is $D = 1.09\,\mathrm{m}$.

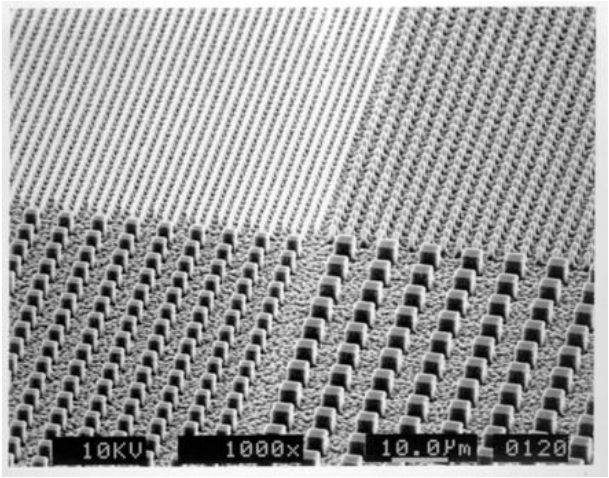

Figure A.3: SEM image of four phase gratings: $p = 3\,\mu\mathrm{m}$, $4\,\mu\mathrm{m}$, $6\,\mu\mathrm{m}$, $8\,\mu\mathrm{m}$.

For measuring the transverse coherence length and thus the angular source size, fractional Talbot imaging of two dimensional phase gratings was used [Gui04]. The Talbot effect occurs during Fresnel-propagation of a coherent wavefront which incorporates regular phase and/or amplitude modulations perpendicular to the direction of propagation. X-ray transmission by

rectangular gratings was used to imprint this periodicity onto the propagating wave. Gratings with profiles $2.9\,\mu\mathrm{m}$ high and etched into a flat silicon substrate [Clo97a] were provided by the Paul-Scherrer-Institute (PSI, Christian David) Switzerland (see Fig. A.3). Neglecting the phase and amplitude modulations of the incoming wave, the periodic transmission function of a grating can thus be decomposed into a Fourier series:

$$T(x) = \sum_{n=-\infty}^{+\infty} \hat{T}^{(n)} \exp\left(2\pi i \frac{n}{p} x\right) \tag{A.3}$$

with $\hat{T}^{(n)}$ the Fourier coefficient of the order n. Propagation of $T(x)$ introduces an additional periodicity: In the ideal case of a perfectly coherent point source, a diffraction order n of a pattern of periodicity p is identically reproduced at multiples of the Talbot distance $D_T = 2p^2/(n\lambda)$. One can calculate that an image taken at half the Talbot distance is shifted by half the period with respect to the initial image and therefore produces the same magnitude of the different diffraction orders. Hence for the sake of simplicity the repetition distance $D_R = D_T/2$ is introduced. Similar to $T(x)$, intensity can be decomposed into a Fourier series with coefficients $\hat{I}^{(n)}$. The gratings can be considered to be pure phase-gratings since $\phi \gg B$ at energies $E \geq 17\,\mathrm{keV}$. Consequently no contrast is expected at $D = 0$ and multiples of D_R whereas a maximum phase-contrast is observed at $D = D_R/2$, $D = 3D_R/2$, $D = 5D_R/2$, etc.. For measuring the coherence, gratings with $4\,\mu\mathrm{m}$, $6\,\mu\mathrm{m}$ and $8\,\mu\mathrm{m}$ pitch were used. First, second and third harmonics of the recorded Fresnel-diffraction patterns were measured by Fourier-transforming radiographs of the gratings taken at different propagation distances which correspond to fractions of D_R. Fig A.4 shows four radiographs taken at different propagation distances $D = 49\,\mathrm{mm}$, $331\,\mathrm{mm}$, $441\,\mathrm{mm}$ and $882\,\mathrm{mm}$ which correspond to $D = D_R/18$, $3D_R/8$, $D_R/2$ and D_R, respectively ($p = 8\,\mu\mathrm{m}$, X-ray energy $E = 17.1\,\mathrm{keV}$). Unlike a coherent point source an extended incoherent source of small angular divergence emits only partially coherent light. Consequently damping of the repeated Talbot signal is observed: The intensity Fourier coefficients $\hat{I}^{(n)}$ are multiplied with the complex degree of coherence $\gamma^c(\lambda D n/p)$. If the angular divergence $Q_\alpha(\theta)$ of the source has a Gaussian shape the damping of the phase-contrast can be directly related to the width σ_α of the source intensity distribution via the Fourier transform of Q_α (van Cittert-Zernike theorem):

$$Q_\alpha(\theta) = \frac{1}{\sqrt{2\pi}\sigma_\alpha} \exp\left(-\frac{\theta^2}{2\sigma_\alpha^2}\right) \tag{A.4}$$

$$\Rightarrow \gamma^c(\lambda D n/p) = \hat{Q}_\alpha(Dn/p) \propto \exp\left(-2\left(\pi\sigma_\alpha D n/p\right)^2\right) \tag{A.5}$$

with the divergence α related to the angular source size via $\alpha = 2.35\sigma_\alpha$. Fig. A.5 shows a three-dimensional simulation of a Gaussian X-ray source intensity distribution. Hence the degree of coherence is proportional to the intensity ratio for a diffraction order n measured for two pictures I_0 and I_1 taken at distances D_0 and D_1, separated by D_R.

$$\left|\frac{\hat{I}^{(n)}_{D_0+D_R}}{\hat{I}^{(n)}_{D_0}}\right| = \left|\frac{\gamma^c\left(\lambda D_0 \frac{n}{p} + p\right)}{\gamma^c\left(\lambda D_0 \frac{n}{p}\right)}\right| \tag{A.6}$$

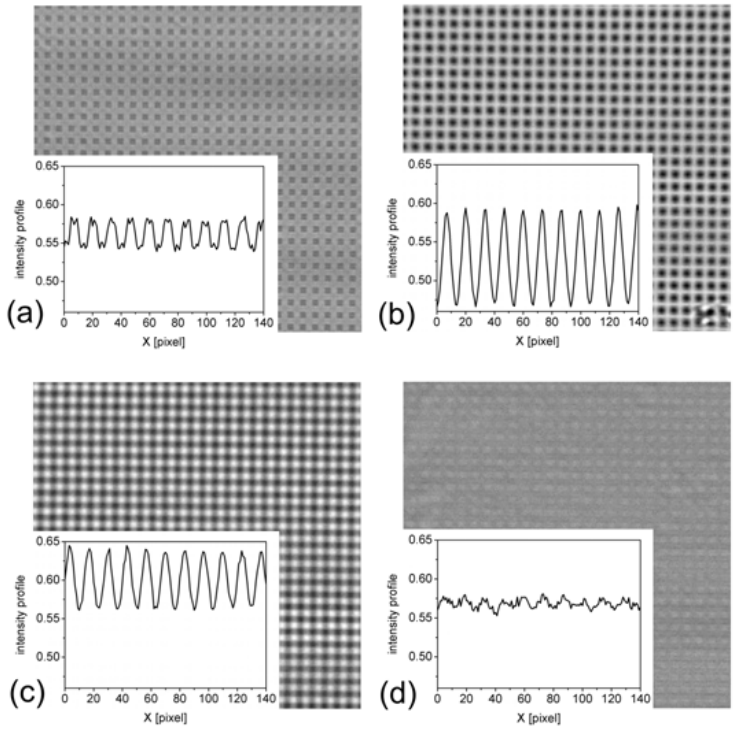

Figure A.4: Radiographs of the $8\mu m$ grating taken at (a) $D = D_R/18 = 49\,\mathrm{mm}$, (b) $D = 3D_R/8 = 331\,\mathrm{mm}$, (c) $D = D_R/2 = 441\,\mathrm{mm}$ and (d) $D = D_R$. Horizontal intensity profiles are depicted in the insets for each picture: Note the vanishing contrast at $D = D_R$.

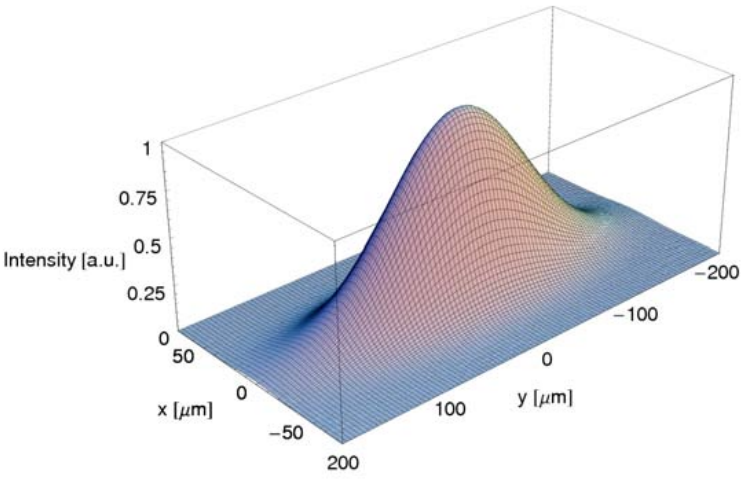

Figure A.5: Gaussian intensity profile of the BAM*line* X-ray source.

The angular divergence α is then obtained by inserting eq. A.5 into eq. A.6

$\mathbf{n}$	$\mathbf{D_0}$ $/\mathbf{D_R}$	$\mathbf{p}$ [μm]	$\mathbf{D_R}$ [mm]	$\alpha^{(\mathbf{ver})}$ [μrad]	$\alpha^{(\mathbf{hor})}$ [μrad]	$\mathbf{s}^{(\mathbf{ver})}$ [μm]	$\mathbf{s}^{(\mathbf{hor})}$ [μm]
2	3/8	8.0	441	0.96	4.73	33.5	165.7
3	1/18	8.0	294	1.18	4.95	41.3	173.2
3	1/6	8.0	294	1.44	4.69	50.3	164.0
3	5/18	8.0	294	1.08	4.61	37.8	161.3
3	7/18	8.0	294	0.89	4.57	31.1	159.9
3	1/2	8.0	294	1.02	-	35.6	-
3	11/18	8.0	294	1.07	-	37.3	-
1	1/2	6.0	497	1.21	4.75	42.5	166.2
2	3/8	6.0	248	0.87	4.70	30.5	164.4
3	1/6	6.0	166	0.87	4.54	30.3	158.7
3	5/18	6.0	166	1.47	4.48	51.3	156.7
3	7/18	6.0	166	1.31	4.55	45.8	159.1
3	1/2	6.0	166	1.42	-	49.9	-
3	11/18	6.0	166	1.19	-	41.7	-
1	1/2	4.0	221	1.43	4.99	49.9	174.6

Table A.1: Results of the Talbot measurements of harmonics $n = 1, 2, 3$ for the horizontal and the vertical direction using Fresnel-propagated radiographs of $8\,\mu\mathrm{m}$, $6\,\mu\mathrm{m}$ and $4\,\mu\mathrm{m}$ gratings. Many points D_0 could be used to evaluate the vertical damping of the third harmonics whereas the horizontal contrast for $n = 3$ vanished for larger D_0 (cf. Fig. A.6).

$$\alpha = \frac{2.35p}{n\pi\sqrt{2(D_1^2 - D_0^2)}}\sqrt{\ln\left|\frac{\hat{I}_{D_0}^{(n)}}{\hat{I}_{D_1}^{(n)}}\right|} \tag{A.7}$$

Table A.1 shows a list of the horizontal and vertical angular divergences as well as the source sizes calculated for the different orders of diffraction and for the different gratings.
By averaging, an angular divergence of $1.16\pm\ 0.21\,\mu\mathrm{rad}$ is found in the vertical plane and $4.69\pm\ 0.17\,\mu\mathrm{rad}$ in the horizontal plane. The corresponding vertical source size is $40.6\pm$ $7.2\,\mu\mathrm{m}$ and the horizontal size $164.0\pm\ 5.8\,\mu\mathrm{m}$. These results are conform with calculations from the machine group, the horizontal spread of the source being a consequence of the bent electron trajectory in the insertion device. The good matching of these observations with the known source characteristics indicates that a possible influence of the X-ray optics (DMM) on the beam coherence is only of small magnitude (unless beam fucusing is used). The horizontal and vertical transverse coherence length l_T is calculated according to eq. A.2: $8\,\mu\mathrm{m}$ are found in the horizontal, $31\,\mu\mathrm{m}$ in the vertical direction. These values can be compared to the fringe spacing in the propagated images given by $\sqrt{\lambda D}$. For the given wavelength $\lambda = 0.725$ Å and the maximum propagation distance $D = 1.09\,\mathrm{m}$ a fringe spacing of $\sim 9\,\mu\mathrm{m}$ is found. Consequently further extending the range of the sample-detector distances would not allow to image

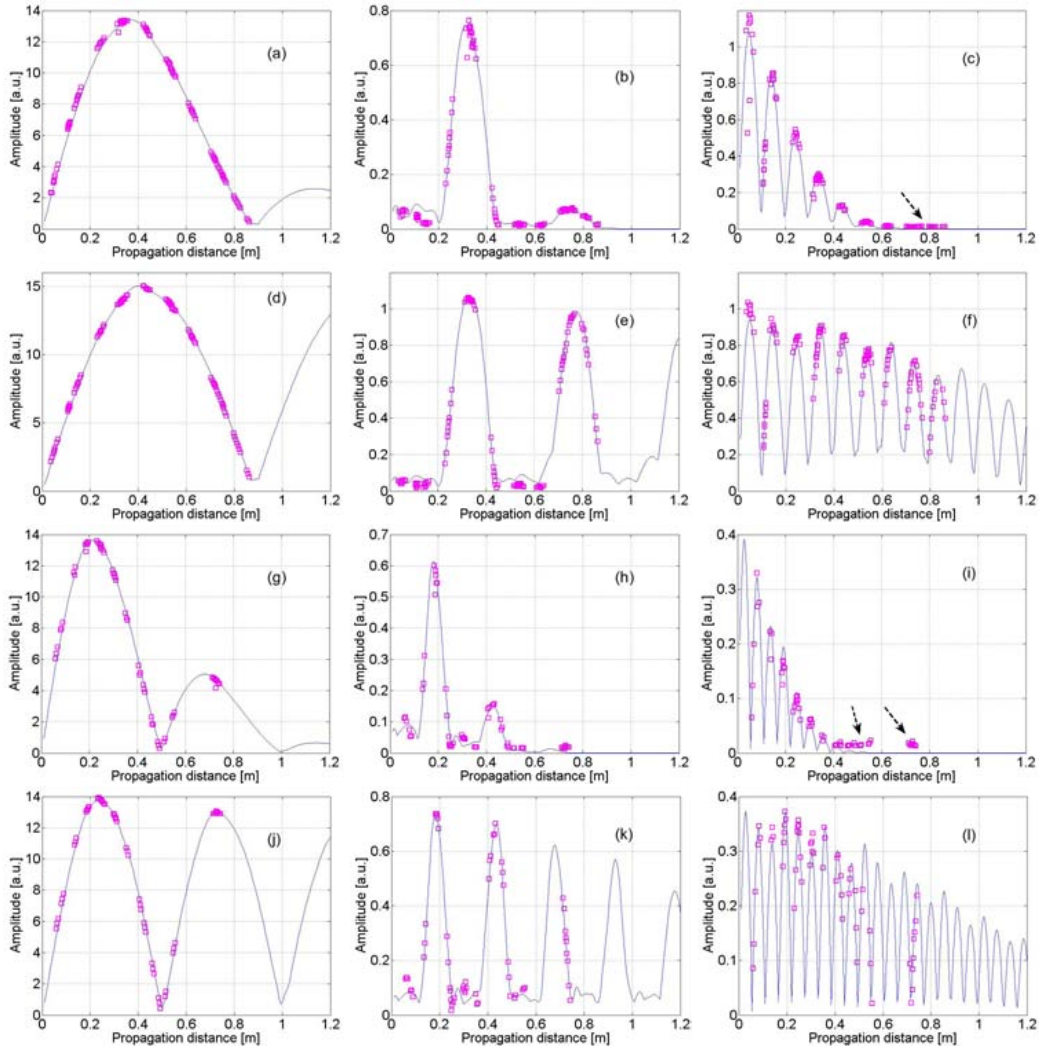

Figure A.6: Measurements of the first three harmonics in the horizontal (graphs a-c, g-i) and in the vertical (graphs d-f, j-l) direction as a function of propagation distance D for the $8\,\mu\mathrm{m}$ (graphs a-f) and the $6\,\mu\mathrm{m}$ grating (graphs g-l). The blue lines show the numerical fit based on a gaussian source distribution. Arrows indicate a completely damped signal.

the interference fringes more efficiently, at least not in the horizontal direction. In conclusion: For the given experimental setup the beam is sufficiently coherent as it is.

Figure A.6 shows the measured amplitudes of first, second and third harmonics in the vertical and in the horizontal direction. These values were calculated from Fresnel-propagated images of the $6\,\mu\mathrm{m}$ and the $8\,\mu\mathrm{m}$ gratings both which were placed to match the horizontal and vertical axes of the detector. From the results a reverse numerical fit was calculated assuming a Gaussian source intensity distribution (eq. A.4) of $40.6\,\mu\mathrm{m}\times\ 164.0\,\mu\mathrm{m}$ full-width half maximum in the vertical and horizontal direction respectively. Note that a broader source distribution results in a stronger damping of all Talbot coefficients ($n = 1, 2, 3$). The good numerical fit is additional proof for the Gaussian source distribution (depicted in Fig. A.5).

A.1.3 Beam stability

It is commonly observed in synchrotron X-ray shadow images that an inhomogeneous (wavy) intensity modulation is imprinted onto the wave after reflection by the DMM. Probably due to stress relaxation by mechanical buckling (stress builds up because of the lattice mismatch between W- and Si-layers) local shifts of the rocking curve are responsible for an inhomogeneous illumination (brightfield) of the radiographs. An advanced method of brightfield normalization was developed in the framework of this thesis and is presented in section B.1. Additionally the incoming X-ray beam is shifting with time, consequently horizontal and vertical displacements of the image background are observed. This beam instability is very inconvenient for imaging. Presumably caused by either the ring electrons, the X-ray source or the mirrors (DMM) it has to be cured. During discussions with scientists from other light sources (APS, ESRF) it was suggested that this phenomenon was probably caused by one or both of the DMM mirrors. Therefore it seemed advantageous to analyze the shifts of an imaged object placed half-way between the DMM and the detector, as well as the shifts of the mirror structure. Choosing an energy of $9.6\,\mathrm{keV}$ and recording high-resolution ($0.7\,\mu\mathrm{m}$) brightfield images over a long time (20 hours) allowed to visualize both the shifting mirror structure ($15\,\mathrm{m}$ upstream of the detector) as well as dust particles on the exit window ($1.5\,\mathrm{m}$ upstream) which appear in the images as strong interferences (phase contrast). Fourier image cross-correlation was then used to retrieve the X- and Y-shifts of these two structures in the images separately (the particular separation algorithm is described in section B.1). Results are shown in Fig. A.7. The red arrows mark times when electrons were injected into the storage ring. Movements of the window and the DMM structure are clearly correlated both revealing some periodic motion of 6-7 hours frequency. The shape of the curves is a possible indication that a cooling system (either of the multilayer or of the wiggler) is responsible for these perturbations. The amplitude of the background shifts was measured for most of the many experiments presented in this work: The effect was found particularly pronounced during low energy ($E \leq 10\,\mathrm{keV}$), high-resolution ($R \leq 1.5\,\mu\mathrm{m}$) measurements while it was hardly detectable when high energies ($E \geq 30\,\mathrm{keV}$) and medium resolution optics ($R \geq 5\,\mu\mathrm{m}$) were used.

A.2 The joint BAM-HMI tomography experiment

Starting in 2003 the micro-computed tomography (μCT) experiment is operated and developed jointly by the BAM (division VIII.3 Radiology) and the HMI (division SF-3 Materials). At the beginning of this thesis the experiment consisted of two main elements: a detector (macroscope) and a sample stage (cf. Fig. A.8a) both assembled on a heavy-duty optical table (Newport Inc.). No phase contrast imaging was feasible with this arrangement because of a lack of high-resolution X-ray converter screens and detector z-translation. The alignment of the sample position and rotation axis, as well as the focusing of the optics had to be done manually and were therefore very time-consuming procedures taken into account that the beamline

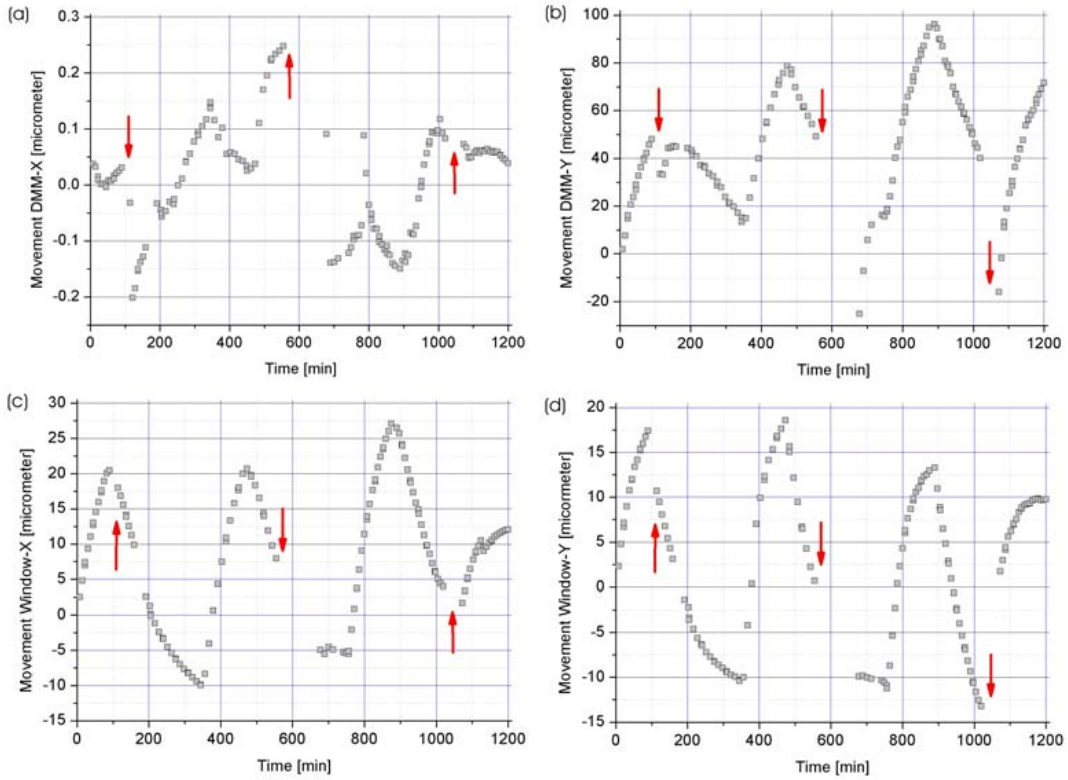

Figure A.7: (a) Horizontal (X) and (b) vertical (Y) shifts of the mirror structure as calculated by image cross correlation of brightfield images. (c) Horizontal and (d) vertical shifts of the image interferences due to dust on the exit window. Arrows mark X-ray beam interruptions due to routinely electron injection (usually every 8 hours).

had to be sealed off each time before taking an X-ray image. From the beginning of an experiment to the launch of the first CT scan, the setting up could easily take 10 hours of time, and the resulting spatial resolution was still limited to the rather poor value of $R \sim 15\,\mu\mathrm{m}$. The development of a new μCT experiment had therefore three aims: 1. high-resolution CT, 2. phase contrast imaging and 2. remotely controlled, semi-automatic setup and alignment. All three aims were attained in the framework of this thesis to the full satisfaction of the operators [Rac06].

A.2.1 Concepts and planning of micro-CT

In order to record high-resolution X-ray images one has to optimize the ensemble of converter screen (scintillator), optics and CCD camera. The quest for high-resolution scintillators has been extensively treated in the thesis of A. Rack [Rac06] and is therefore only briefly described in this work. In addition to the poorly resolving GADOX (Gd_2O_2S) powder screens (doped with F, Ce, Tb or Pr) that were initially used on the BAM*line* , three cerium-doped transparent single-crystal YAG ($Y_3Al_5O_{12}$) screens (doped with Ce) were puchased by the end of 2004 from Saint Gobain S. A., France. Unfortunately the YAG:Ce screens were a disappointment in

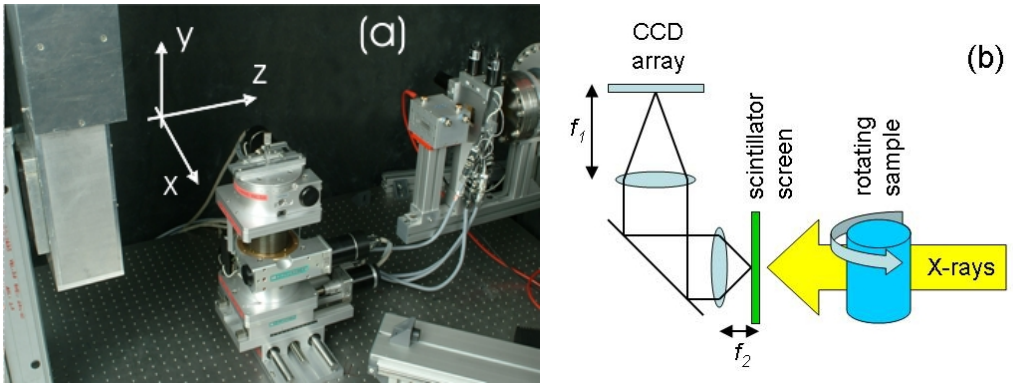

Figure A.8: (a) Photo of the first BAM*line* CT experiment [Rac06]: (from left to right) detector, sample stage, exit window with slits and ionization chamber (arrows indicate convential coordinate axes). (b) Schematic drawing of tomography data acquisition.

terms of resolution (6 µm) in the best case): Probably due to unclean fabrication conditions the substrate emitted light of the same spectral range as the Ce-doped layer (ca. 550 nm) instead of the expected UV-spectrum. Later CWO ($CdWO_4$) and Eu-doped LAG ($Lu_3Al_5O_{12}$) screens fulfilled the demands for high resolution detectors [Koc98]. Today A. Rack is leading an international research program funded by the EU and aiming to produce thin Tb-doped LSO (Lu_2SiO_5) screens by means of liquid film epithaxy and hopefully giving a final answer to the growing demand for high-resolution scintillators [Rac07a]. For medium resolution imaging at lower energies from 10 keV to 20 keV rather thick (0.3 mm) BGO ($Bi_4Ge_3O_{12}$) crystals can be used. Table A.2 shows an overview of the screens which are currently used at BAM*line* , their thickness, best resolving power, emission wavelength and other important characteristics. Until early 2006 the so called *macroscope* was used which employs optics that are combin-

Scintillating material	Substrate material	Thickness of active layer	Max. emission wavelength	Best resolution (at $E \leq 18\,\mathrm{keV}$)
GADOX	quartz glass	10 µm	580 nm	10 µm - 15 µm
BGO	quartz glass	300 µm	480 nm	5 µm
CWO	YAG	25 µm, 55 µm	495 µm	3 µm
LAG:Eu	YAG	4 µm	580 nm, 700 nm	0.7 µm
YAG:Ce	YAG(Ce?)	7 µm, 12 µm, 22 µm	550 nm	6 µm - 7 µm

Table A.2: Overview of the different high-resolution scintillators used at BAM*line* .

ing different Rodenstock lenses with a Nikkor telephoto (180 mm) objective. By the end of 2005 a new *microscope* was planned in cooperation with and ordered from Optique Peter S.A. (France). This microscope is fully motorized and designed to work with Olympus Ultra-Plan Super-Apochromat lenses (UPLSAPO) for highest resolution. A Princeton VersArray 2048B back-illuminated CCD camera was used to acquire all the BESSY measurements which are

reported in this thesis. In addition a Princeton VA 1300B camera is operational at BAM*line* although rarely used. By 2005, a PCO 1200hs CMOS camera was purchased for high-speed radiography but it was used only at the ESRF until now. The main advantages of the Princeton cameras are their high quantum efficiency and large spectral acceptance (80% to 100% for $450\,\mathrm{nm}$ to $750\,\mathrm{nm}$), but a slow readout time ($4.5\,\mathrm{s}$ in *fast*-mode and $45\,\mathrm{s}$ in *slow*-mode) is the price to pay for such a good efficiency. Early 2007, first tomograms were recorded using a loaned PCO4000 CCD camera which has a lower quantum efficiency (50% peak) compared to the Princeton VersArrays but a readout time of only $0.2\,\mathrm{s}$ for full 4072×2720 pixel frames. During beamtimes at the ESRF/ID19 beamline in April and November 2006, high-quality measurements were performed with the FRELON-*2K* camera which has a very fast readout time, better dynamics than both the Princeton and the PCO4000 camera and can therefore be honestly called the state-of-the-art dCCD etector in synchrotron tomography. Clearly in the near future the BAM*line* will have to develop in such a way that many different camera models can be used for radiography and tomography. Table A.3 gives an overview over the available cameras and their main characteristics.

Camera	Chip size	Pixel [μm^2]	Framerate	Dynamics
Princeton VA 2048B	2048×2048	13.5×13.5	0.23 fps	16 bits
Princeton VA 1300B	1340×1300	20×20	0.56 fps	16 bits
PCO (CMOS) 1200hs	1280×1024	12×12	636 fps	10 bits

Table A.3: Overview of the different CCD and CMOS cameras used at BAM*line* .

Phase contrast effects are commonly observed when high-resolution X-ray images are recorded at a synchrotron beamline. Fresnel-propagation taking place over a finite sample-to-detector distance causes interferences which appear as additional fringes in the radiographs. The aim of this work was to use propagation in order to add edge-enhancement and numerical phase-retrieval (holotomography) to the imaging methods that are available at the BAM*line* . Therefore a continuous displacement of the detector with respect to the sample along the beam path had to be installed. Requirements on the precision of this z-translation are very tough, reducing the number of manufacturers who can produce such a motor-stage extending the sample-to-detector distance to at least $1m$ length. Quotations from Micos (Germany), Newport (former Micro-Controle, France), Aerotech (US), Schneeberger (Switzerland) and Johann Fischer Aschaffenburg (JFA GmbH, Germany) were assessed. The latter clearly offered the best quality for the lowest price. By the end of 2004 a $1.125m$ long air bearing translation table was purchased from JFA GmbH with the specifications given in table A.4.

Max. travel	Max. load	Max. deviation	Max. roll	Max. pitch	Max. speed
$1.125\,\mathrm{m}$	$80\,\mathrm{kg}$	$2\,\mu\mathrm{m}$	$2.06''$	$1.25''$	$115\,\mathrm{mm/s}$

Table A.4: Specifications of the z-translation (JFA GmbH).

The limited space in the experimental hutch of the multi-purpose BAM*line* required the μCT setup to move in and out of the hutch before and after each experiment. Therefore all the components had to be mounted onto a station which allowed a fast and precise setup and alignment of both the JFA z-translation and the multi-axis sample stage. Fig. A.9a is a schematic drawing showing the final design of the new CT experiment. Either the BAM macroscope or the Optique Peter microscope can be mounted onto the z-translation slide (both indicated in the drawing). The rack was partly built by GEAT GmbH (Berlin, Germany) and the final assembly took place at the BAM workshop in Adlershof, Berlin. It comprises three motorized stages which allow to tilt the the JFA z-translation (pitch and yaw) by $\pm\ 2\,^\circ$ (independently of the sample positioning) with an additional y-motor moving the rack along with the sample stage up and down by $\pm\ 50\,\mathrm{mm}$. The sample stage comprises another 7 motorized axes (from the bottom to the top): pitch and roll (Huber), y (Huber), x (Micos UPM-160), sample rotation ω (Micos UPR-160) and two piezo positioners (Micos PP-30) for centering the sample.

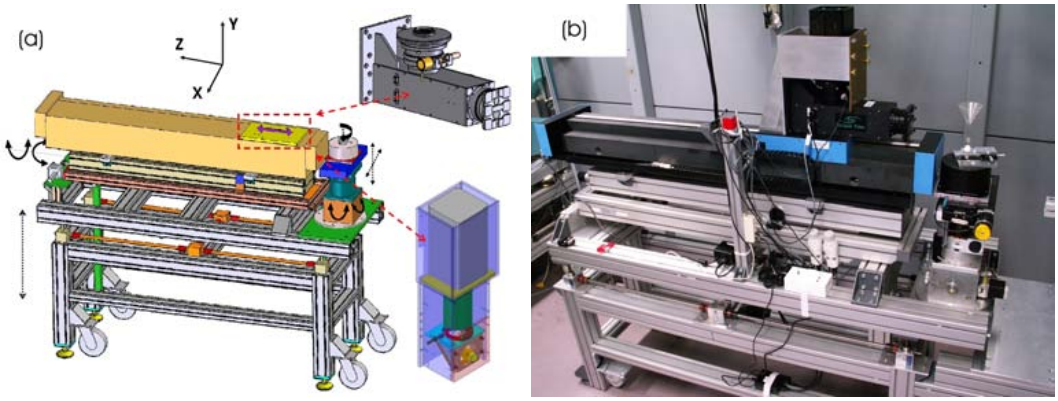

Figure A.9: (a) Schematic drawing of the new CT experiment with two exchangable optics (above: microscope, below: macroscope). (b) Photo of the operational setup (2006).

A.2.2 Thermal and mechanical stability

When the $1.125\,\mathrm{m}$ long z-translation is aligned with sub-micrometer precision to the X-ray beam, thermal and/or mechanical stability are a serious issue. Driving the detector (aluminum construction with brass shielding, ca. $50-\ 60\,\mathrm{kg}$ weight) along the z-axis causes the second stage of aluminum profiles to bend down by $50\,\mu\mathrm{m}$ to $100\,\mu\mathrm{m}$. This bending is parabolic and is countered by moving the whole experiment up or down depending on the position of the detector (an efficient method for measuring the bending is presented in the following paragraph). Additionally thermal drifts can destroy the whole alignment and cause the detector to tilt with respect to the sample stage. Already a temperature change of $1\,\mathrm{K}$ would cause the $2\,\mathrm{m}$ long aluminum profiles which frame the whole experiment to expand or contract by $\sim 50\,\mu\mathrm{m}$ (thermal expansion coefficient $\alpha = 24 \cdot 10^{-6}\ \mathrm{K}^{-1}$ for aluminum). Two computers and electronic motor controllers are installed in the hutch, thus producing a *dangerous* amount of heat. Using a thermocouple and USB acquisition, temperature was measured inside the hutch

as well as directly on an aluminum profile of the CT stage during 6 days of experiment in July 2005. Fig. A.10 shows the temperature signal at these two positions. Although the measured

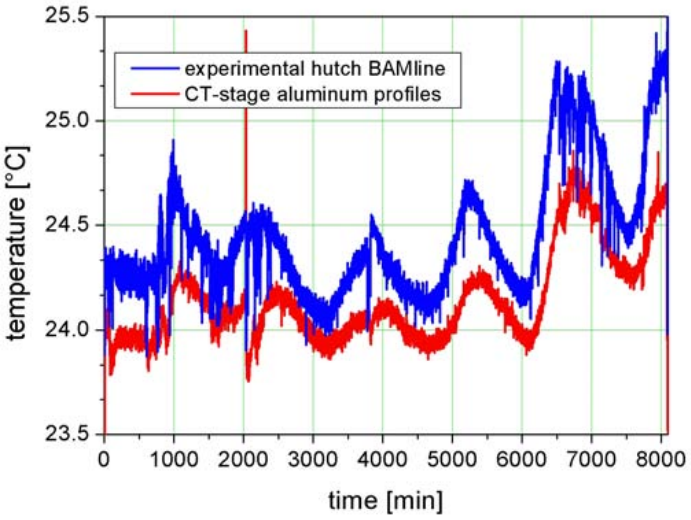

Figure A.10: Temperature measurement in the hutch and directly on an Al-profile

temperature modulations are rather slow (day and night rhythm) and of the order $\pm$ 0.2 K (the fast modulations do not exceed $\pm$ 0.05 K) there is a significant increase in temperature after 5 days yielding a peak-to-peak difference of almost 1 K compared to the beginning of the measurement. Therefore the installation of a special air conditioning system was recommended to BESSY: a large thermal mass should be continuously cooled by a flux of 20 deg C water. Unfortunately, instead a conventional cooling system with a closed electronic loop for temperature regulation was installed. It was not a surprise that the temperature fluctuations after activating the system were found 5 times larger than before.

A.2.3 Alignment of the CT experiment

The alignment of the CT station was divided into three steps: 1. Focusing of the imaging system, 2. Alignment of the detector z-axis with the X-ray beam and 3. Adjustment of the sample rotation axis' tilt. In the framework of a diploma thesis [Sla06] which was supervised by the author, software and a graphical user interface were developed in order to perform all three steps semi-automatically. Compared to the 10 hours one had to spend on manually adjusting the image focus and the rotation axis, the remotely controlled semi-automatic alignment takes 30 minutes at most, thus saving 9 1/2 hours, i.e. more than one beamtime shift, which can now be used for additional experiments.

Fig. A.11 shows the first step, i.e. the focusing of the optics. As an example radiographs of a stack of sintered copper balls [Gru08] is shown before and after the focusing. During user-operation it is more common to image a sheet of thick paper (for high-resolution images) or a sharp thungsten wedge (in low-res mode), although any object which produces a sharp ab-

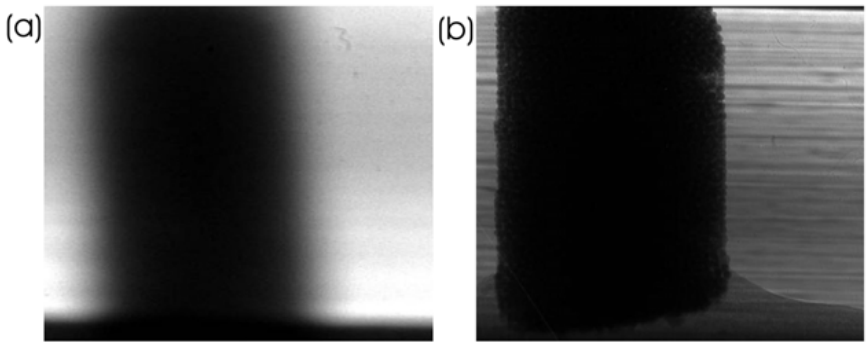

Figure A.11: Radiography (a) before and (b) after focusing the imaging system.

sorption contrast should do the job. Since neither refraction nor diffraction effects contribute to such X-ray contact images (detector placed right behind the sample), the width of the distribution of the pixel gray values (each representing the accumulated X-ray absorption inside the sample along a projection line) maximizes in focus. In other words the standard deviation σ_{gray} of gray values is inversely proportional to the blurring of the projection images. Yet phase contrast effects cannot be avoided when high-resolution images ($R < 1\,\mu\mathrm{m}$) are recorded at moderate energies ($E = 10-12\,\mathrm{keV}$), not even when the object-detector distance is kept small ($D = 10-50\,\mathrm{mm}$). Consequently σ_{gray} might no longer be a good candidate to evaluate the focus because additional image blurring occurs due to partial beam coherence. Fortunately the beam is sufficiently coherent and blurring does not exceed R. In fact the accuracy of the σ_{gray}-method increases significantly with the strong additional dark-bright contrast of the intereference fringes which constitute a phase contrast image (e.g. of a paper sheet).
For the X-ray microscope the focal position is reached by adjusting the distance between the front lens and the scintillator screen. Unlike in optical microscopy, a linear motor (Newport MFA-PP) is used to move the objective revolver towards or away from the screen. The focusing algorithm maximizes σ_{gray} iteratively by taking n images at equidistant positions over the whole interval (travel range of the MFA-PP) then repeating the scan for half the interval centered around the best value of σ_{gray} and so on, until the minimum step size is reached (the first 3 steps for $n = 6$ are depicted in Fig. A.12). This algorithm, although not very fast (typically 4 - 5 minutes), has shown to be very robust for X-ray imaging. Unfortunately the macroscope requires manual adjustment of the lens-to-screen distance which is the reason why the focusing software cannot be used with this setup. Nevertheless a motor was installed to fine adjust the zoom of the Nikkor telephoto remotely (see following section).

In a second step the z-translation of the detector is aligned with the quasi-parallel X-ray beam. A pair of copper slits is closed narrowing the visible beam to a square of approx. 1/20 of the image size. A series of 10 to 20 images is recorded at increasing detector positions ranging from 0 to $1.125\,\mathrm{m}$. Any deviation of the camera path relative to the beam causes inverse shifts of the square beam in the images. These x and y-shifts are calculated by image

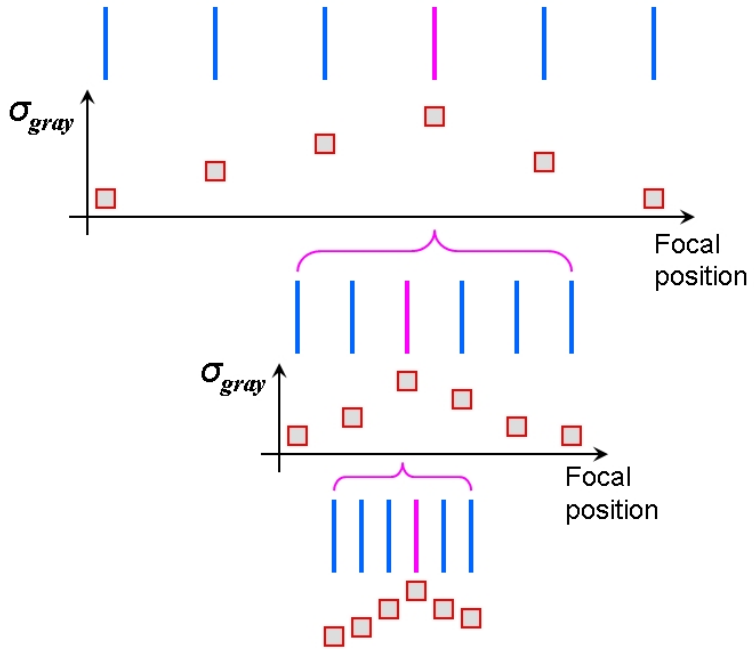

Figure A.12: First three steps of the focusing algorithm ($n = 6$).

cross-correlation and the linear part of these deviations are corrected via two stepping motors: pitch and yaw. The method is depicted in Fig. A.13. Once the pitch and yaw corrections are

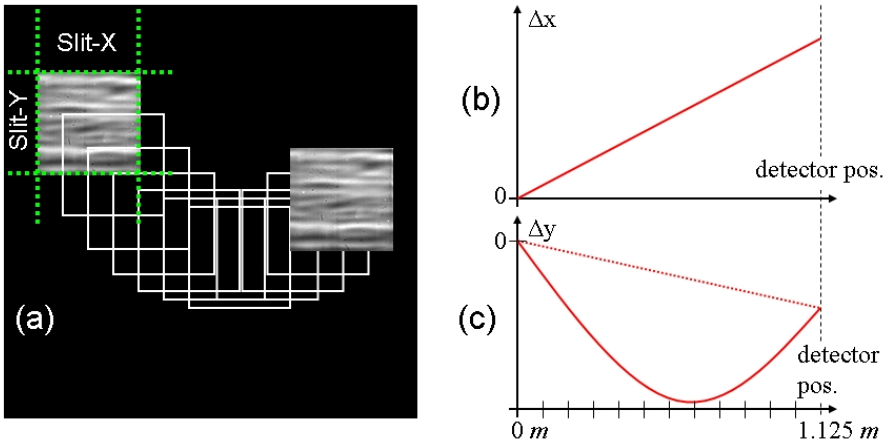

Figure A.13: z-axis alignment: (a) Detector is driven downstrem of the beam and the relative position is found by imaging a small square beam limited by two copper slits. (b) Image cross-correlation is used to retrieve the (x- and y-deviations of the detector movement.

applied the scan is repeated until the z-axis is sufficciently well aligned. Note that while the horizontal tilt is quasi-completely corrected, a vertical parabolic deviation remains which is due to the bending of the aluminum profiles under the weight of the detector. This data is used

as a lookup table to drive the whole experiment up and down when phase contrast images are recorded at many different defocusing positions.
The last step involves the tilt-alignment of the sample rotation axis ω with respect to the detector. Until 2005 this axis was aligned manually using a $5\,\mu\mathrm{m}$ pinhole: Images at $\omega = 0\,^\circ$ and $\omega = 180\,^\circ$ were compared in order to minimize the vertical shift of the pinhole center. This method was quite inaccurate and time-consuming which is why the alignment was automated. Instead of the two-dimensional pinhole the new procedure uses $120\,\mu\mathrm{m}$ to $150\,\mu\mathrm{m}$ sized Cu-balls which are embedded in a thin rod of resin and produce a spherically shaped absorption, independently of the projection angle. Fig. A.14 shows a typical radiograph of the resin and

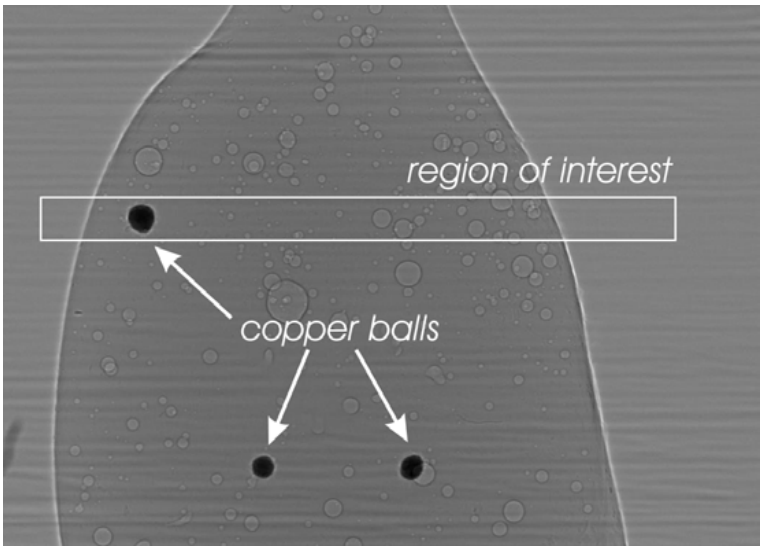

Figure A.14: Sample for alignment of axis tilt. The copper balls appear black in the radiograph due to their strong absorption. For the alignment of the rotation axis a stripe shaped region of interest is selected containing only one single copper ball.

the embedded copper balls. The alignment algorithm asks the user to select a stripe shaped region-of-interest (ROI) containing only one copper ball as well as a binarization threshold. Radiographs of the ROI are taken under four projection angles: $0\,^\circ$, $90\,^\circ$, $180\,^\circ$ and $270\,^\circ$. The center of mass coordinates of the copper ball in every image are easily calculated by applying threshold binarization. If the rotation axis is misaligned the copper ball will in general follow an ellipsoidal trajectory in the images similar to a Lissajous pattern known from electronics. The tilt angles *roll* and *pitch* of the rotation axis with respect to the detector are calculated from the Cu-ball positions using Ritz's construction for the conjugated diameters of an ellipsoid [Sla06]. Fig. A.15 shows the six possible cases of axis tilt. Note that with a perfectly aligned axis the ball moves on a horizontal line while being rotated. The *roll* and *pitch* motors are adjusted and the alignment is repeated until the ultimate precision of the method is reached ($\sim 0.01\,^\circ$). From the final set of images the position of the copper ball at $0\,^\circ$ and $180\,^\circ$ are used to calculate the x-position of the rotation axis in the images (when a real sample is mounted, two piezo-steppers on top of the rotation table are remotely moved to align the sample with

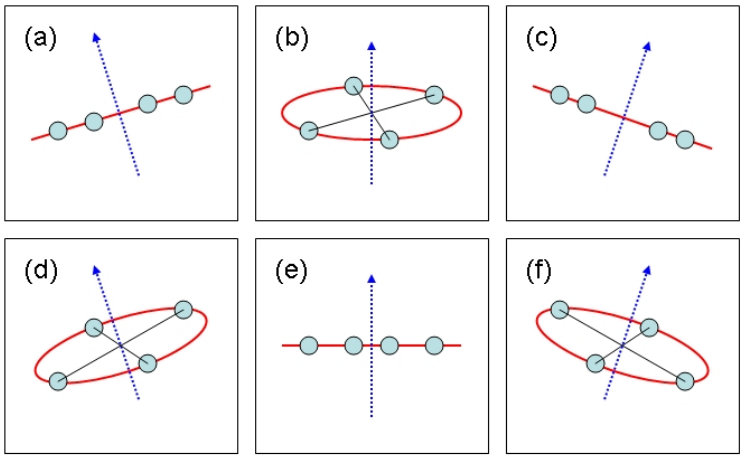

Figure A.15: Imaging a sphere at 0 °, 90 °, 180 ° and 270 ° rotation angle in the six possible cases of axis tilt: (a,c) $roll \neq 0$ and $pitch = 0$, (b) $roll = 0$ and $pitch \neq 0$, (d,f) $roll \neq 0$ and $pitch \neq 0$, (e) $roll = 0$ and $pitch = 0$.

the center of rotation).

A.2.4 Motor precision of the sample stage

During any micro-CT scan two motors are permanently in use: a) The x-motor is moving the sample out off and back into the beam allowing the camera to repeatedly record *bright-field*-images in short time intervals (typically every $5 - 20$ minutes) which are later used for normalization. b) The sample rotation ω typically does a *half-scan*, i.e. $180\,°$ turn with small angular steps which are typically of the order $0.1\,°$ to $0.2\,°$. Together with the Micos-x a third (y) motor can be used to synchronously shift the sample over a 10×10 pixel raster in the (x, y)-plane in order to reduce imaging artifacts (*wobbling*, cf. section B.1). The accuracy of these motors determines the overall quality of the tomographic image which is the reason why the requirements on precision increase significantly with high-resolution imaging. A photo as well as a schematic labelling of the 7-axis sample positioner is shown in Fig. A.16.
In order to estimate possible errors, the precision of the rotation ω-axis (Micos) was measured during tomography while the sample was both turning and being *wobbled* with the Micos x and the Huber y-motor as it used to be the custom during normal user operation. To obtain an accurate measure of the rotation precision, a sample of copper balls embedded in resin was used (the same as shown in Fig. A.14). 740 images were recorded at angular steps of $0.25\,°$ hence a total interval of $185\,°$. The regular pixel-wise x and y-shifts in the sequence (wobbling) were removed by automated image cropping. To the cropped and normalized images a threshold binarization was applied and the center of mass (x, y)-coordinates of one copper ball were calculated for every projection angle. A sinogram (linear horizontal intensity profile versus rotation angle) showing the trajectory of a copper ball (middle line through the stripe shaped ROI in Fig. A.14) is shown in Fig. A.17. Images were recorded using the *macroscope*

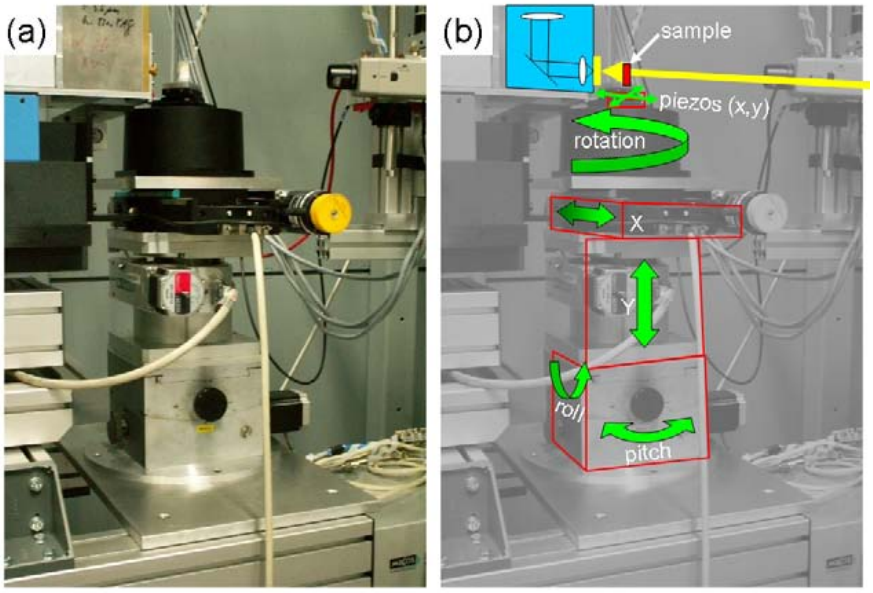

Figure A.16: (a) Photo of the motorized sample stage. (b) Schematic labelling of the seven motor axes of the stage. The X-ray beam is indicated by the yellow arrow.

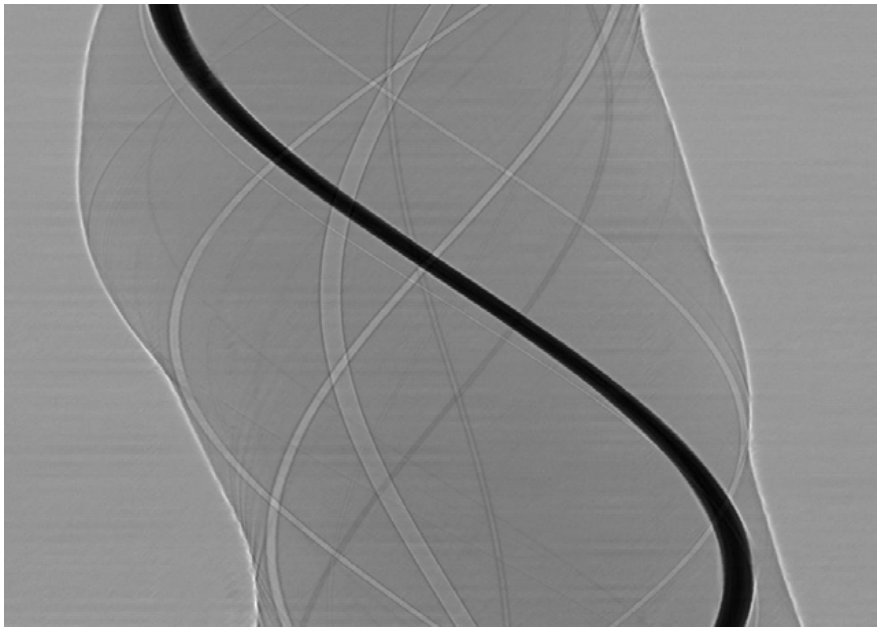

Figure A.17: Sinogram of a single copper ball which was for calibration of the ω-axis.

with an effective pixel size of $\Delta x \approx 3.6\,\mu\mathrm{m}$. The photon energy was set to $17\,\mathrm{keV}$ and the pictures were recorded in phase contrast mode in order to observe the silhouette of the resin. A sinusoidal fit was applied to the x and y coordinates of the copper ball and the difference between measurement and fit was calculated. The two graphs in Fig. A.18 show the residual movement in x and y direction after subtraction of the sine fit. Wobbling the sample and later

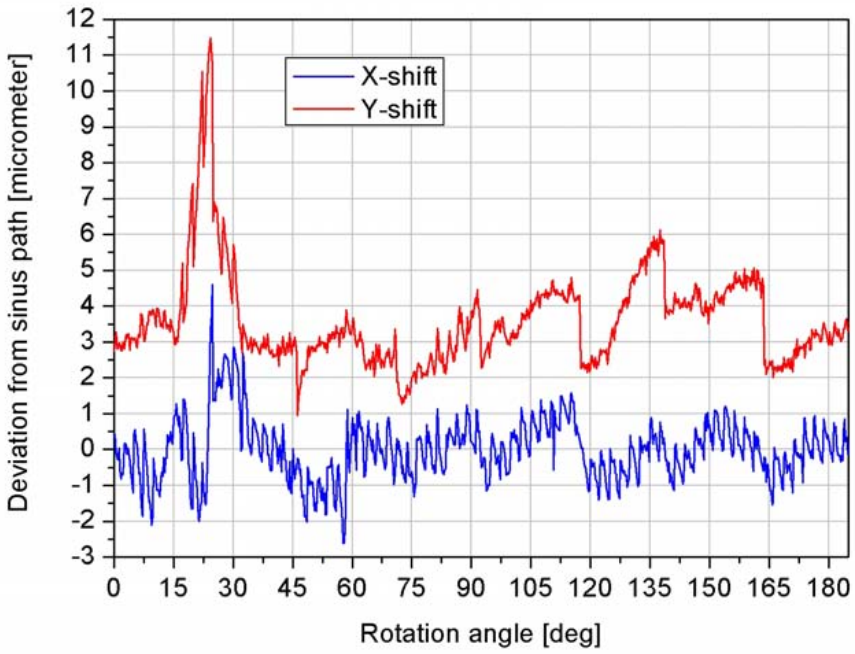

Figure A.18: Residual x and y movement during rotation of a copper ball.

correcting the 10×10 pixel motion requires very accurate knowledge about the exact pixel size which was assumed to be $3.6\,\mu\mathrm{m}$. The results in Fig. A.18 reveal that this assumption was erroneous leading to a fast residual motion with a 10-images periodicity seen in the x-coordinate as well as a slower modulation of 100-images periodicity which is seen in the y-coordinate. The amplitude of the modulation in x-direction is approx. 0.3 pixel and therefore the error in the estimated pixel size must be of the order of 3%. This error is confirmed more or less by the discontinuities seen in the y-coordinates which are of the order of 0.5 pixel corresponding to an error of 5% per step. Both errors are tolerable for a $3.6\,\mu\mathrm{m}$ pixel size but wobbling should not be used for high-resolution imaging.

In addition to these regular deviations we find irregular movements in both x- and y-coordinates reaching amplitudes of 2.5 pixel (see the strong y-movement at $25\,^\circ$ sample rotation). These irregularities were thought to be a result of instabilities in the Huber y-translation (both Micos ω and x are certified by the manufacturer to move with $0.1\,\mu\mathrm{m}$ precision) which is why the same measurement was repeated while moving the Huber y-motor with pixel-wise steps instead of rotating the sample. 900 images were recorded using the Optique Peter microscope at $20\times$ magnification and the Princeton VA 1300B camera. The effective pixel size was $1.0\,\mu\mathrm{m}$ and the X-ray energy was set to $18\,\mathrm{keV}$. The relative and cumulated x- and y-shifts of the sample for each image were calculated using image cross-correlation (cf. section 2.1). Constant and linear x- and y-motion which result from a constant tilt of the y-motor with respect to the detector were subtracted from these results. The residual movements of the sample are depicted in Fig. A.19. The non-linearities in the x-motion are of the order of $\pm\,4\,\mu\mathrm{m}$ which is

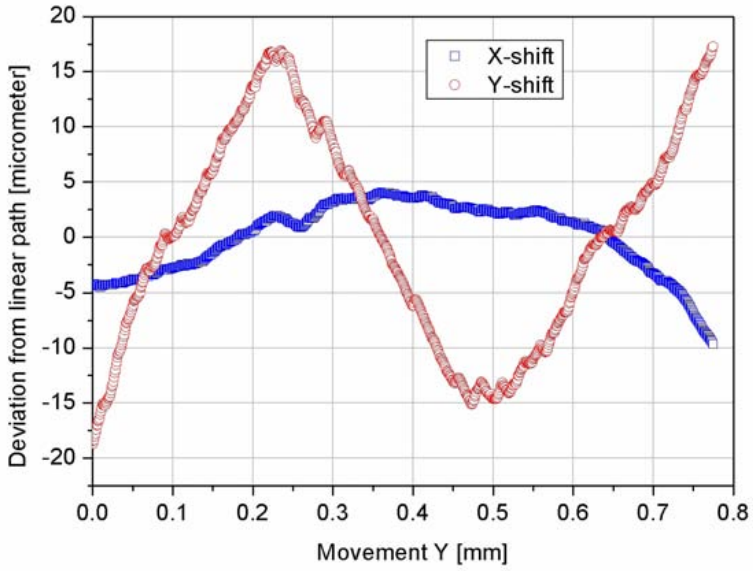

Figure A.19: Non-linear movements during ascent of the Huber y-stage.

very good: Taking the distance between sample and y-stage of $\sim 250\,\mathrm{mm}$ into account these deviations correspond to a tilt of approx $\pm\ 16\,\mu\mathrm{rad}$. However the y-motion contains a *slow* zigzag shaped drift of the order of $\pm\ 15\,\mu\mathrm{m}$ which is much more than what is tolerable for a high-resolution setup. This deviation is probably the result of a bad mechanical guidance leading to an erratic ascent of the Huber y-stage. Consequently large y-displacements be-

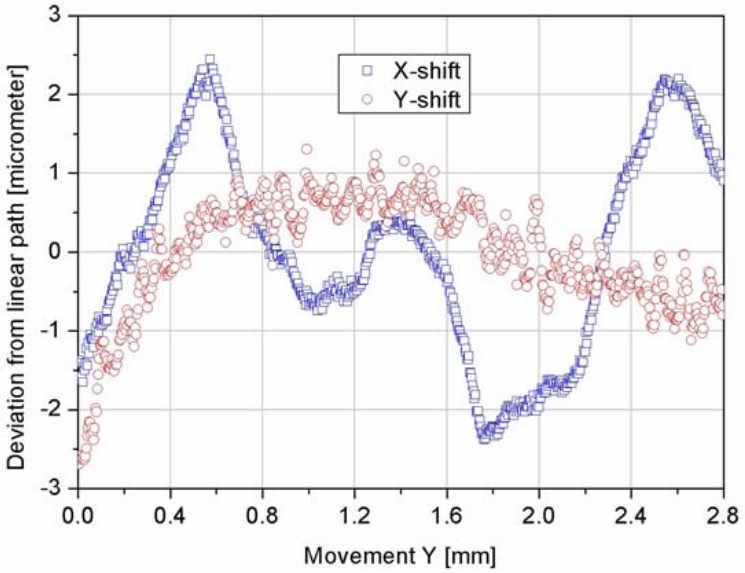

Figure A.20: Non-linear movements during ascent of the Micos UPL-160 stage.

tween two measurements should be avoided at all costs or realignment of the rotation axis tilt will become necessary. An ultra precise levitation table (model Micos UPL-160) was tested

in view of eventually replacing the Huber motor. The resulting x and y non-linearities of the UPL-160 are plotted in Fig. A.20. While the residual x-motion is roughly two times smaller than for the Huber stage, the y-motion has improved by a factor of 15(!) with only small remnant oscillations of the order of $\pm\, 0.5\,\mu\mathrm{m}$. This improvement is the result of a completely different levitation technique and is well within the tolerance range for μCT.

A.2.5 The X-ray macroscope

The X-ray *macroscope* is used since 2003 for radiography and tomography at the BAMline and is fully described in [Rac06], hence only a short overview is given in this work (cf. table A.5). The macroscope commonly uses exchangable Rodenstock front lenses which are manually focused onto the scintillator screen. Despite their large numerical aperture (yielding a very high light throughput) these lenses are not designed for high-resolution imaging. Their chromatic corrections are rather poor and consequently they can only be used for a small range of wavelengths ($500-550\,\mathrm{nm}$), limiting the choice of the scintillator material to GADOX, YAG, BGO and CWO screens (see table A.2). Unfortunately the very thin ($4\,\mu\mathrm{m}$) LAG:Eu screens with their high resolving power have their characteristic emission ($580\,\mathrm{nm}$ and $700\,\mathrm{nm}$) above the tolerance range of the Rodenstock lenses.
Behind the front lens a 45^o mirror redirects the light onto a Nikkor $180/2.8\ ED$ telephoto lens ($f_1 = 180\,\mathrm{mm}$) which is used to refocus the magnified image onto the CCD. Since light propagates along quasi-parralel rays between the two lenses, the total magnification is calculated as the ratio of the two focal distances f_1/f_2 (see schematic Fig. A.8b). Table A.5 lists the available Rodenstock (RS) front lenses, their focusing distance f_1, numerical aperture (NA), total magnification M, effective pixel size Δx, resolving power R and field of view (FOV).

Front lens	f_1 [mm]	NA	M	Δx [μm]	R [μm]	FOV [mm^2]
RS TV-Heligon	21	0.5	$8.6\times$	1.58	$3-4$	3.2×3.2
RS TV-Heliflex	50	0.45	$3.6\times$	3.75	$6-8$	7.7×7.7
RS XR-Heliflex	100	0.33	$1.8\times$	7.5	$15-20$	15.4×15.4
Zeiss Achroplan	8	0.45	$22.5\times$	0.6	$1-2$	1.2×1.2

Table A.5: Overview of the available front lenses and their performance (in combination with Nikkor $180/2.8\ ED$ telephoto and Princeton VA 2048B CCD camera).

The limitations of the conventional optics were overcome in early 2005, replacing the Rodenstock with a Zeiss Achroplan ($20 \times /0.45$) lens and imaging a $4\ \mu m$ thin LAG:Eu screen (together with a $495\,\mathrm{nm}$ Schott glass filter in order to suppress the YAG-substrate's UV-emission). An outstanding resolution of $R \sim 2\,\mu\mathrm{m}$ at $\Delta x = 0.6\,\mu\mathrm{m}$ effective pixel size was registered with this combination [Rac07b]. First phase contrast tomograms could be recorded and a new microscope was ordered by the end of 2005 (see next paragraph). Remotely controlled focusing of the macro-optics was implemented early 2007 by introducing motorized control over

the Nikkor telephoto. Still, mounting and positioning of the scintillator screen and positioning the Rodenstock lenses with respect to the screen remains a time-consuming procedure which is done manually and becomes particularly delicate when spatial resolutions better than $5\,\mu\mathrm{m}$ are needed.

A.2.6 The X-ray microscope

In October 2005 a customized microscope was ordered from Optique Peter S.A. (France). Precise requirements for the system were elaborated, premised on experiences with the BAMline macroscope and similar systems that are operated at the European synchrotron's (ESRF) imaging beamlines. The focusing as well as the camera positioning are fully motorized in order to avoid the time-consuming opening and closing of the experimental hutch. Two microstep motors allow ultra precise positioning of the microscope lenses with respect to the scintillator screen (Newport MFA-PP) as well as rotation of the camera head (Newport NSA12, range: $\pm$ $2\,°$). Three microscopic lenses are mounted simultaneously on a motorized revolver allowing to change the optical magnification quickly during the experiment. The design was optimized to work with Olympus Ultra-Plan Super-Apochromat lenses (UPLSAPO) for high-resolution imaging fully compensating both spherical and chromatic aberrations, from the UV to the near infrared. Drawings as well as a photo of the operational microscope are shown in Fig. A.21.

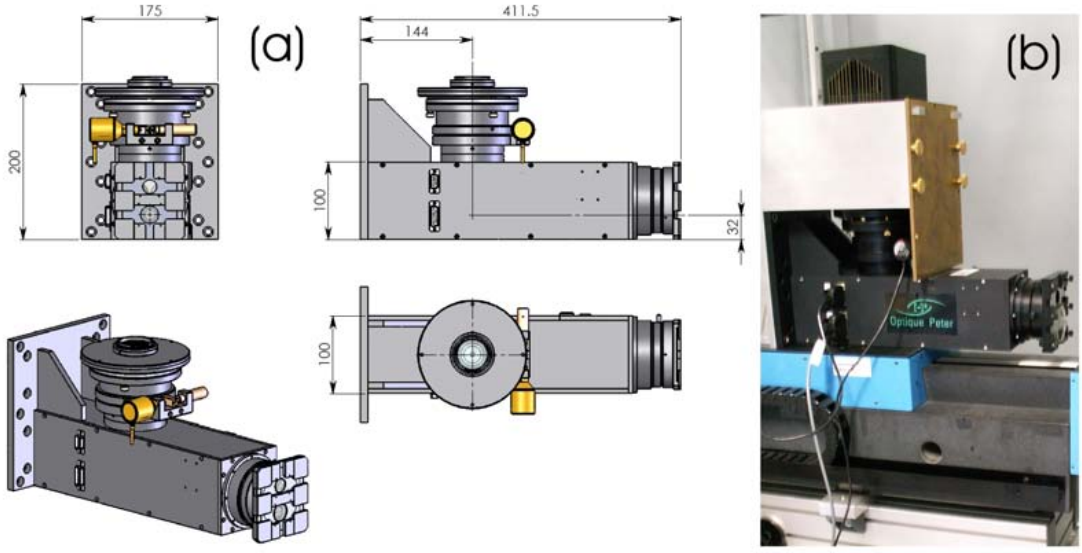

Figure A.21: (a) Schematic drawings of the Optique Peter microscope (dimensions are given in mm). (b) Photo of the operational microscope at BAMline (a $4\,\mathrm{mm}$ brass shield is used to protect the Princeton VA 2048B camera from high-energy X-rays).

Right behind the front lenses two filter wheels (each with three $25.4\,\mathrm{mm}$ wide round sockets) plus one additional filter drawer are integrated into the microscope housing: The first wheel allows to choose among three color glass filters (Thorlabs Inc. $495\,\mathrm{nm}$, $550\,\mathrm{nm}$ and $600\,\mathrm{nm}$) which are used to suppress the characteristic emission of the scintillator substrates; The sec-

ond wheel bears two different neutral density filters (75% and 50% transmission) that can be optionally inserted to reduce light (e.g. when the conversion rate of the scintillator is too high). Similar to the macroscope a $45\,^{\circ}$ mirror redirects the light onto a collimator which combines with an $(2\times)$ *eye-piece* to magnify the image onto the $27.6\times\ 27.6\,\mathrm{mm}^2$ CCD chip. The available front lenses, their numerical aperture (NA), working distance (WD), total magnification M, effective pixel size Δx, resolultion R and field of view (FOV) are summarized in table A.6.

Front lens	NA	WD [mm]	M	Δx [μm]	R [μ m]	FOV [mm^2]
PLAPON $1.25\times$	0.04	5.1	$2.5\times$	5.48	~ 10	11.2×11.2
PLAPON $2\times$	0.08	6.2	$4\times$	3.43	$6-7$	7.0×7.0
UPLSAPO $4\times$	0.16	13.0	$8\times$	1.71	~ 3	3.5×3.5
UPLSAPO $10\times$	0.4	3.1	$20\times$	0.69	~ 0.8	1.4×1.4
UPLSAPO $20\times$	0.75	0.6	$40\times$	0.34	~ 0.5	0.7×0.7

Table A.6: Overview of the available Olympus front lenses for the X-ray microscope (in combination with $2\times$ eye-piece and Princeton VA 2048B CCD camera).

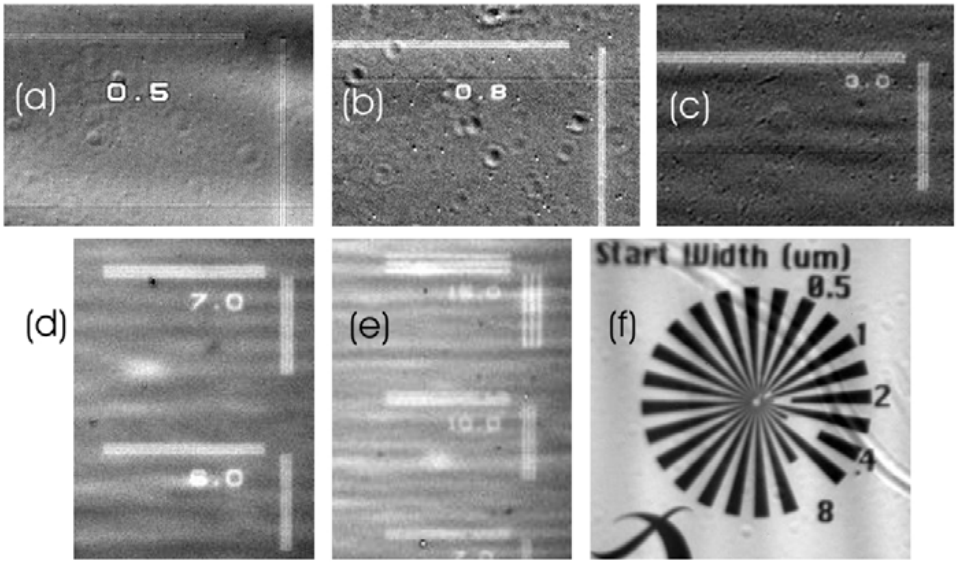

Figure A.22: Resolution test charts imaged with different front lenses: (a) UPLSAPO $20\times$ with a $4\,\mu\mathrm{m}$ LAG:Eu scintillator screen resolves the $0.5\,\mu\mathrm{m}$ pattern, (b) UPLSAPO $10\times$ with LAG:Eu yields a resolution of $0.8\,\mu\mathrm{m}$, (c) Image of the $3.0\,\mu\mathrm{m}$ lines taken with UPLSAPO $4\times$ and $22\,\mu\mathrm{m}$ CWO screen, (d) PLAPON $2\times$ with LAG:Eu screen, (e) PLAPON $1.25\times$ with LAG:Eu, (f) same combination as (a) showing the X-radia Siemens star.

The scintillator nose-cap is a particular design which has been elaborated to solve a very common problem: Finding a sufficiently large region on the scintillator's surface that is free of scratches and kinks which are known to degrade the quality of recorded X-ray images. Two

screens can be mounted simultaneously on the cap (e.g. a $4\,\mu\mathrm{m}$ LAG:Eu screen for high- and a $25\,\mu\mathrm{m}$ CWO screen for medium-resolution imaging). By using screws and manual levers the two scintillators can be exchanged, tilted and positioned in the (x, y)-plane in order to find the ideal *clean* region on the surface.

The highest resolving power of all Olympus front lenses (see table A.6 has been measured by imaging line patterns of different spacing (X-ray resolution test pattern JIMA RT RC-01, Nihon Matech Inc., Japan) as well as a Siemens star (test pattern X500-200-30, X-radia Corp., USA). Images recorded at the limit of resolving power (at $E = 18\,\mathrm{keV}$) are shown in Fig. A.22 for each Olympus front lens. Using the two high-magnification lenses UPLSAPO $20\times$ and UPLSAPO $10\times$, patterns of $0.5\,\mu\mathrm{m}$ and $0.8\,\mu\mathrm{m}$ could be imaged, which is in good agreement with the R-values given by the manufacturer ($0.41\,\mu\mathrm{m}$ and $0.76\,\mu\mathrm{m}$ respectively). For the medium-resolution lenses slightly lower values were found ($3.0\,\mu\mathrm{m}$, 6 - $7\,\mu\mathrm{m}$ and $10\,\mu\mathrm{m}$ for the UPLSAPO $4\times$, PLAPON $2\times$ and PLAPON $1.25\times$ respectively) compared to those given by Olympus ($1.91\,\mu\mathrm{m}$,$3.81\,\mu\mathrm{m}$ and $7.63\,\mu\mathrm{m}$). This discrepancy is probably the result of the finite thickness of the scintillator screen.

Appendix B

Image processing

B.1 Linear correction

When high-resolution radiographs of mm-sized samples are recorded at hard X-ray beamlines (wavelength $\lambda \leq 1\,\mathrm{nm}$), not only the microstructure of the sample but every object encountered along the beam path is imaged: Monochromator mirrors, apertures, attenuation filters, sample container, X-ray converter screen and vacuum windows. Depending on its position along the beam path, an inhomogeneous object may cause phase-enhancement, thus rendering the image post-processing difficult. Stray intensity contributions which are not related to the sample are known to degrade the quality of a tomographic measurement because they are integrated over large areas in the reconstructed 3D images, often obscuring very important structural details of interest. Such stray contributions are conventionally removed from the images by normalization. In the present work, temporal beam instabilities and unwanted sample motion led to the development of an adapted normalization algorithm and numerical motion correction that are now commonly used to improve the quality of high-resolution μCT images recorded at BAMline. Still, factorization of the stray and the sample contributions is the underlying assumption of all such *flatfield* methods. Consequently, random and/or non-linear perturbations (e.g. due to a strong anisotropic phase-contrast) are not or insufficiently reduced by normalization and are bound to produce artifacts in the reconstructed 3D images. Ways of correcting such artifacts that were developed during this thesis are presented in section B.2.

B.1.1 Background normalization

Before reaching the sample, the X-rays pass through a number of optical elements: Mirrors (DMM, DCM), filters (Be-, Cu- and/or Al-foils of $0.05-\ 1.0\,\mathrm{mm}$ thickness), apertures (three pairs of slits can be used at different positions), vacuum windows (two $0.05\,\mathrm{mm}$ Kapton foils) and possibly a sample container (e.g. a boron nitride crucible for high temperature experiments or a capillary filled with water), each adding individual phase and amplitude modulations to the propagating wave. Some of these elements are used to adjust the beam size, monochromaticity and intensity, others are necessary to provide the right environment for the sample. Following sample transmission, the beam is imaged by the detector which comprises an X-ray converter screen (scintillator), microscope lenses and a CCD camera. Every component introduces additional blurring and/or stray intensities to the images and has to be reconsidered as a distinct source of image artifacts. The amplitude of each stray contribution differs with

its origin causing various types of damage to the reconstructed information. To assure a high imaging quality it is therefore necessary to address each contribution separately and find ways of removing it from the images.
Intensity variations that are caused by apertures and/or filters upstream of the DMM are blurred in the recorded images (due to the finite beam divergence) and can be grouped into the amplitude $A(x,y)$ of a quasi-planar incoming wave (dropping for simplicity any time dependence of the form $\exp(i\omega t)$) propagating along the z-axis: $u(x,y) = A(x,y)\exp(i2\pi z/\lambda)$. Modulations caused by the DMM and/or objects further downstream eventually appear amplified by Fresnel-propagation. Considering a number N of such objects intersecting the beam between the DMM and the sample, each object j positioned at a distance Δ_j upstream of the next object $j+1$. If scattering is sufficiently weak inside each object, the thin-lens approximation applies and the wave impinging onto the sample is a series of these N contributions each represented by multiplication with a transmission function $T_j(x,y)$ followed by Fresnel-propagation (convolution of the wave with a complex *propagator* $P_j(x,y,\Delta_j)$)

$$u_{inc}(x,y) = \left(\left(\left(u \cdot T_1 * P_1\right) T_2 * P_2\right) T_3 * \ldots * P_N\right)_{x,y} \tag{B.1}$$

$$T_j(x,y) = \exp\left[i\phi_j(x,y) - B_j(x,y)\right] \tag{B.2}$$

where $\phi_j(x,y)$ and $B_j(x,y)$ represent line-integrals of δ and β along the direction of propagation, i.e. the phase-shift and attenuation due to propagation through the jth object and its immediate environment (cf. section 1.3). Similarly the X-ray interaction with the sample introduces another transmission function and the field impinging on an imaging-plane (x,y) directly behind the sample (subscript '0') can be described by:

$$u_0(x,y) = u_{inc}(x,y) \cdot T_{sample}(x,y) \tag{B.3}$$

Effects which the sample environment might have on the recorded intensities are often neglected, an assumption which is not valid in general (e.g. dust particles on a window sometimes cause stronger stray intensities than the window itself, bubbles may have desastreous effects on 3D images of water immersed samples, see section B.2, etc.). Fresnel-propagation can be applied along a finite sample-to-detector distance d in order to enhance the visibility of the structural features that are mainly comprised in the phase of $T_{sample}(x,y)$. Propagation is again described by convolution of $u_0(x,y)$ with a complex function $P_d(x,y)$:

$$u_d(x,y) = u_0(x,y) * P_d(x,y) \tag{B.4}$$

Measuring the intensity in the image plane transforms the wave into its squared modulus $I_d(x,y) = |u_d(x,y)|^2$. Using eq. B.1-B.4, the measured intensity becomes:

$$I_d(x,y) = \left(u_d^* \cdot u_d\right)(x,y) \tag{B.5}$$

$$= \left|\left(\left(\left(u \cdot T_1 * P_1\right) T_2 * P_2\right) T_3 * \ldots * P_N\right) \cdot T_{sample} * P_d\right|^2 (x,y) \tag{B.6}$$

I_d is measured on a scintillator screen which is used to convert the X-rays to an image of visible light. Scratches and flaws on the surface of this screen result in bright flares which may

saturate the CCD and are very difficult to correct in terms of image normalization. Fig. B.1a shows a typical radiographic image of a rubber sample recorded at $d = 20\,\mathrm{mm}$ propagation distance and using the DMM to select X-rays of $9.6\,\mathrm{keV}$ energy (the effective pixel size was $\Delta x = 0.7\,\mu\mathrm{m}$, at $R \approx 1\,\mu\mathrm{m}$ resolution). The corresponding brightfield image which will be

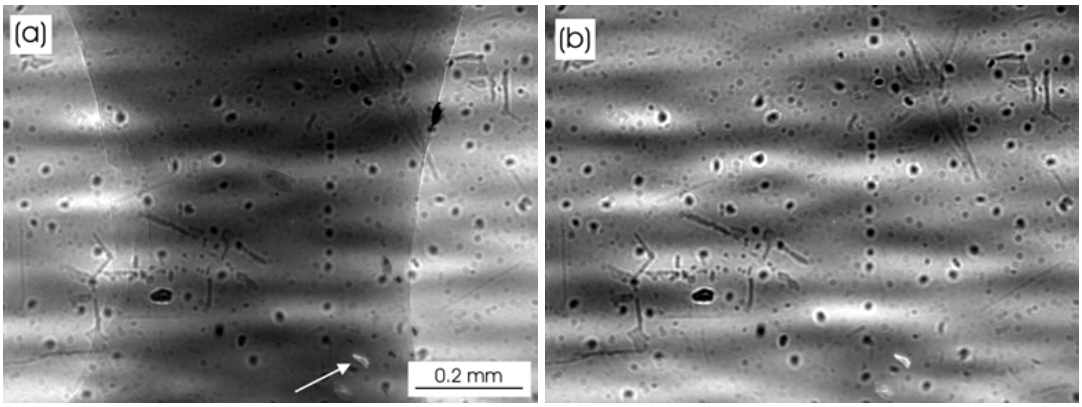

Figure B.1: Typical X-ray images recorded at BAM*line* : (a) Radiography of a rubber sample acquired at $E = 9.6\,\mathrm{keV}$ and $\Delta x = 0.7\,\mu\mathrm{m}$ (the arrow indicates a defect on the scintillator screen); (b) Brightfield image taken after moving the sample out of the beam.

denoted $I_{bf}(x, y, t)$ (recorded at time t after moving the sample out of the beam) is shown in Fig. B.1b. A wavy horizontal intensity modulation is seen in the brightfield image, caused by distortions in the DMM super-lattice (*multilayer stripes*). Additionally circular and linear interference patterns are caused by dust and scratches on the X-ray exit window (two $50\,\mu\mathrm{m}$ thick Kapton foils). A defect due to a flaw on the scintillator screen is seen in the lower part of B.1a and b (indicated by an arrow). It is well known that the characteristics of the multilayer stripes (amplitude and pitch) depend mostly on the chemical elements that are forming the layer-structure (e.g. tungsten and silicon for the BAM*line* DMM) and cannot be avoided unless using the DCM. Assuming that Fig. B.1 represents the general case it is straight forward to obtain a first order background correction by dividing Fig. B.1a by Fig. B.1b. Additionally a pixel-wise subtraction of the CCD array dark current $I_{dc}(x, y)$ is commonly applied to both I_d and I_{bf} and hence the normalized (corrected) intensities are found:

$$I_d^{(corr)}(x, y, t, \theta) = \frac{I_d(x, y, t, \theta) - I_{dc}(x, y)}{I_{bf}(x, y, t) - I_{dc}(x, y)} \tag{B.7}$$

with θ the tomographic projection angle (typically $0\,^\circ$ - $180\,^\circ$). In order to fully account for I_{bf} changing and/or shifting with time, both I_d and I_{bf} would have to be recorded at the same time t and for each projection angle separately. Such a procedure is not applicable due to the reduced time window that is available for one tomographic scan (typically $1 - 2$ hours for $900 - 1500$ projection images) which would not allow to move the sample out of and back into the beam after each angular step. Therefore, amplitude changes as well as lateral shifts in I_{bf} are assumed to be sufficiently slow compared to the image acquisition time and new brigthfield images are acquired only every $50 - 100$ projections, i.e. every $10 - 20$ minutes.

While this assumption may be valid for moderate image resolutions it proves to be insufficient

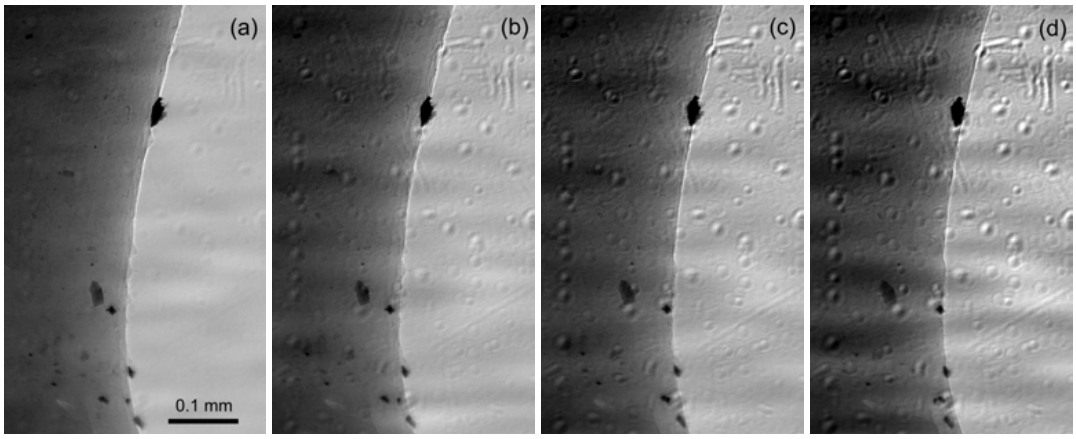

Figure B.2: Standard background normalization applied to four radiographic pictures recorded at (a) t =0 s and θ =0 °, (b) t =3 min and θ =4 °, (c) t =6 min and θ =6 ° and (d) t =9 min and θ =12 °.

when high-resolution images are recorded. Fig B.2 shows the corrected intensities in a region of interest of Fig. B.1a when the standard background normalization is applied to four images recorded at different times ($t \approx 0$ to 9 min) and angular positions ($\theta \approx 0\,°$ to 12 °) of the sample as it is turned during a microtomography scan. Here the same brightfield image (recorded at $t = 0$ s) was used to correct the four radiographs. Note that both the multilayer stripes and the stray intensities caused by the exit window reappear in Figs. B.2b-d, a result of the lateral motion in these contributions which is ignored by the standard normalization method.

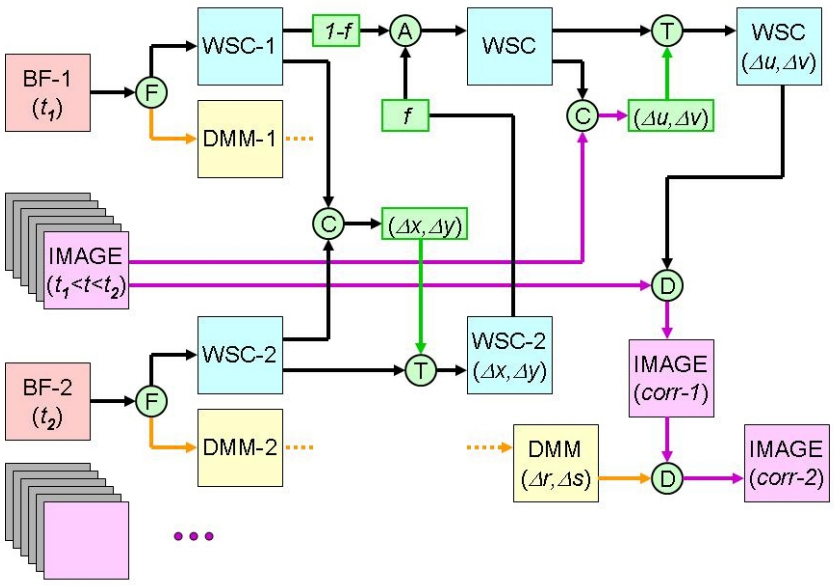

Figure B.3: Schematic diagram of the adapted normalization algorithm.

Without further corrections, 3D reconstruction by filtered back-projection method would introduce a number of imaging artifacts degrading the image quality and obscuring the sample structure which is of interest. In order to avoid the time-consuming acquisition of individual brightfield images for each projection radiograph, an adapted background normalization was developed to correct the shifting stray intensities of the DMM and the exit window separately. A schematic illustration of the algorithm is given in Fig. B.3.
Considering a single radiographic image (similar to Fig. B.1a), recorded at a time t and projection angle θ as part of a common μCT scan. Brightfield images will be recorded in regular time intervals during the scan, particularly one image $I_{bf}^{(1)}(x, y, t_1)$ at a time $t_1 < t$ and another one $I_{bf}^{(2)}(x, y, t_2)$ at $t_2 > t$: the bounds of the interval which includes the image. An anisotropic non-linear median filter F is then applied to both brightfield images using a 81 pixel wide and 21 pixel high structuring element (cf. section 2.2). Applying F to Fig. B.1b yields Fig. B.4a, an image showing only the multilayer stripes (similar to a low-pass filter; images are labeled DMM-1 and DMM-2 in Fig. B.3). Dividing B.1b by Fig. B.4a reveals the stray intensity contributions which are related to the X-ray exit window (note that scintillator defects are also included in Fig. B.4b; Images are labeled WSC-1 and WSC-2 in Fig. B.3).

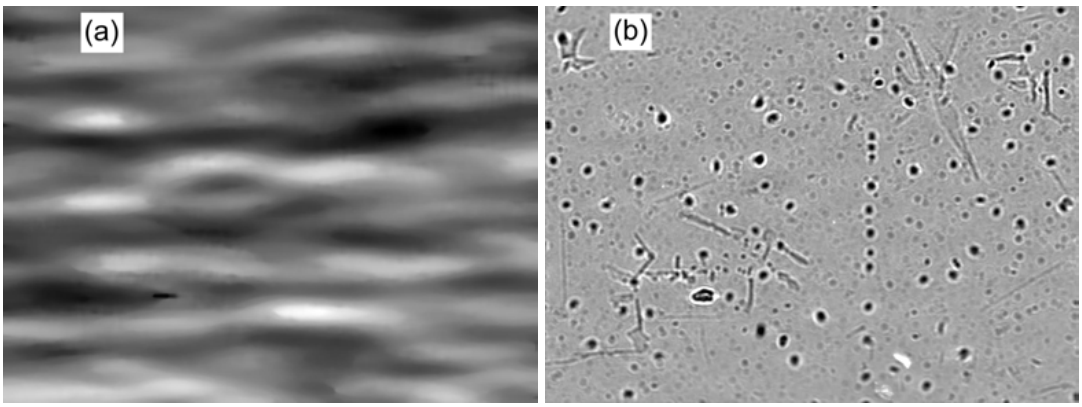

Figure B.4: Filtering two components from the brightfiled images: (a) The wavy horizontal intensity of the DMM (multilayer stripes) is obtained by applying a anisotropic non-linear median filter to Fig. B.1b. (b) Division of the latter by (a) yields an image showing only the stray intensities due to exit window and scintillator defects.

Each of the two components of $I_{bf}^{(2)}(x, y, t_2)$ is then matched with its counterpart obtained from $I_{bf}^{(1)}(x, y, t_1)$ by using Fourier image cross-correlation C. The shifts $(\Delta x, \Delta y)$ of WSC-2 with respect to WSC-1 are thus found and inversed by applying Fourier image-translation T to WSC-2. The same procedure is applied to the component DMM-2. Following their alignment a weighted summation A is applied to the matching components in order to improve statistics and to compensate for an overall decreasing beam intensity (following each electron injection the ring current slowly drops to $1/2$ of its initial value of $\approx 250\,\mathrm{mA}$ until the next injection takes place, 8 hours later). The weighting factors f (for the components WSC-2 and DMM-2) and $1 - f$ (for WSC-1 and DMM-1) are calculated with a simple lever rule yielding

$f = (t_2 - t)/(t_2 - t_1) = 1$ at $t = t_2$ and $f = 0$ at $t = t_1$. Improved images are thus obtained and Fourier image cross-correlation is used to match these components (WSC and DMM) with the background of the projection image $I_d(x, y, t, \theta)$ recorded at time t and projection angle θ. If possible the cross-correlation is restricted to a ROI of the image that does not show the sample (e.g. small regions on the right or left hand side of the sample in Fig. B.1a). First lateral shifts $(\Delta u, \Delta v)$ of the WSC component with respect to $I_d(x, y, t, \theta)$ are thus calculated and reversed by Fourier image-translation T. Second the WSC intensities are removed from $I_d(x, y, t, \theta)$ by division D. Finally the DMM component is matched to the normalized image $I_d^{(corr1)}(x, y, t, \theta)$ then removed by division, yielding an image $I_d^{(corr2)}(x, y, t, \theta)$ which is ideally cleaned from both stray contributions. The lateral shifts $(\Delta u, \Delta v)$ of the DMM and

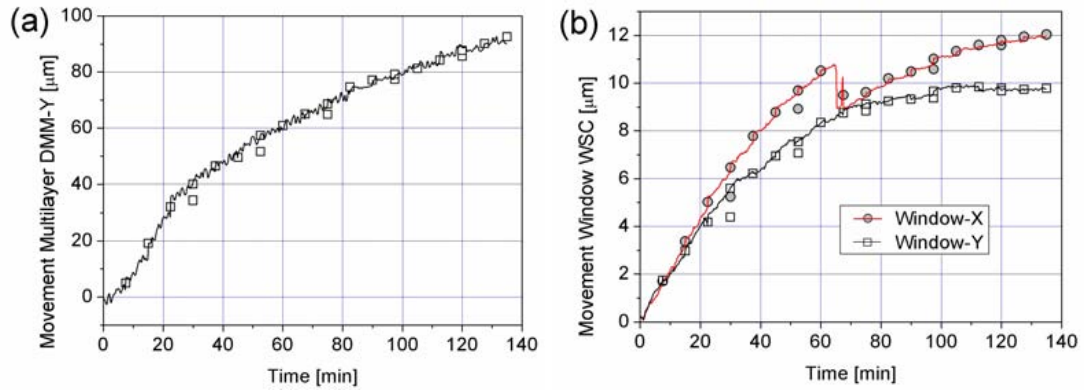

Figure B.5: Lateral shifts of the background intensities calculated from the tomography scan of a rubber sample (recorded at $E = 9.6\,\mathrm{keV}$ and $\Delta x = 0.7\,\mu\mathrm{m}$). The solid line shows the shifts of (a) the DMM (only vertical motion occurred) and (b) the WSC component with respect to the background of each projection image while the hollow rectangles indicate the relative shifts between two sequential brightfield images)

the WSC contributions were thus measured from the tomographic data of the rubber sample (see Fig. B.1a), and are shown in Fig. B.5. Displacements of the DMM background intensities are found to be quasi-vertical reaching $100\,\mu\mathrm{m}$ after $\approx 135\,\mathrm{min}$ of scanning time. The image stray intensities which are related to the exit window (dust and scratches) are found to shift continuously in a diagonal direction measuring 10 to $12\,\mu\mathrm{m}$ by the end of the scan.

B.1.2 Sample motion

For the particular example discussed in the previous paragraph unwanted motion of the sample caused additional perturbations in the angular trajectories of the sinograms. Although for solid samples, movements can be avoided by firmly attaching the sample to its holder and using high-precision motors (cf. section A.1), a finite sample motion is unavoidable when parts of the sample or its environment are liquid (e.g. bubbles forming in water, see also section B.2) or elastic (e.g. rubber). The resulting deviations are of the order of $1-10\,\mu\mathrm{m}$ and require

a *path-correction* in order to avoid severe degradation of the reconstructed three-dimensional structural information. Note that the rubber which was shown in Fig. B.1a contains micron-sized silica particles which are characterized by very strong X-ray attenuation compared to the bulk material. As can be seen in Fig. B.6a the angular trajectory of the particles (marked

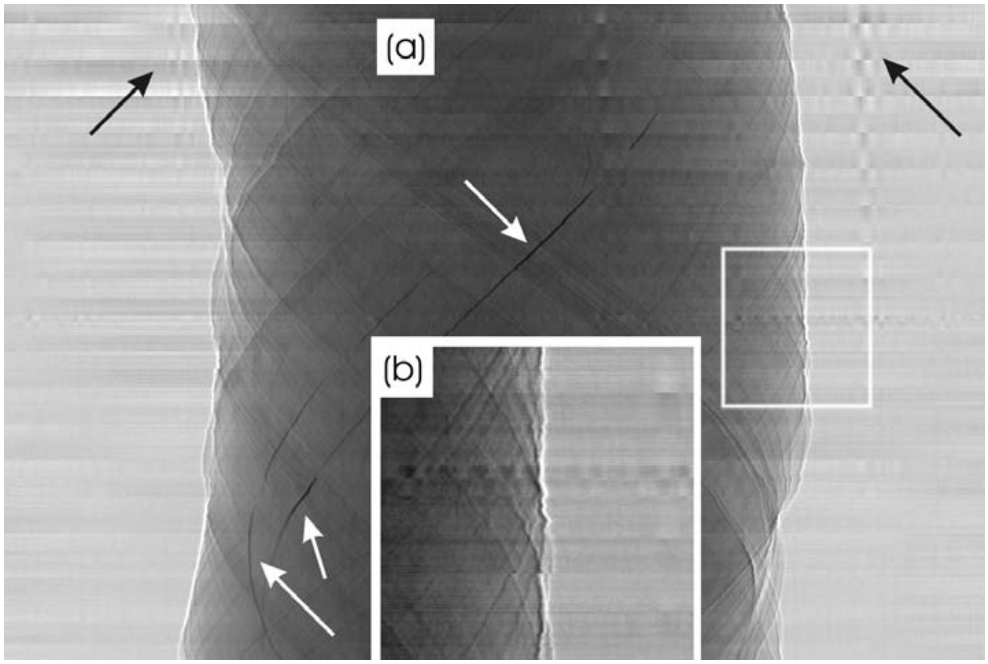

Figure B.6: Sinogram of a high-resolution scan of rubber sample. (a) The sinogram data shows well the sinusoidal trajectory of individual silica particles (appearing dark due to high attenuation, maked by the white arrows) which can be used for motion correction. Intensity variations due to uncorrected shifts in the brightfield images are indicated by black arrows. The inset (b) shows an enlarged view revealing a faint jitter motion.

by white arrows) is well pronounced in the sinograms and their center-of-mass coordinates (x_c, y_c) can thus be found by threshold binarization. Note there are additional stray intensities in the sinogram caused by uncorrected shifts in the brightfield images (indicated by black arrows, see previous subsection for correction methods). The inset Fig. B.6b reveals a fine jitter superimposing onto the x- and y-motion of the sample. This jitter-motion was measured by calculating x_c and y_c for one particle and for all projection angles, then fitting a sinusoidal trajectory to the x-component. The unwanted sample x-motion (which is assumed to align with the residual motion of the silica particle, i.e. neglecting contraction or dilation of the whole sample) corresponds to the difference between measurement and fit whereas the y-motion should ideally be zero.

This idea was already developed in section A.1.3 and is shown in Fig. B.7 (for further applications see [Lan04, Boi05]). In order to avoid that the wrong silica particle is selected the software works only on a small squared ROI that is defined for each picture j to be centered around (x_c, y_c) as calculated from the previous picture $j-1$ (starting coordinates are given by

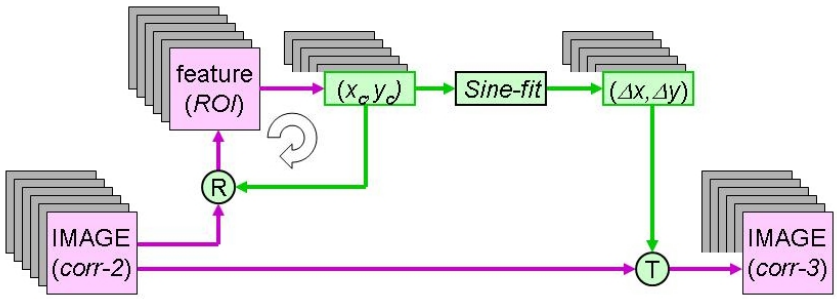

Figure B.7: Schema of the motion correction: Center-of-mass coordinates of a well pronounced feature (e.g. silica particle in rubber) are calculated and a sinusoidal fit is applied to quantify the residual motion wich is then corrected by Fourier image-translation T.

the user). The binarization threshold is adapted depending on the average attenuation of the ROI. The success of this method relies on the possibility to find an isolated small particle with a strongly pronounced absorption contrast. A more robust correction of motion CT artifacts based on detection and fitting of the sample edges is found in [Zer98] and [Sri94].

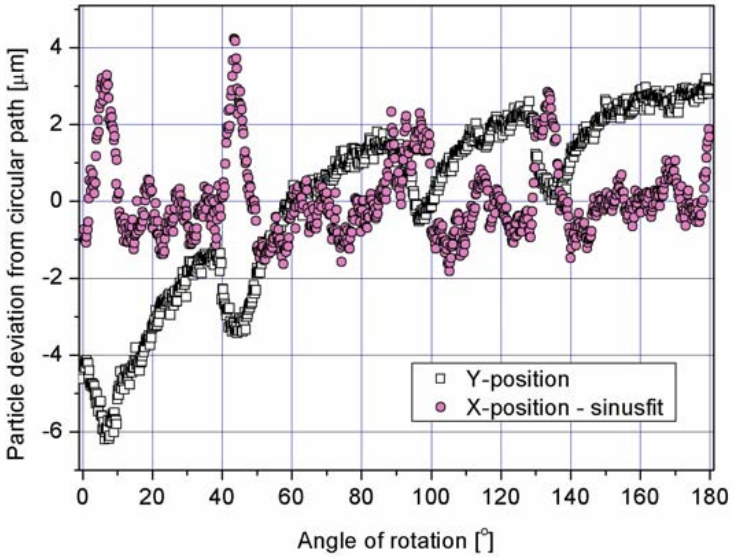

Figure B.8: Residual sample motion found by calculating the center-of-mass of one silica particle in the rubber and fitting the x-component to a sinusoidal trajectory.

Results of the 900 projection images recorded at $0\,^\circ$ - $180\,^\circ$ are shown in Fig. B.8. The residual x and y movements both show fluctuations of the order of $\pm\ 4\,\mu\mathrm{m}$. While the x-motion appears random the y-movement of the sample is of a regular *saw-tooth* shape with a slow linear ascent, the latter probably resulting from a faint misalignment of the rotation axis. These movements are inverted by Fourier image-translation method. A reconstruction of the uncorrected dataset as well as a slice obtained after applying the motion correction (as well as correcting the (x, y)-shifts in the brightfield intesities), are shown in Fig. B.9.

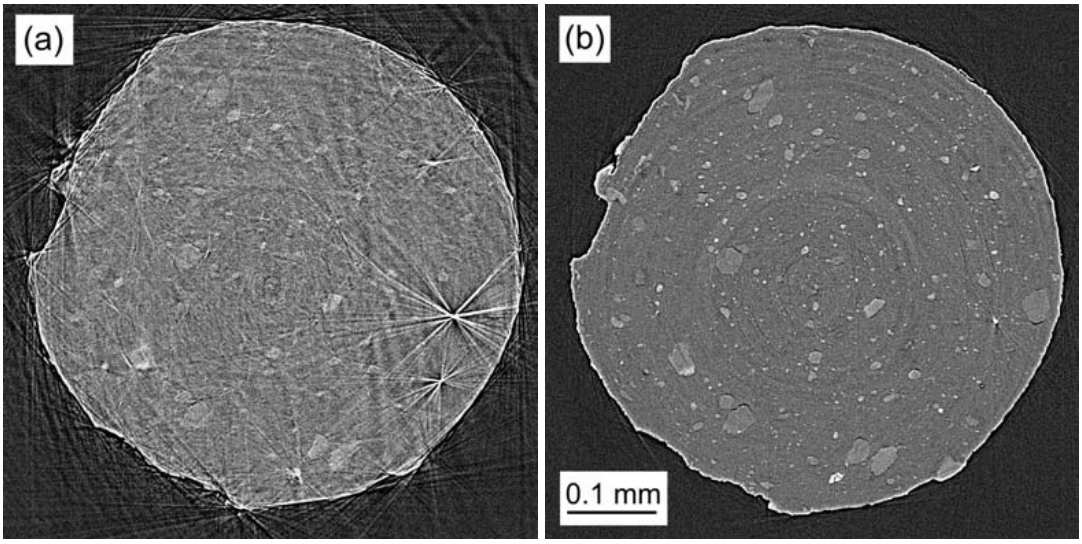

Figure B.9: Effect of advanced linear corrections on a reconstructed tomographic slice. (a) Using radiographic images obtained with standard normalization yields severe artifacts in the 3D image obscuring the structure of interest. (b) The reconstruction from the improved radiographs (applying an advanced brightfield normalization plus motion correction) shows details of μm size that were not visible in (a).

Note that the visibility of the features (silica agglomerates and particles) is strongly improved by the advanced brightfield method and motion correction. The resolution is such that μm-sized details are seen in the improved tomographic slice.

B.2 Correction of non-linear perturbations

Numerous artifacts (spurious contributions in the images which are not related to the sample structure) are known to tomographic imaging leading to an even larger number of methods which can be applied for analytic correction or approximate compensation of these artifacts. While linear methods were developed in the previous section correcting for sample motion and/or stray intensities that appear in the projection and brightfield images, this section is dedicated to 3D imaging artifacts that result from non-linear stray contributions which remain uncorrected when linear normalization is applied. The most prominent artifact types in this work (i.e. which were observed in the image data that is presented in chapter 3) are *ring artifacts*, *pore artifacts*, *spikes* and *bubbles*. These four types will be explained in the following along with methods that were developed for their compensation. For a more complete review on some of these tomographic imaging artifacts see [Boi06, Zer99].

B.2.1 Ring artifacts

X-ray tomographic imaging involves transformation of the radiographic projections (Radon transform) into a three-dimensional image of the object. This transformation is called fil-

tered back-projection and can be simplified to process a stack of individual slices instead of the whole volume, as long as the incoming beam is quasi-parallel (as is the case for images recorded at synchrotron beamlines). Quite often concentric dark and bright rings are seen in the reconstructed slices degrading the quality of the images. They are assumed to be an artificial result of the FBP which appears more pronounced in absorption images while they are less of a problem when phase-enhancement is used. Centered around the axis of sample rotation these circular lines (half circles when $180\,^{\circ}$-scans are performed) appear to be randomly distributed throughout the whole image. Several methods that can eventually be combined have been developed to supress or remove these artifacts.

Regular sample movements (*wobbling*): Commonly ring artifacts are attributed to non-linear variation in the response of the pixels on the CCD detector array. Additionally flaws and scratches on the scintillator surface may cause extreme intensity peaks which are not fully removed by the linear brightfield normalization (see previous section). Such defects maintain a constant position in the recorded images, during rotation and translation of the sample. Therefore, slightly shifting the sample position after each exposure by moving sample and rotation axis with pixel-wise steps over a 10×10 raster in the (x, y) plane changes the position of the defects with respect to the sample quasi-continuously in the images. The position of the sample is easily realigned during brightfield normalization.

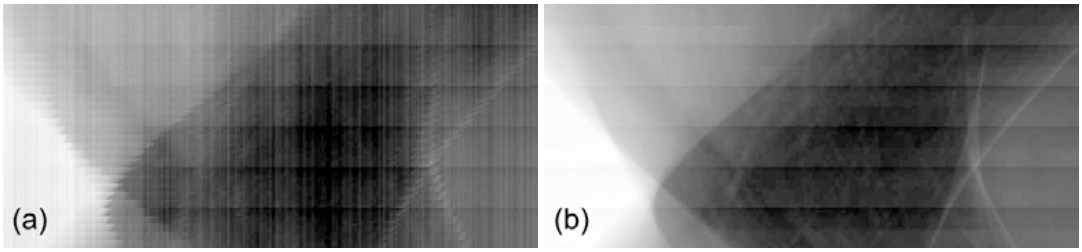

Figure B.10: Regular movements are applied to the sample in order to average stray intensities that are caused by defects on the scintillator and/or CCD and that would lead to ring artifacts in the 3D reconstruction. (a) Sinogram showing the pixel-wise *wobbling* of the sample. (b) The movements are inverted by automated image cropping.

As can be seen from the example shown in Fig. B.10 the x-shifts applied to the sample transform the sinusoidal trajectories of the sinograms into zigzag lines. Additionally a pixel-wise y-step is applied every 10 pictures. During the normalization procedure, both shifts are removed by automated image cropping and a regular sinogram is reobtained (see Fig. B.10b). Any non-linear stray intensity due to defects on the CCD and/or the scintillator screen would normally appear as vertical lines in the sinograms. Using sample *wobbling* these stray intensities are averaged over an area of 10×10 pixels and are thus effectively removed. Note that this method applies well when images are recorded at moderate resolutions while the motor precision for the wobbling was shown to be insufficient for high-resolution measurements ($R \leq 5\ \mu m$, see also section A.2).

Improved signal-to-noise ratio (SNR): Sometimes the conditions for imaging are such that only few X-rays contribute to the contrast forming the images on the CCD array. Consequently the (white) noise level becomes dangerously high compared to the signal strength. This is the case either when very short exposure times are necessary in order to record images at high frame rates (the signal is thus limited by the photon flux density, typically $1 \times 10^{10}\,\mathrm{Ph/s/mm^2}$) or when the detector saturates but the detected light is produced by only few X-rays (e.g. for energies $E > 60\,\mathrm{keV}$ the typical emission rate of YAG or CWO scintillators is > 1000 photons per X-ray). Furthermore non-linear amplification of the image noise occurs during tomographic filtered back-projection. Consequently the SNR in the 3D images is even lower compared to the 2D radiographs. Particularly towards the center of rotation (where the Radon transform is strongly over-sampled) an increase of concentric artifacts is commonly observed which is in contradiction to the SNR expected for this region.

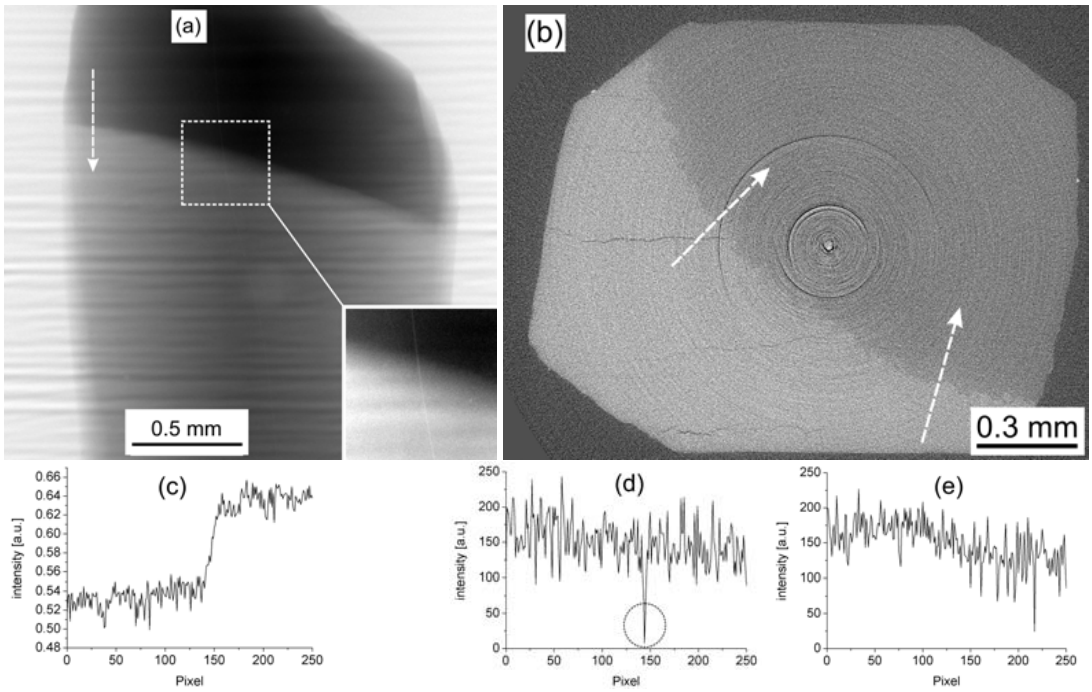

Figure B.11: Noise level in 2D radiographs compared to the 3D reconstruction: (a) Radiographic image showing a fraction of human tooth dentin with a denser enamel cup on the top ($E = 23\,\mathrm{keV}$ and $\Delta x = 1.6\,\mu\mathrm{m}$). An intensity profile was calculated along the dashed arrow (shown in (c)). The inset shows an enlarged view on the dentin-enamel junction (DEJ) revealing uncorrected stray intensities which are caused by a scratch on the scintillator surface. (b) An axial slice reconstructed by FBP method shows a much lower SNR than the radiograph as well as strongly pronounced ring artifacts. Intensity profiles were calculated along the dashed arrows (shown in (d) and (e)). Intensity drops due to ring artifacts stick out (dashed circle) while microcracks and DEJ are burried in the noise.

Volume images reconstructed from noisy projections inevitably contain strong ring artifacts which can be efficiently reduced by improving the statistics. Since the radiographs are nor-

malized by division with brightfield images (see previous section) strong noise in these corrective images has a particularly destructive effect on the reconstructed data and must hence be avoided at all costs. Consequently high SNR brightfield images are commonly obtained by averaging a sequence of $10 - 20$ images. Fig. B.11a shows a radiograph (after brightfield normalization) of a fraction of human tooth dentin (the dark top part representing the denser enamel) as well as an enlarged inset revealing uncorrected stray intensities caused by a scratch on the scintillator surface. An axial section of the 3D data is seen in Fig. B.11b, reconstructed from a set of 900 projection images of relatively low SNR. Note the enamel now appears brighter than the dentin due to the standard representation of tomography data on a $-\log$ scale. Intensity profiles were calculated along the dashed arrows in Fig. B.11a and b and are shown below (Fig. B.11c-e).

While the transition from the dense enamel to less dense dentin is clearly visible in the radiographs (profile shown in Fig. B.11c), this information is burried in the strong noise in the 3D image (profiles shown in Fig. B.11d and e). The reconstructed axial slice is further characterized by numerous ring artifacts that superimpose onto the sample structure and show a well pronounced intensity peak (marked by a dashed circle in profile B.11d) unlike the dentin-enamel junction (DEJ) and the enamel microcracks which are hardly visible. Clearly such 3D data cannot be used for quantitative image analysis.

The reconstructed image is further degraded by stray intensities that are caused by a scratch on the scintillator surface and insufficiently corrected by the linear normalization as shown in the inset of Fig. B.11a. Although the scratch appears only faintly in the projection image the stray intensities are integrated over the 900 radiographs causing a strongly pronounced funnel-shaped artifact and rendering large parts of the 3D data unusable. A frontal slice show-

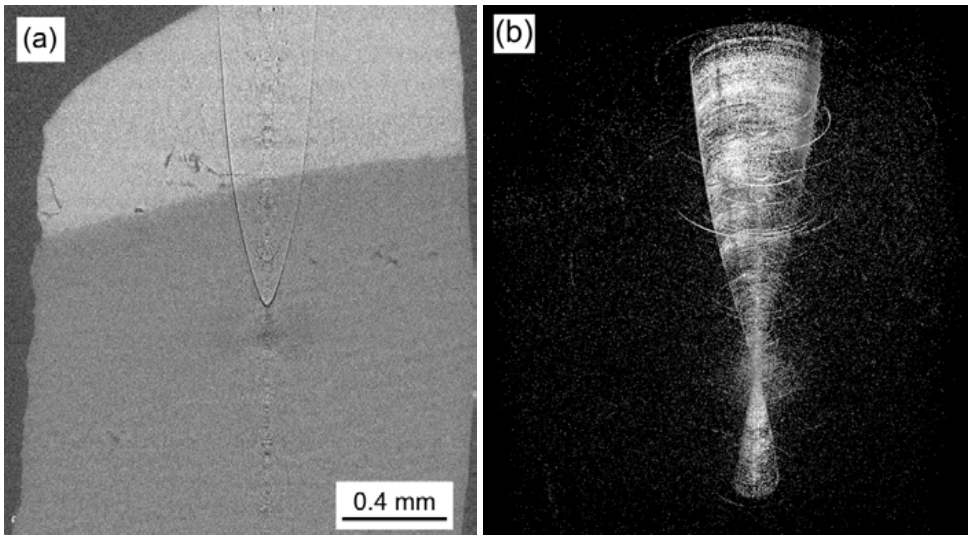

Figure B.12: Funnel shape imaging artifact caused by uncorrected intensity contributions due to a scratch on the scintillator screen: (a) Frontal slice of the 3D data. (b) Perspective view on the artifact (sample is set transparent).

ing this artifact is depicted in Fig. B.12a while by setting the sample transparent the shape of the *funnel-artifact* can be seen from a perspective view (Fig. B.12b). Note that in any axial view (e.g. Fig. B.11b) this funnel artifact is resembling a ring artifact. Unfortunately even the use of sufficiently long exposure times reducing the image noise in order to assure a good 3D reconstruction, a significant number of ring artifacts persists degrading the image quality. Consequently scratches and flaws on the scintillator screen have to be avoided at all costs and wobbling should be applied as long as high-resolution is not demanded.

Filtering of sinograms: Segmentation and removal of ring artifacts from the 3D datasets is a very delicate procedure which is why filtering the responsible spurious intensities prior to tomographic back-projection is the preferred method. The most common method applies a high-pass filter to the intensity profiles which are obtained from angular averaging each sinogram (either a linear Fourier high-pass filter or a non-linear median filter can be used for this purpose). Spurious intensity contributions remaining after application of the high-pass filter are further subtracted line-wise from the sinogram data. This method is very useful to remove the sources of ring artifacts because the responsible non-linear intensities remain at constant positions in the projection images thus forming straight vertical lines in the sinograms, i.e. peaks in the angular average which are then filtered from the smoothed background. This method

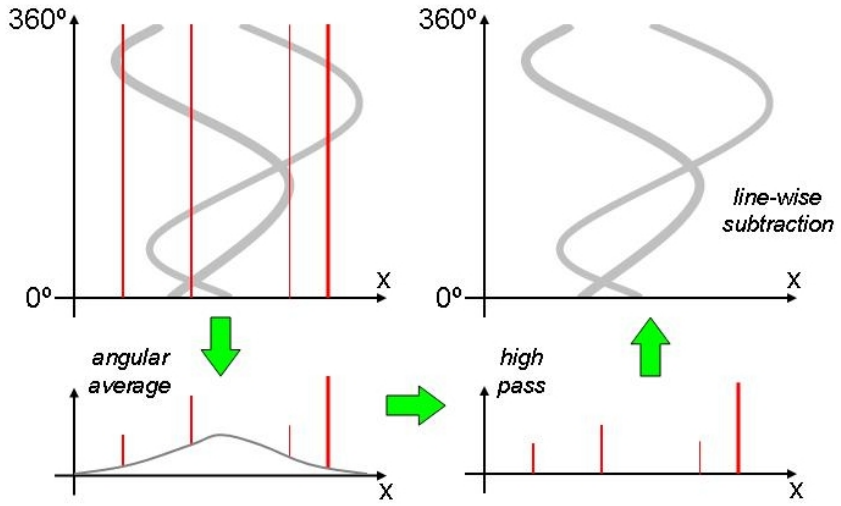

Figure B.13: Schematic illustration of the sinogram filter.

is illustrated in Fig. B.13 and applies particularly well to samples of cylindrical shape and quasi-homogeneous microstructure. Particularly for high-resolution imaging when wobbling the sample is inapplicable because of the limited motor-resolution, filtering the sinograms yields very good results. A reconstructed slice from a cylindrical sample of mono-disperse copper balls [Gru08] is shown in Fig. B.14 with and without application of the sinogram filter prior to reconstruction. Yet caution is demanded when there are small features in the sample

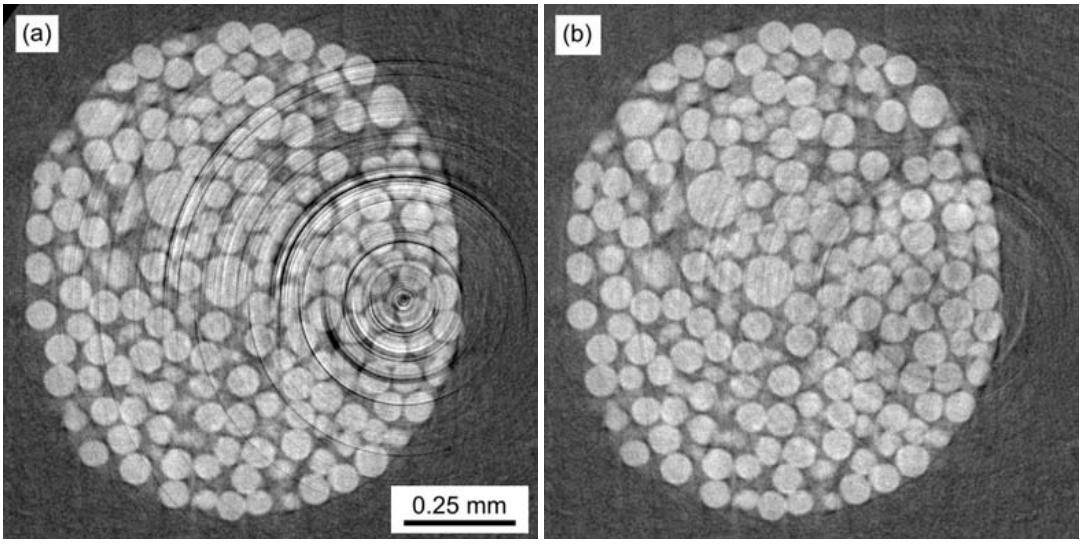

Figure B.14: Application of sinogram filter to a sample of scintered copper balls showing particularly strong ring artifacts. (a) Axial slice reconstructed without applying the filter. (b) Application of the sinogram filter improves the quality of the 3D data significantly.

(e.g. pores in steel, or rough sample edges) causing strong changes in the recorded X-ray attenuation. The sinogram filter may produce circular artifacts instead of removing them.

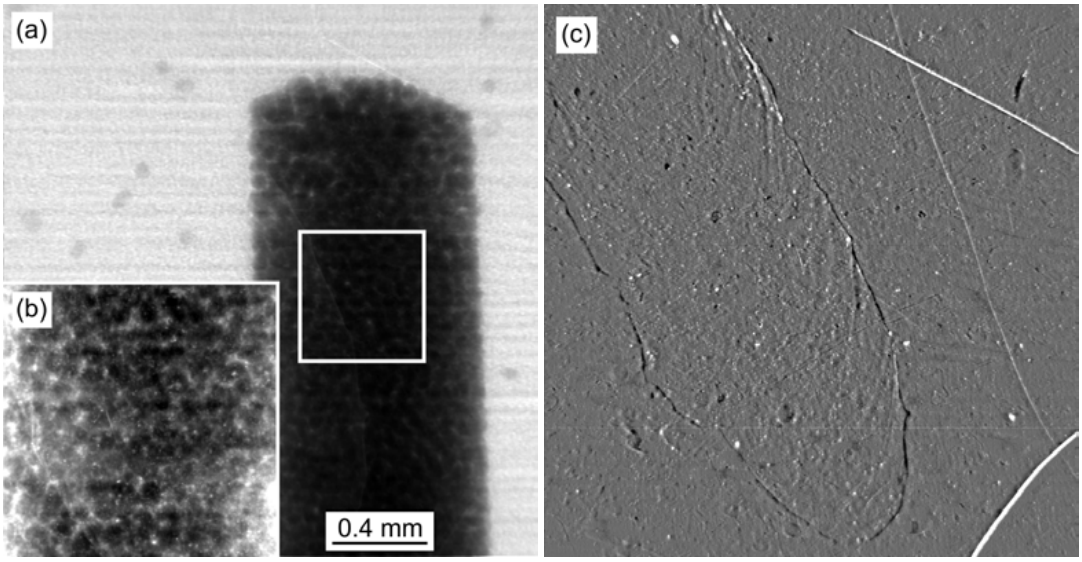

Figure B.15: Detailed analysis of the scintillator defects causing the ring artifacts in Fig. B.14a. (a) Radiography showing the stack of sintered copper balls ($\Delta x = 1.6\,\mu\mathrm{m}$ using a $22\,\mu\mathrm{m}$ thin CWO screen). (b) An enlarged inset reveals that (particularly in the region of maximum absorption) stray intensities, due to flaws and scratches on the scintillator, are hardly corrected at all by the standard brightfield normalization. c) Application of an anisotropic stripe-shaped median (high-pass) filter to the brightfield images reveals the numerous scintillator defects which are responsible for the ring artifacts seen in Fig. B.14a.

For the particular example shown in Fig. B.14 the ring artifacts were caused by non-linear intensity variations due to defects on the scintillator screen. Fig. B.15a shows a radiography of the stack of sintered copper balls along with an inset (Fig. B.15b) showing an enlarged region and revealing flaws and scratches on the scintillator surface that remain quasi-uncorrected after brightfield normalization of the image (particularly in the regions of maximum absorption). A virtual image of the scintillator defects was obtained by applying an non-linear anisotropic stripe-shaped median filter (similar to a high-pass filter) to a brightfield image. The resulting picture (Fig. Fig. B.15c shows a large number of surface defects which may all add spurious intesities and cause ring artifacts in the 3D reconstruction as seen in Fig. B.14a. This virtual image of scintillator defects was tried to correct the non-linear errors resisting the brightfield normalization by applying additional division and/or weighted subtraction to the region of maximum absorption (Fig. B.15b). Unfortunately these additional corrections did not improve the 3D results very much compared to the results of the sinogram-filter.

Detection and removal by 3D particle analysis: For some applications filtering the sinograms is not applicable (e.g. pores in steel), yet the ring artifacts can be detected and subtracted from the three-dimensional reconstruction. Figure B.16 shows the application an 3D algorithm

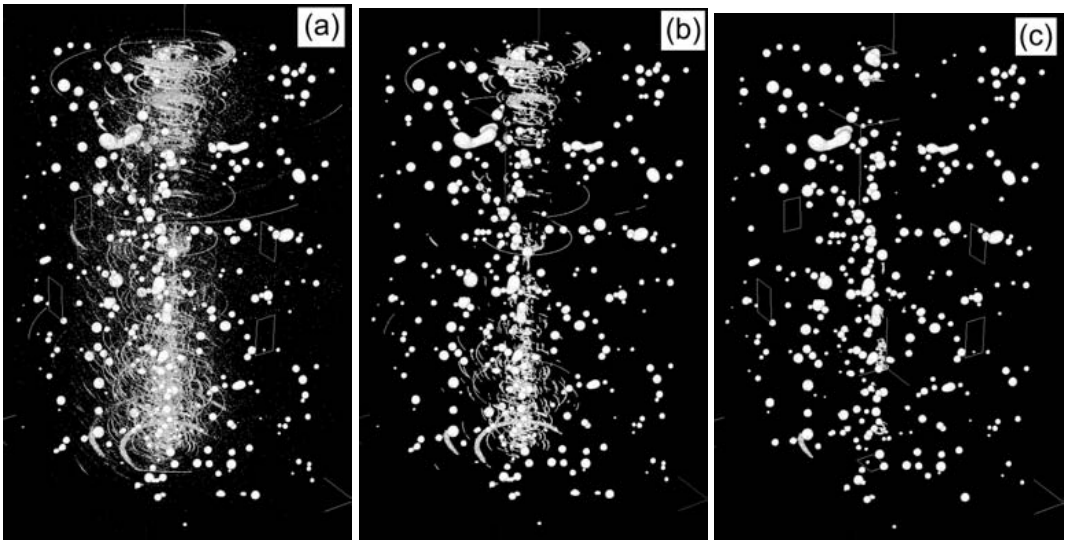

Figure B.16: Perspective views on the porosity in CMSX-10 superalloy in a $0.5 \times 0.5 \times 0.8\ mm^3$ volume [Lin06]. (a) Strong ring-artifacts are binarized along with the *true* porosity. (b) Filtering objects smaller than $9.3\,\mu\mathrm{m}^3$ reduces the artifacts significantly. (c) Additionally filtering flat aspherical objects (less than $17\,\mu\mathrm{m}$ height with a shape factor $F \leq 0.7$) removes the ring artifacts almost completely while preserving the true porosity.

that was developed to remove ring-artifacts which are misinterpreted as pores in samples of Ni-based superalloys due to similar gray values in the data [Lin06]. Volumetric particle analysis was used to label each object in 3D space, calculate its volume V, surface A, shape factor $F = 6V\sqrt{\pi/A^3}$ and lateral dimensions. Based on this data and assuming that the *true* pores

were of larger size, objects with a volume $V < 9.3\,\mu m^3$ were erased from the data. The result of this *size-filter* is shown in Fig. B.16b. Many artifacts are removed yet those of larger size remain in the image. Another particle filter was therefore applied, removing flat aspherical objects with a shape factor $S \leq 0.7$ and measuring less than $17\,\mu m$ in height (along the axis of sample rotation). As can be seen from Fig. B.16c these conditions almost entirely remove the ring-artifacts while preserving the objects which are identified as true pores. The drawback of this 3D particle filter is that it only applies to some specific cases where pores are sufficiently large and well separated from each other in the 3D image.

Slice-wise removal by 2D polar-filtering: A more general approach to correct the 3D images from ring artifacts is called *polar-filtering* refering to a non-linear median filter which is applied after transformation of the axial planes into a polar coordinate system. Although not applied in the framework of this thesis the algorithm merits some mentioning and is illustrated in Fig. B.17 for a phantom image. Considering a reconstructed axial image plane with

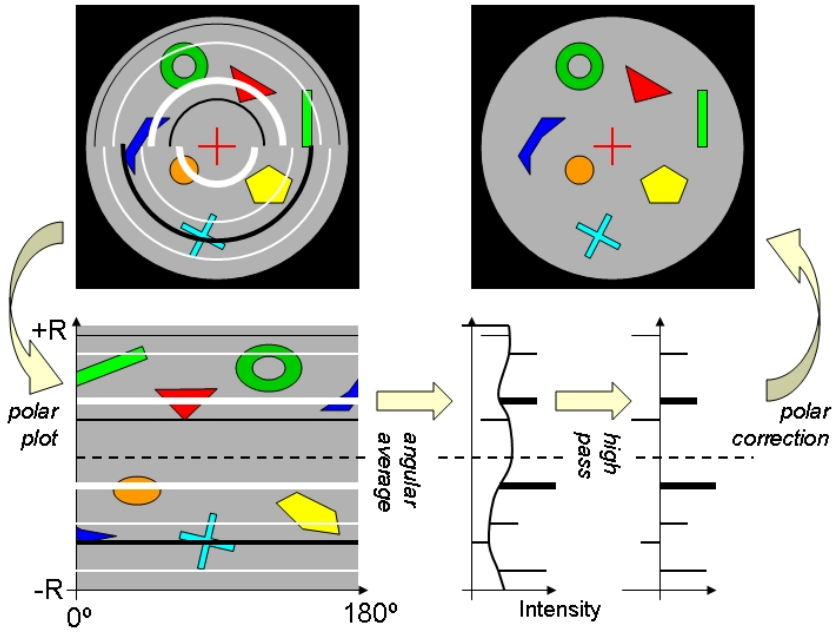

Figure B.17: Schematic illustration of ring artifact removal by polar-filtering [Taf04].

a number of structural details onto which dark and bright semicircular (for $180\,°$ sample rotation) artifacts are superimposed. By redrawing the image in polar coordinates (radius R and angle ϕ, centered around the sample rotation axis) the upper hemisphere of the image plane is mapped onto positive values and the lower hemisphere onto negative values of R. The ring artifacts appear as horizontal lines in the polar plot. Thanks to this convenient representation angular averaging can be applied by summing the intensities along the ϕ-axis (similar to the sinogram filter). Extreme radial intensity contributions caused by the ring artifacts stick out of

this average profile and can be separated from the smooth envelope (which represent the sample structure) by additionally applying a high-pass filter. Positive and negative peak intensities are then back-transformed into Cartesian coordinates where they are found to match with the semi-circular lines of the ring artifacts. The latter can thus be removed by simple subtraction. The algorithm is applied slice-by-slice and eventually combined with additional filters in order to remove spurious intensities which sometimes are found at the tails of the semi-circular artifacts reaching into the opposite side of the image. This method is the most complicated but it is also the most robust because it applies independently of the sample structure.

B.2.2 Pore artifacts

When phase-contrast images are recorded in order to highlight material contrast, because the latter is insufficiently resolved by absorption tomography, and if the sample comprises a significant porosity, strong streak artifacts are often generated tangentially around the pore walls in the 3D image. These stray intensities are an artificial result of back-projecting the extreme phase-shifts occuring at air-material interfaces. Consequently, similar artifacts appear along cracks and at the sample borders. Unlike for attenuation images, there is no linear relationship between phase-contrast and sample thickness. It was suggested [Clo97b] that to a first order approximation the back-projected phase-contrast would be proportional to the 3D Laplacian of the real decrement δ of the refractive index $n(x, y, z)$. However this assumption is only

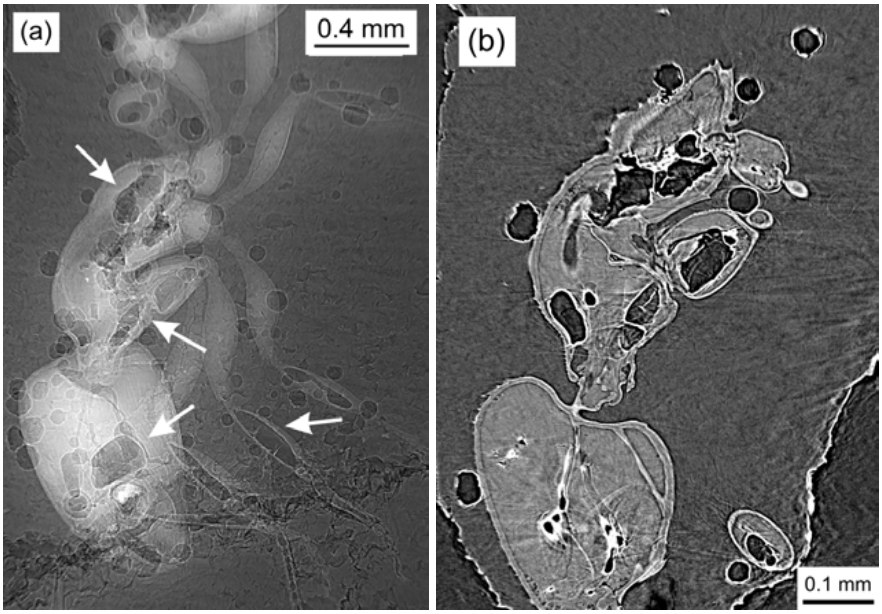

Figure B.18: Pore artifacts degrading the image quality. (a) Radiography of an ant embedded in wax. Note there are pores in the wax as well as hollow spaces in head, organs and ant legs (marked by white arrows). (b) Frontal slice through the 3D reconstruction showing strong streak intensities around the pores caused by incomplete back-projection of the phase-enhanced material-pore interfaces.

valid for short propagation distances. Fig. B.18 shows a radiographic image of a dead ant which was embedded in wax. A relatively low X-ray energy ($E = 7.2\,\mathrm{keV}$) was selected for this measurement, hence phase-enhancement already occured at a rather short propagation distance ($d = 10\,\mathrm{mm}$, the effective pixel size was $\Delta x = 1.6\,\mu\mathrm{m}$). Round pores in the wax surrounding the animal are thus highlighted by Fresnel-propagation but also hollow parts of the head, organs and ant legs (marked by white arrows) show a phase-enhanced silhouette. A frontal slice through the 3D reconstruction of the sample is shown in Fig. B.18b. Although the visibility of the animal tissue is only mildly degraded by the highlighted porosity in the projection image, phase-enhancement at the sample-air interfaces transforms into streak intensities which obscure important details when the 3D image is reconstructed (e.g. the vascular structure inside the head is hardly visible because of voids that cause bright stray intensities that degrading the image region around the voids, see Fig. B.18b).
Retrieving maps of δ from the projection images (holotomography, see section B.3) may solve the problem. Unfortunately the strong phase-shifts caused by pores and cracks cause an even greater problem when phase-retrieval is applied. An example for holotomography of a porous Mg-Al engineering alloy (AZ91, see also section 3.1.4) is shown in Fig. B.19. Fig. B.19a

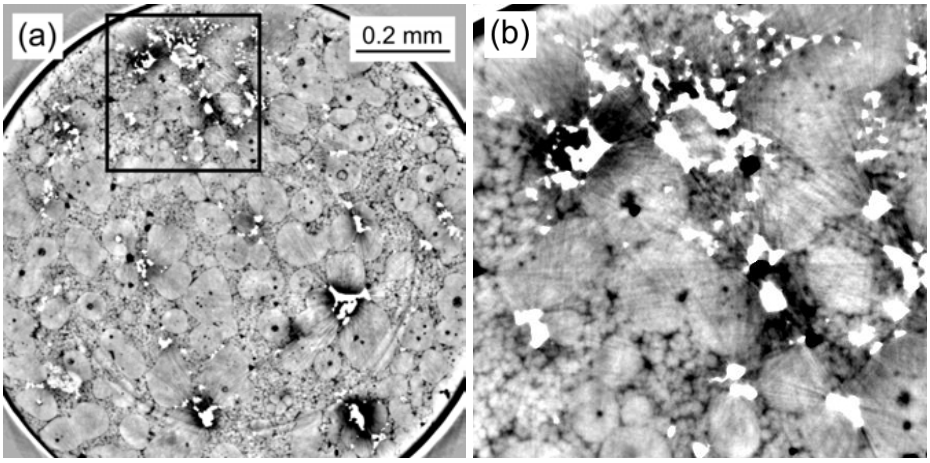

Figure B.19: Holotomography of a porous AZ91 alloy. (a) Axial slice showing how the visibility of the alloy microstructure (round Mg-particles) is degraded by stray intensities that are caused by the porosity (since δ is imaged the pores appear in white). (b) Enlarged view (indicated by the black square in (a)) shows that the white pores are surrounded by a dark corona which is an additional artificial result of the phase-retrieval procedure.

shows an axial slice of a 3D holotomographic reconstruction of a cylindrical sample of AZ91 alloy (recorded at the ESRF beamline ID19 with $\Delta x = 0.7\,\mu\mathrm{m}$ pixel size and $E = 20\,\mathrm{keV}$ X-ray energy). Porosity inside the alloy (cast at $T = 580\,°\mathrm{C}$ with a JSW *thixomolding*-machine) was rather high and stray intensities around the white pores degrade severly the visibility of the globular Mg-particles which characterize the alloy microstructure. In the enlarged view (Fig. B.19b) the structure around the white pores appears dark (*black corona*), an artificial result of the phase-retrieval algorithm which renders the corresponding regions unusable for

image analysis. A significant fraction of the measurement volume is thus obscured by *pore artifacts* which appear to be closely related to *metal artifacts*. The latter are well known in the field of clinical tomography where metallic implants degrade the quality of a cranial scans. Some concepts have been tested to reduce these artifacts but without real success [DM99, Roh98, Boi05]. The best way is to avoid any porosity during sample preparation or more generally speaking: if a weak signal difference has to be detected one should avoid strong signals in the close vincinity (e.g. by complete immersion of the sample with a resin or a harmless liquid with a similar refractive index).

B.2.3 Spikes

Random peak intensities (*spikes*) often appear in radiographic images when high energy X-rays ($E = 50 - 100\,\mathrm{keV}$) are used for imaging, particularly with a polychromatic beam (*white-beam*). The detector is shielded with $4\,\mathrm{mm}$ thick brass and $8\,\mathrm{mm}$ aluminum plates. Still, some

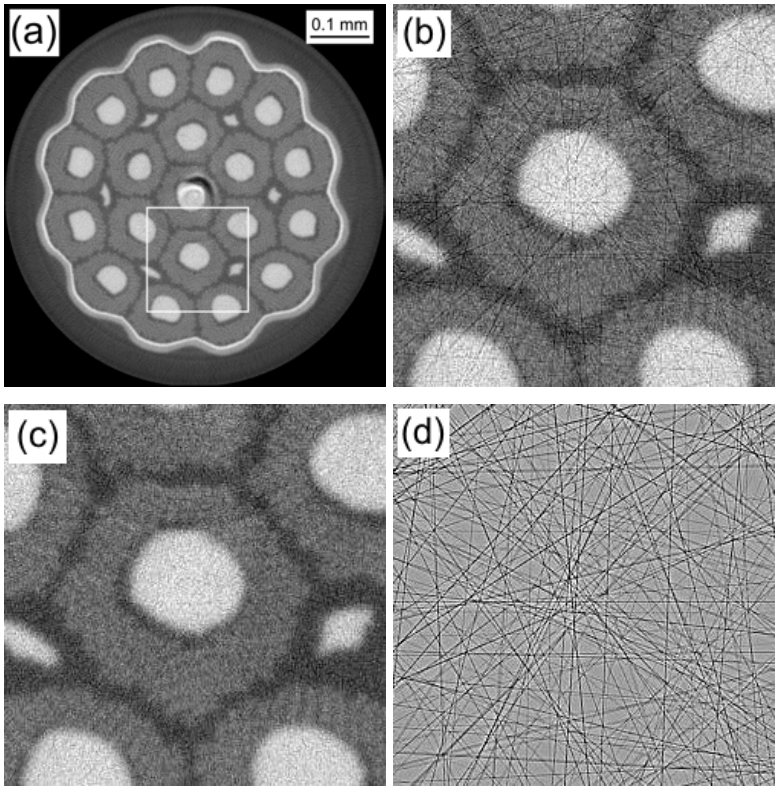

Figure B.20: Example for filtering of the spike artifacts. (a) Axial slice showing the tomographic image of a Nb_3Sn superconducting filament (recorded at the ESRF/ID19, $E = 48\,\mathrm{keV}$ and $\Delta x = 0.7\,\mu\mathrm{m}$). (b) Enlarging a ROI (indicated by the white square in (a)) reveals linear artifacts superimposing randomly onto the sample structure. (c) Filtering bright spots from the radiographs (conditioned median filter) removes the artifacts completely without degrading the image of the sample. (d) The differential image of (b) and (c) reveals the stray intensities caused by the spikes.

X-rays which are scattered by the mirrors and/or by other objects that intersect the beam path, are transmitted and thus impinge directly onto the CCD chip where they cause a burst of charge carriers (spike). In contrast to the stray intensities that were discussed in the previous subsections these spikes appear randomly in the recorded projection images. As a consequence the peak intensities are integrated over straight lines when filtered back-projection is applied to reconstruct 3D images. Filtering these artifacts is done straight-forward by applying a *conditioned* 3×3 median filter to the radiographs (making use of the fact that the spikes are very bright affect only single pixels).
Fig. B.20a shows an axial slice of a superconducting Nb_3Sn filament [Sch07] which was measured during beamtime (MA-104) at the ESRF-ID19 beamline using $48\,\mathrm{keV}$ X-rays and $\Delta x = 0.7\,\mu\mathrm{m}$ pixel size (the resolution was $R > 3\,\mu\mathrm{m}$ due to the $17\,\mu\mathrm{m}$ thick LAG:Eu screen). The enlarged ROI (Fig. B.20b) reveals randomly distributed line-artifacts superimposing onto the sample structure. A 3×3 median filter is applied to the radiographs, conditioned to apply only to those pixels which show a disproportional intensity peak in the radiographs. The result (Fig. B.20c) is free of artifacts, the latter are visualized by calculating the difference image (Fig. B.20d) of the filtered and the unfiltered data. Note that only the line line artifacts caused by the intensity spikes are removed while the sample structure is unchanged.

B.2.4 Bubbles

When water immersed samples are exposed to a high-flux ($10^{10} - 10^{12}\,\mathrm{Ph/s/mm^2}$) of hard X-rays ($E = 20 - 50\,\mathrm{keV}$) as is typically the case during a μCT measurement at synchrotron beamlines, and if phase-contrast is applied in order to highlight the structural details of the sample, formation of gas bubbles in the water is commonly observed in the recorded projection images. Bubbles form, probably as a result of X-ray induced dissociation of H_2O molecules and the formation of free radicals which eventually recombine to H_2 and O_2 gas molecules. This phenomenon has been reported for ice [Mao06] and is observed in water and other liquids (e.g. ethanol). Due to Fresnel-propagation the phase-enhanced silhouettes of the randomly appearing, growing and moving bubbles add very pronounced stray intensities to the radiographic projection images. When transformed into a 3D image these stray contributions are integrated over large volume areas where they obscure the structural features of interest. While measuring samples of human tooth dentin at the ESRF/ID19 beamline, a robust method was developed to improve the image statistics and remove the stray intensities of the gas bubbles from the recorded data. This method is depicted in Fig. B.21 and a detailed report has been written and submitted to *Optics Letters* in June 2007 [Zab07a].
A sequence of three tomographic scans is recorded instead of a simple scan, without unmounting the sample or changing the detector position. By taking into consideration that the bubbles are changing their position and size with time, *time-median* radiographs are constructed from matching image points in identical projections of the sequential scans. In addition, image noise and ring artifacts are strongly reduced if small vertical shifts (10 to $20\,\mu\mathrm{m}$) are applied to the

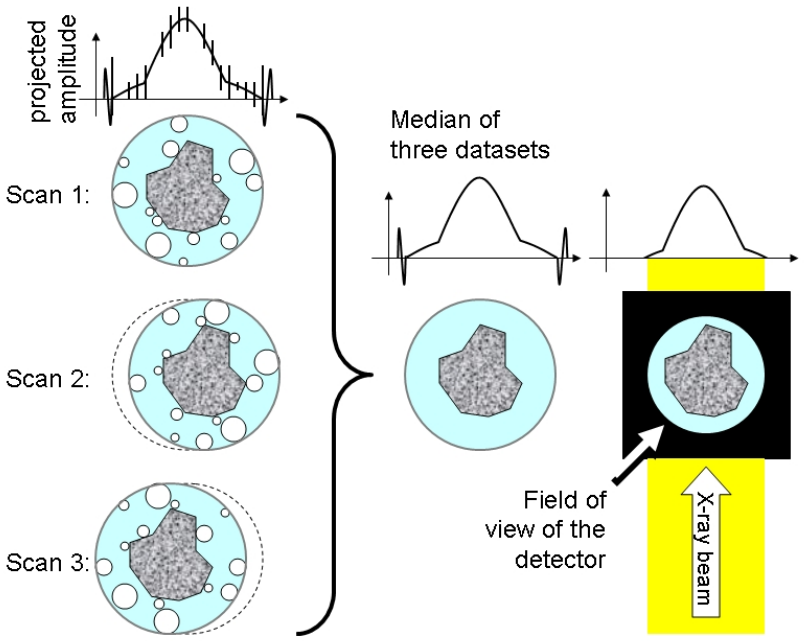

Figure B.21: Schema for calculating time median datasets. Three tomographic scans are aligned and *time-median* radiographs are obtained from matching pixels in the radiographs. The field of view of the detector is chosen such that the strong edge enhancement of the PMMA vial is eclipsed from the 3D reconstruction.

sample between two successive tomographic scans. During standard brightfield normalization every three projections that are belonging to the same projection angle are realigned, i.e. the vertical shifts are numerically reversed by Fourier image cross-correlation and image translation. Recording three scans, each comprising $900 - 1500$ projections, and reconstructing a 3D volume from time-median images has shown to yield excellent results. Fig. B.22a shows a typical radiographic image of a water-immersed fragment of human tooth dentin ($E = 22\,\mathrm{keV}$ and $\Delta x = 0.7\,\mu\mathrm{m}$). Note that the phase-enhanced silhouettes of bubbles are well pronounced while the edge-contrast of the surrounding plastic vial is eclipsed thanks to the limited field of view of the detector. By calculating a time-median image (shown in Fig. B.22b) from three sequential scans, the bubble silhouettes are almost completely removed from the radiograph, whereas the image resolution is unchanged and the statistics are significantly improved.
A closer look at the measurements revealed that bubbles forming on the sample surface (probably due to dissociation of the water inside the sample) expand quickly at a rate of $2-3\,\mu\mathrm{m/s}$ reaching diameters of $60-70\,\mu\mathrm{m}$ until they detach, unite and surface, vanishing from the field of view in an intermittent manner. On the other hand bubbles that are attached to the vial become larger (reaching $120-150\,\mu\mathrm{m}$ in diameter), they hardly move and expand at rather moderate rates of $0.3-0.5\,\mu\mathrm{m/s}$. Typical radiographs show 15 to 25 larger bubbles which can maintain their position for a rather long time (minutes) until they eventually disappear (e.g. due to the fast lateral movement when the sample is moved out of the beam to record bright-

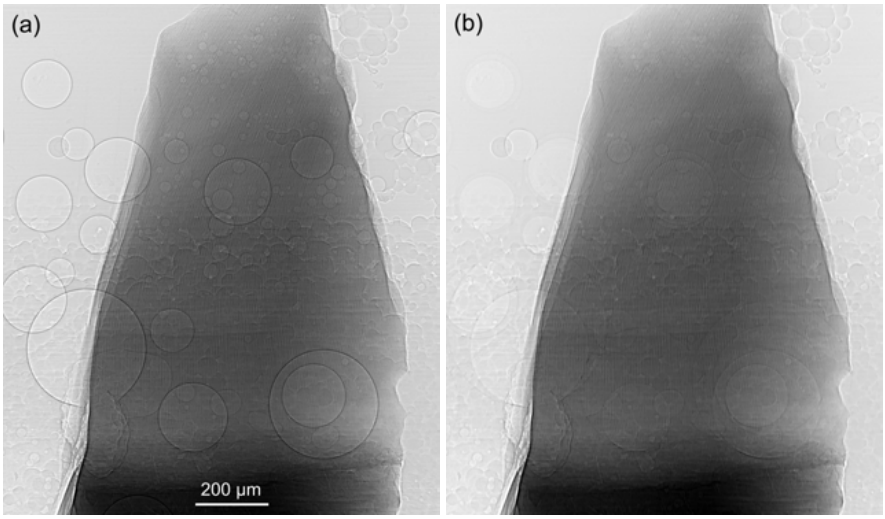

Figure B.22: Time-median method to remove stray intensities caused by gas bubbles from pictures of water-immersed samples: (a) Typical radiography showing a wet fragment tooth dentin. Phase enhanced silhouettes of gas bubbles are observed in close vicinity of the sample. (b) Time-median radiograph of the same sample calculated from three radiographs recorded for the same projection angle during sequential scans.

field images). Silhouettes of bubbles smaller than $20\,\mu\mathrm{m}$ in diameter were hardly visible in the images.

Still, the issue of bubble formation and growth rate, in other words the question "*How fast is the water transformed into gas?*" remains open. A closer view onto the tip of the sample shown in Fig. B.22 reveals that a large amount of small gas bubbles is forming, growing and detaching at high speed at the open top endings of the dentinal tubules (see Fig. B.23).

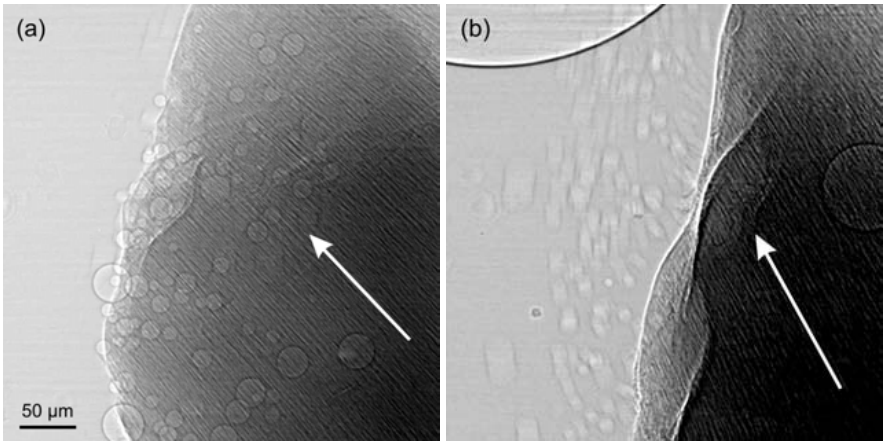

Figure B.23: Gas bubbles forming at the top endings of the micron-sized dentinal tubules: (a) Enlarged view on a fragment tip of tooth dentin (exposure time $0.1\,\mathrm{s}$). White arrows indicate the orientation of the tubules. (b) The same sample immersed in ethanol. Gas bubbles are continuously forming, growing and detaching to float up to the liquid surface.

The maximum possible amount of produced gas can be estimated by considering $1\,\mathrm{mm}^3$ of water which is exposed to X-rays of $20\,\mathrm{keV}$ photon energy and a typical photon flux density of $10^{12}\,\mathrm{Ph/mm^2/s}$ (output of the undulator used at the EDRF/ID19 beamline). The binding energy (free enthalpy) of a single water-molecule is $20\,\mathrm{kJ/mol} = 0.2\,\mathrm{eV}$. Note this is 5 orders of magnitude smaller that the energy of one photon. Approx. SI7% of the radiation is absorbed in $1\,\mathrm{mm}^3$ of water corresponding to $7 \times 10^{10}\,\mathrm{Ph/s}$. The 3×10^{18} molecules present in $1\,\mathrm{mg}$ H_2O could thus be dissociated at a maximum rate of 7×10^{15} molecules/s, i.e. $2\,\mu\mathrm{g/s}$. In terms of gas this corresponds roughly to a rate of $2\,\mathrm{mm}^3/\mathrm{s}$. After 8 minutes $\sim 1\,\mathrm{mm}^3$ water would be consumed which is fortunately not in agreement with the experimental observations. It can therefore be assumed that the majority of free radicals recombine into water molecules and only a tiny fraction transforms into gas. Heating effects were not observed.

B.3 Phase-retrieval: Theory and implementation

A large number of numerical methods (*phase-retrieval* algorithms) have been developed over the last decade in order to obtain the best possible approximation of $\phi(x, y)$ - the linear projection (along z) of the real decrement δ of the sample refractive index $n(x, y, z)$ which is encoded in the phase of the sample transmission function $T(x, y)$. X-ray phase contrast is commonly obtained via Fresnel-propagation of partially coherent synchrotron light and the appropriate interference fringes are observed when high-resolution images are recorded at moderate sample-detecor distances. Under certain assumptions, the analytic transformation of the phase-shifts $\phi(x, y)$ into Fresnel-diffraction patterns can be linearized in reciprocal space [Gui77]. Thus approximate solutions of the phase-retrieval problem can be obtained from one or more phase contrast images. Different X-ray imaging experiments (e.g. double crystal or phase-stepping interferometers, inline holography, analyzer based imaging systems, etc.) are known to generate various types of phase contrast in the recorded radiographs leading to different numerical approaches which have been optimized to provide the best solution to each particular phase-retrieval problem (for a review see [Mom03, Pag06]).
The quest for $\phi(x, y)$ may be called an *inverse problem*. In contrast to a *direct problem* which constists of quantifying the effect of a given cause, the associated inverse problem attempts to infer the cause from a measured effect which is for the given case comprised in one or many images. Additionally phase-retrieval is often called an *ill-posed* problem implying that (a) no solution exists, or (b) an infinite multiplicity of non-unique solutions exists which may not be distinguished from each other. In most cases this ill-posed problem can fortunately be *cured* by adding relatively few *a priori* information and/or using iterative corrections.

B.3.1 Methods based on contrast transfer functions

The most common way to retrieve maps of $\phi(x, y)$ from Fresnel-propagated X-ray images $I_D(x, y)$ is to assume a linear relationship between $\hat{I}_D$ and $\hat{\phi}$ in reciprocal space. The methods

based on this linear assumption (sometimes refered to as *first Born approximation* in analogy to scattering theory) are called *contrast transfer function* methods (CTF). One or many radiographs, recorded at different propagation distances $D = dL/(d+L)$ (L the source-sample distance and d the sample-detector distance, see section 1.3) may be used to calculate $\phi(x,y)$. If absorption is not negligible, a minimal set of two radiographs is required to retrieve maps of $\phi(x,y)$ and $B(x,y)$. Considering the transmission of an incoming wave by a *thin* object (so that internal scattering can be neglected). The outgoing wave directly behind the object is the product of the incoming amplitude $u_{inc}(x,y)$ with a transmission function $T(x,y) = \exp[i\phi(x,y) - B(x,y)]$ wherein $\phi(x,y)$ and $B(x,y)$ represent line integrals of δ and β along the direction of propagation z. For the sake of simplicity $u_{inc} \mapsto 1$ and only $T(x,y)$ is considered. Hence convolution of $T(x,y)$ with a function $P_D(x,y)$ occurs when Fresnel-propagation is applied over a propagation distance D and $u_D(x,y) = (T * P_D)_{x,y}$. The measured intensity is thus given by $I_D(x,y) = |u_D(x,y)|^2$ (see eq. 1.25).
Writing u_D in reciprocal space allows to express Fresnel-propagation simply in terms of a multiplication and $\hat{u}_D(f_x,f_y) = \hat{T}(f_x,f_y)\cdot\hat{P}_D(f_x,f_y)$ with $\hat{P}_D(f_x,f_y) = \exp[-i\pi\lambda D(f_x^2+f_y^2)]$ and (f_x,f_y) the *spatial frequencies*, conjugate to (x,y). According to Parcival's theorem, the Fourier transform $\hat{I}_D$ of the recorded intensity I_D is the autocorrelation of $\hat{u}_D$:

$$\hat{I}_D(f_x,f_y) = \iint_{-\infty}^{\infty} dxdy \exp\left[i2\pi\left(f_x x + f_y y\right)\right] I_D(x,y) \tag{B.8}$$

$$= (\hat{u}_D * \hat{u}_D^{cc})_{f_x,f_y} \tag{B.9}$$

where the superscript 'cc' denotes the complex conjugate. In order to find a simple expression of $\hat{I}_D$ it is convenient to restrict the calculations to one coordinate x (f respectively) and insert $I_D = u_D \cdot u_D^{cc}$ into eq. B.8

$$\hat{I}_D(f) = \frac{1}{\lambda D}\int_{-\infty}^{\infty} dx\, e^{i2\pi fx}\int_s dt\, T(t)e^{i\pi\frac{(x-t)^2}{\lambda D}}\int_s dt'\, T^{cc}(t')e^{-i\pi\frac{(x-t')^2}{\lambda D}} \tag{B.10}$$

$$= \iint_s dtdt'\left\{\int_{-\infty}^{\infty} dx\, e^{i2\pi x\left(f-\frac{t}{\lambda D}+\frac{t'}{\lambda D}\right)}\right\} T(t)T^{cc}(t')e^{\frac{i\pi}{\lambda D}(t^2-t'^2)} \tag{B.11}$$

$$= e^{-i\pi\lambda D f^2}\int_s dt\, T(t)T^{cc}(t-\lambda Df)e^{i2\pi ft} \tag{B.12}$$

introducing s for the integration over the object exit surface. The integral in the curved brackets (eq. B.11) yields a Kronecker delta $\delta_K(t'-t+\lambda Df)$ which was used to reduce eq. B.11 to a single line integral (eq. B.12). A symetric form of $\hat{I}_D$ is obtained by changing variables $t \mapsto t + \lambda Df/2$:

$$\hat{I}_D(f) = \int_s dt\, T\left(t+\frac{\lambda Df}{2}\right)T^{cc}\left(t-\frac{\lambda Df}{2}\right)e^{i2\pi ft} \tag{B.13}$$

Under the assumption that phase variations in $T(x)$ are sufficiently *smooth*, in other words $|\phi(x) - \phi(x-\lambda Df)| << 1$, and neglecting absorption $B(x)$, eq. B.13 can be simplified:

$$\hat{I}_D(f) = \int_s dt\, \left[1 + i\left(\phi\left(t+\frac{\lambda Df}{2}\right) - \phi\left(t-\frac{\lambda Df}{2}\right)\right)\right]e^{i2\pi ft} \tag{B.14}$$

$$= \delta_D(f) + i\left[e^{-i\pi\lambda D f^2} - e^{i\pi\lambda D f^2}\right]\hat{\phi}(f) \tag{B.15}$$

$$= \delta_D(f) + 2\sin(\pi\lambda D f^2)\hat{\phi}(f) \tag{B.16}$$

The last formula is remarkable simple compared to the conventional calculations of $I_D(x)$ which demand to evaluate the Fresnel-integral by using their geometric representation (Cornu spiral). The term $2\sin(\pi\lambda D f^2)$ is called the contrast transfer function (CTF) of $\phi(x)$ and it is straight forward to include *weak* absorption properties of the object, i.e. $B(x) << 1$ which adds a term $-2\cos(\pi\lambda D f^2)\hat{B}(f)$ to eq. B.16 (the CTF of $B(x)$).
For a single image of a phase object (i.e. $B(x) = 0$), $\phi(x)$ can be obtained by solving eq. B.16 for $\hat{\phi}$ and applying an inverse Fourier-transformation (iFFT). Before this method is applied, a small term $\epsilon(f)$ has to added to the right hand side of eq. B.16 in order to avoid the roots of the CTF. It has been shown that if N Fresnel-propagated images are recorded at suitable distances D the quality of the retrieved phase-maps can be significantly improved [Zab05]. A solution for $\hat{\phi}(f)$ is found by the *least squares* method, minimizing the cost function

$$S_c = \frac{1}{N}\sum_{j=1}^{N}\int df\ \left|\hat{I}_{D_j}^{(exp)}(f) - \hat{I}_{D_j}^{(CTF)}(f)\right|^2 \tag{B.17}$$

with $\hat{I}_D^{(exp)}$ the Fourier transform of the experimentally recorded images and $\hat{I}_D^{(CTF)}$ given by eq. B.16. Calculating the roots of the first derivative of eq. B.17 with respect to $\hat{\phi}$, i.e. $\partial S_c/\partial\hat{\phi} = 0$ results in the following phase-retrieval formula:

$$\hat{\phi}(f) = \frac{\sum_{j=1}^{N}\hat{I}_{D_j}^{(exp)}(f)\cdot\sin(\pi\lambda D_j f^2)}{\epsilon(f) + \sum_{j=1}^{N} 2\sin^2(\pi\lambda D_j f^2)} \tag{B.18}$$

wherein a small *a priori* term $\epsilon(f)$ has been introduced for regularization of the CTF roots. By choosing $3-4$ propagation distances D_j in such a manner that the roots of the corresponding CTFs do not overlap but rather compensate each other to yield a smooth function in the denominator on the right hand side of eq. B.18, the effect of $\epsilon(f)$ can be reduced and improved phase-maps are obtained [Zab05]. The distances D_j are calculated by a thumb rule:

$$\lambda D \approx \left[38.4\cdot\Delta x^2 + 0.4\cdot\Delta x - 0.1\right]\cdot k - 9.9\cdot\Delta x + 4.7 \tag{B.19}$$

with k an integer, Δx the pixel size in μm, λ in $0.1\,\mathrm{nm}$ and D in mm. Eq. B.19 was found by numerical optimization of the propagation distances. To include weak absorption ($B(x) << 1$) the cost function B.17 is minimized with respect to $\hat{B}$ and $\hat{\phi}$ and solving the resulting homogeneous system of two linear equations yields

$$\hat{B}(f) = \frac{1}{2\Delta}\left[K\sum_{j=1}^{N}\hat{I}_{D_j}^{(exp)}\sin(\pi\lambda D_j f^2) - S\sum_{j=1}^{N}\hat{I}_{D_j}^{(exp)}\cos(\pi\lambda D_j f^2)\right] \tag{B.20}$$

$$\hat{\phi}(f) = \frac{1}{2\Delta}\left[C\sum_{j=1}^{N}\hat{I}_{D_j}^{(exp)}\sin(\pi\lambda D_j f^2) - K\sum_{j=1}^{N}\hat{I}_{D_j}^{(exp)}\cos(\pi\lambda D_j f^2)\right] \tag{B.21}$$

with the following coefficients (where α replaces the term $\pi\lambda D_j f^2$):

$$K = \sum_{j=1}^{N} \sin(\alpha)\cos(\alpha)\,, \quad S = \sum_{j=1}^{N} \sin^2(\alpha)\,, \quad C = \sum_{j=1}^{N} \cos^2(\alpha) \quad and \quad \Delta = SC - K^2 \tag{B.22}$$

A small $\epsilon(f)$ may be added to the denominator Δ for regularization. It has been shown [Clo99a, Tur04] that (B.20) and (B.21) can be reduced back to a single equation in the case of an object with a homogeneous and known composition. The detector response can be included by multiplying eq. B.16 with the *modulation transfer function* (MTF) and calculating $\hat{B}$ and $\hat{\phi}$ for a finite detector blurring. Yet, due to white noise in typical radiographic images (which would be amplified by deconvolution of the detector response) this method is often impractical.

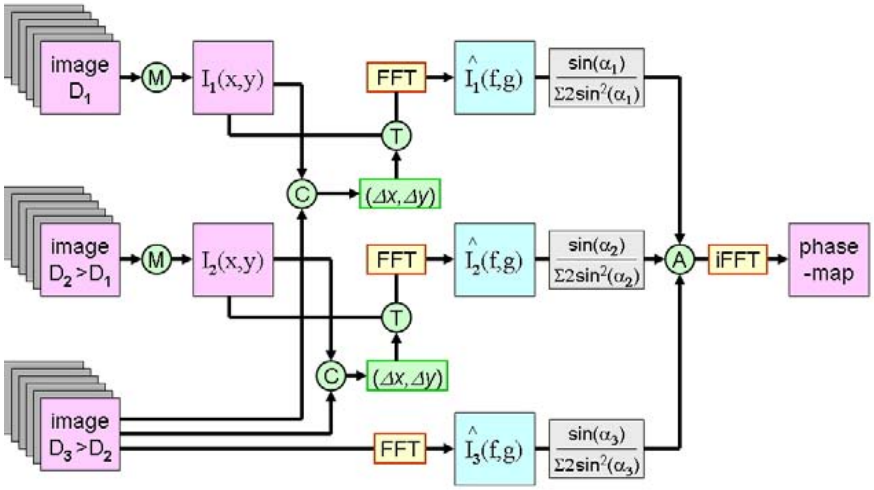

Figure B.24: The CTF phase-retrieval method for a set of three Fresnel-propagated images.

Implementation of the CTF-method for pure phase objects is depicted in Fig. B.24. Considering a set of N Fresnel-propagated radiographs recorded at increasing propagation distances $D_1 < D_2 < \ldots < D_N$. Following brightfield normalization (cf. section B.1) the images $I_1 \ldots I_{N-1}$ are rescaled (operator M in Fig. B.24) to compensate for the finite source-sample distance L, in other words the magnification $M = (d + L)/L$ taking place at increasing sample-detector distances d. The rescaled images are aligned with I_N via image cross-correlation (C in Fig. B.24) followed by image translation (T). Fourier transforms of the matching images are obtained by fast Fourier-tranformation [Fri05] and the reciprocal intensities $\hat{I}_{D_j}$ are multiplied by factors $\sin(\alpha_j)/\sum_j 2\sin^2(\alpha_j)$, wherein $\alpha = \pi\lambda D f^2$. Finally the filtered images are summed (A) and back-transformed into real-space (iFFT) to obtain an approximate phase-map $\phi(x)$. If absorption is not weak but the distribution of $\beta(x, y, z)$ inside the sample is sufficiently homogeneous, an additional image $I_0(x, y)$ (recorded directly behind the sample, $D \approx 0\,\mathrm{m}$) can be used to construct pure phase images

$I_{D_1}/I_0, I_{D_2}/I_0, \ldots, I_{D_N}/I_0$.
Holotomography uses $3-4$ tomographic datasets recorded at appropriate propagation distances. For each angluar projection the corresponding radiographic images are aligned and a phase-map $\phi(x,y,\theta)$ is calculated with the CTF algorithm. An iterative error correction may additionally be used to refine the result by re-applying the algorithm, thus minimizing the difference between the recorded intensities $I_{D_j}(x,y,\theta)$ and $|\exp(i\phi(x,y,\theta)) * P_{D_j}|^2$. The retrieved phase-maps are then transformed into a 3D volume by standard filtered back-projection. Note that unlike for absorption radiographs the images of $\phi(x,y,\theta)$ are not mapped onto a $-\log$ scale. The resulting tomogram is a representation of $\delta(x,y,z)$ and thus of the averaged electron density inside the material since $\delta \propto \lambda^2 \rho_{el}$. Applications of this method are shown in chapter 3.

B.3.2 Transport of intensity equation

Unlike the PM, the transport of intensity equation (TIE) differs from the standard CTF method by the underlying laws of physics that are used to derive this method [Tea83]. The TIE is obtained when a wave-*Ansatz* $u(x,y,z) = \sqrt{I(x,y,z)}\exp[i\phi(x,y,z)]$ is inserted into the paraxial equation (cf. section 1.3).

$$\nabla_\perp \left[I(x,y,z)\nabla_\perp \phi(x,y,z)\right] = -\frac{2\pi \partial I(x,y,z)}{\lambda \partial z} \tag{B.23}$$

Eq. B.23 may also be obtained from purely geometrical considerations and the energy conservation law. Note that by convention z is used here to descibe the sample-detector distance. Under certain conditions eq. B.23 may be solved for ϕ [Pag98]:

$$\phi(x,y,z) = -\frac{2\pi}{\lambda}\nabla_\perp^{-2}\left(\nabla_\perp\left\{\frac{1}{I(x,y,z)}\nabla_\perp\left[\nabla_\perp^{-2}\frac{\partial I(x,y,z)}{\partial z}\right]\right\}\right) \tag{B.24}$$

and by replacing $\partial I/\partial z$ with $(I(x,y,z) - I(x,y,\Delta z))/\Delta z$ a phase-retrieval algorithm is obtained (∇ and the inverse operator are commonly applied in reciprocal space in terms of their Fourier representation, cf. section 2.1). The drawback of the TIE algorithm is that it applies only to short propagation distances and *thin* objects.

B.3.3 Combined methods and iteration

It can be shown that the TIE and CTF methods converge similarly for the case of pure phase objects in the small distance limit $D \mapsto 0$ [Gui05]. For non-negligible absorption of the object however, the two approaches do not coincide. A combined method was elaborated in view of reconciling the two formulae in order to create an improved robust algorithm for the phase retrieval of *mixed objects* (i.e. smooth phase-shifts and non-negligible absorption).
Assuming a mixed object function with smooth phase-shifts and making an *Ansatz* similar to the one used to derive the TIE algorithm, i.e. $T(x,y) = a(x,y)\exp[i\phi(x,y)]$ with $a(x,y) =$

$\sqrt{I_0(x,y)}$, and inserting $T(x,y)$ into eq. B.13 yields a generalized CTF formulation:

$$\begin{aligned}\hat{I}_D(f) &= \int_s dt\, a\left(t+\frac{\lambda D f}{2}\right) a\left(t-\frac{\lambda D f}{2}\right) \\ &\quad \times \left[1+i\phi\left(t+\frac{\lambda D f}{2}\right)-i\phi\left(t-\frac{\lambda D f}{2}\right)\right] e^{i2\pi f t} \qquad \text{(B.25)} \\ \Rightarrow \hat{I}_D(f) &= \hat{I}_D^{\phi=0}+2\sin(\pi\lambda D f^2) FT\{I_0(x)\cdot\phi(x)\} \\ &\quad +\frac{\lambda D}{2\pi}\cos(\pi\lambda D f^2) FT\{\frac{\partial(I_0'\cdot\phi)}{\partial x}\} \qquad \text{(B.26)}\end{aligned}$$

The Taylor expansions $a(t+\lambda D f)+a(t-\lambda D f)\approx 2a$ and $a(t+\lambda D f)-a(t-\lambda D f)\approx 2\lambda D f a'$ were used to obtain eq. B.26 which coincides with the TIE for $D\mapsto 0$. The Fourier transform (FT) of the intesity in the absence of phase-shifts is denoted $\hat{I}_D^{\phi=0}$ and can be calculated from measured values of $a(x)$. The drawback of this generalization is that eq. B.26 is not invariant under the transformation $\phi\mapsto\phi+$ const. but in practice this problem is solved by assuming $\phi=0$ outside the object [Yam04].

This combined method was applied to retrieve the phase maps from holotomography data which was acquired during the experiment MA-104 at the ESRF-ID19 beamline (see chapter 3). For each sample several tomographic datasets were acquired at $N+1$ propagation distances $D_{0,1,\ldots,N}$ whereby the image I_0 represents an absorption radiograph ($D_0\approx 0$) and respectively. A first estimate of $\hat{\phi}_0(f)$ is obtained from the Fresnel-propagated images $I_{D_1},\ldots I_{D_N}$ by using eq. B.18. Then a normalized phase map is obtained from the real part of the inverse Fourier transform $\phi_0(x)=\Re\{FT^{-1}\hat{\phi}_0\}/I_0$ and an improved phase map is calculated

$$\hat{\phi}_1(f)=\frac{\sum_{j=1}^{N}\left[\hat{I}_{D_j}^{(exp)}(f)\cdot\sin(\pi\lambda D_j f^2)-\frac{\lambda D}{2\pi}\cos(\pi\lambda D_j f^2)\cdot FT\{\frac{\partial\Phi}{\partial x}\}\right]}{\epsilon(f)+\sum_{j=1}^{N}2\sin^2(\pi\lambda D_j f^2)} \qquad \text{(B.27)}$$

wherein $\Phi=\phi_0(x)I_0^{\prime(lp)}/I_0$ and $I_0^{\prime(lp)}$ is the first derivative with respect to x of the absorption image after application of a *low-pass* filter. The latter is conventionally applied in reciprocal space and accounts for the fact that the projected absorption of the sample is a smooth function keeping the corrections to the CTF small. The corrected phase map $\phi_1(x)$ is calculated in real space and eq. B.27 is applied iteratively aiming to minimize $|\phi_j-\phi_{j-1}|$.

Bibliography

[Abr04] M. D. Abramoff, P. J. Magelhaes and S. J. Ram. Image Processing with ImageJ. Biophotonics International **11**, 36–42 (2004).

[Ada78] M. Adams and G. Sines. Crack extension from flaws in a brittle material subjected to compression. Tectonophysics **49**, 97–118 (1978).

[Ai92] S. H. Ai, V. Lupinic and M. Maldini. Creep fracture mechanisms in single crystal superalloys. Scripta Metall. Mater. **26**, 579–584 (1992).

[Alk02] J. Alkemper, R. Mendoza and P. W. Voorhees. Morphological evolution of dendritic microstructures. Adv. Eng. Mater. **4**, 694–697 (2002).

[Ann95] S. Annavarapu and R. D. Doherty. Inhibited coarsening of solid-liquid microstructures in spray casting at high volume fractions of solid. Acta Metall. Mater. **43**, 3207–3230 (1995).

[Atk87] B. K. Atkinson (ed.). *Fracture mechanics of rock*. (Academic Press London, 1987).

[Bar06] C. G. Barkla. Polarisation in Secondary Röntgen Radiation. Proc. R. Soc. (London) **77**, 247 (1906).

[Bas04] M. Bastuerk, M. Bichler, A. Dlouhy, H. Tatlisu, B. Zamani and M. Zawisky. Application of neutron radiography in aerospace industry and geology. In *16th World Conference on Nondestructive Testing, WCNDT 2004*, volume 9. (NDT.net, Montreal, Canada, 2004). http://www.ndt.net/article/wcndt2004/pdf/aerospace/264_bastuerk.pdf.

[Ber05] R. Bergmann and E. Zabler. *Methoden der zerstörungsfreien Prüfung: Methoden, Anwendungen, Bewertungen und Ausblick*, volume CR 013 von *CR-Schriftreihe Produktionstechnik*. (Robert Bosch GmbH, 2005).

[Bes06] P. Besuelle, G. Viggiani, N. Lenoir, J. Desrues and M. Bornert. X-ray micro CT for studying strain localization in clay rocks under triaxial compression. In J. Desrues, G. Vigianni and P. Besuelle (eds.), *Advances in X-ray Tomography for Geomaterials*, pages 35–52. (ISTE Ltd., London, UK, 2006).

[Bie67] Z. T. Bieniawski. Mechanism of brittle fracture of rock part II - experimental studies. Int. J. Rock Mech. Min. Sci. **4**, 407–423 (1967).

[Bob98] A. Bobet and H. H. Einstein. Fracture coalescence in rock-type materials under uniaxial and biaxial compression. Int. J. Rock Mech. Min. Sci. **35**, 863–888 (1998).

[Boh13] N. Bohr. On the Constitution of Atoms and Molecules I. Philos. Mag. **26**, 1–25 (1913).

[Boi05] M. Boin. *Kompensation von Artefakten bei der Rekonstruktion tomographischer Datensätze*. Master's thesis, Berufsakademie Berlin - FB Wirtschaft und Informatik, Germany, 2005.

[Boi06] M. Boin and A. Haibel. Compensation of ring artifacts in synchrotron tomographic images. Opt. Express **14**, 12071–12075 (2006).

[Bra13] W. L. Bragg. The diffraction of short electromagnetic waves by a crystal. Proc. Cambridge Phil. Soc. **17**, 43–57 (1913).

[Bra14a] W. H. Bragg and Peirce S. E. The absorption coefficients of x-rays. Phil. Mag. **18**, 626–630 (1914).

[Bra14b] W. L. Bragg. The diffraction of short electromagnetic waves by a crystal. Proc. R. Soc. (London), Ser. A **89**, 468–489 (1914).

[Bra56] R. N. Bracewell. Strip Integration in Radio Astronomy. Aust. J. Phys. **9**, 198–217 (1956).

[Bra65] R. N. Bracewell. *The Fourier Transform and Its Applications*, pages 108–112. (McGraw-Hill, New York, 1965).

[Bro76] R. A. Brooks and G. Di Chiro. Statistical limitations in x-ray reconstructive tomography. Med. Phys. **3**, 237–240 (1976).

[Bru97] U. Brueckner, A. Epishin and T. Link. Local X-ray diffraction analysis of the structure of dendrites in single-crystal nickel-base superalloys. Acta Mater. **45** (1997).

[Can90] N. P. Cannon, E. M. Schulson, T. R. Smith and H. J. Frost. Wing cracks and brittle compressive fracture. Acta Metal. Mater. **38**, 1955–1962 (1990).

[Cha97] D. Chapman, W. Thomlinson, R. E. Johnston, D. Washburn, E. Pisano, N. Gmür, Z. Zhong, R. Menk, F. Arfelli and D. Sayers. Diffraction Enhanced X-ray Imaging. Phys. Med. Biol. **42**, 2015–2025 (1997).

[Che98] S.-W. Chen, C.-C. Lin and C. Chen. Determination of the melting and solidification characteristics of solders using differential scanning calorimetry. Metall. Mater. Trans. A **29** (1998).

[Clo97a] P. Cloetens, J.-P. Guigay, C. De Martino and J. Baruchel. Fractional Talbot imaging of phase gratings with hard x rays. Opt. Lett. **22** (1997).

[Clo97b] P. Cloetens, M. Pateyron-Salome, J.-Y. Buffiere, G. Peix, J. Baruchel, F. Peyrin and M. Schlenker. Observation of microstructure and damage in materials by phase sensitive radiography and tomography. J. Appl. Phys. **81**, 5878–5886 (1997).

[Clo99a] P. Cloetens. *Contribution to Phase Contrast Imaging, Reconstruction and Tomography with Hard Synchrotron Radiation: Principles, Implementation and Applications*. PhD thesis, Vrije Universiteit Brussel, Belgium, 1999.

[Clo99b] P. Cloetens, W. Ludwig, J. Baruchel, D. Van Dyck, J. Van Landuyt, J. P. Guigay and M. Schlenker. Holotomography: Quantitative phase tomography with micrometer resolution using hard synchrotron radiation x rays. Appl. Phys. Lett. **75**, 2912–2914 (1999).

[Com23] A. H. Compton. A quantum theory of the scattering of X-rays by light elements. Phys. Rev. **21**, 483–502 (1923).

[Cor63] A. M. Cormack. Representation of a Function by its Line Integrals, with some Radiological Applications. J. Appl. Phys. **34**, 2722–2727 (1963).

[Cra59] R. Craig, P. Gehring and F. Peyton. Relation of structure to the microhardness of human dentin. J. Dent. Res. **38**, 624–630 (1959).

[Cui99] O. Cuisenaire and B. Macq. Fast Euclidean distance transformation by propagation using multiple neighborhoods. Comput. Vis. Image Und. **76**, 263–172 (1999).

[Cur98] P. Curie, Mme. P. Curie and G. Bémont. Sur une nouvelle substance fortement radio-active, contenue dans la pechblende. Comptes rendus de l'Académie des Sciences, Paris **127**, 1215–1217 (1898).

[Dav95] T. J. Davis, D. Gao, T. E. Gureyev, A. W. Stevenson and S. W. Wilkins. Phase-contrast imaging of weakly absorbing materials using hard X-rays. Nature **373**, 595 – 598 (1995).

[Dej96] R. J. Dejus and M. S. del Rio. XOP: A graphical user interface for spectral calculations and x-ray optics utilities. Rev. Sci. Instrum. **67**, 1–4 (1996).

[Des06] J. Desrues, G. Viggiani and P. Besuelle (eds.). *Advances in X-ray Tomography for Geomaterials*, ISTE Ltd., London, UK, 2006.

[Die99] H.J. Diepers, C. Beckermann and I. Steinbach. Simulation of convection and ripening in a binary alloy mush using the phase-field method. Acta Metall. **47**, 3663–3678 (1999).

[Dis64] J. P. Dismukes, L. Ekstrom and R. J. Paff. Lattice Parameter and Density in Germanium-Silicon Alloys. J. Phys. Chem. **68** (1964).

[DM99] B. De Man, J. Nuyts, P. Dupont, G. Marchal and P. Suetens. Reduction of metal streak artifacts in X-ray computed tomography using a transmission maximum a posteriori algorithm. In *Nuclear Science Symposium, 1999, vol. 2*, pages 850–854. (IEEE, 1999).

[Dun62] R. J. Dunham. Classification of carbonate rocks according to depositional texture. In W. E. Ham (ed.), *Classification of carbonate rocks*, pages 108–121. (Am. Assoc. Petrol. Geol. Mem. 1, 1962).

[Dys95] A. V. Dyskin, L. N. Germanovich, R. J. Jewell, H. Joer, J. S. Krasinski, K. K. Lee, J.-C. Roegiers, E. Sahouryeh and K. B. Ustinov. Some experimental results on three-dimensional crack propagation in compression. In H.-P. Rossmanith (ed.), *Mechanics of jointed and faulted rock*, pages 91–96, Balkema, 1995.

[Dys03] A. V. Dyskin, E. Sahouryeh, R. J. Jewell, H. Joer and K. B. Ustinov. Influence of shape and locations of initial 3-D cracks on their growth in uniaxial compression. Eng. Fract. Mech. **70**, 2115–2136 (2003).

[Ein05] A. Einstein. Über einen, die Erzeugung und Verwandlung des Lichtes betreffenden, heuristischen Gesichtspunkt. Ann. Phys. **17**, 132–148 (1905).

[Eld47] F. R. Elder, A. M. Gurewitsch, R. V. Langmuir and H. C. Pollock. Radiation from Electrons in a Synchrotron. Phys. Rev. **71**, 829–830 (1947).

[Ell82] J. C. Elliot and S. D. Dover. X-ray microtomography. J. Microsc. **126**, 211–213 (1982).

[Ell97] J. C. Elliot. Structure, crystal chemistry and density of enamel apatites. Dental Enamel **205**, 54–72 (1997).

[Eno86] Y. Enomoto, M. Tokuyama and K. Kawasaki. Finite volume fraction effects on Ostwald ripening. Acta Metall. **34**, 2119–2128 (1986).

[Eno87] Y. Enomoto, K. Kawasaki and M. Tokuyama. The time dependent behavior of the ostwald ripening for the finite volume fraction. Acta Metall. **35**, 915–922 (1987).

[Epi02] A. Epishin, T. Link, U. Brückner and P. D. Portella. Investigation of Porosity in Single-Crystal Nickel-Base Superalloys. In J. Lecomte-Beckers, M. Carton, F. Schubert and P. J. Ennis (eds.), *Proceedings of the Seventh Conference on Materials for Advanced Power Eng.*, pages 217–226. (Schriften des Forschungszentrum Jülich, Reihe Energietechnik, Band 21, 2002).

[Epi04] A. Epishin and T. Link. Mechanisms of high-temperature creep of nickel-based superalloys under low applied stresses. Phil. Mag. **84**, 1979 – 2000 (2004).

[Fan02] Z. Fan. Semisolid metal processing. Int. Mater. Rev. **47**, 1–37 (2002).

[Fle74] M. C. Flemings. *Solidification Processing*. Materials Science and Eng. (McGraw-Hill, 1974).

[Fle91] M. C. Flemings. Behaviour of Metal Alloys in the Semisolid State. Metall. Trans. A **22A**, 957–981 (1991).

[Fol59] R. L. Folk. Practical petrographic classification of limestones. Bull. Am. Assoc. Petrol. Geol. **43**, 1–38 (1959).

[Fol74] R. L. Folk. *Petrology of sedimentary rocks*. (Hemphill Publishing, Austin, Texas, 1974).

[Fra91] P. Fratzl, J. L. Lebowitz, O. Penrose and J. Amar. Scaling functions, self-similarity, and the morphology of phase-separating systems. Phys. Rev. B **44**, 4794–4811 (1991).

[Fre95] J. T. Fredrich, B. Menendez and T.-F. Wong. Imaging the pore structure of geomaterials. Science **268**, 276–279 (1995).

[Fri05] M. Frigo and S. G. Johnson. The design and implementation of FFTW3. Proceedings of the IEEE **93**, 216–231 (2005).

[Ger94] L. N. Germanovich, R. L. Salganik, A. V. Dyskin and K. K. Lee. Mechanisms of brittle fracture of rock with pre-existing cracks in compression. PAGEOPH **143**, 117–149 (1994).

[Gil69] R. S. Gilmore, R. P. Pollack and J. L. Katz. Elastic properties of bovine dentine and enamel. Arch. Oral Biol. **15**, 787–796 (1969).

[GM04] F. Garcia-Moreno, M. Fromme and Banhart J. Real-time X-ray radioscopy on metallic foams using a compact micro-focus source. Adv. Eng. Mater. **6**, 416 (2004).

[Goe99] J. Goebbels, B. Illerhaus, G. Weidemann and K. Pischang. Characterization of Volume Properties of Powder Metallurgical Parts by Computerized Tomography. Mater. Sci. Forum **308-311**, 867–872 (1999).

[Gol04] B. Golosio, A. Somogyi, A. Simionovici, P. Bleuet, J. Susini and L. Lemelle. Non-destructive three-dimensional elemental microanalysis by combined helical x-ray microtomographies. Appl. Phys. Lett. **84**, 2199–2200 (2004).

[Goo96] J. W. Goodman. *Introduction to Fourier Optics*. Electrical Eng. Series. (McGraw-Hill, Singapore, 1996).

[Got06] B. Gotliv, J. S. Robach and A. Veis. The composition and structure of bovine peritubular dentin: Mapping by time of flight secondary ion mass spectroscopy. J. Struct. Biol. **156**, 320–333 (2006).

[Gör01] W. Görner, M. P. Hentschel, B. R. Müller, H. Riesemeier, M. Krumrey, G. Ulm, W. Diete, U. Klein and R. Frahm. BAMline: the first hard X-ray beamline at BESSY II. Nucl. Instrum. Methods Phys. Res., Sect. A **467-468**, 703–706 (2001).

[Gra91] W. Graeff and K. Engelke. In S. Ebashi, M. Koch and E. Rubenstein (eds.), *Handbook on Synchrotron Radiation Vol. 4*, pages 361–405. (Elsevier Science Publishers B.V., Swansea, 1991).

[Gri24] A. A. Griffith. The theory of rupture. In *1st Int. Congr. on Applied Mech.*, pages 55–63, Delft, 1924.

[Gru08] R. Grupp. *In situ Synchrotron Tomographie von Sinterprozessen*. PhD thesis, University of Dresden, Germany, 2008.

[Gui77] J.-P. Guigay. Fourier transform analysis of Fresnel diffraction patterns and in-line holograms. Optik **49**, 121–125 (1977).

[Gui04] J.-P. Guigay, S. Zabler, P. Cloetens, C. David, R. Mokso and M. Schlenker. The partial Talbot effect and its use in measuring the coherence of synchrotron X-rays. J. Synchrotron Rad. **11**, 476–482 (2004).

[Gui05] J.-P. Guigay, T. Yamanaka, P. Cloetens and R. Boistel. Can the transport of intensity equation and the transfer function approaches be reconciled ? Poster presentation, Coherence 2005, Porquerolles, France, 2005.

[Hea06] D. Healy, R. R. Jones and R. E. Holdsworth. Three-dimensional brittle shear fracturing by tensile crack interaction. Nature **439**, 64–67 (2006).

[Hel92] H. v. Helmholtz. Elektromagnetische Theorie der Farbenzersteuung. Ann. Phys. **48** (1892).

[Hem03] O. Hemberg, M. Otendal and H. M. Hertz. Liquid-metal-jet anode electron-impact x-ray source. Appl. Phys. Lett. **83** (2003).

[Hen81] M. Hennion, D. Ronzaud and Guyot P. Kinetics of unmixing in Al—Zn single crystals studied by neutron small angle scattering. Acta Metall. **30**, 599–610 (1981).

[Hir03] T. Hirono, M. Takahashi and S. Nakashima. In situ visualization of fluid flow image within deformed rock by X-ray CT. Eng. Geol. **70**, 37–46 (2003).

[Hoe65] E. Hoek and Z. T. Bieniawski. Brittle fracture propagation in rock under compression. Int. J. Fract. Mech. **1**, 137–155 (1965).

[Hor85] H. Horii and S. Nemat-Nasser. Compression-induced microcrack growth in brittle solids: axial splitting and shear failure. J. Geophys. Res. **90**, 3105–3125 (1985).

[Hou73] G. N. Hounsfield. Computerized Transverse Axial Scanning (Tomography): Part I, Description of System. Brit. J. Radiol. **46**, 1016–1022 (1973).

[Hoy91] J. J. Hoyt. On the coarsening of precipitates located on grain boundaries and dislocations. Acta Metall. Mater. **39**, 2091–2098 (1991).

[Iva44] D. Ivanenko and I. Pomeranchuk. On the Maximal Energy Attainable in a Betatron. Phys. Rev. **65**, 343 (1944).

[Jac81] D. F. Jackson and D. J. Hawkes. X-ray attenuation coefficients of elements and mixtures. Phys. Rep. **70**, 169–233 (1981).

[Jan01] C. Janssen, F. C. Wagner, A. Zang and G. Dresen. Fracture process zone in granite: a microstructural analysis. Int. J. Earth Sci. **90**, 46–59 (2001).

[Jol76] P. A. Joly and R. Mehrabian. The rheology of a partially solid alloy. J. Mater. Sci. **11**, 1393–1418 (1976).

[Kai99] S. K. Kailasam, M. E. Glicksman, S. S. Mani and V. E. Fradkov. Investigation of microstructural coarsening in Sn-Pb Alloys. Metall. Mater. Trans. A **30**, 1541–1547 (1999).

[Kam95] C. Kammer (ed.). *Aluminium-Taschenbuch Band 1: Grundlagen und Werkstoffe*, pages 54–55. (Aluminium-Zentrale Düsseldorf, 15. Auflage, 1995).

[Kas01] K. T. Kashyap and T. Chandrashekar. Effects and mechanisms of grain refinement in aluminium alloys. Bull. Mater. Sci. **24**, 345–353 (2001).

[Ker40] D. W. Kerst. Acceleration of Electrons by Magnetic Induction. Phys. Rev. **58**, 841 (1940).

[Ket05] R. Ketcham. Three-dimensional grain fabric measurements using high-resolution X-ray computed tomography. J. Struct. Geol. **27**, 1217–1228 (2005).

[Khi34] A. Khintchine. Korrelationstheorie der stationären stochastischen Prozesse. Math. Ann. **109**, 604–615 (1934).

[Kin99] J. H. Kinney, M. Balooch, G. W. Marshall and Marshall S. J. A micromechanics model of the elastic properties of human dentine. Arch. Oral Biol. **44**, 813–822 (1999).

[Kir04] S. Kirste. *Entwicklung einer 64 bit-Software zur Separation morphologischer Strukturen in dreidimensionalen Bildern*. Master's thesis, Berufsakademie Berlin - FB Wirtschaft und Informatik, Germany, 2004.

[Kle02] S. Kleiner, O. Beffort, A. Wahlen and P. J. Uggowitzer. Microstructure and mechanical properties of squeeze cast and semi-solid cast Mg-Al alloys. J. Light Metals **2**, 277–280 (2002).

[Koc98] A. Koch, C. Raven, P. Spanne and A. Snigirev. X-ray imaging with submicrometer resolution employing transparent luminescent screens. J. Opt. Soc. Am. A **15**, 1940–1951 (1998).

[Kom97] J. Komenda and P. J. Henderson. Growth of pores during the creep of a single crystal nickel-base superalloy. Scripta Mater. **37**, 1821–1826 (1997).

[Kos14] W. Kossel. Verhandlungen der Deutschen Physikalischen Gesellschaft **16**, 953 (1914).

[Kos20] W. Kossel. Z. Phys. **1**, 119–134 (1920).

[Laj74] E. Z. Lajtai. Brittle fracture in compression. Int. J. Fract. **10**, 525–536 (1974).

[Lan03] E. N. Landis, E. N. Nagy and D. T. Keane. Microstructure and fracture in three dimensions. Eng. Fract. Mech. **70**, 911–925 (2003).

[Lan04] A. Lange, M. P. Hentschel and J. Schors. Direct iterative reconstruction of computed tomography trajectories (DIRECTT). In *16th World Conference on Nondestructive Testing, WCNDT 2004*. (NDT.net, Montreal, Canada, 2004).

[Lan06] E. N. Landis. X-ray tomography as a tool for micromechanical investigations of cement and mortar. In J. Desrues, G. Vigianni and P. Besuelle (eds.), *Advances in X-ray Tomography for Geomaterials*, pages 79–93. (ISTE Ltd., London, UK, 2006).

[Lau12] M. v. Laue, W. Friedrich and P. Knipping. Interferenz-Erscheinungen bei Röntgenstrahlen. Sitzungsberichte Bayerische Akademie Wissenschaften Mathematisch-physikalishe Klasse, 303–322 (1912).

[Lax80] V. Laxmann and M. C. Flemings. Deformation of semi-solid Sn-15 Pct Pb alloy. Metall. Trans. A **11**, 1927–1937 (1980).

[Len03] N. Lenoir, Marello S., G. Viggiani, P. Besuelle, J. Desrues and M. DiMichiel. X-ray micro tomography characterization of strain localization upon deviatoric loading of saturated fine-grained stiff soils. In J. Otani and Y. Obara (eds.), *X-ray CT for Geomaterials*, volume 1, pages 147–155, A.A. Balkema Publishers, Kumamoto, Japan, 2003.

[Lif61] I. M. Lifshitz and V. V. Slyozov. The kinetics of precipitation from supersaturated solid solutions. J. Phys. Chem. **19**, 35–50 (1961).

[Lim07] N. Limodin, L. Salvo, M. Suery and M. DiMichiel. In situ investigation by X-ray tomography of the overall and local microstructural changes occurring during partial remelting of an Al-15.8 wt.% Cu alloy. Acta Mater. **55**, 3177–3191 (2007).

[Lin06] T. Link, S. Zabler, A. Epishin, A. Haibel, M. Bansal and Thibault X. Synchrotron tomography of porosity in single-crystal nickel-base superalloys. Mater. Sci. Eng., A **425**, 47–54 (2006).

[Lou95] W. R. Loué and M. Suéry. Microstructural evolution during partial remelting of Al-Si7Mg alloys. Mater. Sci. Eng., A **203**, 1–13 (1995).

[Luc04] P. W. Lucas. *Dental Functional Morphology: How Teeth Work*. (Cambridge Univ. Press, 2004).

[Lud04] O. Ludwig, M. DiMichiel, P. Falus, L. Salvo and M. Suery. In-situ 3D microstructural investigation by fast X-ray microtomography of Al-Cu alloys during partial remelting. In *Semisolid Proceedings*, Cyprus, 2004.

[Lun03] I. Lunati, P. Vontobel, W. Kinzelbach and E. Lehmann. Laboratory visualization of two-phase flow in a natural fracture by neutron tomography. In *Groundwater in Fractured Rocks*, volume 7, UNESCO IHP-VI, SERIES ON GROUNDWATER, Prague, Czech Republic, 2003. http://people.web.psi.ch/vontobel/images/GWFR2003_eabst.pdf.

[Mal93] T. Malzbender. Fourier Volume Rendering. ACM T. Graphic. **12**, 233–250 (1993).

[Mao06] W. L. Mao, H. Mao, Y. Meng, P. J. Eng, M. Y. Hu, P. Chow, Y. Q. Cai, J. Shu and R. J. Hemley. X-ray-Induced Dissociation of H_2O and Formation of an O_2-H_2 Alloy at High Pressure. Science **314**, 636–638 (2006).

[Mas90] T. B. Massalski. 1. In H. Okamoto, P. R. Subramaniam and L. Kacprzak (eds.), *Binary alloy Phase diagrams*. (The Materials Information Society, 1990).

[Mas07] B. C. Masschaele, V. Cnudde, M. Dierick, P. Jacobs and Vlassenbroeck J. Van Hoorebeke, L. UGCT: New X-ray radiography and tomography facility. Nucl. Instrum. Methods Phys. Res., Sect. A **580**, 266–269 (2007).

[Mat03] T. Matsushima, H. Saomoto, K. Uesugi, A. Tsuchiyama and T. Nakano. Detection of 3-D irregular grain shape of Toyoura sand at SPring-8. In J. Otani and Y. Obara (eds.), *X-ray CT for Geomaterials*, volume 1, A.A. Balkema Publishers, Kumamoto, Japan, 2003.

[May03] S. C. Mayo, T. J. Davis, T. E. Gureyev, P. R. Miller, D. Paganin, A. Pogany, A. W. Stevenson and S. W. Wilkins. X-ray phpase-contrast microscopy and microtomography. Opt. Express **11**, 2289–2302 (2003).

[Mei23] L. Meitner. Über eine mögliche Deutung des kontinuierlichen β-Strahlenspektrums. Z. Phys. A **19**, 307–312 (1923).

[Men04] R. Mendoza, I. Savin, K. Thornton and P. W. Voorhees. Topological complexity and the dynamics of coarsening. Nature **3**, 385–388 (2004).

[Men06] R. Mendoza, K. Thornton, I. Savin and P. W. Voorhees. The evolution of interfacial topology during coarsening. Acta Mater. **54**, 743–750 (2006).

[Miy76] T. Miyahara, H. Kitamura, S. Sato, M. Watanbe, S. Mitani, E. Ishiguro, T. Fukushima, T. Ishii, S. Yamaguchi, M. Endo, Y. Iguchi, H. Tsujikawa, T. Sugiura, T. Katayama, T. Yamakawa, S. Yamaguchi and T. Sasaki. SOR-RING, An electron storage ring dedicated to spectroscopy. Part. Accel. **7**, 163–175 (1976).

[Mod99] M. Modigell and J. Koke. Time dependent rheological properties of semi-solid metal alloys. Mech. Time-Depend. Mat. **3**, 15–30 (1999).

[Mod06] P. Modregger, D. Lübbert, P. Schäfer and R. Köhler. Magnified x-ray phase imaging using asymmetric Bragg reflection: Experiment and theory. Phys. Rev. B **74**, 054107 (2006).

[Mok07] R. Mokso, P. Cloetens, E. Maire, W. Ludwig and J.-Y. Buffière. Nanoscale zoom tomography with hard x rays using Kirkpatrick-Baez optics. Appl. Phys. Lett. **90**, 144104 (2007).

[Mom03] A. Momose. Phase-sensitive imaging and phase tomography using X-ray interferometers. Optics Express **11**, 2303–2314 (2003).

[Moo95] D. E. Moore and D. A. Lockner. The role of microcracking in shear-fracture propagation in granite. J. Struct. Geol. **17**, 95–114 (1995).

[Mü04] B. R. Müller and M. P. Hentschel. Synchrotron radiation refraction topography for characterization of lightweight materials. X-Ray Spectrom. **33**, 402–406 (2004).

[MW02] E. D. Manson-Whitton, I. C. Stone, J. R. Jones, P. S. Grant and B. Cantor. Isothermal grain coarsening of spray formed alloys in the semi-solid state. Acta Mater. **50**, 2517–2535 (2002).

[Naf04] S. Nafisi, R. Ghomashchi and A. Charette. The influence of grain refiner on the microstructural evolution of Al-7%Si and A356 in the Swirled Enthalpy Equilibration Device (SEED). In *S2P-8-Proceedings*, Cyprus, 2004.

[Nak04] Y. Nakashima, T. Nakano, K. Nakamura, K. Uesugi, A. Tsuchiyama and S. Ikeda. Three-dimensional diffusion of non-sorbing species in porous sandstone: computer simulation based on X-ray microtomography using synchrotron radiation. J. Contam. Hydrol. **74**, 253–264 (2004).

[Nir00] B Niroumand and K. Xia. 3D study of the structures of primary crystals in a rheocast Al-Cu alloy. Mater. Sci. Eng., A **283**, 70–75 (2000).

[Nyq28] A. Nyquist. Certain topics in Telegraph transmission theory. In *Transactions of the A. I. E. E.*, pages 617–644, 1928.

[Ohs00] J. Ohser and F. Mücklich. *Statistical Analysis of Microstructures in Materials Science*. Statistics in Practice. (John Wiley & Sons Ltd., 2000).

[Oht01] T. Ohtani, T. Nakano, Y. Nakashima and H. Muraoka. Three-dimensional shape analysis of miarolitic cavities and enclaves in the Kokkonda granite by X-ray computed tomography. J. Struct. Geol. **23**, 1741–1751 (2001).

[Ost00] W. Ostwald. Über die vermeintliche Isomerie des roten und gelben Quecksilberoxids und die Oberflächenspannung fester Körper. Z. Phys. Chem. **34**, 495 (1900).

[Ota03] J. Otani and Y. Obara (eds.). *X-ray CT for Geomaterials - Soils, Concrete, Rocks - International Workshop on X-ray CT for Geomaterials*, Kumamoto, Japan, November 6-7 2003.

[Pag98] D. Paganin and K. A. Nugent. Noninterferometric phase imaging with partially coherent light. Phys. Rev. Lett. **80**, 2586–2589 (1998).

[Pag06] D. M. Paganin. *Coherent X-Ray Optics*. Oxford series on synchrotron radiation. (Oxford University Press, Oxford, 2006).

[Par97] O. Paris, M. Fährmann, E. Fährmann, T. M. Pollock and P. Fratzl. Early stages of precipitate rafting in a single crystal Ni-Al-Mo model alloy investigated by small-angle X-ray scattering and TEM. Acta Mater. **45**, 1085–1097 (1997).

[Pas89] D. H. Pashley. Dentin: a dynamic substrate: a review. Scanning Microscopy **3**, 161–174 (1989).

[Pel93] P. J. N. Pells. Uniaxial Strength Testing. In J. A. Hudson (ed.), *Comprehensive rock Eng.: principles practice and projects*, pages 67–85. (Elsevier Science Publ. Co., 1993).

[Pfe06] F. Pfeiffer, T. Weitkamp, O. Bunk and C. David. Phase retrieval and differential phase-contrast imaging with low-brilliance X-ray sources. Nature **2**, 258–261 (2006).

[Pla98] D. Plaza, J. Asensio, J. A. Pero-Sanz and J. I. Verdeja. Microstructure, a Limiting Parameter for Determining the Eng. Range of Compositions for Light Alloys: The Al-Cu-Si System. Mater. Charact. **40**, 145–158 (1998).

[Que77] D. Quemada. Rheology of concentrated disperse systems and minimum energy dissipation principle. Rheol. Acta **16**, 82 (1977).

[Rac06] A. Rack. *Charakterisierung komplexer Materialsysteme mittels Synchrotron-Tomographie und 3D-Bildanalyse*. PhD thesis, Fak. III, Prozesswissenschaften, Technical University of Berlin, Germany, 2006.

[Rac07a] A. Rack, T. Martin, M. Couchaud, P.-A. Douissard, A. Cecilia, A. Danilewsky and T. Baumbach. Thin LSO-based mixed-crystal grown by liquid phase epitaxy for high resolution X-ray imaging. Poster presentation, SCINT2007 – North Carolina, USA, 2007.

[Rac07b] A. Rack, S. Zabler, B. R. Müller, H. Riesemeier, G. Weidemann, A. Lange, J. Goebbels, M. Hentschel and W. Görner. High resolution synhrotron-based radiography and tomography using hard X-rays at the BAMline (BESSY II). Nucl. Instrum. Methods Phys. Res., Sect. A, doi:10.1016/j.nima.2007.11.020 (2007).

[Rad17] J. Radon. Über die Bestimmung von Funktionen durch ihre Integralwerte längs gewisser Mannigfaltigkeiten. Berichte über die Verhandlungen der Sächsischen Akademie der Wissenschaften zu Leipzig - Mathematische Naturwissenschaftliche Klasse **69**, 262–277 (1917).

[Rat01] L. Ratke and P.W. Voorhees. *Growth and Coarsening*. (Springer, 2001).

[Rav96] C. Raven, A. Snigirev, I. Snigireva, P. Spanne, A. Souvorov and V. Kohn. Phase-contrast microtomography with coherent high-energy synchrotron x rays. Appl. Phys. Lett. **69**, 1826–1828 (1996).

[Rei83] P. Reimers and J. Goebbels. New Possibilities of Nondestructive Evaluation by X-ray Computed Tomography. Mater. Eval. **41**, 732–737 (1983).

[Rön95] W. C. Röntgen. Über eine neue Art von Strahlen. Aus den Sitzungsberichten der Würzburger Physik.-medic. Gesellschaft (1895).

[Roh98] T. Rohlfing, D. Zerfowski, J. Beier, P. Wust, N. Hosten and F. Felix. Reduction of Metal Artifacts in Computed Tomographies for the Planning and Simulation of Radiation Therapy. In H. U. Lemke, M. V. Vannier, K. Inamura and A. G. Farman (eds.), *CAR'98, Computer Assisted Radiology and Surgery*, pages 57–62. (Elsevier Sci., Tokyo, Japan, 1998).

[Ros98] P. Roschger, P. Fratzl, J. Eschberger and K. Klaushofer. Validation of quantitative backscattered electron imaging for the measurement of mineral density distribution in human bone biopsies. Bone **23**, 319–326 (1998).

[Row06] D. J. Rowenhorst, J. P. Kuang, K. Thornton and P. W. Voorhees. Three-dimensional analysis of particle coarsening in high volume fraction solid-liquid mixtures. Acta Mater. **54**, 2027–2039 (2006).

[Rue06] A. Rueda. *Untersuchung der Mikrostruktur und des Fliessverhaltens binärer thixotroper Legierungen mit Synchrotronstrahlung*. Master's thesis, Technical Univerity of Berlin, Germany, 2006.

[San94] F. Sanford. Some Experiments in Electric Photography. Phys. Rev. (Series I) **2**, 59–61 (1894).

[San03] F. Sanford. On an Undescribed form of Radiation. Phys. Rev. (Series I) **17**, 441–465 (1903).

[Sch49] J. Schwinger. On the Classical Radiation of Accelerated Electrons. Phys. Rev. **75**, 1912–1925 (1949).

[Sch81] G. Schramm. *Optimization of Rotovisco Tests*. (Gebrüder Haake GmbH, 1981).

[Sch99] E. M. Schulson, D. Iliescu and C. E. Renshaw. On the initiation of shear faults during brittle compressive failure: a new mechanism. J. Geophys. Res. **104**, 695–705 (1999).

[Sch03] C. G. Schroer, M. Kuhlmann, T. F. Günzler, B. Lengeler, M. Richwin, B. Griesebock, D. Lützenkirchen-Hecht, R. Frahm, E. Ziegler, A. Mashayekhi, D. R. Haeffner, J.-D. Grunwaldt and A. Baiker. Mapping the chemical states of an element inside a sample using tomographic x-ray absorption spectroscopy. Appl. Phys. Lett. **82**, 3360–3362 (2003).

[Sch07] C. Scheuerlein, M. DiMichiel and A. Haibel. On the formation of voids in internal tin Nb3Sn superconductors. Appl. Phys. Lett. **90**, 132510 (2007).

[Sha49] C. E. Shannon. Communication in the presence of noise. In *Proceedings of the IRE*, pages 10–21, 1949.

[She90] A. H. Sherry and R. Pilkington. In B. Wilshire and R. W. Evans (eds.), *Proc. 4th Int. Conf. On Creep and Fracture of Eng. Mat. and Struct.*, pages 333–344. (The Inst. of Metals, London, Swansea, 1990).

[Sla06] J. Slaby. *Automatisierung der Justierung eines Synchrotron-Tomographiemessaufbaus*. Master's thesis, Berufsakademie Berlin - FB Wirtschaft und Informatik, Germany, 2006.

[Sni95] A. Snigirev, I. Snigireva, V. Kohn, S. Kuznetsov and I. Schelokov. On the possibilities of x-ray phase contrast microimaging by coherent high-energy synchrotron radiation. Rev. Sci. Instrum. **66**, 5486–5492 (1995).

[Soi90] P. Soille and L. Vincent. Determining watersheds in digital pictures via flooding simulations. In M. Kunt (ed.), *Visual Communications and Image Processing*, Kapitel 1360, pages 240–250. (SPIE, 1990).

[Spi80] E. Spiller. Recent Developments towards high resolution X-ray imaging. Nucl. Instrum. Methods **177**, 187–192 (1980).

[Sri94] C. Srinivas and M. H. M. Costa. Motion-Compensated CT Image Reconstruction. In *ICIP94, International Conference on Image Processing*, pages II: 849–853. (IEEE, 1994).

[Taf04] P. Tafforeau. *Aspects Phylogenetiques et foncionnels de la microstructure de l'email dentaire et de la structure tridimensionelle des molaires chez les primates fossiles et actuels: Apports de la microtomographie a rayonnement X synchrotron*. PhD thesis, University of Montpellier II, France, 2004.

[Tak57] S. Takahashi. Rotation Radiography. Japan Society for Promotion of Science, 164 (1957).

[Tak84] S. Takajo, W. A. Kaysser and G. Petzow. Analysis of particle growth by coalescence during liquid phase sintering. Acta Metall. **32**, 107–113 (1984).

[Tea83] M. R. Teague. Deterministic phase retrieval: a Green's function solution. J. Opt. Soc. Am. **73**, 1434–1441 (1983).

[Tes01] W. Tesch, N. Eidelman, P. Roschger, F. Goldenberg, K. Klaushofer and P. Fratzl. Graded microstructure and mechanical properties of human crown dentin. Calcif. Tissue Int. **69**, 147–157 (2001).

[Thi87] W.K. Thieringer and L. Ratke. The coarsening of liquid Al-Pb-Dispersions. Acta Metall. **35**, 1237–1244 (1987).

[Tod06] H. Toda, K. Minami, M. Kobayashi, K. Uesugi, A. Takeuchi and T. Kobayashi. Observation of Precipitates in Aluminum Alloys by Sub-Micrometer Resolution Tomography Using Fresnel Zone Plate. Mater. Sci. Forum **519-521**, 1361–1366 (2006).

[Tom56] D. H. Tomboulian and P. L. Hartman. Spectral and Angular Distribution of Ultraviolet Radiation from the 300-Mev Cornell Synchrotron. Phys. Rev. **102**, 1423–1447 (1956).

[Tsa03] C.-S. Tsao, C.-Y. Chena, T.-Y. Kuob, Linc T.-L. and Yu M.-S. Size distribution and coarsening kinetics of δ' precipitates in Al-Li alloys considering temperature and concentration dependence. Mater. Sci. Eng., A **363**, 228–233 (2003).

[Tur04] L. Turner, B. Dhal, J. Hayes, A. Mancuso, K. Nugent, D. Paterson, R. Scholten, C. Tran and A. Peele. X-ray phase imaging: Demonstration of extended conditions for homogeneous objects. Opt. Express **12**, 2960–2965 (2004).

[Tzi00] E. Tzimas and A. Zavaliangos. Evolution of near-equiaxed microstructure in the semisolid state. J. Mater. Sci. Technol. **289**, 228–240 (2000).

[Ugg04] P. J. Uggowitzer and H. Kaufmann. Evolution of globular microstructure in New Rheocasting and Super Rheocasting semi-solid slurries. Fundamentals of Thixoforming Processes **75**, 525–530 (2004).

[Ver03] A. Vervoort, M. Wevers, R. Swennen, S. Roels, M. Van Geet and E. Sellers. Recent advantages of X-ray CT and its applications for rock material. In J. Otani and Y. Obara (eds.), *X-ray CT for Geomaterials*, volume 1, A.A. Balkema Publishers, Kumamoto, Japan, 2003.

[Vin91] L. Vincent and P. Soille. Watersheds in Digital Spaces: An Efficient Algorithm Based on Immersion Simulations. In *Transactions on Pattern analysis and Machine Intelligence*, volume 13, Kapitel 6, pages 583–598. (IEEE, June 1991 1991).

[Vla07] J. Vlassenbroeck, M. Dierick, B. C. Masschaele, V. Cnudde, L. Van Hoorebeke and P. Jacobs. Software tools for quantification of X-ray microtomography at the UGCT. Nucl. Instrum. Methods Phys. Res., Sect. A **580**, 442–445 (2007).

[Voo85] P. W. Voorhees. The theory of Ostwald ripening. J. Stat. Phys. **38**, 231–252 (1985).

[Voo92] P. W. Voorhees. Ostwald ripening of two-phase mixtures. Annu. Rev. Mater. Sci. **22**, 197–215 (1992).

[Wag61] C. Wagner. Theorie der Alterung von Niederschlagen durch Umlösen (Ostwald-Reifung). Z. Elektrochem. **65**, 581–591 (1961).

[Wan98] R. Wang and S. Weiner. Strain-structure relations in human teeth using Moire fringes. J. Biomech. **31**, 135–141 (1998).

[War96] J. A. Warren and B. T. Murray. Ostwald ripening and coalescence of a binary alloy in two dimensions using a phase-field model. Modell. Simul. Mater. Sci. Eng. **4**, 215–229 (1996).

[Wei98] S. Weiner and H. D. Wagner. The material bone: structure- mechanical function relations. Ann. Rev. Mat. Sci. **28**, 271–298 (1998).

[Wei99] S. Weiner, A. Veis, E. Beniash, T. Arad, J. W. Dillon, B. Sabsay and F. Siddiqui. Peritubular dentin formation: crystal organization and the macromolecular constituents in human teeth. J. Struc. Biol. **126**, 27–41 (1999).

[Wie30] N. Wiener. Generalized harmonic analysis. Acta Math. **55**, 117–258 (1930).

[Wil96] S. W. Wilkins, T. E. Gureyev, D. Gao, A. Pogany and A. W. Stevenson. Phase-constrast imaging using polychromatic hard X-rays. Nature **384**, 335–338 (1996).

[Win02] B. Winkler, K. Knorr, A. Kahle, P. Vontobel, E. Lehmann, B. Hennion and G. Bayon. Neutron imaging an neutron tomography as non-destructive tools to study bulk-rock samples. Eur. J. Mineral. **14**, 349–354 (2002).

[Wol97] T. L. Wolfsdorf, W.H.J. Bender and P. W. Voorhees. The morphology of high volume fraction solid-liquid mixtures: an application of microstructural tomography. Acta Mater. **45**, 2279–2295 (1997).

[Yam04] T. Yamanaka. *Reconstruction de la phase pour l'imagerie 3D utilisant le rayonnement synchrotron coherent*. Master's thesis, UFRIMA, France, 2004.

[Zab05] S. Zabler, P. Cloetens, J.-P. Guigay, J. Baruchel and M. Schlenker. Optimization of phase contrast imaging using hard x rays. Rev. Sci. Instrum. **76**, 073705 (2005).

[Zab06] S. Zabler, P. Zaslansky, H. Riesemeier and P. Fratzl. Fresnel-propagated imaging for the study of human toth dentin by partially coherent x-ray tomography. Opt. Express **14**, 8584–8597 (2006).

[Zab07a] S. Zabler, P. Cloetens and P. Zaslansky. Fresnel-propagated submicrometer x-ray imaging of water-immersed tooth dentin. Opt. Lett. **32**, 2987–2989 (2007).

[Zab07b] S. Zabler, A. Rueda, A. Rack, H. Riesemeier, Zaslansky P., I. Manke, F. Garcia-Moreno and J. Banhart. Coarsening of grain-refined semi-solid Al-Ge32 alloy: X-ray microtomography and in situ radiography. Acta Mater. (2007).

[Zab07c] S. Zabler, K. Thermann, N. Harthill, J. Tiedemann, I. Manke, A. Rack and H. Riesemeier. High-resolution tomography of cracks, porosity and microstructure in greywacke and limestone. Submitted to J. Struct. Geol., 2007.

[Zan00] A. Zang, F. C. Wagner, S. Stanchits, C. Janssen and G. Dresen. Fracture process zone in granite. J. Geophys. Res. **105**, 23651–23661 (2000).

[Zas06] P. Zaslansky, A. A. Friesem and S. Weiner. Structure and mechanical properties of the soft zone separating bulk dentin and enamel in crowns of human teeth: Insights into tooth function. J. Struct. Biol. **153**, 188–199 (2006).

[Zer98] D. Zerfowski. Motion Artifact Compensation in CT. In *Int. Symposium on Med. Imaging*. (SPIE, San Diego CA, USA, 1998).

[Zer99] D. Zerfowski, H. Grabowski, R. Krempien, S. Hassfeld and M. Walz. Aufbereitung medizinischer Bilddaten. Informatik Forsch. Entw. **14**, 2–9 (1999).

Appendix C

Acknowledgment

Diese Doktorarbeit wurde am Hahn-Meitner-Institut Berlin (HMI), in enger Kooperation mit der Bundesanstalt für Materialforschung (BAM) und dem Max-Planck Intitut für Kolloid und Grenzflächenforschung (MPIKG) angefertigt. Mein besonderer Dank gilt deshalb Prof. John Banhart, für die Betreuung und die Möglichkeit, diese 3 Jahre in der Abteilung SF3 zu doktorieren. Dr. Alexander Rack sei für die vielen Stunden bei BESSY, sein Vertrauen, seine kritische wissenschaftliche Haltung und seinen Reichtum an immer neuen Ideen gedankt. An Rainer Grupp, Dr. Ingo Manke und Dr. Astrid Haibel ebenfalls vielen herzlichen Dank für Diskussion und tatkräftige Unterstützung bei den Messungen. The first few months at HMI, I shared the office with Dr. Sahoo who I thank a lot for the discussions we had about metallic alloys and their microstructure. Danke an die "Neutronentomographen" - Dr. Nikolay Kardjilov und Andre Hilger - sowie an die Diplomanden - Antonio Rueda, Jakob Slaby und Mirko Boin - für die viele Hilfe, Geduld und v. a. die sehr gute Arbeit, die sie geleistet haben. Ganz besonders wichtig für das Gelingen dieser Arbeit war die Hilfe von Dr. Christian Abromeit. Glücklicherweise hat sich Jörg Bajorat liebevoll um jede Festplatte und um jeden der zahlreichen Mikroprozessoren, die an dieser Arbeit beteiligt waren, gekümmert. Yvonne Herzog hatte immer das passende Formular, und die Metallographie - Werner Rönnfeld, Claudia Leistner, Holger Kropf und Christiane Förster - immer die passende Legierung.
Dr. Jürgen Goebbels, Dr. Gerd Weidemann und Dr. Heinrich Riesemeier ein ganz besonders grosser Dank für die unzähligen Meetings bei der BAM und v.a. für die Unterstützung bei den zahlreichen BAM*line* Messkampagnen. Thomas Wolk hat sich meine Bewunderung durch seinen unermüdlichen Tatendrang und Optimismus bei der Lösung unzähliger Soft- und Hardwareprobleme an der CT-Steuerung verdient (Danke Tom, ohne Dich hätten wir alle längst aufgegeben). Monika Klinger und Herr Heimbach haben einen unverzichbaren Beitrag bei der Konstruktion und dem Bau des "neuen" CT-Aufbaus geleistet. Dr. Bernd Müller sei gedankt für seine Ordentlichkeit, seine an Wunder grenzende Fähigkeit, jedes Semester einen tauglichen Nutzerplan für die BAM*line* zu erstellen, und einfach für die vielen tausend Kleinigkeiten.
I would further like to thank Dr. Paul Zaslansky, for *pressurizing* and *pushing* me to do what I did not want to do but what I ended up doing a lot: writing papers. Thank you Paul, for the good and for the bad times. Further thanks go to Prof. Peter Fratzl and Prof. John Currey, for support, discussion and help with these publications, as well as to Dr. Oskar Paris for volunteering to read and assess this thesis. Prof. Joachim Ohser, Dr. Katja Schladitz and Michael Godehardt provided help, support and licenses for the 3D image analysis with MAVI. Thank

you, also for the good discussions and the excellent workshop in Kaiserslautern.
Prof. J. Tiedemann und Bjoern Kremmin vielen Dank für die Steine und die Ideen zum Projekt der Rissuntersuchung. Karsten Thermann, der bis zum Schluss dieser Arbeit unermüdlich Gesteinsdaten rekonstruiert und mit ausgewertet hat, ein ganz besonders grosses Danke und viel Erfolg.
The contribution of Dr. Peter Cloetens and Dr. Jean-Pierre Guigay to this work is significant. Most of the instrumental work at the BAM*line* as well as the phase-retrieval software is based on what I learned from these two, during my master's thesis and later discussions at the ESRF/ID19 beamline. Thank you, Peter and Jean-Pierre. During these three years, I wrote a lot of 2D and 3D imaging software, and would therefore like to thank Dr. Luc Salvo for teaching me 'image analysis' and programming 'C' while I was, first a student, and later a trainee in his group at INPG/GPM2 in Grenoble, France.
Zuguterletzt danke ich Astrid und den Kindern - Melissa, Felina und Thaddäa - für die viele Geduld und Unterstützung, die mir das Schreiben dieser Arbeit ermöglicht haben. Meinen Eltern, und ganz besonders meinem Vater, Dr. Erich Zabler, dafür, dass er mich bereits 2001 für Röntgentomographie begeisterte, lange bevor ich jemals eine Beamline von innen gesehen hatte.